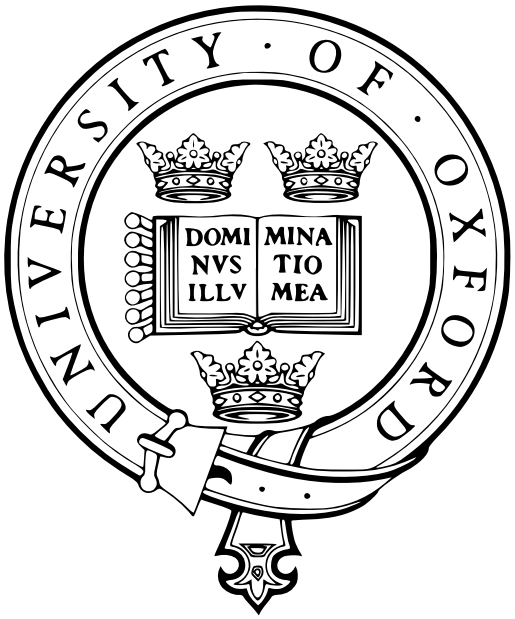


Driven Colloidal Particles in Optical Potential Energy Landscapes

Miranda Bell-Davies

Lincoln College
University of Oxford

Supervisor: Prof. Roel P. A. Dullens

A thesis submitted for the degree of
Doctor of Philosophy

Michaelmas 2022

Abstract

The structure and dynamics of colloidal particles in optical potential energy landscapes is studied. Experiments use paramagnetic or optically anisotropic colloidal particles interacting with lines or pairs of time-dependent optical traps. First, the pairwise interactions of the paramagnetic particles are measured using pairs of optical traps. We test a novel data analysis method under various conditions and calculate the magnetic susceptibility of the particles. Next, we measure the structure and dynamics of chains of paramagnetic colloids in a sinusoidal optical potential of varying depth. At well defined chain lengths, we observe a transition from an asymmetric, strongly pinned state to a free-sliding, symmetric state as the optical potential decreases. We then analyse the frictional dynamics of the same system under a constant driving force and observe a transition from low to high friction as the optical potential increases. We model the dynamics of the chains in the low and high friction regimes. The simple hard sphere model developed for the high friction regime is used to derive an equation which predicts the transition point from low to high friction. Next, we drive the chains through a time-dependent optical potential with an oscillating depth. We analyse the synchronisation of the chain's motion to the oscillations of the potential and characterise the dynamics, observing a novel mode of motion involving the simultaneous nucleation of kinks and anti-kinks. Finally, we study the dynamics of a single optically anisotropic dumbbell particle interacting with a repulsive optical trap controlled by a time-delayed feedback protocol. We observe a transition from diffusive to driven dynamics which is modelled using delay-differential equations. We find that this transition coincides with the maximum work done on the particle and a local minimum in the mutual information between the particle and the trap.

Declaration

This thesis is submitted for the degree of Doctor of Philosophy in Physical and Theoretical Chemistry at the University of Oxford. No part of this thesis has been accepted or is currently being submitted for any degree, diploma, certificate or other qualification in this University or elsewhere. This thesis is wholly my own work, except where indicated.

Contents

Abstract **i**

Declaration **iii**

1 Introduction **1**

1.1 The Frenkel-Kontorova model 2

1.2 Colloidal model systems 3

1.3 Scope of this thesis 5

2 Theoretical background and experimental methods **7**

2.1 The Langevin equation 8

2.2 Properties of colloidal suspensions 9

2.2.1 Diffusion 9

2.2.2 Diffusion versus driving forces 10

2.2.3 Drag force from the solvent 11

2.2.4 Gravity 11

2.2.5 Inter-particle interactions 11

2.2.6 Optical trapping 15

2.3 Experimental methods 18

2.3.1 Samples 18

2.3.2 Experimental setup 19

2.3.3 Particle tracking 24

2.4 Brownian Dynamics simulations 25

3 Measuring pair potentials with optical traps 27

3.1 Introduction 28

3.2 Theory 29

3.3 Experimental methods 31

3.3.1 Experimental setup 31

3.3.2 Characterising the optical trap contribution 33

3.3.3 Calculating the full potential by joining each measurement 35

3.3.4 Zero-field pair potential measurements 36

3.4 Results and discussion 37

3.4.1 Pair potential measurement 37

3.4.2 Different trap strengths 39

3.4.3 Different magnetic fields 40

3.4.4 Magnetic susceptibility 41

3.5 Conclusions 42

4 Aubry-type transition of undriven colloidal chains in a periodic potential 45

4.1 Introduction 46

4.2 Theory 48

4.2.1 The Frenkel-Kontorova model for flexible chains in a periodic potential . 48

4.2.2 Ground states 49

4.2.3 Metastable states 52

4.2.4 Finite chains in a sinusoidal potential 53

4.2.5 Rigid, finite chains in a sinusoidal potential 54

4.3 Experimental methods 56

4.4 Results and discussion 57

4.4.1 Chain structure 57

4.4.2 Symmetry . . . 62
4.4.3 Chain dynamics . . . 63
4.4.4 Chain energy . . . 66
4.5 Conclusions . . . 68

5 Friction of driven colloidal chains in a periodic potential 71
5.1 Introduction . . . 72
5.2 Theory . . . 74
5.2.1 Langevin equation of a rigid chain driven through a sinusoidal potential . 74
5.2.2 Average velocity of a driven rigid chain . . . 75
5.2.3 Driven flexible chains . . . 78
5.3 Experimental methods . . . 79
5.3.1 Critical velocity measurements . . . 79
5.3.2 Simulations . . . 81
5.3.3 Kink tracking . . . 81
5.4 Results and discussion . . . 83
5.4.1 Critical velocity . . . 83
5.4.2 Dynamics in the weak substrate limit . . . 84
5.4.3 Dynamics in the strong substrate limit . . . 90
5.5 Conclusions . . . 100

6 Synchronisation of driven colloidal chains in an oscillating periodic potential 103
6.1 Introduction . . . 104
6.2 Theory . . . 106
6.2.1 Deterministic average velocity . . . 107
6.2.2 Noise . . . 109
6.3 Experimental methods . . . 110
6.4 Results and discussion . . . 112

6.4.1 Average velocity measurements . . . 112
6.4.2 Modified low frequency theory . . . 115
6.4.3 Kink dynamics . . . 116
6.5 Conclusions . . . 120

7 Time-delayed feedback of a colloidal particle in an optical trap 123
7.1 Introduction . . . 124
7.2 Theory . . . 125
7.2.1 Particle on a ring . . . 125
7.2.2 Time-delayed feedback . . . 127
7.2.3 Stochastic thermodynamics . . . 129
7.3 Experimental methods . . . 133
7.3.1 Colloidal dumbbell particles and experimental setup . . . 133
7.3.2 Measurement of the background potential and drag constant . . . 135
7.3.3 Trap force measurement . . . 136
7.3.4 Simulations . . . 137
7.4 Results and discussion . . . 138
7.4.1 Dynamics . . . 138
7.4.2 Stochastic delay differential equations . . . 142
7.4.3 Stochastic thermodynamics . . . 146
7.5 Conclusions . . . 147

Appendix 149
A Drag constant of chains of N particles . . . 149
B Matching the experimental interaction parameter to simulations . . . 150
C Average distance between particles in a flat landscape . . . 152
D Chain breakage . . . 153

Bibliography **155**

Acknowledgements **175**

Chapter 1

Introduction

Competing length-, time- and energy-scales determine the behaviour of many physical systems. For example, the competition between two different lattice constants in layered materials can produce materials with periodic superstructures [1,2]. Competing length scales are also essential to the formation of quasicrystals [3], and can also produce disordered or jammed structures [4,5], with consequences for the electronic, magnetic and mechanical properties [5–7]. Likewise, the competition between different relaxation times, delay times and oscillation periods can lead to complex non-linear dynamics. The synchronisation of modern clocks, flashing fireflies and circadian rhythms, for instance, all involve the coupling of oscillators with competing frequencies [8]. Delay times also play an important role in the regulation of biological rhythms [9], as well as causing periodicity in predator-prey populations [10] and the formation of traffic jams [11].

When a system is driven out of equilibrium, competition also arises between the external driving force and the relaxation of the system towards equilibrium. In biology, for instance, the competition between the relaxation timescales of active and passive processes regulates the many complex cycles essential to life [12]. Driving forces can produce chaotic motion, such as in weather systems [13], but often driven system will reach a steady state where energy is inputted and dissipated at a constant rate [14]. Non-equilibrium steady states govern everything from celestial orbits [15] to the metabolism of all living organisms [16].

Often, non-equilibrium steady states can be modelled as the motion of a particle or ensemble of particles over a potential energy landscape. A classic example is a particle driven over a sinusoidal potential; a model which applies the motion of a pendulum [17] and the transport of

electrons through a crystal [18], among other examples. Depending on the competition between the driving force and force from the potential, the model enters a pinned state, a steady state characterised by stick-slip motion of the particle, or a running steady state. These general phenomena govern the friction between surfaces on the atomic [19] to tectonic scale [20]. Studying universal models such as a particle on a periodic potential can thus give insights into many seemingly unrelated systems.

1.1 The Frenkel-Kontorova model

A related model important to this thesis is the Frenkel-Kontorova (FK) model, which consists of an infinite chain of harmonically interacting particles on a rigid sinusoidal substrate [21], shown in figure 1.1. Despite its simplicity, the FK model displays many of the aforementioned phenomena under different conditions, including complex phase behaviour, chaotic or steady state motion, and synchronisation. The model was originally proposed in 1938 to describe the dynamics of dislocations in crystals [22], but has since been applied to a multitude of systems composed of interacting periodic structures, including crystalline surfaces [6], grain boundaries [23], periodic lattice distortions such as those responsible for charge density waves [24, 25], atomic spins [26], interacting vortices in type-II superconductors [25, 27], and even the bases of a DNA chain [28] or the coils of a protein [29].

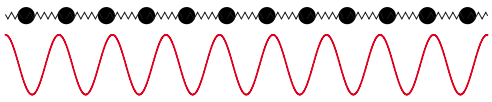


Figure 1.1: Frenkel-Kontorova model of a harmonic chain in a sinusoidal substrate.

The structure of all of these systems depend on the competition between the inherent length and energy scales of each component; that is, the distance between particles in the chain versus the wavelength of the substrate and the stiffness of the chain versus the depth of the substrate. When the chain is free to expand and contract, its phase diagram is a "Devil's staircase" of ground states with different values of the mismatch between the chain and the substrate's spacing [30]. If the ratio between the length scales is instead fixed at an irrational value, the ground state of the chain undergoes a remarkable structural transition from a pinned to free-sliding state as the substrate depth decreases, known as the Aubry transition [31].

The response of the FK model to an external driving force depends intrinsically on its structure. In the pinned phase, the motion of the chain is mediated by the movement of kinks and anti-kinks. Kinks and anti-kinks are defined as a region where a potential well contains one extra or missing particle respectively [32]. The process of creating and moving a kink can have a large energy barrier, which limits the mobility of the chain [33, 34]. Conversely, in Aubry's free sliding phase, an infinitesimal force is enough to move the chain across the substrate without resistance. This prediction has found exciting technological implications in the vanishing friction between atomically smooth surfaces, recently observed in several atomic force experiments [35–39]. Aubry's free sliding phase also governs the gliding of defects under stress [40] and has been used to model the metal to insulator transition in charge density waves [25].

The response of an FK system to an external driving force can be altered by adding an oscillating component to either the driving force or the substrate depth. This introduces competition between the time-scales of the oscillations and the chain's motion over the substrate. The chain's motion may synchronise to the oscillations, so that the average velocity as a function of the driving velocity resembles another "Devil's staircase" of mode-locked, synchronous steps separated by asynchronous regions [25]. Synchronised steps of this kind have been observed in the current of coupled superconducting Josephson junctions [41]. Substrate oscillations have also been shown to reduce friction [42], although the mechanism behind this is still poorly understood.

1.2 Colloidal model systems

One major challenge in the study of Frenkel-Kontorova problems in atomic or biological systems is the difficulty of observing structure and dynamics at the single particle level; a need that can be met experimentally using colloidal models [43]. Colloids are defined purely by their size; a colloidal suspension contains a phase with at least one length-scale on the order of nanometres to micrometres [44]. Many biological [45], pharmaceutical [46] and industrial [47] substances are colloidal suspensions, making them an important field of study in their own right, but synthetic colloidal particles are also extensively used as "test tube simulations" to mimic atomic systems [48].

Colloidal suspensions explore phase space in the same way as atoms [49] because they undergo Brownian motion – a random walk arising from the bombardment of the particle by thermally excited solvent molecules [50]. The use of colloids to study phase behaviour is particular attractive because they are so versatile. Colloidal interactions can be modified by changing their surface chemistry, for instance through the addition of charged surface groups [51] or adsorbing polymers [52]; by adding depletants [53]; or by exploiting the response of particles to an external electric [54] or magnetic field [55]. Additionally, a smorgasbord of colloidal shapes can be synthesised, from spheres to raspberries [56,57], peanuts [58], bananas [59] and more [60–62]. By employing all of these tools, colloids have been used to study the structure of many types of liquid-like [63,64], crystalline [62,63,65–67], liquid crystalline [54,59,68,69], glassy [63,70] and gel-like [71] phases.

As well as revealing the equilibrium phase behaviour of particles with different shapes and interactions, colloidal suspensions have also been used extensively as dynamic models [64,72,73]. Brownian motion has an experimentally accessible timescale of seconds rather than nanoseconds, and while it lacks the inertial term present in atomic motion, it does mimic the long-time dynamics of atoms. Colloidal particles can therefore be used to model the motion of atomic systems whose long-time dynamics, primarily determined by the system's structure, dominate [74], for example the dynamics of dense phases [75] or motion over a potential energy landscape [76].

Colloids are readily manipulated using external fields [77–80] and, of particular importance in this thesis, optical traps [81]. The simplest optical trap is a focused laser beam which interacts with a colloidal particle to create a Gaussian potential [82]. These can be used to measure the force between a probe particle and its surroundings [83], making optical trapping a powerful tool in the micro-rheology of colloidal suspensions [84,85] and biological materials [86,87], or measuring the interactions between particles [88,89]. More complex optical landscapes can be created either by rapidly time-sharing laser beams between different positions, using the interference of multiple beams, or manipulating the beam's wavefront using holograms [82]. These techniques have been used to create patterned potential landscapes which alter the diffusion [90–92] and phase behaviour of colloidal monolayers [93–96]. The addition of an external driving force or time-dependent component to the optical potential has been used for particle sorting [97,98], to study non-equilibrium driven steady states [72,99,100] with complex collec-

tive dynamics [76, 101–103], and test the theories of stochastic thermodynamics [104–111]. The diversity of techniques available makes optical trapping a versatile tool with ever more exciting applications.

Our experiments combine many of these techniques in order to create colloidal model systems. We use magnetic fields to tune the interactions between our particles and optical traps to create periodic, time-dependent potential energy landscapes. We place chains of attractive magnetic particles in a periodic optical potential, forming a colloidal analogue of the Frenkel-Kontorova model. Our ability to control the parameter space allows the systematic study of phenomena such as the Aubry transition, friction, synchronisation and feedback at the single particle level.

1.3 Scope of this thesis

In this thesis, we study the structure and dynamics of colloidal chains or single particles interacting with quasi-one dimensional optical potential energy landscapes of increasing complexity.

Chapter 2 introduces the theoretical background and experimental methods important in the rest of the thesis. Beginning with the Langevin equation of motion for a colloidal particle, we discuss the many types of forces acting on a colloidal system, including Brownian forces, gravity, drag, internal interactions, and optical traps. We then describe our experimental samples and optical setup, some general data analysis methods, and the Brownian Dynamics simulations used to supplement our experiments.

In chapter 3, we measure the pair potential of the paramagnetic particles used in subsequent chapters. We measure the distribution of pairs of particles inside two optical traps and use a new data analysis technique to convert this into the pair potential. We test the sensitivity of the method to the trap strength and its applicability to measuring both repulsive and attractive pair potentials. We use the results to calculate the magnetic susceptibility of the particles, which agrees well with literature values.

In chapter 4, we create a colloidal analogue of the Frenkel-Kontorova model consisting of chains of up to 20 paramagnetic particles in a sinusoidal optical substrate. We study the phase behaviour of the system by slowly decreasing and then increasing the depth of the optical

potential. We find that different chain lengths show slightly different, but related, phase transitions. All of these transitions are characterised by a sudden loss of reflectional symmetry and a decrease in mobility; the signatures of a finite Aubry transition.

Having characterised the phase behaviour of the chains, we then study their dynamics under a constant driving force in chapter 5. This system is a model of atomic friction. We measure the de-pinning force of the chains, observing a transition from low to high friction. We model the dynamics in the low friction regime as a small, uniform expansion. In the high friction limit, we observe the creation, translation and annihilation of kinks. We develop a hard sphere kink model and derive simple expressions for the kink creation energy and resulting friction force. This model successfully predicts the transition from low to high friction.

Chapter 6 introduces an additional level of complexity into the system by making the optical substrate potential time dependent. We oscillate the depth of the potential at different amplitudes and frequencies, causing the driven motion of the chain to synchronise to the oscillations. We measure the effect of chain length, oscillation amplitude and frequency on the synchronisation and analyse the dynamics. We observe an exotic mode of motion involving travelling kink/anti-kink pairs.

In chapter 7, we study a time delayed feedback driven system. We analyse the dynamics of experiments involving an optically anisotropic dumbbell particle, which behaves as a particle on a ring, interacting with a repulsive optical trap. We study the dynamics of the particle over several orders of magnitude of delay time, observing a transition from diffusive to driven behaviour. By modelling both regimes using delay differential equations, we derive a condition for a stable driven steady state. This result is used to rationalise the non-monotonic delay time dependence of the work done on the particle and mutual information between the particle and trap.

Chapter 2

Theoretical background and experimental methods

Abstract

In this thesis, we study the dynamics of driven colloidal particles in optical potential energy landscapes. This chapter discusses the theoretical background and experimental setup used throughout the rest of the thesis. In the first section, we introduce the Langevin equation, which describes the motion of a colloidal particle subject to deterministic and fluctuating forces. Next, we describe the interactions between colloidal particles, in particular the dipole-dipole interaction between paramagnetic colloids. Optical trapping is then discussed in terms of its theoretical basis and its uses in constructing potential energy landscapes. In the experimental section, we describe the colloidal particles, experimental setup, image analysis techniques and Brownian Dynamics simulations used in chapters 3 to 6 (chapter 7 uses different experimental methods which will be discussed in section 7.3).

2.1 The Langevin equation

Newton's second law of motion, $\sum \mathbf{F} = m\mathbf{a}$, describes the acceleration, $\mathbf{a}$, of a particle of mass m subject to external forces $\sum \mathbf{F}$. In the case of a colloidal particle in a solvent, these forces may arise from external fields, interactions between other colloidal particles, the drag force from the solvent (which is proportional to the particle's velocity) and a fluctuating force arising from the random bombardment of the particle by thermally excited solvent molecules. The resulting equation of motion is a Langevin equation:

$$m\frac{d^2\mathbf{r}}{dt^2} = \mathbf{F}_{ext}(\mathbf{r},t) + \xi(t) - \zeta\frac{d\mathbf{r}}{dt}\ . \tag{2.1}$$

Here, $m\frac{d^2\mathbf{r}}{dt^2}$ is the inertial term, $\xi(t)$ is the fluctuating force, $-\zeta\frac{d\mathbf{r}}{dt}$ is the drag force from the solvent, and $\mathbf{F}_{ext}(\mathbf{r},t)$ represents all other external forces acting on the particle. The inertial term is often ignored in colloidal systems because it is quickly dissipated by the surrounding fluid. The importance of inertial forces relative to viscous forces is quantified by the Reynolds number [112],

$$\mathrm{Re} = \frac{\rho v a}{\eta}, \tag{2.2}$$

where ρ is the solvent density, v is the particle velocity, a is the particle's hard sphere radius and η is the solvent viscosity. Colloidal systems have typical values of $a = 1\,\mu\mathrm{m}$, $\rho = 1\times10^3\,\mathrm{kg\,m^{-3}}$, $\eta = 1\times10^{-3}\,\mathrm{Pa\,s}$, and typical velocities arising from driving forces and thermal motion on the order of $v = 0.1\,\mu\mathrm{ms}^{-1}$ to $10\,\mu\mathrm{ms}^{-1}$, giving $\mathrm{Re} \approx 1\times10^{-7}$ to 1×10^{-5}. The inertial term may therefore be set to 0. This leads to the following *over-damped* Langevin equation:

$$\frac{d\mathbf{r}}{dt} = \zeta^{-1}(\mathbf{F}(\mathbf{r},t) + \xi(t)). \tag{2.3}$$

This is the central equation of motion which describes the colloidal particles in every experiment in this thesis.

2.2 Properties of colloidal suspensions

In this section, we will discuss each term in equation 2.3 in the context of the colloidal suspensions used in this thesis. We start with the fluctuating force, followed by the drag force, gravity, interactions with other colloidal particles and finally optical trapping forces.

2.2.1 Diffusion

The fluctuating force, $\xi(t)$, is the characteristic feature of a Langevin equation. When there is a separation of timescales between rapidly and slowly changing variables – in our case, the solvent molecules and the colloidal particles respectively – the fast variables can be assumed to exert a delta-correlated force on the slow variables. This force has a Gaussian probability distribution with mean $\langle \xi(t) \rangle = 0$ and correlation function

$$\langle \xi(t)\xi(t') \rangle = 2\zeta k_B T \delta(t - t'), \tag{2.4}$$

where k_B is Boltzmann's constant, T is the temperature, ζ is the drag constant of the particle, and $\delta(t-t')$ is a Dirac delta function. In the absence of other external forces, thermal fluctuations cause the particle to move in a random walk. Mathematically, a random walk may be described using either the mean squared displacement (MSD) of the particle from its starting position or the probability distribution of the displacements. Both descriptions will be used throughout the thesis.

From equation 2.3, it is possible to derive the following expression for the MSD, $\langle \delta r^2 \rangle$ [113]:

$$\langle \delta r^2 \rangle = 2dDt, \tag{2.5}$$

where d is the number of dimensions the particle diffuses in and D is the diffusion coefficient, equal to

$$D = \frac{k_B T}{\zeta}. \tag{2.6}$$

The timescale of diffusion is quantified by the Brownian time, τ_B, defined as the average time taken for a particle to diffuse over its own diameter, $2a$. This may easily be found by rearranging

equation 2.5:

$$\tau_B = \frac{2a^2}{dD}. \tag{2.7}$$

For colloidal particles with a radius of around $a = 1\,\mu\text{m}$, τ_B is typically on the order of 10 s.

A random walk may also be described by the particle's probability distribution over time for a given starting position $\mathbf{r}_0$ [114],

$$P(\mathbf{r}, t) = \frac{1}{\sqrt{4\pi D t}} \exp\left[-\frac{(\mathbf{r} - \mathbf{r}_0)^2}{4Dt}\right]. \tag{2.8}$$

When a particle is also subject to an external potential $U(\mathbf{r})$, Brownian motion allows the particle to explore the potential such that its long-time probability distribution becomes the Boltzmann distribution,

$$P(\mathbf{r}, t \to \infty) = N \exp(-\beta U(\mathbf{r})), \tag{2.9}$$

where $\beta = (k_B T)^{-1}$ and N is a normalisation constant. The Boltzmann distribution is used extensively throughout the thesis both to model the distribution of particle positions in a potential and as a way to measure the potential, $\beta U(\mathbf{r})$, from an experimentally determined $P(\mathbf{r})$.

2.2.2 Diffusion versus driving forces

The importance of thermal fluctuations compared to the deterministic forces in the Langevin equation is quantified by the Péclet number (Pe), defined as the ratio between the rate of diffusive and directed transport [115]. The former may be quantified by the Brownian time, τ_B, and the latter by the time taken for a force $F = \zeta v$ to drive a particle over its own diameter at velocity v, $\tau_F = 2a/v$, giving a Péclet number of

$$\text{Pe} = \frac{\tau_B}{\tau_F} = \frac{a\zeta v}{k_B T}. \tag{2.10}$$

When $\text{Pe} \gg 1$, the effect of diffusion can be ignored and a deterministic version of the Langevin equation with $\xi(t) = 0$ makes a good approximation. In our experiments, typical values are $v = 1\,\mu\text{m}\,\text{s}^{-1}$, $\zeta = 6.1 \times 10^{-8}\,\text{kg}\,\text{s}^{-1}$, and $a = 1.4\,\mu\text{m}$, giving $\text{Pe} = 20$. Our experiments are therefore often in a regime where thermal fluctuations can be ignored, but they become important

at smaller driving velocities of $\sim 0.1\,\mu\mathrm{m\,s}^{-1}$.

2.2.3 Drag force from the solvent

Colloidal particles moving in a solvent experience a drag force equal to the velocity times the drag constant, ζ. According to the Stokes equation, the drag constant of a spherical particle at infinite dilution is $\zeta_0 = 6\pi\eta a$ [112]. Our particles, however, sediment to the bottom of the sample cell and therefore diffuse parallel to a wall, increasing the drag on the particle. The drag constant parallel to the wall, $\zeta^{\parallel}$, at a height z, is given by Faxen's correction [116],

$$\zeta^{\parallel}(z) = \zeta_0 \left[1 - \frac{9}{16}\left(\frac{a}{z}\right) + \frac{1}{8}\left(\frac{a}{z}\right)^3 - \frac{45}{256}\left(\frac{a}{z}\right)^4 - \frac{1}{16}\left(\frac{a}{z}\right)^5\right]^{-1}. \tag{2.11}$$

In practice, z is difficult to measure so ζ is usually measured directly from the MSD of the particles.

2.2.4 Gravity

Colloidal suspensions exist in a sedimentation-diffusion equilibrium whereby the rate of sedimentation due to gravity is balanced by the rate of diffusion due to thermal fluctuations. The resulting probability distribution is a Boltzmann distribution with a characteristic length scale of, h_g, the gravitational height [50]:

$$P(z) = Ne^{-z/h_g}, \qquad \text{with} \qquad h_g = \frac{3k_BT}{4\pi g\Delta\rho a^3}, \tag{2.12}$$

where N is a normalisation constant, z is the height, g is the acceleration due to gravity, and $\Delta\rho$ is the difference in density between the particle and the solvent. When $h_g \ll a$, as is always the case in this thesis, particles sediment to the bottom of the sample cell and fluctuations in z are insignificant.

2.2.5 Inter-particle interactions

Colloidal particles can have many types of inter-particle interactions depending on factors such as their surface chemistry and response to external fields. Here we will introduce the interactions

relevant to our experiments, which use paramagnetic colloidal spheres with acidic surface groups in the presence of a polymeric stabiliser and a magnetic field.

DLVO theory

When spherical colloidal particles are dispersed in a solvent, their pairwise interactions can be described by the Derjaguin-Landau-Verwey-Overbeek (DLVO) theory [44]. The pair potential, illustrated in figure 2.1, consists of an attractive Van der Waals potential and a repulsive double layer potential:

$$U_{DLVO}(r) = U_{VdW}(r) + U_{DL}(r). \tag{2.13}$$

The Van der Waals attraction is approximately [117]

$$U_{VdW}(d) = -\frac{Aa}{12d}, \tag{2.14}$$

at small distances $d = r - 2a \ll 2a$, where A is the Hamaker constant, a positive constant which accounts for all of the molecular interactions.

The double layer repulsion occurs because surface groups dissociate, producing a surface charge on the particle which is surrounded by a layer of oppositely charged ions. The overlap of the double layers of two particles results in an effective entropy-driven repulsion described by a

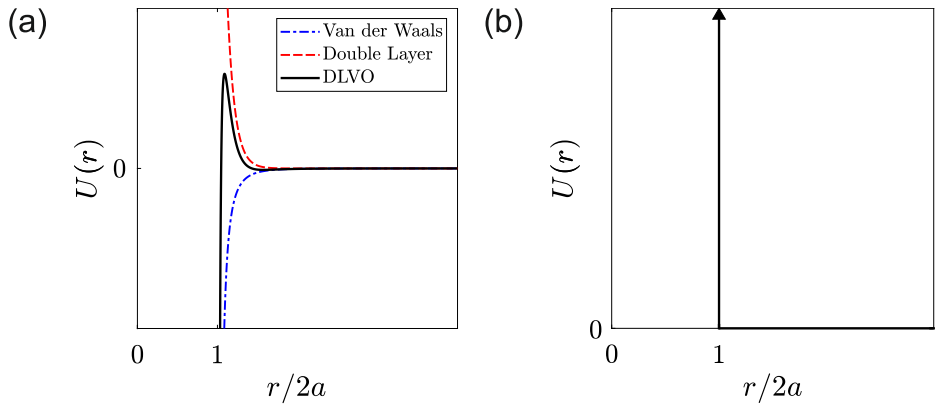


Figure 2.1: (a) The DLVO potential, U_{DLVO} (black), and its two components, the Van der Waals attraction, U_{VdW} (blue $-\cdot$), and the double layer repulsion, U_{DL} (red $--$), and. (b) The hard sphere potential, U_{HS}

screened coulomb potential [44]:

$$U_{DL}(r) = \begin{cases} \infty & r < 2a \\ k_B T^2 Z^2 \lambda_B \left(\frac{\exp(2\kappa a)}{1+2\kappa a}\right)^2 \frac{\exp(-\kappa r)}{r} & r \geq 2a \end{cases}. \tag{2.15}$$

Here Z is the number of unit charges on the particle surface, κ^{-1} is the Debye length, and λ_B is the Bjerrum length, equal to the distance at which the interaction energy between two elementary charges equals $k_B T$. The DLVO potential, shown in figure 2.1, tends to $-\infty$ at $r = 2a$, followed by a local maximum from the repulsive, short ranged $U_{DL}(r)$ and a local minimum from the attractive, longer ranged U_{VDW}, which dominates at large r.

Hard Spheres

As the particle radius, a, increases, U_{DLVO} is increasingly dominated by the double layer repulsion, U_{DL}, which scales as e^a, as opposed to $U_{VdW} \propto a$. The range of U_{DL}, quantified by κ^{-1}, also becomes relatively small compared to the radius. The result is a potential which increasingly resembles the much simpler hard sphere potential, shown in figure 2.1b:

$$U_{HS}(r) = \begin{cases} \infty & r < 2a \\ 0 & r \geq 2a \end{cases}. \tag{2.16}$$

Recent experiments on melamine formalydehyde spheres with $a = 1.4\,\mu\text{m}$ in a water-ethanol mixture have shown that colloidal particles can be excellent hard sphere model systems [118].

A hard-sphere-like potential may also be produced by adding polymeric stabilisers [119]. Sections of the polymer are hydrophobic and adsorb onto the surface of the particle, while other sections are hydrophilic and extend into the solvent to form hair-like structures. This leads to a short ranged, entropic repulsion between particles due to the loss in configurational entropy of the polymer "hairs". We use this effect to stabilise our particles.

Paramagnetic particles

In this thesis we use paramagnetic particles made of iron oxide nanoparticles evenly dispersed throughout a polystyrene matrix [120]. Each iron oxide nanoparticle has a single magnetic

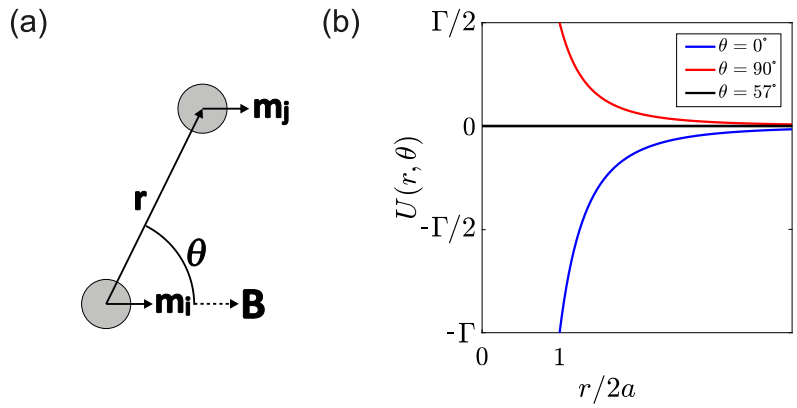


Figure 2.2: (a) The coordinates of two particles in a magnetic field. (b) The pair pair potential between two particles in a magnetic field at an angle $\theta = 0^{\circ}$(red), 90°(blue) and 57°(black).

domain. In the absence of a magnetic field, the domains' orientations fluctuate, so the particle has zero magnetic moment. Within a magnetic field, however, the domains align and give the particle a non-zero magnetic moment. In small magnetic fields, the magnetic moment is proportional to the applied field; $\mathbf{m} = \chi \mathbf{B}$, where χ is the magnetic susceptibility [120].

The magnetic field, $\mathbf{B}_i$, generated by a particle with magnetic moment $\mathbf{m_i}$ is given by [121]

$$\mathbf{B}_i = \frac{\mu_0}{4\pi r^3} \left[3(\mathbf{m_i} \cdot \hat{r})\hat{r} - \mathbf{m}_i\right], \tag{2.17}$$

where $\mathbf{r}$ is the distance from the particle. The interaction between this field and a second particle with magnetic moment $\mathbf{m}_j$ is

$$U_{ij} = -\mathbf{m}_j \cdot \mathbf{B}_i = -\mathbf{m}_i \cdot \mathbf{B}_j. \tag{2.18}$$

The pairwise interaction energy between two particles with $\mathbf{m}_{i,j} = \chi \mathbf{B}$ separated by a distance $\mathbf{r}$ is therefore

$$U_{ij} = -\frac{\mu_0}{4\pi r^3} \left[3(\mathbf{m}_i \cdot \hat{r})(\mathbf{m}_j \cdot \hat{r}) - \mathbf{m}_i \cdot \mathbf{m}_j\right] = -\frac{\mu_0 \chi^2 B^2}{4\pi r^3}(3\cos^2(\theta) - 1), \tag{2.19}$$

where θ is the angle between $\mathbf{r}$ and $\mathbf{B}$, as illustrated in figure 2.2a. The potential is attractive when $\theta < \cos^{-1}(1/\sqrt{3}) \approx 57^{\circ}$, the magic angle where $U_{ij} = 0$, and repulsive otherwise, as shown in figure 2.2b. In this thesis, we use magnetic fields aligned either along the x direction, which cause the particles assemble into chains parallel to the field, or along the z direction, which causes particles confined by gravity to the xy plane to experience a repulsive potential.

The strength of the interaction can be quantified by the dimensionless interaction parameter Γ, defined as

$$\Gamma = -\frac{U(2a, 0°)}{k_B T} = 2\frac{U(2a, 90°)}{k_B T} = \frac{\mu_0 \chi^2 B^2}{16 k_B T \pi a^3}. \tag{2.20}$$

When $\Gamma \gg 1$, the interactions dominate over thermal fluctuations and particles aggregate into rigid chains. We typically have interaction parameters of $\Gamma = 30 - 90$, enough to cause particles to aggregate into flexible chains where the inter-particle distances fluctuate slightly both parallel and perpendicular to the magnetic field.

2.2.6 Optical trapping

In this thesis, we make use of optical trapping to create a range of potential energy landscapes. Optical trapping uses a focused laser beam to exert an attractive or repulsive force on a particle, depending on the refractive index difference between the particle and the solvent. Depending on the ratio of the particle radius, a, to the wavelength of the light, λ, optical trapping may be explained in terms of either ray optics ($a \gg \lambda$) or an electric dipole approximation ($a \ll \lambda$) [82]. In our case a and λ are both $\approx 1\,\mu\text{m}$, but we will use ray optics to provide a simple, intuitive explanation of optical trapping.

Figure 2.3 shows a particle with a greater refractive index than the solvent in an optical trap. Rays from the laser are refracted by the particle, leading to a change in the light's momentum and hence an equal and opposite change in the particle's momentum. When a

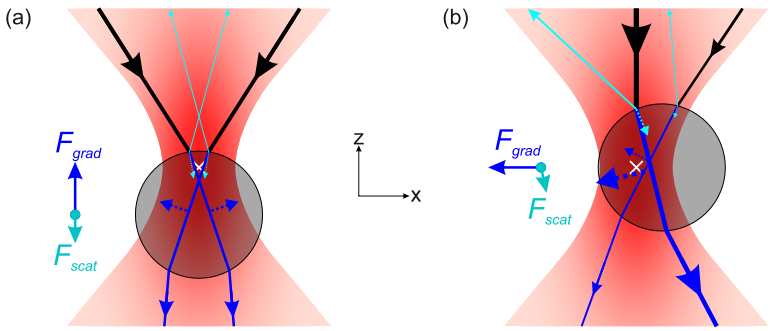


Figure 2.3: A particle with refractive index greater than the solvent in an optical trap whose focal point is marked with a white ×. The particle is displaced from the centre of the trap in (a) z and (b) in x. Solid lines show rays and dashed lines show the particle's change in momentum. Incoming rays are shown in black, refracted rays in blue and scattered rays in cyan, and the thickness of the line represents the intensity of the ray.

particle is displaced from the focal point in the z direction, as in figure 2.3a, the net force from the refracted rays, known as the gradient force, is towards the focal point of the laser beam. Some light is also scattered, and the net scattering force is away from the direction of light propagation. Figure 2.3b shows a particle displaced from the focal point in the x direction. Again, the net gradient force is towards the focal point and the net scattering force points downwards and slightly away from the focal point. For stable trapping to occur in 3D, the gradient force must be larger than the scattering force. However, in our experiments the particle is trapped against the bottom of the sample cell, so scattering is not relevant.

Overall, in our 2D setup, a particle with greater refractive index than the solvent is attracted to the centre of a focused laser beam, while a particle with lower refractive index is repelled, which is important in chapter 7. The trapping potential can be described by a Gaussian function with depth V_0 and stiffness k:

$$U_T(\mathbf{r}) = \pm V_0 \exp\left(-\frac{k}{2V_0}(\mathbf{r}-\mathbf{r}_0)^2\right), \tag{2.21}$$

where $\mathbf{r}$ is the position of the particle and $\mathbf{r}_0$ is the trap position. Both V_0 and k are proportional to the laser power and the trap width, $w = \sqrt{V_0/k}$, is a constant proportional to the diameter of the beam at the focal point.

Acoustic optical deflectors

We use acoustic optical deflectors (AODs) to control the position of our optical trap and create optical landscapes. Figure 2.4(a) is a diagram of a typical AOD. It functions as a tuneable diffraction grating consisting of a piezo-electric transducer connected to a TeO_2 crystal [122]. Applying a radio-frequency oscillating voltage to the transducer transmits ultrasound through the crystal, creating a standing density wave. This acts as a diffraction grating, splitting the beam into a zeroth and first order beam. Adjusting the frequency of the voltage changes the wavelength of the standing wave, and therefore the diffracted angle of the first order beam. The faces of the crystal are angled such that the first order beam is parallel to the incoming beam when the frequency of the voltage is in the middle of the AOD's working range. By placing two AODs at 90°, as shown in figure 2.4b, it is possible to steer the (1,1) beam (first order refracted by both AODs) in the x and y directions.

Optical landscapes

AODs are capable of switching between multiple predefined positions at a rate of up to 10^5 Hz, significantly faster than the typical Brownian time of 1 s, so that a colloidal particle effectively experiences a superposition of multiple optical traps. In principle, it is therefore possible to create any potential which can be decomposed into a sum of multiple Gaussians. In chapters 4, 5 and 6, we use this to create a line of traps with spacing $\lambda = 3.2\,\mu$m, forming a sinusoidal potential [123]. Note that when scanning the line from left to right, the laser exerts a small driving force on the particle to the left, so it is important to scan the line of traps from left to right and then right to left in order to avoid this effect.

Figure 2.5 shows the potential from each trap in a line of traps, $U_n(x)$, in black and the total potential, $U_T(x)$, in blue. $U_T(x)$ is given by the sum

$$U_T(x) = \lim_{N\to\infty} -\sum_{n=-N}^{N} V_0 \exp\left(-\frac{k}{2V_0}(x - n\lambda)^2\right), \tag{2.22}$$

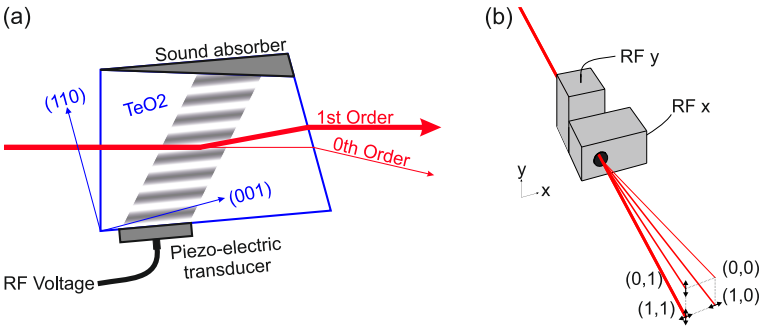


Figure 2.4: Diagram of (a) the operation of an AOD and (b) the deflection of a laser beam passing through two crossed AODs.

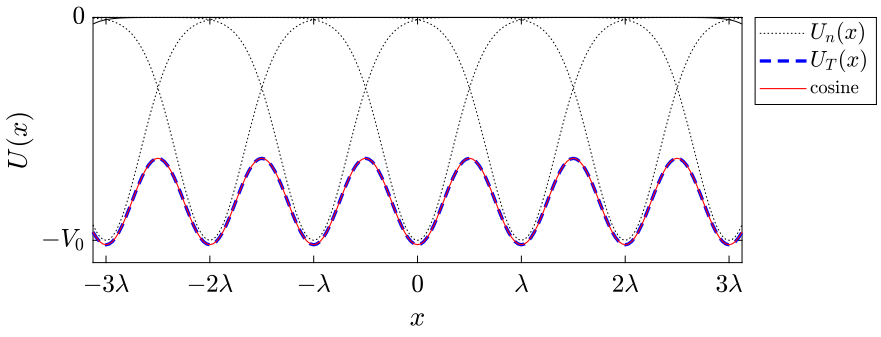


Figure 2.5: Potential of a line of optical traps. Black dotted lines show the potential of each trap, the blue dashed line shows the total potential and the red line shows equation 2.25.

which, for small λ, may be expressed as the Fourier series

$$U_T(x) = \frac{1}{2}c_0 + \sum_{m=1}^{\infty}\left[c_m \cos\left(\frac{2\pi m x}{\lambda}\right) + b_m \sin\left(\frac{2\pi m x}{\lambda}\right)\right], \tag{2.23}$$

where $b_m = 0$ and

$$c_m = \frac{2}{\lambda}\int_{-\lambda/2}^{\lambda/2} U_T(x)\cos\left(\frac{2\pi m x}{\lambda}\right)dx = -\frac{2V_0}{\lambda}\sqrt{\frac{2\pi V_0}{k}}\exp\left(-\frac{2\pi^2 m^2 V_0}{\lambda^2 k}\right). \tag{2.24}$$

When λ is small, the $m > 1$ terms may be ignored and

$$U_T(x) = \frac{c_0}{2} + c_1 \cos\left(\frac{2\pi x}{\lambda}\right). \tag{2.25}$$

The red line in figure 2.5 shows the sinusoidal approximation, which works very well for the wavelengths used throughout this thesis.

2.3 Experimental methods

In this section we describe the particles, sample cells and experimental setup used in chapters 3, 4, 5 and 6. Chapter 7 is based on re-analysed data collected by a former PhD student using different particles and a different experimental setup, which we will describe in chapter 7.

2.3.1 Samples

Our samples contain a very dilute mixture of Invitrogen^{TM} Dynabeads^{TM} M-270 Carboxylic Acid particles [124] dispersed in a solution of 0.05wt% NaN_3, a biocide, and 0.1wt% F68, a pluronic stabiliser. Figure 2.6a shows an SEM image of the Dynabeads and 2.6b shows an SEM image of their cross section [120], where the iron oxide nanoparticles show up as bright spots which are evenly distributed throughout the particle. These particles have a very low polydispersity of $< 3\%$ and their magnetic properties are highly consistent between batches. Table 2.1 lists the particle's key properties.

Our samples are made by pipetting 90 µl of the colloidal suspension into a Hellma cell. These are quartz cells with internal dimensions of 20 mm×9 mm×200 µm. An example is shown in figure 2.6c. The cells were cleaned by immersing them in 2% Hellmanex solution at 40° for

Name	Symbol	Value
Radius	a	$1.4\,\mu m$
Drag constant	ζ	$6.14 \times 10^{-8}\,kg\,s^{-1}$
1D Brownian Time	τ_B	$59\,s$
Density	ρ	$1.6\,g\,cm^{-3}$
Gravitational Height	h_g	$0.06\,\mu m$

Table 2.1: Characteristic properties of Invitrogen^{TM} Dynabeads^{TM} M-270 Carboxylic Acid particles. The radius and density were obtained from the manufacturer [124] while the drag constant was measured from the MSD of particles in a typical sample cell.

1h; rinsing with water, ethanol, and then water; drying with compressed air and then in an 80°oven; and finally plasma cleaning immediately before inserting the colloidal suspension. All solutions used for sample preparation and cleaning were filtered through hydrophilic PES syringe filters just before use to remove dust and bacteria. Samples were prepared by pipetting 90 µl of the colloidal suspension into a clean Hellma cell and sealing by firmly pressing a large piece of bluetack into the inlets. Samples prepared in this way last between 2 weeks and 2 months before particles begin to stick to each other and the bottom of the cell.

2.3.2 Experimental setup

Experiments were performed on a custom built optical setup which combines simultaneous imaging, optical trapping, driving, and magnetic fields. Figure 2.7 shows a diagram and photo of the optical setup. All optical elements are mounted in a Thorlabs cage system supported by passively damped posts. The high quality machining of Thorlabs components combined with a robust design ensured sufficient mechanical stability of the setup.

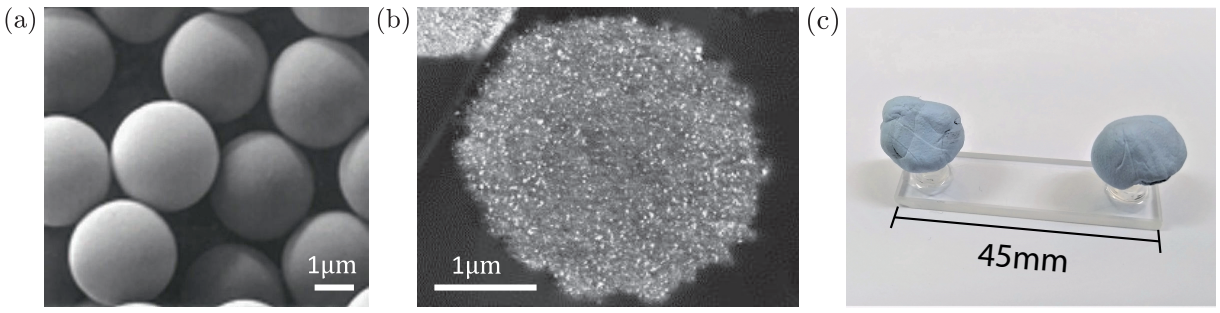


Figure 2.6: (a) SEM image of Dynabeads^{TM} reproduced from [124] (b) SEM image of the cross-section of a Dynabead reproduced from [120]. White spots show the iron oxide nanoparticles. (c) Photo of a sealed Hellma cell.

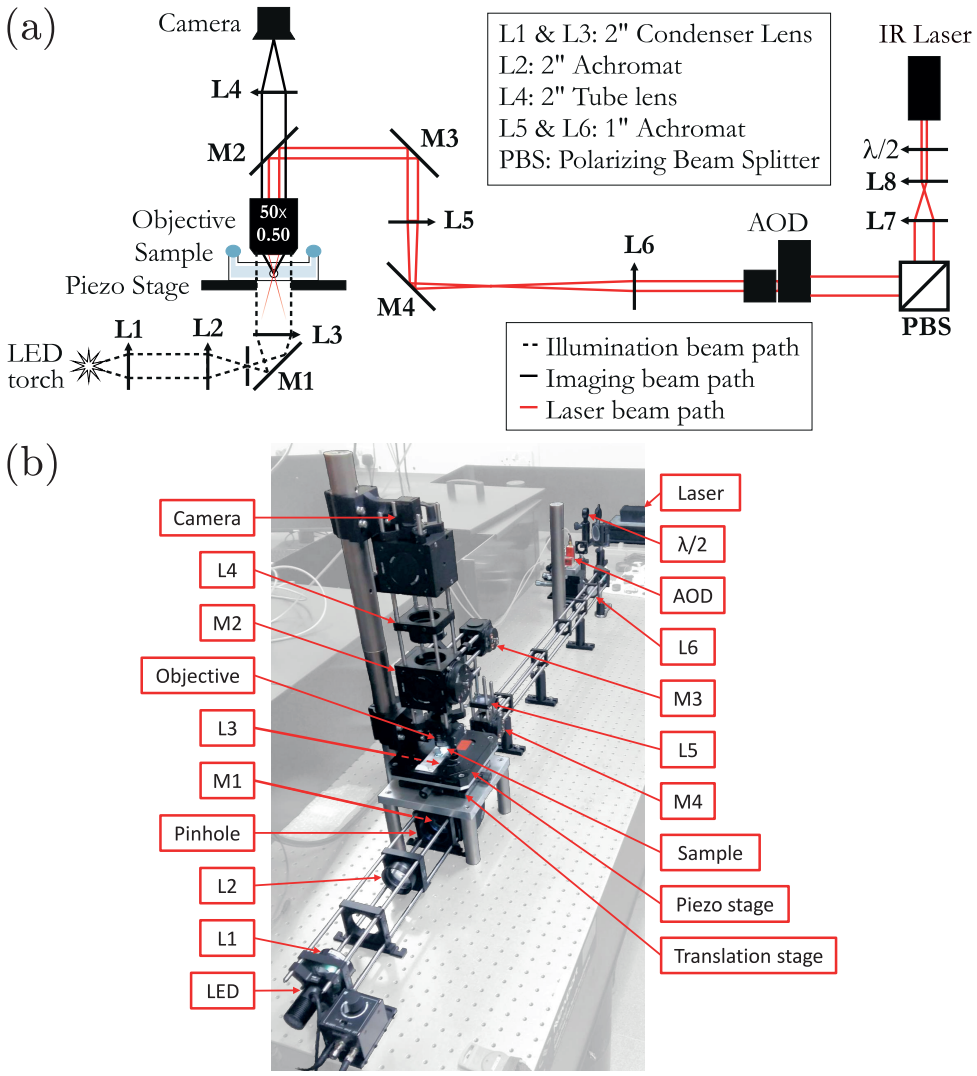


Figure 2.7: (a) Ray diagram of the optical setup. Arrows labelled L represent lenses and lines labelled M are mirrors. (b) Photo of the optical setup, showing each component in (a).

Imaging

The sample is illuminated from below using Köhler Illumination. Lenses 1 and 2 image the LED onto a pinhole, which lets through only the centre of the image. Lens 3 defocuses this light at the sample plane, so that no features of the LED are projected onto the sample plane, giving even illumination, and the light is collimated (i.e. all rays are parallel). The sample is imaged with a 4f system consisting of the trapping objective and a tube lens (L4). The objective is an Olympus 50× air objective with a long working distance of 10.6 mm and numerical aperture of 0.5. The camera is a Ximea XiQ with am image resolution of 2048×2048. Images were taken at frame rates ranging from 10 Hz to 100 Hz. Image acquisition is controlled via a custom written Labview interface which simultaneously controls the piezo stage and AOD, enabling the image

timestamps to be matched up with the position of the stage and trap configuration.

Driving

The sample is mounted on a translation stage and a piezo-electric stage (PI-542.2CD), which is controlled via the Labview interface. The latter is used to drive the sample cell at a constant velocity v_d by repositioning the sample at a rate of 40 Hz and a precision of 0.4 nm. In the camera reference plane, this is equivalent to applying a force of ζv_d to the particle via the solvent.

Optical trapping

An 1064 nm IR laser beam of up to 5 W is used to create the optical trap. The beam passes through a $\lambda/2$ wave-plate before being expanded by lenses 7 and 8, then reflected by the polarising beam splitter, which acts with the $\lambda/2$ wave-plate to reduce the intensity. The expanded beam is steered in the x and y directions by two AODs as described in section 2.2.6. Lenses 5 and 6 image the AOD output into the back focal plane of the objective, which then focuses the laser onto the sample from above. The lenses are aligned so that the laser and image are both in focus at the sample plane.

The optical traps were first calibrated by measuring the laser power at the sample. Figure 2.8 shows the measured power after the AOD (a) and at the sample (b) as a function of the input power. The power is linear at the sample up to 400 mW and plateaus after about 1.5 W. We therefore avoided using laser powers of more than 1.5 W in the experiments.

The trap profile was then measured by driving a particle across lines of traps separated by a distance of λ =14 µm, 7 µm, 4.25 µm and 3.5 µm, allowing us to see both the Gaussian and

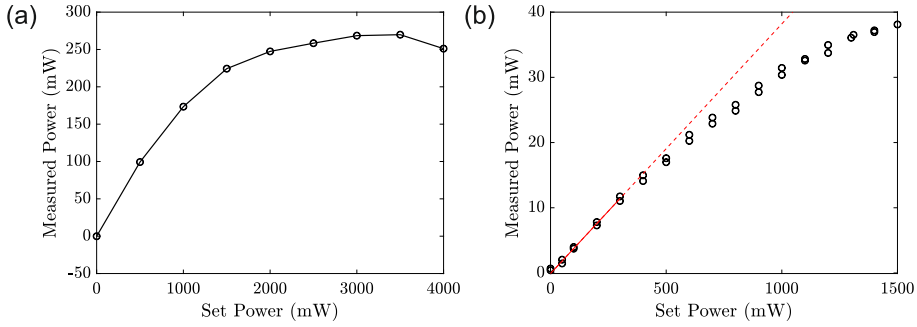


Figure 2.8: Measured vs. set power after the AOD (a) and at the sample (b)

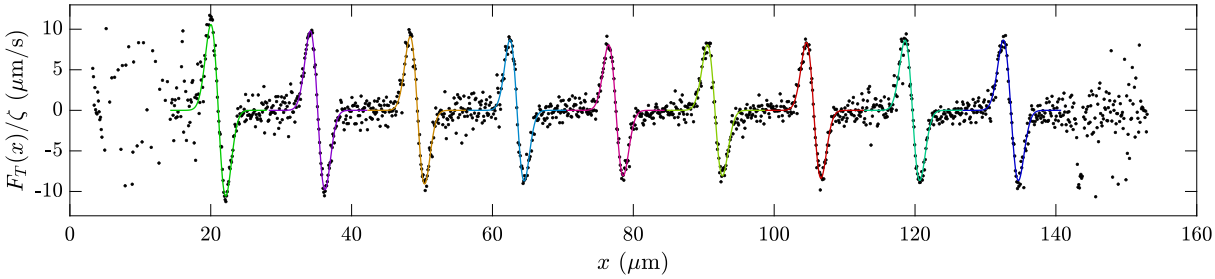


Figure 2.9: Force measurement of 9 traps separated by λ =14 µm. Coloured lines show each fit.

sinusoidal regimes. In each case, the trap force was measured from the particle trajectories by binning the instantaneous particle velocity in the x direction as follows [125]:

$$F_T(x) = \zeta \left(\frac{\langle x(t+\Delta t) - x(t) \mid x \leq x(t) < x + \delta x \rangle}{\Delta t} - v_d \right). \tag{2.26}$$

This may be derived by averaging the Langevin equation 2.3 over x and rearranging. Note that the *positive* difference, $x(t + \Delta t) - x(t)$, must be used to approximate dx at time t, not the negative or central difference. This is because only the positive difference is equal to $\zeta^{-1}F(x,t)$; the negative and central differences contain an additional $-2D(\partial(\ln p(x,t))/\partial x)_t$ term [14] which introduces errors into the measurement at low driving velocities.

At large trap separations, the measured force is composed of a separate Gaussian for each trap. Figure 2.9 shows the force measured when $\lambda = 14$. By fitting each trap with the Gaussian force,

$$F_T = -k(x - x_T) \exp\left[-\frac{(x - x_T)^2}{2w^2} \right], \tag{2.27}$$

we found a beam waist of $w = (1.04 \pm 0.02)$ µm – an important constant of the experimental setup. There is a small variation in the trap stiffness across the field of view. The trap force is sinusoidal when $\lambda \lesssim 4.25$ µm.

Magnetic field

A magnetic field is generated by placing two small permanent magnets on the sample stage at a distance R from the sample. The magnetic field in the middle of the magnets, where there field gradient is 0, can be treated as uniform on the length scale of the field of view. The field strength between the magnets follows a power law $B \propto R^{-p}$ and the field's orientation depends

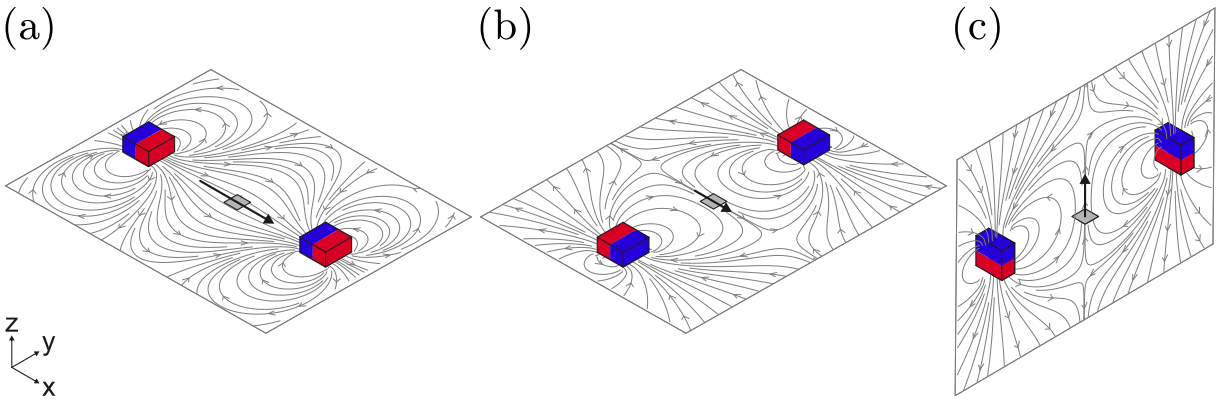


Figure 2.10: Magnetic field between two magnets in three different configurations. Red and blue indicate the north and south pole of the magnets respectively. Grey lines show the magnetic field director, the small central square represents the imaging field of view (not to scale) and the black arrows highlight the magnetic field direction within the field of view.

on the orientation of the magnets. Figure 2.10a shows the configuration we use to create a field along the x direction. The magnets are positioned at $(\pm R, 0)$ with their N-S axes pointing end to end along the x direction. We can only fit $R < 60\,\text{mm}$ on the stage, so to create a very weak field in x we place the magnets at $(0, \pm R)$ pointing along along $-x$, as shown in figure 2.10b. To create a field in z, we place the magnets upright at $(0, \pm R)$ as in 2.10c.

The magnetic field strength was calibrated using a Gauss-meter. Figure 2.11 shows the field strength in between the magnets for the magnetic configurations in figure 2.10(a) and 2.10(c). The distance R is measured from the centre of the sample to the inner edge of the magnets. Both are fit with the power law $B = m/R^p + c$, giving $p \approx 2$ in each case. The configuration in figure 2.10(b) was only used at one separation of $R = 45\,\text{mm}$, giving a field strength of $0.32\,\text{mT}$.

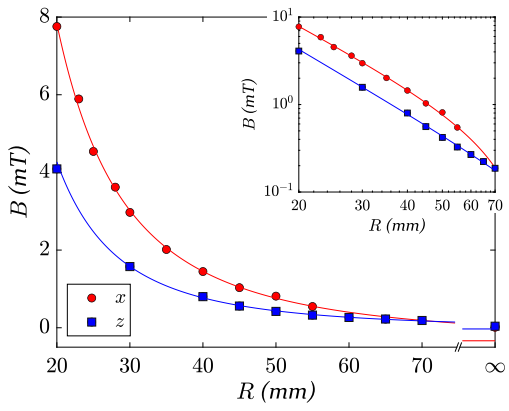


Figure 2.11: Magnetic field strength between two magnets. Red circles correspond to figure 2.10a and blue squares to 2.10c. The inset shows the same data on a log-log plot.

2.3.3 Particle tracking

To track the particles from our microscopy data, we use two different image analysis algorithms depending on the type of experiment. For experiments with a single particle or where particles never come into contact, we use Labview's built in circle finding algorithm. This allows live particle tracking with sub-pixel accuracy. The circle finding algorithm fails at separations of 3.2 µm (approximately 1.2 diameters, or one wavelength), so experiments involving chains of particles required a different approach.

Figure 2.12(a-g) shows each step of the particle tracking algorithm used on chains of particles. Figure 2.12(a) shows a typical image from our experiments. The particles are too dark relative to the background to use a standard peak-finding method, so we instead developed a method which makes use of the dark ring around the particles to identify them. First, we identify the background by finding all parts of the image above a threshold (b), which are not surrounded by pixels below the threshold (c). We set the background to the threshold value and apply Gaussian smoothing to the image (d). Particles now appear as bright spots surrounded by a dark ring. Next, we use a watershed algorithm on the inverse of (d) to identify the regions of the image associated with each particle. These regions are shown in different colours in (e). Finally, we use each region as a mask on the original image (f) to calculate the centroid of each particle. The result is shown in (g). Occasionally we misidentify interstitials as particles, for example in (h). These are similar in size and brightness to the particles, so we remove them by removing any positions with at least 3 neighbours closer than 1 diameter. This works well because it is not possible for a particle to be less than 1 diameter from its neighbour, and interstitials are typically only detected between three or more close together particles.

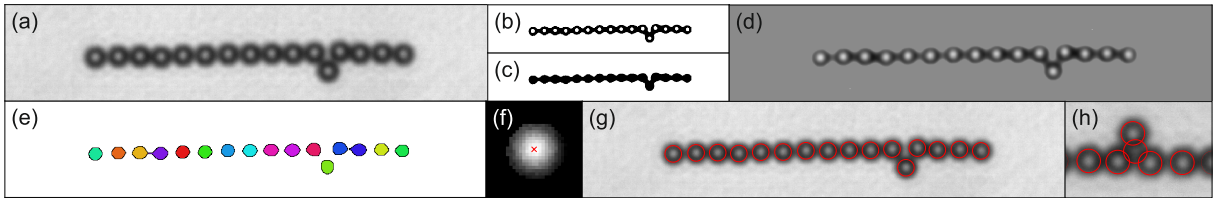


Figure 2.12: Image analyses procedure. (a) Raw image. (b) Thresholded image. (c) Thresholded image with the holes filled. (d) Image with background removed and Gaussian smoothing applied. (e) result of the watershed algorithm on the inverse of (d). (f) Masked image. (g) Tracked particle positions plotted over the original image. (h) An misidentified interstitial.

2.4 Brownian Dynamics simulations

We use Brownian Dynamics simulations [126] throughout this thesis to supplement our experiments. Our experiments are generally in quasi-one-dimensional geometries, so we perform all simulations in 1D. The simulations are based on a discrete version of the Langevin equation (equation 2.3) where the position of a particle at time $t + \Delta t$ is

$$x_i(t+\Delta t) \approx x_i(t)+\frac{dx_i}{dt}\Delta t = x_i(t)+\frac{\Delta t}{\zeta}\left[F_T(x_i(t),t) + F_d + \sum_{j\neq i} F_{int}(x_i(t),x_j(t))\right]+\sqrt{\frac{2k_BT\Delta t}{\zeta}}\Xi, \tag{2.28}$$

where $F_T(x_i,t)$ is the force from the optical traps, F_d is a constant driving force, $F_{int}(x_i,x_j)$ are the inter-particle forces, and Ξ is a normally distributed random number with mean 0 and variance 1.

The pairwise interactions consist of the following attractive magnetic term and repulsive screened Coulomb term:

$$U_{int}(x) = \Gamma\left[-\left(\frac{\sigma}{x}\right)^3 + 1.1822\frac{\exp(\kappa\sigma)}{\sigma^2+\kappa\sigma^3}\frac{\exp(-\kappa x)}{x}\right], \tag{2.29}$$

where σ is the equilibrium distance between particles in a chain, which is equal to the diameter, $2a$, only when the repulsive part is hard sphere-like ($\kappa \to \infty$). The potential is truncated at 10σ. The factor of 1.1822 in the screened Coulomb part of the potential compensates for the fact that the non-nearest neighbour interactions compress the chain slightly. This causes the average spacing, s, to be slightly smaller than the position of the potential minimum in U_{int} at $s_{min} = 1.002\sigma$. The factor of 1.1822 is numerically calculated to give an equilibrium spacing of 1σ in a chain of 20 particles. We use various different values of Γ, but the Debye screening length is always $\kappa = 80\sigma^{-1}$ to give a relatively hard repulsive term.

In chapters 4 to 6, the optical trapping force $F_T(x_i,t)$ is a sinusoidal force with a wavelength of $(8/7)\sigma$. Simulations are carried out using scaled units where $\tau_B = 1,\ k_BT = 1,\ \sigma = 1$. We use a time step of $\Delta t = 10^{-6}\tau_B$, smaller than the typical value of 10^{-5}, because of the large driving velocities used. The simulation box has periodic boundary conditions over a length of 100λ, much larger than the length of the chain plus the truncation length of the pair potential,

so the chain can never interact with itself, but small enough that if the chain breaks, the two halves may join together again during the simulation.

Acknowledgments

Arran Curran is thanked for building the optical trapping setup and writing its control software, Taiki Yanagishima and Joanne Verweij for help with the colloidal samples, and Berend van der Meer for simulation code. Josh Abbott-Scott, Ivo Buttinoni, Joseph Hutchinson and Arran Curran are thanked for useful discussions.

Chapter 3

Measuring pair potentials with optical traps

Abstract

In this chapter, we use a pair of optical traps to measure the pair potential of the paramagnetic particles used throughout the thesis. Both the sign and the magnitude of the interaction strength are controlled by using different orientations and magnitudes of the magnetic field. We use a new method of analysing the experiments which accounts for the Gaussian trap profile and measures the interaction energy directly, rather than by measuring a force. We test the robustness of the method by varying trap strength and show that it gives consistent results for both attractive and repulsive potentials. The measured magnetic susceptibility of the particles is consistent with a SQUID measurement and literature values. The method is simple to implement and widely applicable to different types of pair potentials and optical trap geometries.

3.1 Introduction

The interactions between colloidal particles are fundamental to their stability, structure and dynamics [127]. These interactions are typically approximated by a pair potential, which describes the interaction energy between the two particles purely as a function of the distance between them, ignoring any third body interactions. Detailed knowledge of the pair potential is of paramount importance in modelling the behaviour of colloidal suspensions [44, 128]. While pair potentials can sometimes be inferred from bulk measurements such as the magnetisation [129], it is often desirable to measure the interactions in situ from particle coordinates.

The most common techniques for measuring pair potentials from particle coordinates fall into two categories in which the pair potential is either measured from an inversion of the equilibrium pair distribution function, $g(r)$, [130–140], or from the diffusion of pairs or small clusters of particles in optical traps [51, 89, 141–152]. Methods based on $g(r)$ have many advantages over optical trap methods, including the simplicity of the experimental setup required and the statistical advantages of an ensemble versus pairwise measurement. However, $g(r)$ techniques have only been shown to work for repulsive potentials or those with an attractive potential minimum of less than $2k_BT$ [130–140]. This is because $g(r)$ methods typically require an equilibrium configuration in a liquid or gas-like phase, and so they are not appropriate for particles with strongly attractive potentials which often form meta-stable gels or glassy phases [153, 154].

Optical trap methods use either blinking [51, 141, 142] or constantly illuminated traps [88, 89, 143–148, 150, 151] to measure the pair potential. In the blinking trap method, the traps are used to position pairs of particles at a set separation. The particles are then released and the distribution of particle separations some delay time later is used to deduce the pair potential via a Fokker-Plank equation [51]. This method has the advantage of not including any optically induced interactions, but can be sensitive to errors from hydrodynamic interactions [146, 155]. The main disadvantage comes from the number of cycles of trapping and releasing required to gather sufficient statistics; typically around two million frames, or 5 hours of experimental time, for each initial separation [156]. On the other hand, methods based on measuring the distribution of particles in constantly illuminated optical traps are significantly easier to implement, requiring no custom written automation software, and have much shorter experimental times. The main disadvantages are the introduction of optically-induced pair interactions and the need

for an accurate calibration of the trapping potential which does not drift over the course of the experiment. Despite these sources of error, two comparisons of the blinking and continuous trap methods on the same samples showed that both gave very similar results [146, 156]. Constantly illuminated trap methods are therefore preferable from a practical point of view.

Several different trap geometries can be used, of which a two trap configuration is most suitable for attractive potentials. The data can be analysed either by calculating an interaction *force* from the mean deviation of the particles from the trap centre [143–146], or the interaction *energy* from the distribution of particle positions [88, 89, 147, 148, 150, 151]. The latter has the advantage of giving multiple data points for each trap separation, potentially cutting down on the number of experiments required. It is also free of integration errors. Despite these advantages, previous experiments using pairs of optical traps almost exclusively use force-based methods.

Here we use pairs of optical traps to measure the pair potential of paramagnetic particles in magnetic fields. We calculate the interaction energy from the distribution of inter-particle separations by accounting for the contribution from the optical trap. Previous experiments using the same type of analysis have either measured the trap term directly, thus introducing additional noise into the calculation, or assumed a parabolic trap term. We instead use a new method which accounts for the Gaussian trap profile at the large distances from the trap centre, which becomes important when measuring strong pair potentials. Our method can be applied more generally to any trap geometry. We test the method on attractive and repulsive potentials and at different trap strengths. We use the result to calculate the magnetic susceptibility of the particles, which is consistent with a SQUID measurement and literature values.

3.2 Theory

Here we describe the theoretical basis of our method for measuring the pair potential between two particles using optical traps. This theory was provided by Codina, Dobnikar and Pagonabarraga.

The probability distribution of finding a pair of particles at positions $\mathbf{r}_1$ and $\mathbf{r}_2$ separated by a distance $R = ||\mathbf{r}_1 - \mathbf{r}_2||$, when subject to a trapping potential $U_T(\mathbf{r_i})$ and an isotropic pair potential $U_{int}(R)$, is given by the Boltzmann distribution

$$P(\mathbf{r}_1, \mathbf{r}_2) = N \exp\left[-\beta \left(U_{int}(R) + U_T(\mathbf{r}_1) + U_T(\mathbf{r}_2)\right)\right], \tag{3.1}$$

where $\beta = (k_B T)^{-1}$ and N is a normalisation constant. In order to extract the pair potential, $U_{int}(R)$, we must reduce this multi-dimensional distribution $P(\mathbf{r}_1, \mathbf{r}_2)$ to a one-dimensional probability distribution of the distance between particles, $P(R)$. We do this by combining all positions $(\mathbf{r}_1, \mathbf{r}_2)$ which are separated by the same distance, R, using the following integral:

$$P(R) = I_0^{-1} \iint d\mathbf{r}_1 d\mathbf{r}_2 \; \delta\left(R - ||\mathbf{r}_1 - \mathbf{r}_2||\right) \exp\left[-\beta\left(U_{int}(R) + U_T(\mathbf{r}_1) + U_T(\mathbf{r}_2)\right)\right], \tag{3.2}$$

where I_0^{-1} is a normalisation constant and $\delta(R - ||\mathbf{r}_1 - \mathbf{r}_2||)$ is the Dirac delta function. We can take the pair potential contribution, $\exp(-\beta U_{int}(R))$, outside the integral to give

$$P(R) = \exp\left[-\beta U_{int}(R)\right] I(R)/I_0 \text{ , where} \tag{3.3}$$

$$I(R) = \iint d\mathbf{r}_1 d\mathbf{r}_2 \delta(R - ||\mathbf{r}_1 - \mathbf{r}_2||) \exp\left[-\beta(U_T(\mathbf{r}_1) + U_T(\mathbf{r}_2))\right]. \tag{3.4}$$

We have now separated the probability distribution into two terms; the pair potential contribution, $\exp(-\beta U_{int}(R))$, and the trap contribution, $I(R)$. We can therefore extract $U_{int}(R)$ from the measured probability distribution $P(R)$ of two particles in an optical trap by rearranging equation 3.3 as follows:

$$\beta U_{int}(R) = -\ln P(R) + \ln I(R) - \ln I_0. \tag{3.5}$$

When particles do not interact (i.e. $U_{int}(R) = 0$), $\ln P(R) = \ln I(R)/I_0$. The trap term, $\ln I(R)$, may therefore be interpreted as the log of the probability, $\ln P(R)$, of finding two non-interacting particles at a distance R when subject to a trap potential $U_T(\mathbf{r_i})$. In principal, $I(R)$ may therefore be measured experimentally from the $P(R)$ of two non-interacting particles in the trap, or equivalently, any two independent trajectories of a particle in the trap. However, this introduces additional noise into the measurement and only gives $I(R)$ over an experimentally accessible range of R. When the trap potential is known, it is therefore preferable to *calculate* $I(R)$ from equation 3.4. In the special case of harmonic traps with $U_T \approx {}^{k}/_{2}\left[\alpha y^2 + (x \pm l)^2\right]$, the integral can be performed analytically to give the following trap term:

$$I(R) = \frac{2\pi^{3/2} R}{k\beta\sqrt{\alpha}} \exp\left[-\frac{\beta k}{4}(R^2 + l^2)\right] I_0(L) \sum_{p=0}^{\infty} (-1)^p \frac{\Gamma(p + {}^1/_2)}{\Gamma(p+1)} \left((\alpha - 1)\frac{R}{l}\right)^p \frac{I_p(L)}{I_0(L)}, \tag{3.6}$$

where α is the trap asymmetry, $L = k\beta R l/2$, I_p is the modified Bessel function of the first kind, and $\Gamma(x)$ is the Gamma function (equal to $(x-1)!$ for positive integer x). When the trap

potential is not harmonic, as is the case in our experiment, the integral in equation 3.4 must be performed numerically. We describe our numerical integration method in more detail in section 3.3.2.

Equation 3.5 is the master equation which we use throughout this chapter to measure the pair potential. Using this equation, it is possible to find a section of the pair potential over some range of R from a single measurement. The stronger $U_T(\mathbf{r_i})$ or $U_{int}(R)$, the narrower this range becomes, making it necessary to perform multiple measurements using different optical trap separations in order to sample different regions of $U_{int}(R)$. Crucially, each measurement has a different normalisation constant, I_0, which cannot be calculated without already knowing $U_{int}(R)$. In order to stitch each measurement together, we must therefore estimate I_0 by minimising the difference between equivalent points in successive measurements, which we will discuss in section 3.3.3.

3.3 Experimental methods

3.3.1 Experimental setup

In this chapter we use the particles, sample cells and optical trapping setup described in section 2.3. The particles are paramagnetic and have a radius of $a = 1.4\,\mu\text{m}$. We use the permanent magnets described in section 2.3.2 to create magnetic fields ranging from $B = 0$ to $1\,\text{mT}$ oriented either horizontally (along x) or vertically (along z). This gives the particles a dipolar pair potential as described in section 2.2.5. Depending on the orientation of the particles relative to the field, θ, the interaction is attractive or repulsive and has the form

$$\beta U_{int}(R) = \Gamma \left(\frac{2a}{R}\right)^3 \frac{(1 - 3\cos^2\theta)}{2}, \tag{3.7}$$

where the interaction parameter Γ, defined in equation 2.20, depends on the field strength, B, and the magnetic susceptibility of the particles, χ, according to $\Gamma \propto \chi^2 B^2$.

We create a double well trapping potential using two optical traps separated by a distance l, as shown in figure 3.1. Each trap has the Gaussian profile described in section 2.2.6, which

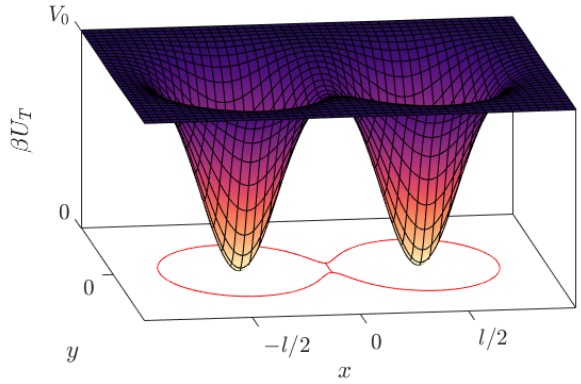


Figure 3.1: Potential energy of two traps separated by a distance l.

overlap to give a total potential of

$$U_T(x,y) = V_0 \exp\left[-\frac{\alpha k}{2V_0}y^2\right]\left(\exp\left[-\frac{k}{2V_0}\left(x-\frac{l}{2}\right)^2\right]+\exp\left[-\frac{k}{2V_0}\left(x+\frac{l}{2}\right)^2\right]\right), \quad (3.8)$$

where k is the trap stiffness in the x direction, V_0 is the trap depth, and α is the asymmetry of the trap, defined as the ratio between the trap stiffnesses in the x and y directions.

Each experiment consists of multiple measurements at different trap separations l in order to probe different regions of $U_{int}(R)$. We begin each experiment by placing one particle in each trap at $l = 20$. The trap separation is then reduced in steps from 20 µm to 5 µm, or until the pair potential became sufficiently strong to force one of the particles out of its trap. The chosen step size varied depending on the trap strength and field strength, but was typically around 0.1 µm. Each measurement consists of 2×10^4 frames recorded at 20 Hz, corresponding to a total measurement time of $30\tau_B$ (where τ_B is the Brownian time, defined in equation 2.7). Particles are tracked in real time using Labview's built in circle finding algorithm. This allows us to record a large number of frames without generating prohibitively large volumes of data. Note that the circle finding algorithm becomes inaccurate at distances of $R \lesssim 4$ µm. We therefore ignore any data with $R < 4$ µm.

In order to analyse each experiment, we first calculate a histogram of the distance between particles, $P(R)$, from each measurement. We then calculate the pair potential from the histogram using the following equation:

$$\beta U_{int}(R) = -\ln P(R) + \ln I(R) - \ln I_0, \quad (3.9)$$

where $\ln I(R)$ is the trap contribution and $\ln I_0$ is the normalisation term. We will explain how the latter two terms are calculated in the next two sections.

3.3.2 Characterising the optical trap contribution

Calculating the trap term, $\ln I(R)$, requires an accurate measurement of the trap separation (l), stiffness (k), depth (V_0) and asymmetry (α). We obtain these constants at each trap strength from a calibration experiment with no magnetic field, so that the particles do not interact over the distances probed during the experiment.

First, we find the real trap separation, l, assumed to be equal to the average distance between the particles, at each *set* trap separation by the following power law $\langle R\rangle = a l_{set}^{p}$. An example of this measurement from a calibration experiment with a trap depth of $V_0 = 12 k_B T$ is shown in figure 3.2(a). We obtain $\langle R\rangle = 0.996 l_{set}^{1.014}$, showing that the AOD calibration is fairly accurate. We use these fitted values of the trap separation to calculate the trap term, $\ln I(R)$.

Next, the trap potential is characterised from the probability distribution of the distance between the particles and the trap centres using the Boltzmann distribution, $U_T(\mathbf{r}) = -\ln\langle P(\mathbf{r})\rangle$, where the trap centres are assumed to be at the average particle position so that $\mathbf{r} = \mathbf{r_p} - \langle \mathbf{r_p}\rangle$. U_T is averaged over all trap positions and the trap stiffness and asymmetry are found by fitting parabolas to the measured trap potential in x and y, excluding the region with $r > 0.5\,\mu$m, as shown in figure 3.2(b). This gave asymmetries of $\alpha = 1.04 - 1.12$ for each calibration experiment. The trap depth, V_0, was then calculated from the measured stiffness using the trap width $w = \sqrt{V_0/k} = (1.04 \pm 0.02)\,\mu$m measured from the calibration experiments in section

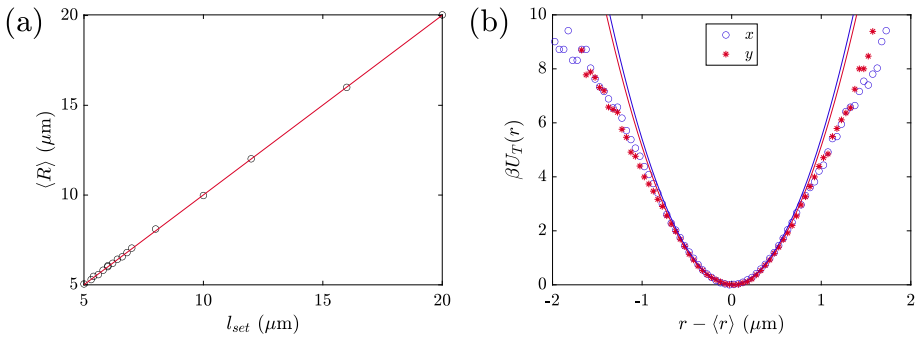


Figure 3.2: (a) Measured trap separation, $\langle R\rangle$, vs. set trap separation, l_{set}, (black circles) for an experiment with $B = 0$ and $V_0 = 12 k_B T$. The red line is the power law fit $\langle R\rangle = 0.996 l_{set}^{1}.014$. (b) Measured trap potential in the x (blue circles) and y direction (red stars). Red and blue lines show the parabolic fits $U_T(x) = \frac{1}{2} k x^2$ and $U_T(y) = \frac{1}{2} k \alpha y^2$ respectively.

2.3.2.

Finally, we used our measured trap parameters to calculate $\ln I(R)$ using a Monte Carlo integration of equation 3.4, restated here:

$$I(R) = \iint d\mathbf{r}_1 d\mathbf{r}_2 \delta(R - ||\mathbf{r}_1 - \mathbf{r}_2||) \exp\left[-\beta(U_T(\mathbf{r}_1) + U_T(\mathbf{r}_2))\right]$$

Figure 3.3a illustrates the principle behind Monte-Carlo integration; in order to find the area under a curve $f(x)$, N points with coordinates (x_n, F_n) are chosen at random within a box, and the area is approximately equal to the area of the box multiplied by the proportion of points below the curve, i.e. $F_n \leq f(x_n)$. To apply this method to the integral in equation 3.4, we chose N randomly distributed 5-dimensional sets of points $[x_1, y_1, x_2, y_2, F]$ within the red box shown in figure 3.3b and accept all points where F is less than the integrand, $F \leq \exp\left[-\beta(U_T(\mathbf{r_1}) + U_T(\mathbf{r_2}))\right]$. $I(R)$ is then calculated from a histogram of the distances between all accepted points. The box is defined by $0 \leq F \leq 1$ (the maximum value

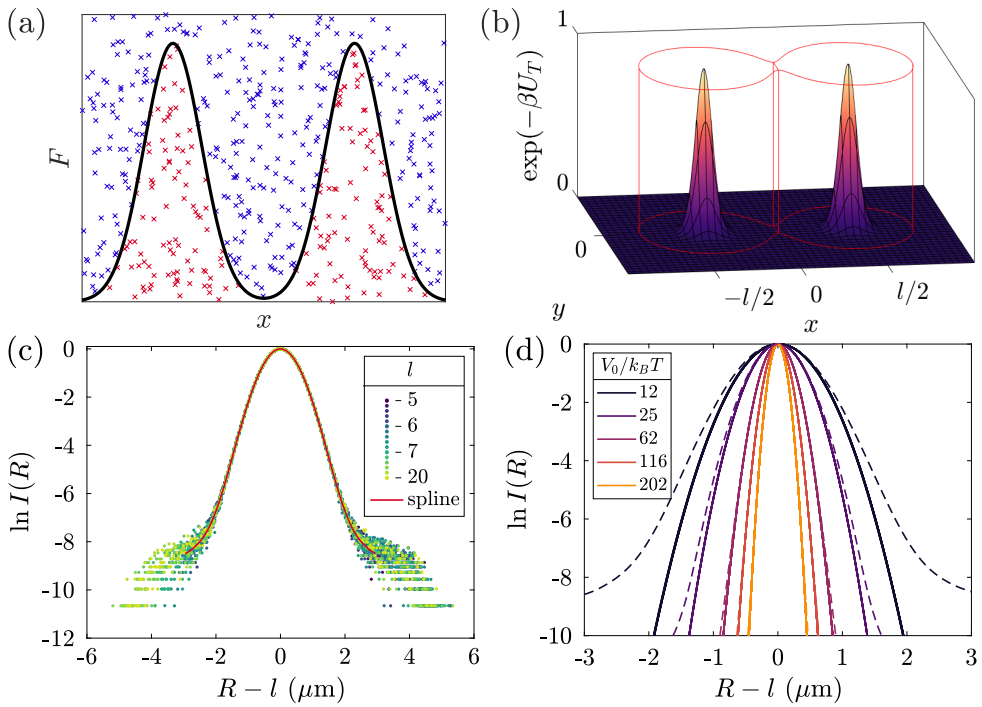


Figure 3.3: (a) Diagram of the Monte-Carlo integration of an arbitrary function $F = f(x)$ (black line). Red points have $F_n \leq f(x_n)$. (b) 3D visualisation of the 5D integrand, $\exp\left[-\beta(U_T(\mathbf{r_1}) + U_T(\mathbf{r_2}))\right]$, in the (x_1, y_1) plane with $x_2 = l/2$, $y_2 = 0$. Red lines show the region within which the N 5D points, $[\mathbf{r}_1, \mathbf{r}_2, F]$, are generated. (c) The trap term, $\ln I(R)$, vs. $R - l$, with trap parameters of $k = 4.5 \times 10^{-8}$ kg/s, $\alpha = 1.06$, $V_0 = 12k_BT$, and $l = 5\,\mu$m to $20\,\mu$m (purple to yellow dots). The red line is a smoothing spline fit. (d) Trap term calculated using the Monte-Carlo method (dashed lines) and harmonic trap approximation in equation 3.6 (solid lines) for all trap strengths from $V_0 = 12k_BT$ (black) to $202k_BT$ (yellow).

of the integrand), $x_1 \geq 0$ and $x_2 \leq 0$ (because the particles are never in the same trap), and $\beta U_T(\mathbf{r_i}) \leq \min\{\ln(100N), 0.999V_0\}$. The cut-off $\beta U_T(\mathbf{r_i}) \leq \ln(100N)$ was chosen to reduce the computation time by avoiding generating points with less than a one in $100N$ chance of being accepted. The second cut-off of $\beta U_T(\mathbf{r_i}) \leq 0.999V_0$ is used for very weak potentials where the first cut-off is fulfilled even as $r \to \infty$.

The calculated trap term, $\ln I(R)$, is shown in figure 3.3c for the experiment with $V_0 = 12k_BT$ and all trap separations from $l = 5\,\mu\text{m}$ (purple) to $l = 20\,\mu\text{m}$ (yellow). When plotted against $R - l$, all $\ln I(R)$ collapse onto the same curve. We therefore fit all of the calculated $\ln I(R)$ with a smoothing spline, shown in red, and use this fit to calculate $\ln I(R)$ for the pair potential measurements in order to reduce the noisiness of $\ln I(R)$. Figure 3.3d shows all trap terms for trap strengths of $V_0 = 12k_BT$ to $202k_BT$ calculated using the Monte-Carlo method (dashed lines) compared to the harmonic approximation in equation 3.6 (solid lines). The harmonic approximation is only valid when $V_0 > 62k_BT$, hence, we use the numeric Monte-Carlo trap term in all experiments.

3.3.3 Calculating the full potential by joining each measurement

When the pair potential is calculated at each different trap separation, the result is a set of un-normalised segments of $U_{int}(R)$ which do not fit together to form a continuous function because they each have a different normalisation constant, I_0. This is illustrated in figure 3.4a and b. In order to obtain the full $U_{int}(R)$, we need to stitch together successive measurements, $U^i(R)$, by maximising the overlap between them as illustrated in figure 3.4b and c.

The difference between successive measurements $U^i(R)$ and $U^{i+1}(R)$ is minimised by shifting U^{i+1} up by the weighted average of the difference between the two curves. In order to

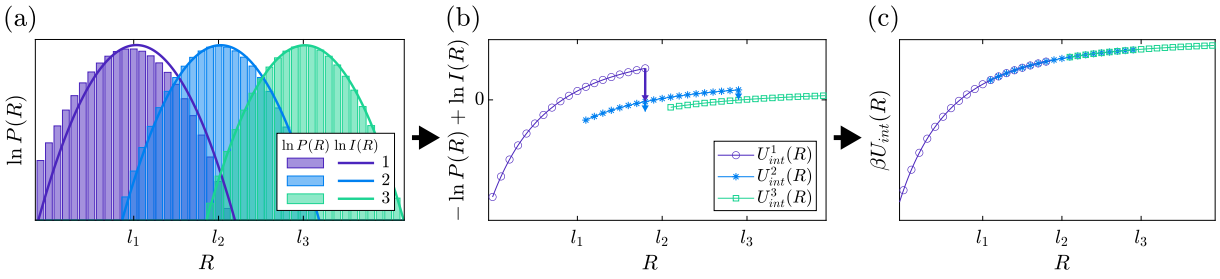


Figure 3.4: (a) Three measured distance histograms, $\ln P(R)$, with corresponding trap terms, $\ln I(R)$. (b) The un-normalised segments of $U_{int}(R)$ calculated from (a). (c) The normalised $U_{int}(R)$ calculated by maximising the overlap between successive measurements in (b)

minimise the effect of the noisy region where $P(R)$ is small, $P^i(R)P^{i+1}(R)$ is used as a weighting as follows:

$$U^{i+1}_{norm}(R) = U^{i+1}(R) + \frac{\sum_R (U^i(R) - U^{i+1}(R))P^i(R)P^{i+1}(R)}{\sum_R P^i(R)P^{i+1}(R)}. \tag{3.10}$$

In this way, $U_{int}(R)$ can be calculated without assuming a model for the form of $U_{int}(R)$.

3.3.4 Zero-field pair potential measurements

We verify the accuracy of the trap term calculated from each calibration experiment by using it to measure the pair potential from the calibration experiment. Because there is no magnetic field, we expect the pair potential to have no R dependence at separations larger than one diameter. Any deviations are considered artefacts of the measurement process. The result from calibration experiments with different trap depths are shown in figure 3.5. The measured pair potential at $V_0 = 12k_BT$ is mostly flat, as expected, with a total variation in magnitude of less than $1k_BT$. The measurements with stronger traps, however, have random oscillatory features with a magnitude of several k_BT and range of around 1 µm, whose location and magnitude were not consistent between experiments. These errors may arise from optical aberrations, drift, or even dust in the sample, and cannot easily be corrected for. However they are always within $2-8\%$ of the trap depth. Therefore, the sensitivity of the pair potential measurements is limited to an average of 5% of the trap depth.

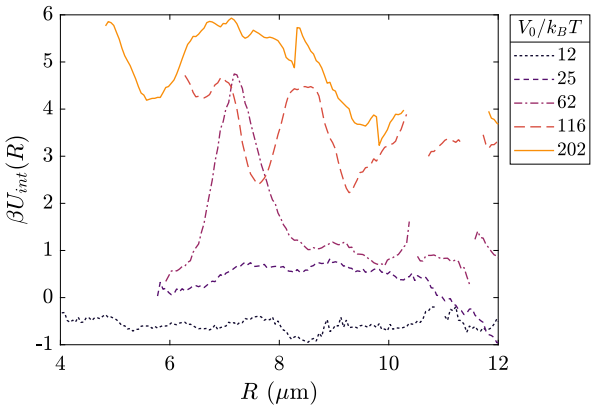


Figure 3.5: Measured $U_{int}(R)$ from all calibration experiments with no magnetic field and trap depths of $V_0 = 12k_BT$ (black dots) to $202k_BT$ (solid yellow).

3.4 Results and discussion

In this section we discuss the results of our pair potential measurement under various different conditions. Table 3.1 lists the parameters used in each experiments. First we demonstrate the result of each stage of the data analysis used to measure the pair potential using experiment one ($\mathbf{B} = 1x$ and $V_0 = 25k_BT$) as an example. Next, we test the efficacy of the method at different trap strengths using experiments one to four and eight. We then use weak traps to measure the pair potential at different field strengths and orientations (experiments five to twelve). From these, we calculate the magnetic susceptibility of our particles and compare the result to a bulk SQUID measurement and literature values.

Exp. no.	$\|B\|$ (mT)	arg(B)	V_0 (k_BT)
1	1	x	25
2	1	x	62
3	1	x	116
4	1	x	202
5	0.55	x	23
6	0.75	x	23
7	0.9	x	23
8	1	x	23
9	0.25	z	12
10	0.5	z	12
11	0.8	z	23
12	1	z	23

Table 3.1: Experimental parameters in each experiment. Experiment 1 is discussed in section 3.4.1, $1-4$ in section 3.4.2, and $5-12$ in section 3.4.3. Magnetic field strength, B, in mT, axis of the field orientation relative to the trap axis, and trap depth, V_0, in k_BT. The same calibration was used for each set of experiments, except where the trap strength is different.

3.4.1 Pair potential measurement

Figure 3.6 shows the result of each stage of the analysis of experiment 1. Figure 3.6a shows the mean particle separation, $\langle R \rangle$, at each trap separation, l_{set}. The effect of the attractive potential can clearly be seen in the way $\langle R \rangle$ increasingly deviates from $\langle R \rangle = l$ as l decreases. The same trend can be seen in the probability distributions, $\ln P(R)$, shown in figure 3.6b plotted against $R - l$. The numerically obtained trap term, $\ln I(R)$, is shown in red. At low l, the distributions are highly asymmetric and the minimum is at $R < l$ as the attractive $U_{int}(R)$ distorts $P(R)$ towards low R. After $l > 12$ (light green), there is good agreement between $\ln P(R)$ and $\ln I(R)$.

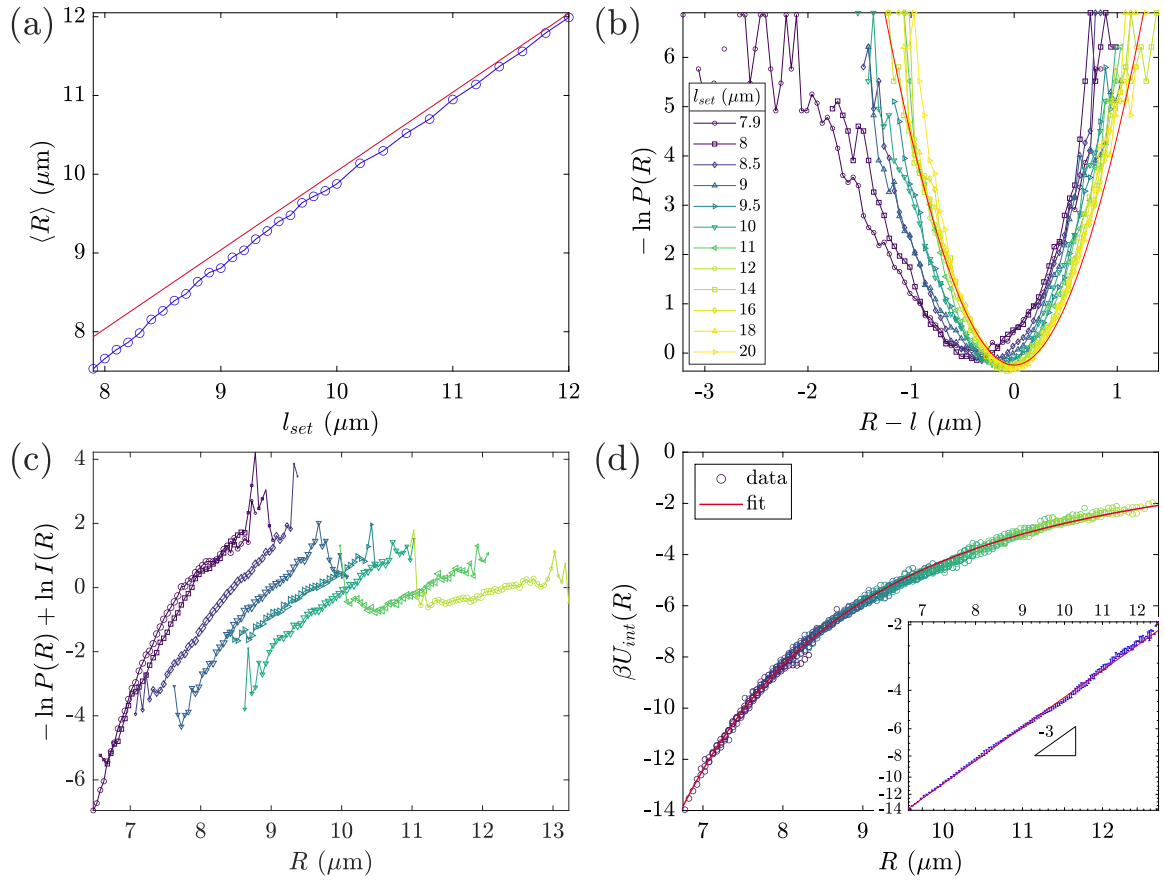


Figure 3.6: Analysis of experiment 1, showing (a) the average particle separation, $\langle R \rangle$, vs. the set trap separation, l_{set}, in blue. The red line shows the real vs. set trap separation measured from the calibration experiment. (b) $-\ln P(R)$, calculated from a distance histogram, vs. $R-l$, for measurements at different trap separations from l =7.9 μm (purple) to 20 µm (yellow). The red line is the trap term, $-\ln I(R)$, calculated from the calibration experiment. (c) Un-normalised measurements of the pair potential, $U_{int}(R) = -\ln P(R) + \ln I(R)$, at the same trap separations as in (c). The size of the points is proportional to $\ln P(R)$. (d) Final measurement of $U_{int}(R)$. In the main plot, the coloured points show each measurement and the red line is a fit to $U_{int}(R) = -\Gamma R^{-3} + c$. In the inset, blue points show the average $U_{int}(R)$.

Figure 3.6c shows the un-normalised $U_{int}(R)$ measured by subtracting the trap term, $\ln I(R)$, from the distance histograms, $\ln P(R)$, while figure 3.6d shows the full $U_{int}(R)$ obtained by joining up each individual measurement as described in section 3.3.3. In the main graph, points show $U_{int}(R)$ from each measurement from $l = 7.9$ µm to 12 µm (purple to yellow) with a fit to $U_{int}(R) = -\Gamma(2a/R)^3$ in red. In the inset, $U_{int}(R)$ is averaged in R and plotted on a logarithmic scale. There is excellent agreement with the R^{-3} fit, verifying the accuracy of the method.

3.4.2 Different trap strengths

In this section we test the robustness of the method to different trap strengths by comparing the results from the strongest magnetic field along x with B =1 mT at several different trap strengths, V_0. Figure 3.7a shows the measured $U_{int}(R)$ and fits to $U_{int}(R) = -\Gamma(2a/R)^3$ at different values of V_0 on linear and logarithmic axes. All curves agree well with the fits except the one at $V_0 = 116k_BT$, where there are large deviations at $R \approx 8\,\mu$m and 5.5 µm. Similar errors were observed in some other experiments and their origin is unclear; possible explanations include drift in the experimental setup, optical aberrations which would vary depending on the drift, or dust in the samples.

The measured $U_{int}(R)$ from the two strongest trap strengths extends to a much lower R. This is because the potential barrier to particles escaping the traps increases with increasing V_0. The trade off is that the width of $P(R)$ also decreases, leading to less overlap between successive measurements and so increasing the required number of measurements. The deviation from the trap centre also decreases, increasing the impact of errors due to miss-calibration and optical aberrations. For this reason, we use weak traps in the next section, where we measure $U_{int}(R)$ at different magnetic field strengths.

Figure 3.7b shows the Γ extracted from each fit. There appears to be an increase in Γ with increasing V_0. Since the fit is dominated by the strong $U_{int}(R)$ at low values of R, it is possible that the absence of this data is responsible for an underestimate of Γat low V_0. Conversely, using

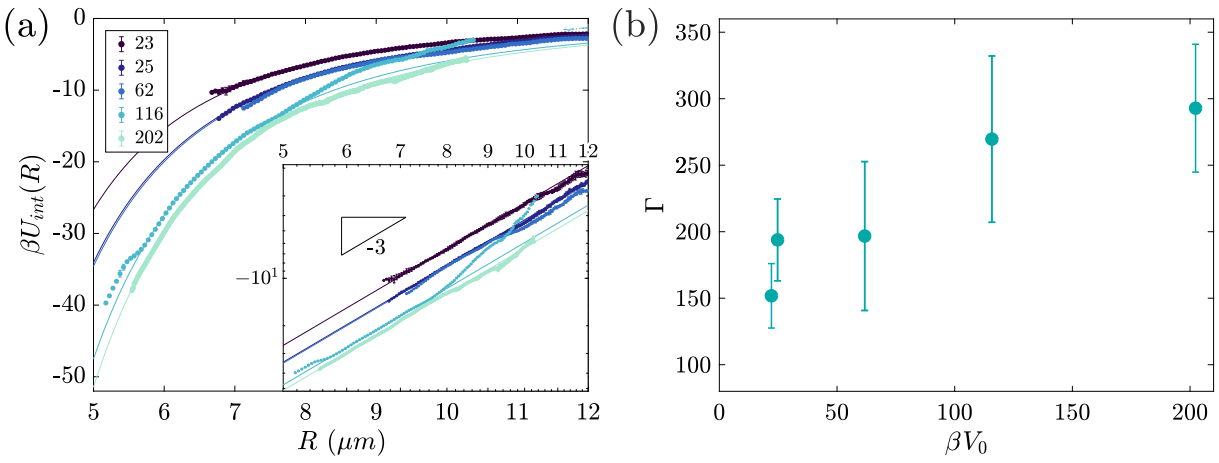


Figure 3.7: (a) $U_{int}(R)$ (points) measured at different trap strengths from $V_0 = 23k_BT$ (dark blue) to $202k_BT$ (light green), with fits to $U_{int}(R) = -\Gamma(2a/R)^3$ (lines). (b) Γ from each fit. Error bars show the standard deviation of Γ from fitting each individual measurement to $U_{int}(R) = -\Gamma(2a/R)^3 + c$

a stronger trap amplifies calibration errors, possibly leading to an overestimate of Γat high V_0. Because each measurement was taken with a different pair of particles and we expect a 20% variation in the magnetic susceptibility due to polydispersity in the iron oxide content of each particle [157], it is difficult to determine whether this trend is statistically significant. Further experiments on the same pair of particles would be necessary.

3.4.3 Different magnetic fields

In this section we use weak traps to measure the pair potential of our particles in magnetic fields of 0 mT to 1 mT oriented along both x and z, giving repulsive or attractive potentials respectively. Note that the experiments with $\mathbf{B} = 0.25z$, $0.5z$ and $0.8z$ used the same pair of particles, whereas all other experiments used different pairs.

Figure 3.8 shows the measured $U_{int}(R)$ from each experiment. The experiments with $\mathbf{B}$ along z are shown in red and x in blue. All curves agree well the R^{-3} fits. Figure 3.8b shows the Γ from each fit. All Γ sit on a straight line and, crucially, the attractive and repulsive Γ are consistent with one another. This suggests that our method works equally well for attractive and repulsive potentials.

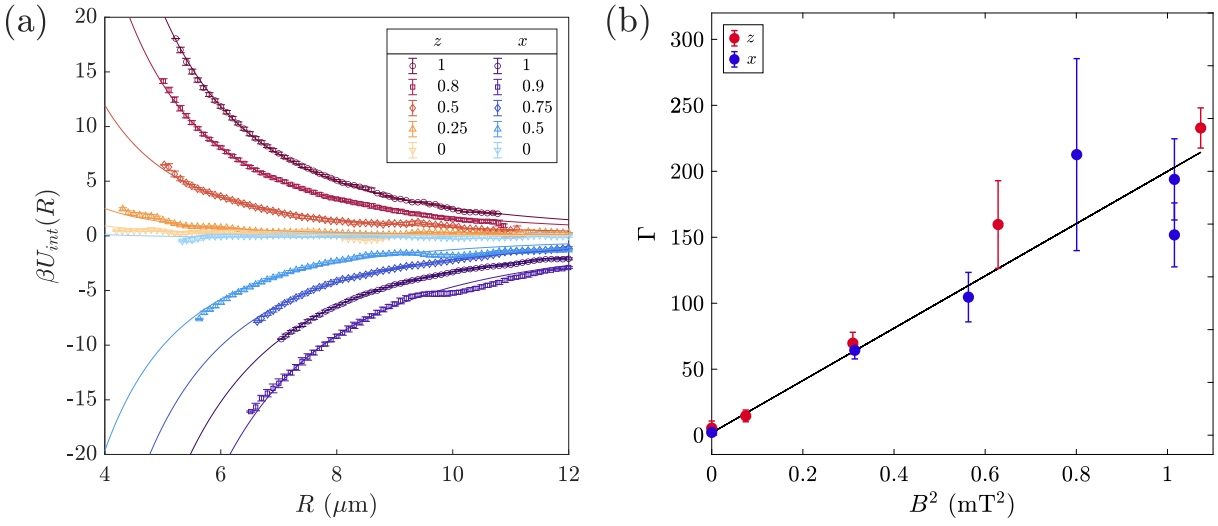


Figure 3.8: (a) $U_{int}(R)$ (points) measured at different field strengths from $B = 0$ (light) to 1 mT (dark). Red points have the field oriented along z and blue points along x. Lines show fits to $U_{int}(R) = (\Gamma/2)(2a/R)^3$ or $U_{int}(R) = -\Gamma(2a/R)^3$ for $\mathbf{B}$ along z or x respectively. (b) Γ from each fit. Red and blue points show repulsive and attractive potentials respectively. The error bars are calculated from the standard deviation of Γ from fitting each individual measurement to $U_{int}(R) = (+\frac{1}{2}/-1) \times \Gamma(2a/R)^3 + c$

3.4.4 Magnetic susceptibility

Figure 3.9 shows Γ measured from all of the experiments, including those using strong traps. Fitting all points with a straight line, shown in black, gives a magnetic susceptibility of $\chi = (10.3 \pm 0.5) \times 10^{-12}\,\mathrm{Am^2T^{-1}}$. Including only the weak trap points gives $\chi = (9.5 \pm 1.0) \times 10^{-12}\,\mathrm{Am^2T^{-1}}$. The equivalent dimensionless volume magnetic susceptibilities $\chi_v = (3\mu_0/4\pi a^3)\chi$ are 1.13 ± 0.05 and 1.04 ± 0.1 respectively.

In order to compare our method to an established technique, we measure the magnetisation of a dried, bulk sample of particles using a SQUID magnetometer (superconducting quantum interference device). These apply a magnetic field pulse to the sample and measure the resulting magnetic moment with excellent sensitivity. The magnetisation per particle, m_p, is then calculated from the mass of the sample. Figure 3.10 shows the result. The susceptibility reaches a plateau at $B \approx 200\,\mathrm{mT}$ and is approximately linear at $B \lesssim 2\,\mathrm{mT}$, roughly following the expected form [158]

$$m = m_0 \left[\coth(\alpha B) - \frac{1}{\alpha B} \right]. \tag{3.11}$$

Fitting a straight line to the points with $B \leq 1\,\mathrm{mT}$ gives $\chi = 8.4 \times 10^{-12}\,\mathrm{Am^2T} - 1$, corresponding to $\chi_v = 0.92$, slightly lower than the value measured using optical traps. This difference is not surprising given that any water left in the sample during the SQUID measurement would lead to a slight underestimate of χ.

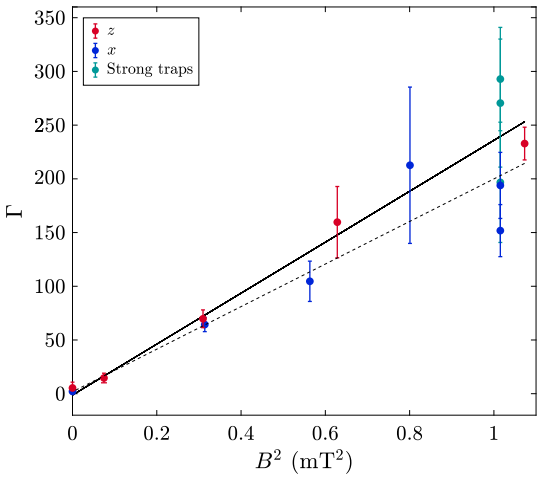


Figure 3.9: Γfrom all experiments. Red points have B along z, blue along x, and cyan along x with $V_0 > 60 k_B T$. The dashed line shows a linear fit to only the points measured with a weak trap (red and blue circles), while the solid line shows a fit to all points

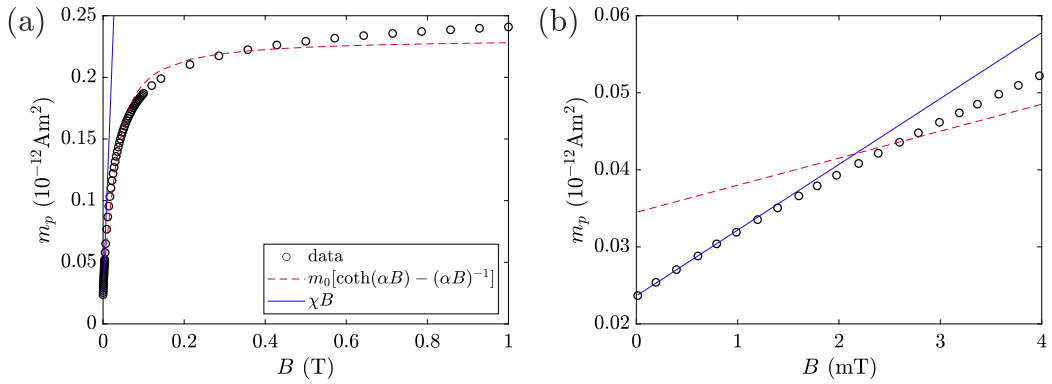


Figure 3.10: SQUID measurement of the magnetisation per particle (black circles) at 0-1 T (a) and 0-1 mT(b), with a linear fit (blue solid line) and a fit to equation 3.11 (red dashed line).

Comparing our measured χ_v to literature values is also appropriate because Invitrogen Dynabeads are advertised as being extremely consistent between batches. However, literature values for the χ_v vary wildly from 0.17 to 1.2 [129, 140, 153, 157, 159–164]. Those measured from bulk samples tend to be somewhat lower than those based on microscopic measurements of individual particles [160]. The main reason for the variation, however, is the wide range of magnetic field strengths over which the magnetic moment is assumed to increase linearly with B, from 0.1 T for the smallest value [159] to 0.5 mT for one of the largest [140]. Our SQUID measurement, however, shows that $m(B)$ is sub-linear down to at least 1 mT. Of those papers which measure χ_v over less than 2 mT [140, 153, 157, 164, 165], we find an average value of $\chi_v = 1.0 \pm 0.2$, consistent with our measurement both with and without the strong trap data points. This implies that our method of measuring pair potentials is as accurate as other techniques in the literature.

3.5 Conclusions

We have measured the pair potential of paramagnetic particles using a novel technique based on the probability distribution of the distance between two particles in an optical trap. Pair potentials were measured in magnetic fields up to 1 mT parallel and perpendicular to the sample plane, demonstrating that the method works consistently for both repulsive and attractive long ranged potentials. Zero field experiments showed that the precision of the method was approximately 5% of the trap strength. The maximum strength of the attractive potential measured was $40k_BT$; a significant improvement on other techniques. The magnetic susceptibility of the particles was found to be $\chi_v = 1.13 \pm 0.05$, consistent with literature values. We tested the sensi-

tivity of our technique to the trap strength by measuring a strongly attractive potential in traps with a depth of 25 to $202 k_B T$. Using stronger traps allowed us to measure the pair potential at smaller distances, where the attraction between the particles was strongest but more data using the same pair of particles is required to determine with statistical significance whether this lead to a systematic increase in the measured interaction parameter. Overall, our method of measuring pair potentials is widely applicable to many types of optical trap configurations and pair potentials, but is particularly suited to strongly attractive potentials, which are challenging to measuring using other techniques. Furthermore, the method is easy to implement and requires relatively little experimental and computation time.

Acknowledgments

This work was done in collaboration with Joan Codina, Ignacio Pagonabarraga and Jure Dobnikar. Simon Cassidy is thanked for the SQUID measurement.

Chapter 4

Aubry-type transition of undriven colloidal chains in a periodic potential

Abstract

In this chapter we measure the structure and dynamics of paramagnetic colloidal chains in a one-dimensional sinusoidal potential created with a line of optical traps. In particular, we probe the metastable states of the chains by slowly decreasing and then increasing the substrate potential. We study three different chain lengths, all of which show transitions from a state with no kinks to the state with the maximum number of kinks as the substrate decreases, followed by a transition to a state with zero, one or two kinks, depending on the chain length, when the substrate increases again. We measure the asymmetry, mobility and relative energy of each state, observing a finite analogue of the Aubry transition characterised by an increase in asymmetry and a decrease in mobility as the optical potential increases.

4.1 Introduction

Incommensurate systems, in which the ratio between the length-scales of each component is irrational, are ubiquitous in nature and technology [21, 30]. Examples include adsorbed surface layers [166, 167], intercalation compounds [6], magnetic super-lattices [168] and charge density waves [24]. These materials can have desirable properties; incommensurate graphite makes a better anode in lithium ion batteries than commensurate graphite [169], while incommensurate surfaces [35, 36, 170, 171] or lubricant layers [172] can have very low friction. Defects in crystals [173–176], grain boundaries [23, 177] and magnetic domain walls [178] can also be modelled as incommensurate systems, making this an important area of research for a wide range of materials.

One of the simplest models of an incommensurate system is the Frenkel-Kontorova model. This consists of an infinite one dimensional chain of harmonically interacting particles on a sinusoidal substrate potential [22]. The properties of the system depend on the interplay between competing length scales (particle spacing vs. substrate wavelength), energy scales (chain stiffness vs. substrate depth), and whether or not the chain is able to expand and contract (free vs. fixed ends). Remarkably, when an incommensurate infinite chain has fixed ends and the substrate potential is below some critical value, it exists in a free-sliding state. As the substrate potential increases, the chain undergoes a structural "transition by breaking of analyticity" into a pinned state, known as the Aubry transition [31]. A similar transition occurs in finite chains with free ends, this time characterised by a breaking of the ground state's reflectional symmetry [179,180]. In both cases, a structural transition is accompanied by a change in the pinning potential experienced by the chain.

Optical traps provide a convenient method for systematically studying Aubry-type transitions in experiments because they can be used to create periodic potentials with tunable substrate depth and lattice spacing. Bylinskii *et al.* [34,181] used chains of up to six ions driven through a periodic optical substrate to study a finite Frenkel-Kontorova-like system. They observed a transition from frictionless sliding to stick-slip dynamics accompanied by the appearance of kinks and discontinuities in the particle positions analogous to the Aubry transition. Kiethe *et al.* [182, 183] also observed some structural signatures of the Aubry transition between two adjacent ion chains in an extended optical trap. Brazda *et al.* [184] instead used a driven 2D

colloidal monolayer on an optical substrate to observe a pinned to free-sliding transition. They also studied the structure of a simulated undriven colloidal monolayer, observing a "coexistence region" where the structure changed hysteretically as a function of the substrate depth. This simulated static structural transition occurred at the same substrate depth as the experimental dynamic transition, but the authors did not measure it experimentally.

All of these experiments use particles with purely repulsive interactions held together by an extended harmonic optical trap. This leads to several key differences between the experiments and a typical atomic incommensurate system. The repulsive potential is concave, whereas the Lennard-Jones or Morse type potentials typical of atomic interactions have a convex attractive branch. This convex branch can cause chain breaking and phases with alternating long and short bonds [185], neither of which were observed in previous experiments. Furthermore, because the chain or monolayer is held together by an extended harmonic potential, it cannot freely diffuse so "free-sliding" phases can only be measured from the response to a driving force. Finally, it is important to study the edges of the system as the nature of the structural transition depends on whether the ends are fixed or free.

These recent experiments leave a gap which we address by creating a colloidal model system consisting of one-dimensional chains of paramagnetic colloidal particles in a sinusoidal optical potential. We study undriven chains in this chapter and driven chains in the next chapter, where we will directly compare the structure and dynamics in both cases. The colloidal pair potential contains a repulsive hard-sphere part and an attractive convex part, making it qualitatively similar to many atomic interactions. The chains are held together solely by their attractive pair potential, so have truly free ends, enabling expansion and contraction. We characterise the structure of the various states of the chains, observed at different depths of the optical potential, in terms of the average particle spacing, number of kinks, and symmetry. We then measure the mean squared displacement of the chains, observing a pinned to free-sliding transition in a undriven chain reminiscent of the Aubry transition. Finally, we use our knowledge of the optical and inter-particle energy to estimate the relative energies of each state.

4.2 Theory

In this section we will introduce the theory underpinning the structure and dynamics of flexible undriven chains in periodic potentials, beginning by introducing the Frenkel-Kontorova (FK) model. We describe its ground states and metastable states in the original model as presented in Braun and Kivshar [21], and its generalisations to finite chains. We then focus on the energy and dynamics of finite chains in the limit of very strong inter-particle interactions.

4.2.1 The Frenkel-Kontorova model for flexible chains in a periodic potential

A flexible chain in a periodic potential may be modelled using the Frenkel-Kontorova (FK) model. In its original form, the FK model consists of a one-dimensional (1D), infinite harmonic chain in a sinusoidal potential, as illustrated in figure 4.1.

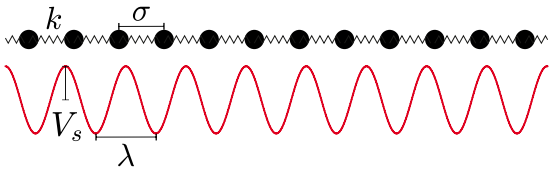


Figure 4.1: Diagram of the FK model, showing the sinusoidal substrate potential with depth V_s and wavelength λ, and the harmonic chain with equilibrium spacing σ and stiffness k.

This form is useful because any anharmonic pair potential $U_{int}(x_{ij})$ may be approximated as harmonic by expanding in a Taylor series about the equilibrium particle spacing, σ, and retaining only the nearest neighbour harmonic terms:

$$U_{int}(x_{ij}) \approx \frac{k}{2}(x_{ij} - \sigma)^2, \tag{4.1}$$

where $k = U''_{int}(\sigma)$ is the stiffness of the harmonic interactions. Note that σ is only equal to the particle diameter, $2a$, when the pair potential has a hard sphere repulsive term. Similarly, any periodic substrate potential may be approximated by the first term in its Fourier expansion, giving the sinusoidal potential

$$U_{sub}(x) = V_s \left[1 - \cos\left(\frac{2\pi x}{\lambda}\right)\right], \tag{4.2}$$

where V_s is the depth of the substrate potential and λ is its wavelength, shown in figure 4.1.

The infinite chain may have either fixed or free ends, leading to slightly different phase behaviour. Since we deal with finite chains in this thesis, which can easily expand and contract, we use free ends. In this case, the ground state of the chain is uniquely defined by the relative length and energy scales of the chain and the substrate. The latter is often quantified by the dimensionless relative stiffness g, given by [21]

$$g = \frac{k}{4V_s}\left(\frac{\lambda}{2\pi}\right)^2, \tag{4.3}$$

which is large when the chain is stiff or the substrate weak.

The competition between the length-scales is quantified by the ratio between the equilibrium particle spacing of the chain, σ, and the wavelength, λ. This ratio is often written in terms of the misfit, P, given by [21]

$$P = \frac{\sigma}{\lambda} - \text{int}\left\{\frac{\sigma}{\lambda}\right\}, \tag{4.4}$$

where int $\{...\}$ indicates rounding to the nearest integer, so that P always falls between $-1/2$ and $1/2$. For example, $P = 0$ when $\sigma = \lambda, 2\lambda, ...$ and $P = \frac{1}{2}$ when $\sigma = 1/2\lambda, 3/2\lambda, ...$ The misfit is therefore a measure of how close the equilibrium particle spacing is to an integer multiple of the wavelength. It is used because chains with different values of σ/λ but the same $|P|$ have the same phase diagram. Throughout this thesis, we use $\sigma/\lambda \approx 7/8$, giving a misfit of $P \approx -1/8$.

4.2.2 Ground states

When a free-end chain is placed in a substrate, it will expand or contract to an average particle spacing s. The average spacing has an associated window number, w, which is directly equivalent to the misfit but with the average spacing, s, in place of the equilibrium spacing, σ:

$$w = \frac{s}{\lambda} - \text{int}\left\{\frac{s}{\lambda}\right\}. \tag{4.5}$$

When $w = 0$, there is an average of one particle per integer number of wavelengths, so that every particle sits in a potential minimum. A fractional window number of the form $w = p/q$ can be obtained by having an average of q particles every $p + mq$ wavelengths, where m is an integer.

The structure of the ground state (GS) of a chain with $w = p/q$ is a regular array of p equally spaced kinks or anti-kinks every mq wavelengths. Kinks and anti-kinks are defined as a region where a potential well contains one extra or missing particle respectively. Starting from the state with one particle every m wavelengths, an (anti-)kink is created by shifting every particle to the right of the (anti-)kink (right)leftwards by one wavelength. Mathematically, the structure of the (anti-)kink is expressed in terms of the distance between each particle, x_n, and its hypothetical position in the $w = 0$ state at the bottom of the n^{th} substrate minimum, $n\lambda$:

$$u_n = x_n - n\lambda. \tag{4.6}$$

The equation of an (anti-)kink in the FK model is given by [21]

$$u_n = x_n - n\lambda = \frac{2\lambda}{\pi} \tan^{-1}\left[\exp\left(-z\frac{n\lambda - x_k}{d}\right)\right], \tag{4.7}$$

where $z = -\text{sign}(P)$ is the kink charge (positive for kinks, negative for anti-kinks), x_k is the kink position, and $d = \lambda\sqrt{g}$ is the kink width, which decreases with increasing substrate depth. Figure 4.2a and b show u_n and the corresponding particle positions for a kink and anti-kink respectively. The limiting values of u_n are $u_{n\to-\infty} = 0$ and $u_{n\to\infty} = \pm\lambda$, reflecting the fact that the particles to the right of the (anti-)kink are shifted by one wavelength to the (right) left. A ground state made of regularly spaced kinks is shown in figure 4.2c, while the $w = 0$ state is

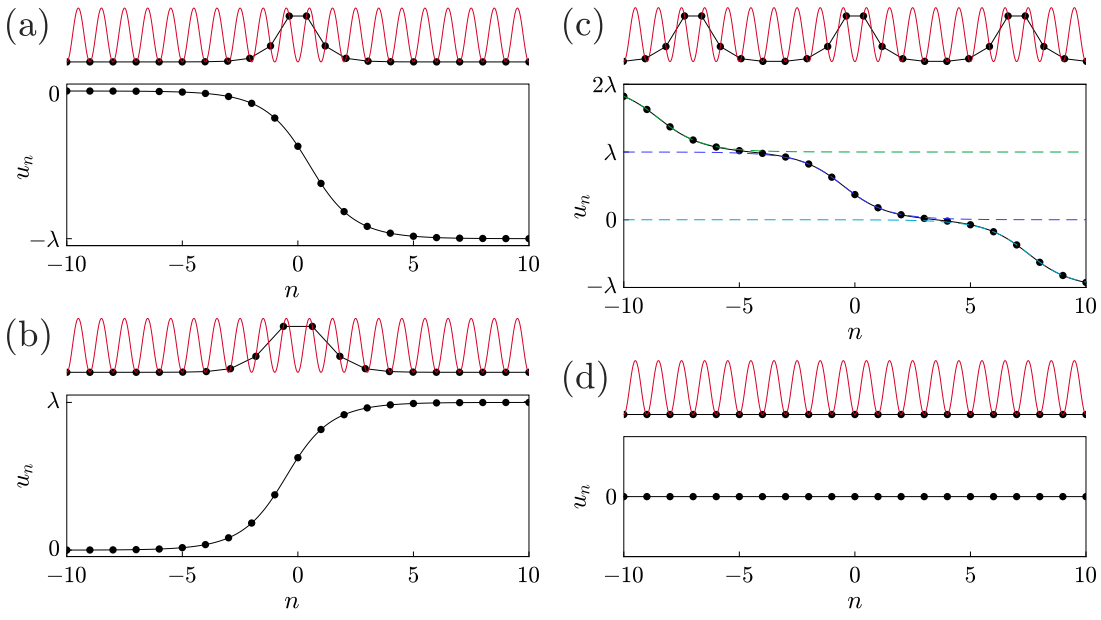


Figure 4.2: (a-d) The position of the n^{th} particle (black circle) on the substrate potential (red) and its corresponding u_n, in (a) a kink, (b) an anti-kink, (c) a cnoidal wave and (d) the $w = 0$ state.

shown in figure 4.2d for comparison.

The ground state of a chain is uniquely described by its window number, w, which describes the density of kinks or anti-kinks. We will now discuss how w varies as a function of the relative stiffness, g, and misfit, P. In the limit of very strong substrates ($g \to 0$) or very small misfits ($P \to 0$), the ground state of the chain has every particle sitting in a potential minimum such that $w = 0$. In the limit of very weak substrates, the ground state is very close to the equilibrium state of the chain in the absence of a substrate, so $w \to P$. As the substrate depth increases, w goes through a series of phase transitions from P to 0 via many intermediate states [186]. These states are shown in the $|P|$, g^{-1} phase diagram in figure 4.3 [30]. Each coloured tongue shows the region where the ground state corresponds to a different value of w. The light blue tongues show large regions where w is a low order fraction ($1/2$, $1/3$...), darker blue shows higher order tongues (such as $w = 2/5, 3/7$...), and the grey region contains many more tongues too thin to plot. At the bottom of the phase diagram (very weak substrates), there are many tongues of both low and high order. As the substrate potential increases, the low order tongues widen while the high order tongues in the gaps between them shrink, so that high order states become less likely. When $g^{-1} \lesssim 1$, incommensurate states with irrational w exist between the tongues, but when g^{-1} is above this critical threshold, only rational, commensurate states are allowed [21].

Changing the substrate potential ($V_s \propto g^{-1}$) at a fixed P, as we do in our experiments, is

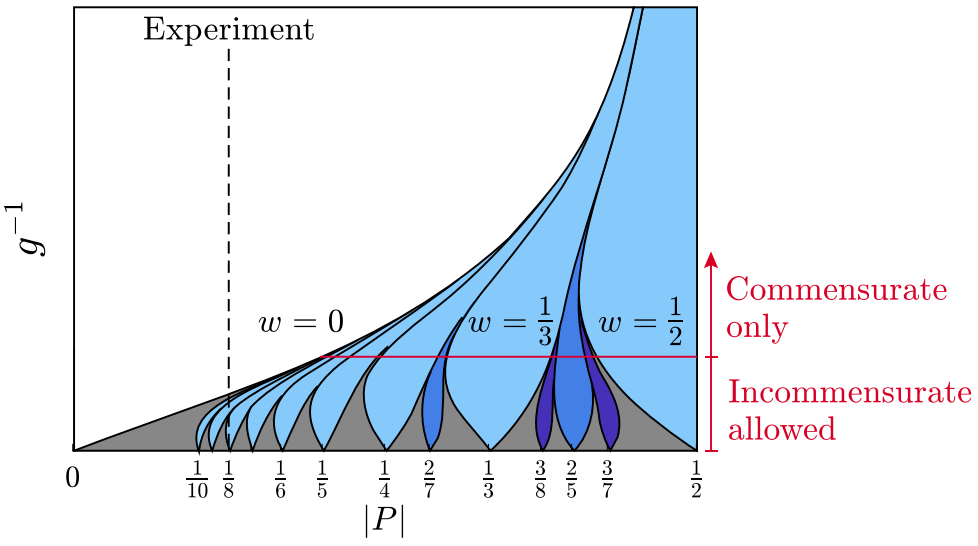


Figure 4.3: A sketch of the phase diagram of a free-end chain with misfit P and relative substrate depth g^{-1}, reproduced from [30]. The white region shows the $w = 0$ phase, light blue tongues show low order states with $w = 1/2$, $1/3, ...1/n$, darker blue tongues show higher order states, and the grey region contains many high order and incommensurate states. The red line shows the value of g^{-1} below which incommensurate (irrational w) states exist. The vertical dashed line shows the experimental $|P|$.

equivalent to moving vertically in the diagram (shown with a dashed line in figure 4.3). As the substrate potential increases from zero, w enters a low order phase close to P. For example, if $P \approx -1/8$ as in our experiments, increasing g^{-1} causes the chain to transition from the $w = P$ state into the $w = -1/8$ state. As g^{-1} increases further, w decreases in steps to the $w = -1/9$ state, then $-1/10$ and so on, until the chain eventually enters the $w = 0$ state. Between each large, low order step, w passes through a series of smaller, higher order steps. Each transition manifests as a change in the number of kinks or anti-kinks in the chain.

4.2.3 Metastable states

As well as the ground state, the chain may have many metastable states. These may have a different window number to the ground state, or the same window number but an irregular arrangement of kinks. Metastable states exist because there is an energy barrier associated with adding or removing a kink at the end of the chain or moving the kink by one wavelength. Figure 4.4 illustrates the origin of this energy barrier; in order to move a kink, a particle must travel over a potential maximum. This barrier is known as the Peierls Nabarro barrier, and it increases with increasing substrate depth [21]. A larger energy barrier must be overcome in order to create a kink at the end of the chain. This barrier is responsible for the metastability of the $w = 0$ state in weak substrates, for example.

The existence of many metastable states makes finding the ground state extremely challenging both theoretically and experimentally. It is therefore important to note that this thesis only studies the states which are experimentally accessible. We refer to these states as *metastable* states because and we do not attempt to determine whether any of them are the ground state.

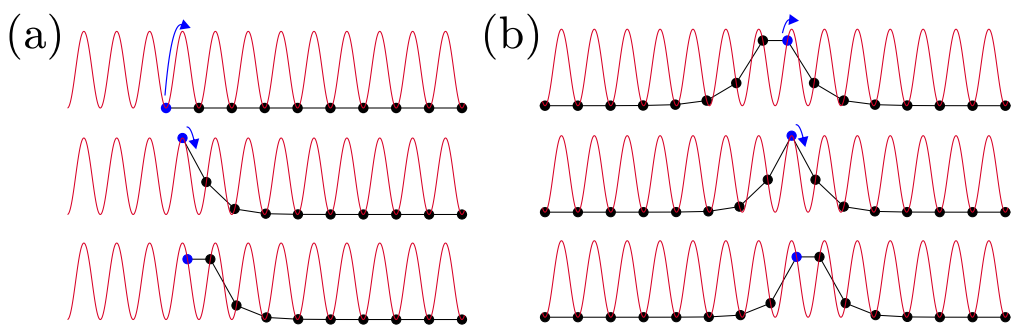


Figure 4.4: Illustration of the energy barrier when (a) a kink is created at the end of a chain and (b) moved one wavelength along the chain. The particle whose movement contributes most to the energy barrier is shown with a blue arrow.

4.2.4 Finite chains in a sinusoidal potential

The FK model deals with infinite chains. Our experimental system, however, consists of chains of up to 20 particles. The phase behaviour of finite chains is less well studied than infinite free-end chains, but has been shown experimentally [34] and theoretically [179, 180, 187] to share some similar features. In particular, Sharma *et al.* [180] and Braiman *et al.* [179, 187] independently showed that finite free end chains undergo a symmetry breaking transition equivalent to the Aubry transition – the free-sliding to pinned "transition by breaking of analyticity" present in infinite, fixed end chains.

This transition is most easily illustrated with odd numbered chains with an odd number of (anti)kinks, for example the $N = 5$ chain shown in figure 4.5. When the substrate depth ($\propto g^{-1}$) is small, as in figure 4.5a, the ground state and all metastable states of the chain are in the "analytical" regime where there is reflectional symmetry about the central particle, which sits on a potential maximum when N is odd. When the substrate depth increases beyond a critical value, it becomes more favourable to move the central particle either to the left or the right of the potential maximum, hence breaking the reflectional symmetry and creating a degenerate (left or right) ground state, shown in figures 4.5b and c. Metastable states also show analogous symmetry breaking transitions, but not necessarily at the same value of g as the ground state transition [180]. Sharma and Braiman *et al.* have shown that this reflectional symmetry breaking is the equivalent of the Aubry transition for finite chains [180, 187]. However, the free-sliding mode present in the infinite FK model at high g does not exist in finite chains [21] except for specific chain lengths in the rigid chain limit, which we will discuss in the next section.

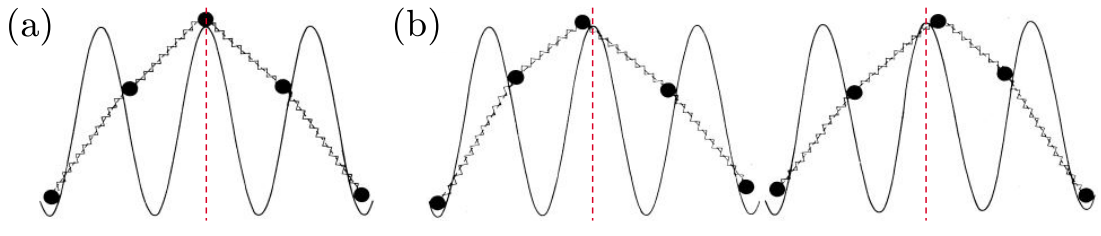


Figure 4.5: Ground states of a finite FK chain (a) before and (b) after the transition by breaking of reflectional symmetry, reproduced from [187]. The red line is the axis of symmetry.

4.2.5 Rigid, finite chains in a sinusoidal potential

It is useful to consider the limiting behaviour of a finite chain as the relative stiffness, g, tends to infinity. In this limit, the chain is rigid and all particles spacings are equal to the equilibrium particle spacing, σ.

Energy

Figure 4.6a shows the position and substrate potential of each particle in rigid chains of one to nine particles with the centre of mass at $x_{cm} = 0$ and $\sigma/\lambda = 7/8$ ($P = -1/8$), similar to our experiments. The total energy is the sum of the inter-particle energy, which is constant, and the substrate energy of each particle,

$$\mathcal{U}_{tot}(x_{cm}) = -V_s \sum_{n=-\frac{(N-1)}{2}}^{\frac{(N-1)}{2}} \cos\left(\frac{2\pi(x_{cm}+n\sigma)}{\lambda}\right) + \mathcal{U}_{int}, \tag{4.8}$$

where we have used $\mathcal{U}$ to denote the energy of the whole chain, as opposed to U, the energy of a single particle. Equation 4.8 simplifies to [188]

$$\mathcal{U}(x_{cm}) = -V_s \frac{\sin(N\pi\sigma/\lambda)}{\sin(\pi\sigma/\lambda)} \cos\left(\frac{2\pi x_{cm}}{\lambda}\right) = -V_s f_N \cos\left(\frac{2\pi x_{cm}}{\lambda}\right), \tag{4.9}$$

where $f_N = \sin(N\pi\sigma/\lambda)/\sin(\pi\sigma/\lambda)$, shown in figure 4.6b, is ratio between the total potential acting on the chain and that of a single particle. The sign of f_N, which alternates depending on

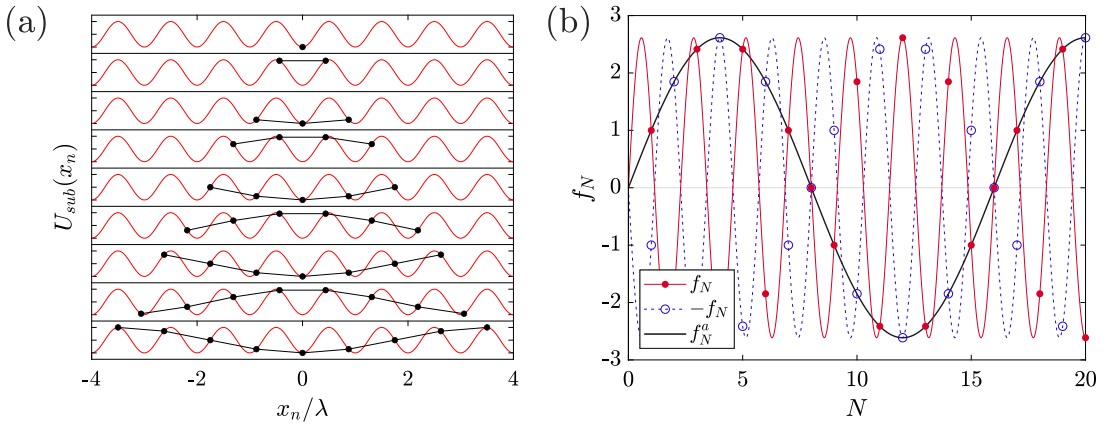


Figure 4.6: (a) Energy of each particle in rigid chains of $N = 1$ to 9 when $x_{cm} = 0$. (b) f_N versus chain length. The solid red line shows f_N and red dots show the value at integer N. The blue dashed line shows $-f_N$, and the black line shows the aliased form of f_N defined in equation 4.10.

whether N is odd or even, indicates whether the minimum energy of the chain occurs at $x_{cm} = 0$ (positive f_N) or $x_{cm} = \lambda/2$ (negative f_N).

Because f_N oscillates with a very small period of $\pi\sigma/\lambda$, it is often more convenient to use an aliased form where σ/λ is replaced by the misfit, $P = \sigma/\lambda - \text{int}\{\sigma/\lambda\}$ [189]:

$$f_N^a = \frac{\sin(\pi N P)}{\sin(\pi P)}, \tag{4.10}$$

shown in black in figure 4.6b. The magnitude of the aliased and non-aliased versions of f_N are equal for all integer N, while the sign is only equal for odd N. Importantly, $f_N = 0$ when the chain length is an integer multiple of $|P^{-1}|$ [188], which we denote N_0. This is because the substrate potentials of each particle always cancel each other out, as can be seen for the $N = 8$ chain in figure 4.6a. As a result, the energy of chains with $N = N_0, 2N_0, ...$ does not depend on the position of their centre of mass, therefore they experience no energy barrier to sliding across the substrate in the rigid chain limit. In our experiments, $N_0 \approx 8$.

Dynamics

The dynamics of an undriven rigid chain can be described by the Langevin equation of its centre of mass, found by summing the Langevin equations of each particle as follows:

$$\frac{dx_{cm}}{dt} = \frac{1}{N}\sum_n \frac{dx_n}{dt} = \frac{1}{N\zeta}\sum_n \left[F_{sub}(x_n) + \sum_{m\neq n} F_{int}(x_n, x_m) + \xi_n(t) \right]. \tag{4.11}$$

The total substrate contribution, $\mathcal{F}_{sub}(x_{cm})$, can be found by differentiating equation 4.9 to obtain $\mathcal{F}(x_{cm}) = f_N V_s (2\pi/\lambda)\sin(2\pi x_{cm}/\lambda)$. The inter-particle force is zero even without assuming a rigid chain because $F_{int}(x_n, x_m) = -F_{int}(x_m, x_n)$, so the pairwise contributions to the total inter-particle force cancel each other out. Assuming the fluctuating forces, $\xi_n(t)$, are all independent, they sum to a normally distributed random number $\xi_N(t)$ with

$$\langle \xi_N(t) \rangle = 0 \qquad \text{and} \qquad \langle \xi_N(t)\xi_N(t') \rangle = 2k_B T \zeta N \delta(t - t'). \tag{4.12}$$

This assumption is only true if we neglect hydrodynamic interactions. These arise because the motion of one particle, whether as a result of thermal fluctuations or driving forces, transfers momentum to the surrounding solvent. This creates long-ranged flows in the solvent, which in

turn exert a force on other particles [50]. To account for this effect, we replace $(N\zeta)$ in equations 4.11 and 4.12 with an effective drag constant, ζ_N. There are several theoretical expressions for the drag constant of a rigid chain of spheres which have received experimental confirmation [190]. However, we find experimentally that this approximation significantly underestimates the drag constant of our chains (see appendix A), so we instead use the empirical expression $\zeta_N = \zeta(N+1)/2$.

The overall Langevin equation for the centre of mass of a rigid, undriven chain then becomes

$$\frac{dx_{cm}}{dt} = \frac{1}{\zeta_N}\left[f_N V_s \frac{2\pi}{\lambda}\sin\left(\frac{2\pi x_{cm}}{\lambda}\right) + \xi_N(t)\right]. \tag{4.13}$$

The centre of mass of a finite, rigid chain of N particles in a sinusoidal potential therefore behaves as a single particle with drag constant ζ_N in a sinusoidal potential of depth $V_s f_N$.

4.3 Experimental methods

Our colloidal model system consists of chains of paramagnetic particles (radius $a = 1.4\,\mu\text{m}$) in a line of optical traps. We use the sample cells described in section 2.3.1. The line of 30 optical traps create a one-dimensional sinusoidal substrate with a wavelength of $\lambda = 3.21\,\mu\text{m}$. Using the experimentally measured equilibrium particle spacing of a chain of $N = 16$, $\sigma = (2.82 \pm 0.05)\,\mu\text{m}$, this gives a misfit of $P \approx -1/8$ and $N_0 \approx 8$, where N_0 is the chain length which experiences zero substrate force in the rigid chain limit. The depth of the substrate, V_s, was calibrated at laser powers of 125 mW, 250 mW, 375 mW and 500 mW by driving a single particle over the potential and measuring its critical velocity [123], giving substrate depths of $V_s = (6.9 \pm 0.5)\,k_BT$, $(12.9 \pm 0.6)\,k_BT$, $(19.9 \pm 0.5)\,k_BT$, and $(26.8 \pm 0.6)\,k_BT$. This process is described in sections 5.2.2 and 5.3.

A magnetic field of $B = 0.55\,\text{mT}$ is created along the x axis of the sample using permanent magnets as described in section 2.3.2, causing the particles to form chains in the field direction. We use chain lengths of 8, 16 and 20 particles, equivalent to N_0, $2N_0$, and $2.5N_0$. These chains are effectively one-dimensional with inter-particle interactions of

$$U_{int}(x) = U_{HS} - \Gamma\left(\frac{\sigma}{x}\right)^3. \tag{4.14}$$

We do not use the interaction parameter, Γ, measured in chapter 3 because that measurement probed the long-ranged interactions at separations greater than 5 µm, whereas these experiments probe the interactions at separations close to one diameter (2.8 µm). At small separations, we expect the dipole approximation to break down [161] and other contributions to the pair potential to be present. Instead, we measure an effective interaction parameter of $\Gamma = 88 \pm 5$ by matching the experiments in this chapter to simulations. This process is described in appendix B.

We use the method used by Sharma *et al.*, Mandelli *et al.* and Brazda *et al.* [180,184,191] to probe the structure of each chain as a function of the substrate depth and in different metastable states. Each chain is initially placed in a line of optical traps with a strong laser power of 500 mW ($V_s = 27\,k_BT$). By moving the stage slowly back and forth, we force the chain into a stretched state where all particles sit near a potential minimum and the average separation is approximately one wavelength. The chain is allowed to equilibrate for 1 minute, then the substrate depth is slowly decreased to zero in steps of 10 mW every 100 s, equivalent to 1.7 Brownian times (the Brownian time, τ_B, is defined in equation 2.7 as the time taken for the particle to diffuse over its own diameter). The potential is then increased again from $V_s = 0\,k_BT$ to $27\,k_BT$ in steps of the same size. This process allows us to probe the different states adopted by the chain in the forward and backwards halves of the experiment.

4.4 Results and discussion

In this section we characterise the structure of the metastable states adopted by the three chain lengths studied at different substrate potentials by analysing the average particle spacing, s, the associated number of kinks, N_k, and an asymmetry parameter. We then measure the pinning potential experienced by the chain from its mean squared displacement. Finally, we estimate the relative energies of each state.

4.4.1 Chain structure

A simple way to characterise the state of a free-end chain as a function of substrate depth, V_s, is to look at the average spacing between particles, s. This spacing is associated with an average number of kinks in the chain, $N_k = N - N_{wells}$, via the relation $N_{\text{wells}} = \text{int}\,\{(N-1)s/\lambda\}$, where N_{wells} is the number of substrate minima occupied by the chain. The number of kinks is

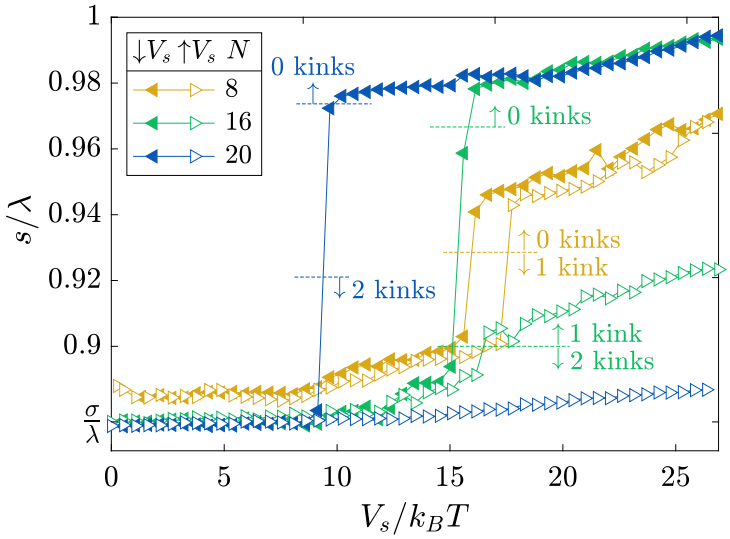


Figure 4.7: Average spacing, s, against substrate depth, V_s, as V_s decreases (filled $\triangleleft$) and increases ($\triangleright$), in chains of $N = 8$ particles (yellow), $N = 16$ (green) and $N = 20$ (blue). Annotated dashed lines indicate the regions where the number of kinks, N_k, changes.

therefore given by

$$N_k = (N-1)\,\mathrm{int}\left\{1 - \frac{s}{\lambda}\right\}. \tag{4.15}$$

At the beginning of each experiment, we initialise each chain in a state with all particles at the bottom of a substrate potential minimum, or well, such that $N_k = 0$ and s is close to λ. The average spacing, s, of the three chains with $N = 8$, 16 and 20 particles is shown in figure 4.7 as a function of the substrate depth, V_s. The triangular symbols point in the direction of time; beginning in the top right corner of the graph, moving left along the lines of $\triangleleft$ symbols as V_s is slowly decreased from $27\,k_BT$ to 0, then following the $\triangleright$ symbols to the right as V_s increases back to $27\,k_BT$. The $N = 8$ chain has a slightly lower initial s as the $N = 16$ and 20 chains, reflecting the fact that it can contract further without adding any kinks, as indicated by the horizontal dotted lines marking the boundaries between the regions where s corresponds to 0, 1 and 2 kinks.

In the first half of the experiment, as V_s decreases, there is a slow decrease in the average spacing of all three chains, followed by a sudden drop in s to slightly larger than the equilibrium spacing, σ. This sudden drop in s occurs across the boundary where the number of kinks changes from zero to one in the $N = 8$ chain and zero to two in the $N = 16$ and $N = 20$ chains. As V_s decreases further, s continues to decrease until approximately $10\,k_BT$, when it reaches a plateau

at $s = \sigma$ (allowing for polydispersity). Overall, all three chains transition from a state with no kinks to the maximum possible value of $N_k = 1$ or 2 for $N = 8$ or $N = 16$ and 20 respectively.

In the second half of the experiment, where we increase V_s again, each chain behaves differently. The $N = 8$ chain follows the first half of the experiment in reverse with a small amount of hysteresis, showing a rapid transition from N_k =1 to 0 at $V_s \approx 16\,k_BT$. The average spacing of the $N = 16$ chain also follows the first half of the experiment until V_s reaches $15\,k_BT$. At this point, instead of jumping from $N_k = 2$ to $N_k = 0$ as in the first half of the experiment, s makes a smaller jump to the value where N_k first reaches 1. The chain then remains in the $N_k = 1$ state throughout the rest of the experiment, but s continues to increase with increasing V_s. The $N = 20$ chain shows different behaviour again, as s increases very slowly with increasing V_s without showing any sharp transitions, so that $N_k = 2$ throughout the second half of the experiment. In summary, as the substrate potential changes from $V_s = 27\,k_BT \rightarrow 0\,k_BT \rightarrow 27\,k_BT$, the $N = 8$, 16 and 20 chains transition from $N_k = 0 \rightarrow 1 \rightarrow 0$, $N_k = 0 \rightarrow 2 \rightarrow 1$, and $N_k = 0 \rightarrow 2 \rightarrow 2$ respectively.

From the different states of the chains in each half of the experiment, we can assume that each chain has one accessible stable state with $s \approx \sigma$ at low V_s, but several metastable states at high V_s, each characterised by its number of kinks, N_k. We now rationalise which transitions between states are possible using the position of the particles at the edges of the chain. Diagrams of the possible states with $N_k = 0$ ($s = \lambda$), $N_k = 1$ ($s = (N-2/N-1)\,\lambda$), and $N_k = 2$ ($s = \sigma$) are shown for each chain length in figure 4.8. In the $N = 8$ chain, the transition from the $N_k = 1$ to the $N_k = 0$ state is possible because the two edge particles sit just outside of the nearest potential maximum, so there is no substrate energy barrier to expansion. This transition therefore becomes possible when the substrate is strong enough to overcome the inter-particle energy barrier associated with expanding the chain. The same is true of the $N_k = 2 \rightarrow 1$

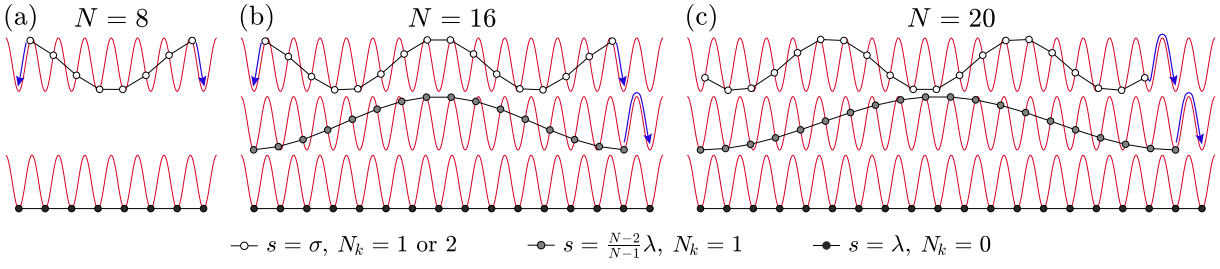


Figure 4.8: Chains of $N = 8$ (a), 16 (b) and 20 (c) particles with $s = \sigma$ (top), $N_k = 1$ (middle), and $s = \lambda$ (bottom).

transition in the $N = 16$ chain. In contrast, in order for the $N = 16$ chain to transition from the $N_k = 1$ to 0 state, one of the edge particles must hop over a substrate maximum. This process has too great an energy barrier to occur within our experimental time frame. There is a similar energy barrier associated with the $N_k = 2 \rightarrow 1$ and $1 \rightarrow 0$ transitions of the $N = 20$ chain, so these also do not occur. Transitions in the opposite direction from the $N_k = 0 \rightarrow 1 \rightarrow 2$ states always have a substrate energy barrier, but this is balanced by the decrease in the inter-particle energy due to the chains' contraction when the substrate is sufficiently weak. This behaviour highlights the crucial role of the chain's edges in determining whether a state is accessible.

We now examine the local structure of each state by looking at the positions of each particle, x_n and the distance between a particle and its two neighbours, $s_n = (x_{n+1} - x_{n-1})/2$, as opposed to the average distance, s. Figure 4.9a-c shows the position of each particle in chains with $N = 8$, 16 and 20 as the substrate potential first decreases, and then increases again, over time. The particles are coloured by the spacing between the particle and its neighbours, s_n, with blue indicating the equilibrium spacing, σ, and red indicating one wavelength, λ. We will first discuss the structure of all chains in their initial high V_s state, followed by their low V_s state, and then we will discuss each chain in its final high V_s state separately.

When the chains are in the $N_k = 0$ state at the start of the experiment, particles in all three chains are initially fairly evenly spaced at the bottom of the substrate minima, as can be seen in an example image of the $N = 16$ chain at $t = 0$ in figure 4.9d(i). As V_s decreases from $27\,k_BT$ to $15\,k_BT$, we begin to see pairs of red coloured particles in between groups of blue or green particles in figure 4.9a-c. The blue/green particles represent groups of closely spaced particles, each of which is separated by a long bond represented by the pair of red particles. An example of this type of structure is shown in figure 4.9d(ii). By looking at the positions of the red particles in figures 4.9a-c, we can see the long bond rapidly switching between different particles, so that at any one time each chain may contain different combinations of groups of two to five particles. As V_s decreases, the shorter s_n approaches σ, the longer s_n increases, and the average group size increases. This occurs in all chains, but is particularly noticeable in the $N = 20$ chain because the $N_k = 0$ state exists for longer. This is consistent with the behaviour of a modified Frenkel-Kontorova model with a convex inter-particle potential [185]. Because the attractive term of our pair potential is convex, an evenly spaced chain is higher in energy than a chain with long bonds followed by several short bonds [185]. The chain is prevented from

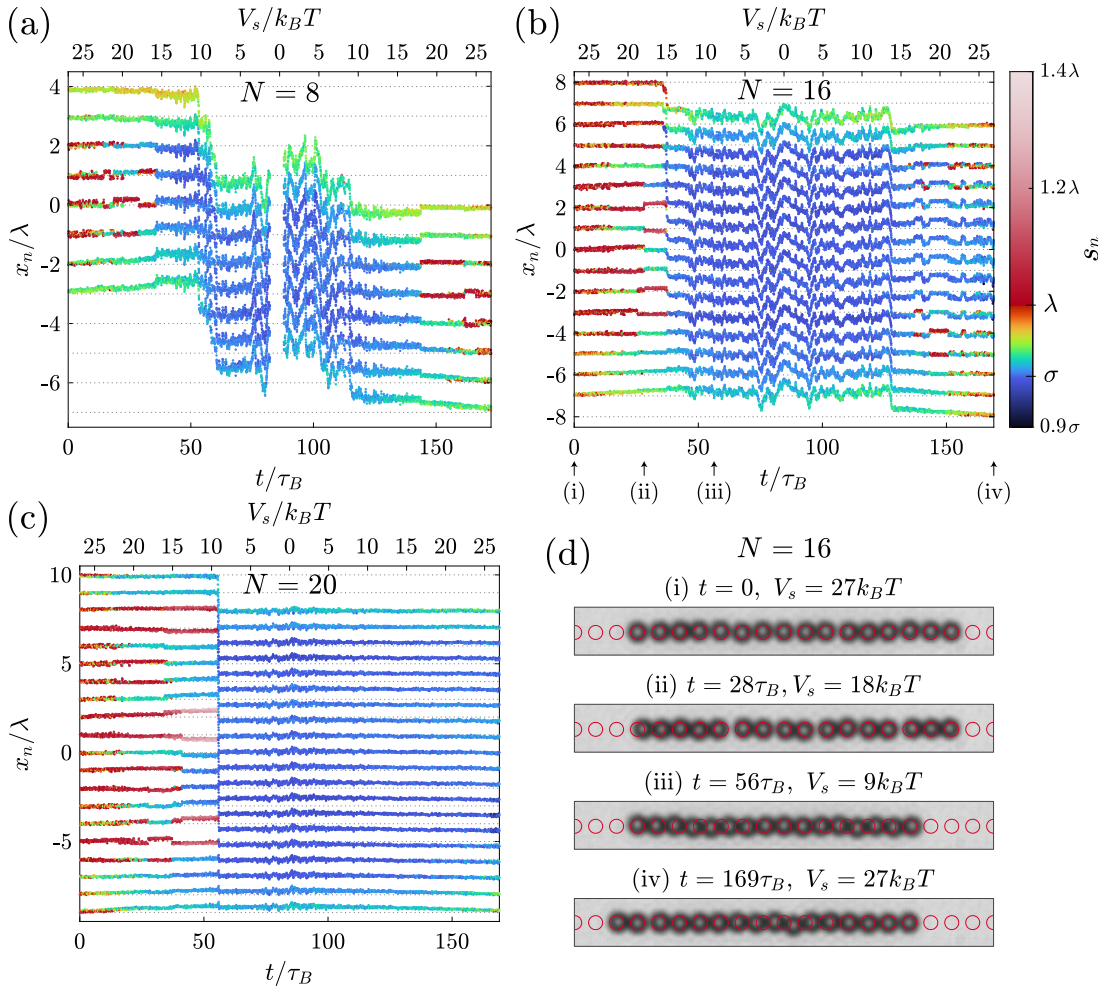


Figure 4.9: (a-c) Positions of each particle, x_n, in chains with N =8 (a), 16 (b), and 20 (c), over time, coloured by their nearest neighbour spacing, s_n. Note that (a) has some missing data where the software controlling the laser power temporarily froze. The top x axis shows the substrate depth, V_s, as it decreases then increases over time. Grey lines indicate the positions of the substrate minima. (d) Images from the $N = 16$ experiment. Red circles show the trap positions.

rupturing completely by the strong substrate potential, hence the increase in the long bond length with decreasing V_s.

In the middle of each experiment, when $V_s \lesssim 10\,k_BT$, all particles are coloured blue, indicating $s_n \approx \sigma$, with no significant structural features. A snapshot of this state is shown in figure 4.9d(iii). The structure does not noticeably change throughout the $V_s \lesssim 10\,k_BT$ region.

In the final part of the experiment, when V_s increases from 15 to 27 k_BT, each chain behaves slightly differently. The $N = 8$ chain returns to its original $N_k = 0$ state, and once again has groups of short bonds separated by longer bonds. When the $N = 16$ chain transitions to the $N_k = 1$ state at $V_s = 16\,k_BT$, we see the appearance of one longer bond and a large compressed region with $s_n \approx \sigma$, in which there is a kink. This can be clearly seen in the final image in

figure 4.9d(iv), where there is a long bond between the second and third particles, and a slightly buckled kink at the tenth particle. The $N = 20$ chain remains in the $N_k = 2$ state, and particles remain even spaced with $s_n \approx \sigma$ throughout the chain.

4.4.2 Symmetry

The transitions observed in figures 4.7 and 4.9, from the $s \approx \sigma$ state at low V_s to the various states present at high V_s, resemble the symmetry breaking transition studied by Braiman and Sharma *et al.* [179, 180]. They defined the equivalent of an Aubry transition in finite chains as the appearance of metastable states or ground states which break the reflection symmetry about the centre of the chain. We quantify the asymmetry of our chains using an asymmetry parameter, $\langle \Delta x_n^2 \rangle$, defined as the mean squared difference between the particles in the original chain and in the chain reflected about its centre of mass:

$$\langle \Delta x_n^2 \rangle = \frac{1}{N} \sum_{n=(N-1)/2}^{(N+1)/2} \left(x_n + x_{-n} - 2x_{cm} \right)^2 . \tag{4.16}$$

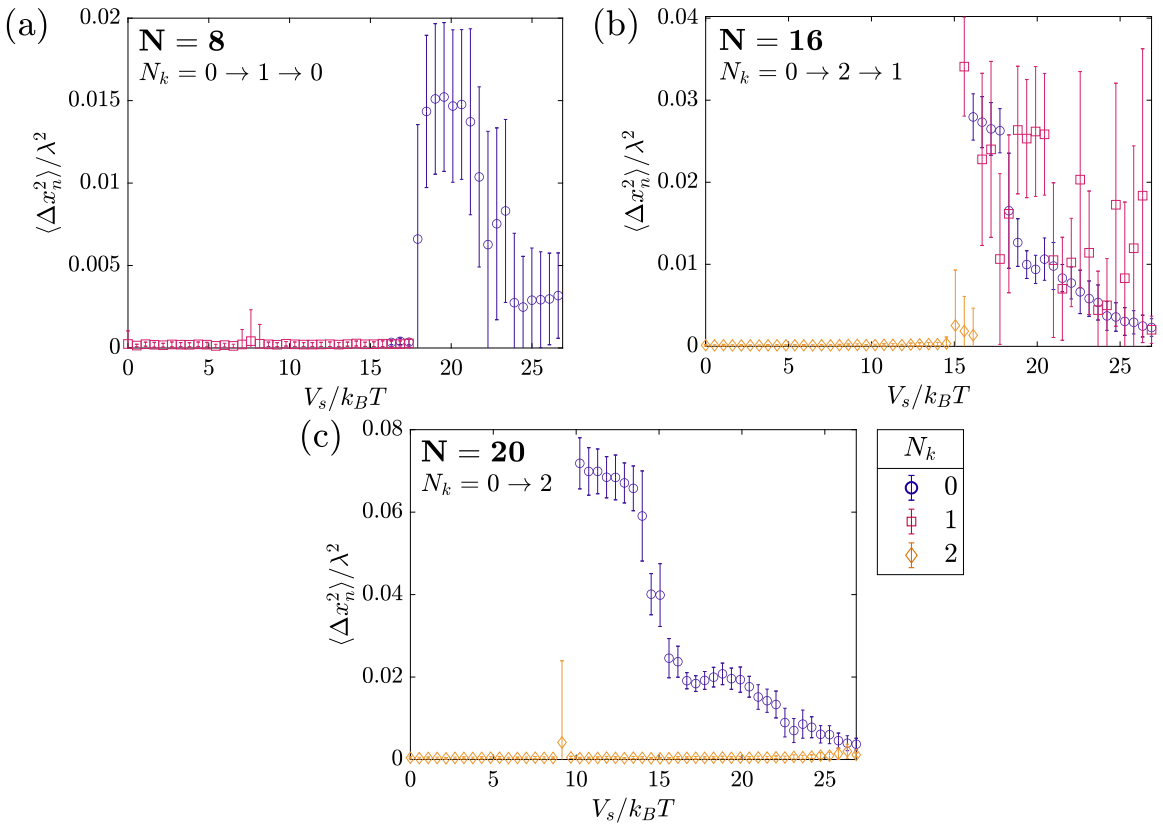


Figure 4.10: Asymmetry, $\langle \Delta x_n^2 \rangle$, of the $N_k = 0$ (blue circles), $N_k = 1$ (pink squares) and $N_k = 2$ (yellow diamonds) states of chains with $N = 8$ (a), 16 (b) and 20 (c) as a function of the substrate potential, V_s.

When the chain is perfectly symmetric, $\langle \Delta x_n^2 \rangle = 0$.

Figure 4.10 shows this asymmetry parameter, $\langle \Delta x_n^2 \rangle$, as a function of V_s. Where the chain is in the same state in both the increasing and decreasing halves of the experiment, we take the average. Otherwise, both states are shown. The $N_k = 2$ state of the $N = 20$ chain has low asymmetry at all V_s, but in all other cases, there is an abrupt transition from very low asymmetry to high asymmetry as V_s increases and N_k decreases. This suggests that the chains do undergo the finite Aubry transition of Braiman and Sharma *et al.* [179, 180], but while they only studied odd-numbered chains, we have observed the transition in even numbered chains. Furthermore, the lack of a transition for the $N = 20, N_k = 2$ state is consistent with Sharma's observation that not all metastable states undergo the transition at the same substrate depth. Interestingly, the asymmetry of the $N_k = 0$ state is largest just before the transition, and decreases with increasing V_s as the particles approach the bottom of their wells.

4.4.3 Chain dynamics

We have shown that our chains undergo a finite equivalent of an Aubry transition, in which the symmetric state with $s \approx \sigma$ present at low V_s transitions to several asymmetric metastable states with $N_k = 1$ or 0. In order to determine whether these structural changes are also accompanied by a de-pinning transition, we measure the mobility of the chain using the mean squared displacement (MSD, $\langle \delta x^2 \rangle$) of its centre of mass, x_{cm}. Figure 4.11 shows the MSDs at several different substrate depths. A completely flat MSD, such as those seen at high V_s in the first half of each experiment, shown in dark blue in figures 4.11a-c, indicates that the chain is strongly pinned to the substrate potential. MSDs which initially have a gradient of one but then reach a plateau are indicative of slightly weaker pinning, for example the MSDs of the $N = 20$ chain in the increasing V_s half of the experiment shown in red in figure 4.11c. When the MSD always has a gradient close to one, such as those of the $N = 8$ and 16 chains in weak V_s shown in light blue or yellow in 4.11a-b, the pinning potential is too small to be measured over our experimental timescale.

The stiffness of the pinning potential acting on by the chain can be extracted from the plateau value of the MSD. We assume the chains are pinned to the substrate by an approximately sinusoidal potential $\mathcal{U}_{pin}(x_{cm})$ with a depth of V_{pin}. At the bottom of the well, the potential is

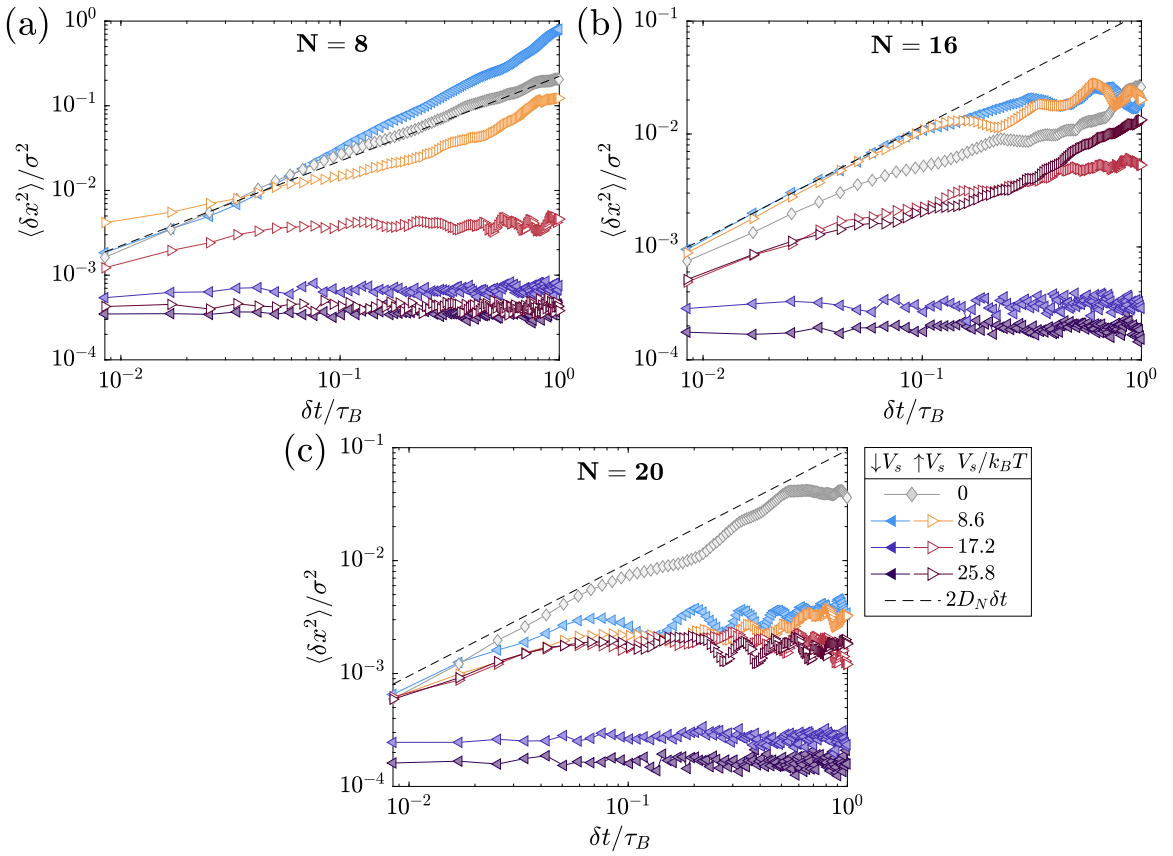


Figure 4.11: MSDs of the centre of mass in x of chains with $N = 8$ (a), 16 (b) and 20 (c) at $V_s = 26$, 17, 9 and $0\,k_BT$ (dark to light) from the decreasing (blue) and increasing (red) half of the experiment.

approximately harmonic with stiffness $V_{pin}(2\pi/\lambda)^2$:

$$\mathcal{U}_{pin}\left(x_{cm}\right) \approx V_{pin}\left[1-\cos\left(\frac{2\pi(x_{cm}-x_{min})}{\lambda}\right)\right] \approx V_{pin}\left(\frac{2\pi}{\lambda}\right)^2 \frac{(x_{cm}-x_{min})^2}{2}, \tag{4.17}$$

The plateau value of the MSD, $\langle \delta x^2 \rangle_{\delta t \to \infty}$, is therefore related to V_{pin} via [192]

$$\frac{V_{pin}}{k_BT} = \frac{2}{\langle \delta x^2 \rangle_{\delta t \to \infty}} \left(\frac{\lambda}{2\pi}\right)^2. \tag{4.18}$$

The finite duration of our experiments limits the lowest value of V_{pin} that can be measured. This is because we measure the value of the MSD at $t = \tau_B$, not $t \to \infty$. If the MSD is still diffusive at this point, we will measure an apparent "plateau value" of $\langle \delta x^2 \rangle = 2(k_BT/\zeta_N)\tau_B = \sigma^2\zeta_1/\zeta_N$, where ζ_1 and ζ_N are the drag constants of one particle and a chain of N particles respectively. Substituting this in equation 4.18 gives a resolution of $V_{pin} > 2(\zeta_N/\zeta_1)(\lambda/2\pi\sigma)^2$.

The pinning potential depth per particle, V_{pin}/N, is plotted against V_s in figure 4.12. The three different chain lengths show slightly different behaviour so we will discuss them separately.

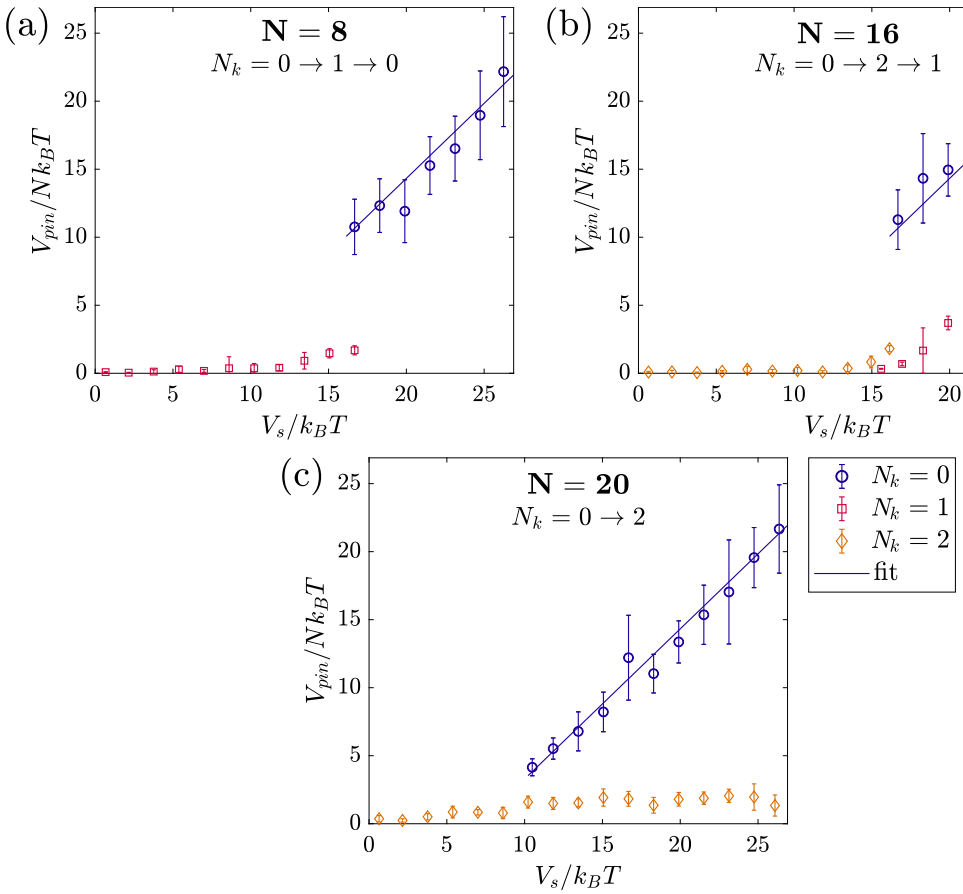


Figure 4.12: Pinning potential depth per particle, V_{pin}/Nk_BT, against substrate depth, V_s/k_BT, for chains of $N = 8$ particles (a), $N = 16$ (b) and $N = 20$ (c), in a state with $N_k = 0$, 1 and 2 (blue, red and yellow respectively). The solid blue line is a linear fit to all three $N_k = 0$ states, which is shown as a guide to the eye.

In weak substrates of $V_s \lesssim 8\,k_BT$, the pinning depth acting on the $N = 8$ chain is very low, close to the experimental resolution. This is what we would expect from the rigid chain limit of an $N = 8 \approx N_0$ chain, which predicts that the total substrate potential is zero at all centre of mass positions when N an integer multiple of N_0. As V_s increases, V_{pin} remains very low until $V_s \approx 8\,k_BT$, when it starts to increase slightly, consistent with the slight increase in s observed in figure 4.7 at a similar V_s. V_{pin} then shows a dramatic increase at $V_s \approx 16\,k_BT$ as the state changes from the $N_k = 1$ state with $s \approx \sigma$ to the $N_k = 0$ state. Above this point, V_{pin} increases linearly with V_s, slowly approaching the maximum possible value of $V_{pin} \to NV_s$, the pinning potential experienced by a rigid chain with $s = \lambda$. This behaviour is consistent with the fact that s slowly approaches λ as V_s increases.

The $N = 16$ chain shows a similar transition to the $N = 8$ chain in the decreasing V_s half

of the experiment. At low V_s, V_{pin} is close to the experimental resolution, as expected from the rigid chain limit. V_{pin} then shows a slight increase, which we attribute to the increase in s, followed by a large increase at $V_s \approx 16\,k_BT$ when the chain transitions to the $N_k = 0$ state. In the increasing V_s half of the experiment when the chain goes from the $N_k = 2$ to $N_k = 1$ state, there is a more gradual increase in V_{pin}. This is because the kink can diffuse freely in the middle of the chain, suggesting that there is a low Peierls-Nabarro energy barrier to moving the kink from one potential well to the next – much less than the energy barrier needed to remove a kink from the chain. The kink diffusion can also be seen in the particle positions in figure 4.9, where the blue coloured ($s_n \approx \sigma$) particles forming the kink are far more mobile than the orange $s_n \approx \lambda$ particles at the edge. Interestingly, the V_{pin} of the $N_k = 1$ chain does not seem to increase with V_s, implying that the kink's motion is limited more by the length of the chain than the Peierls-Nabarro barriers.

Unlike the $N = 8$ and 16 chains, the $N = 20$ chain shows significant pinning at all $V_s > 0$, consistent with the fact that the $N = 20$ chain feels the maximum substrate potential in the rigid chain limit. The pinning potential experienced by the chain in the $N_k = 2$ state, present throughout the increasing V_s half of the experiment, increases sub-linearly with increasing V_s. This may be because the two kinks become more mobile as the chain stretches, compensating for the increase in the substrate potential. The $N_k = 0$ state feels the same V_{pin} per particle as the other two chains, falling onto the same straight line which approaches V_s as $V_s \to \infty$.

Overall, we see an abrupt transition from high to low V_{pin} only when the chain transitions from the $N_k = 0$ state into the $s \approx \sigma$ ($N_k = 1$ or 2) state. Otherwise, the change in V_{pin} is more gradual. The presence of mobile kinks in the lower energy metastable states of the longer chains significantly decreases their pinning potential, but it does not cause free sliding because the kinks cannot diffuse beyond the ends of the chain.

4.4.4 Chain energy

Next, we estimate the relative energies of the two states adopted by each chain in the first and second halves of the experiment at high V_s. It is impossible to determine whether either state is the ground state, but we can establish which is the more stable state. We do so by estimating the total substrate potential, $\mathcal{U}_{sub}$, and the magnetic part of the inter-particle potential, $\mathcal{U}_{sub}$, from the (x, y) coordinates of each particle. We do not include a repulsive

contribution to the inter-particle potential because we assume the repulsive part is hard-sphere-like. The energies are calculated relative to a chain with uniform spacing $s = \sigma$ and centre of mass at $x_{cm} = \lambda/4, y_{cm} = 0$, where the substrate contribution is the same for all chain lengths, and we use two-dimensional coordinates to account for small fluctuations in the y direction, visible in figure 4.9d. The substrate contribution to the energy per particle is therefore given by equation 2.25 for the total trap potential:

$$\frac{\mathcal{U}_{sub}}{Nk_BT} = \frac{c_0}{2} + \frac{1}{N}\sum_{n=1}^{N}\left[\frac{c_0}{2} - V_s\cos\left(\frac{2\pi x_n}{\lambda}\right)\right]\exp\left(-\frac{k}{2V_0}y_n^2\right), \tag{4.19}$$

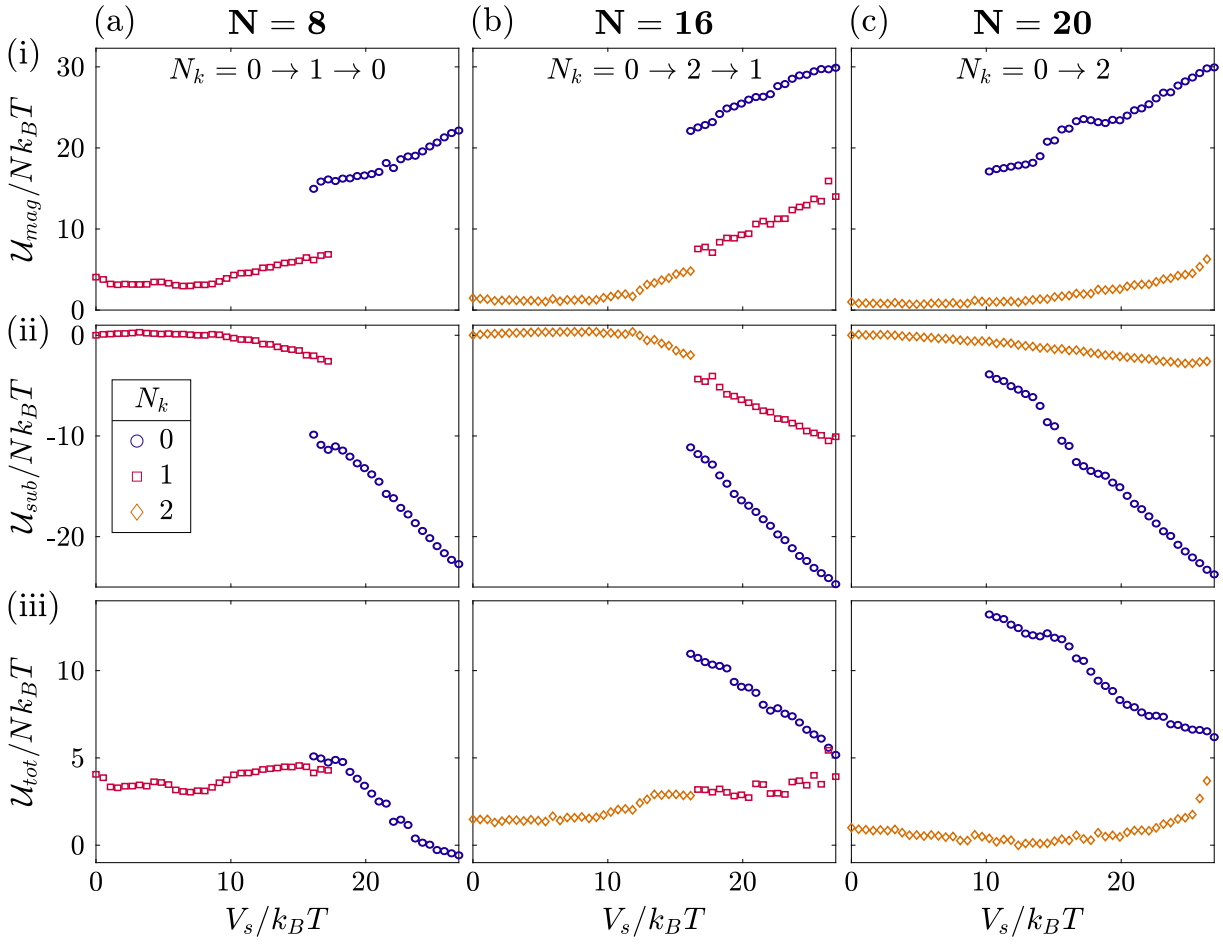


Figure 4.13: Magnetic (i), substrate (ii) and total (iii) contribution to the energy per particle in chains of 8 (a), 16 (b) and 20 (c) particles, averaged over the increasing and decreasing V_s halves of the experiment. Red circles, magenta squares and blue diamonds indicate states with $N_k = 0$, 1 and 2 respectively.

where c_0 is the trap depth defined in equation 2.24. The magnetic part of the inter-particle energy is

$$\frac{\mathcal{U}_{mag}}{Nk_BT} = \frac{\Gamma}{N}\sum_{j>i}\sum_{i=1}^{N-1}\frac{\sigma^3}{2r_{ij}^3}\left(1-3\frac{x_{ij}^2}{r_{ij}^2}\right)+\frac{1}{(j-i)^3} \tag{4.20}$$

We use an effective interaction parameter of $\Gamma = 88.4$ obtained by comparing the experiments to simulations with different values of Γ, as described in appendix B.

Figure 4.13 shows the substrate, magnetic, and total energy, $\mathcal{U}_{tot} = \mathcal{U}_{sub} + \mathcal{U}_{mag}$, as a function of V_s, for the $N = 8$, 16 and 20 chains. The states containing $N_k = 0$, 1 and 2 kinks are shown in blue, pink and yellow respectively. Where the chain is in the same state in both halves of the experiment, we take the average. At low V_s, both the magnetic and substrate contributions to the energy of all chains are close to 0, as expected given that all chains are in the rigid chain limit with $s \approx \sigma$. At high V_s, all states have a negative substrate contribution and positive magnetic contribution whose magnitude increases with increasing V_s, reflecting the fact that the chains become more stretched and particles sit closer to the bottom of a potential well. In the $N = 8$ chain, there is only a small window at $V_s \approx 15\,k_BT$ where both the $N_k = 1$ and $N_k = 0$ states coexist. Within this window, the greater $\mathcal{U}_{mag}$ of the $N_k = 0$ state is balanced by its lower $\mathcal{U}_{sub}$, so the total energy of the two states is almost identical. In the $N = 16$ and 20 chains, where there is a coexistence region between the $N_k = 0$ state and the $N_k = 1$ or 2 state respectively, we can compare the energy of both states as a function of V_s. In both chains, the $N_k = 0$ state has a larger energy than the $N_k = 1$ or 2 state when it first appears at $V_s \approx 15\,k_BT$, but the difference between the two states decreases as the substrate contribution to the total energy decreases faster than the magnetic contribution with increasing V_s. At the highest V_s we measure, the two states have a similar energy, suggesting that the $N_k = 0$ state will eventually become the most stable at substrate depths beyond the reach of these experiments.

4.5 Conclusions

We have created a colloidal Frenkel-Kontorova type system consisting of flexible chains of paramagnetic particles with $N = 8,\ 16$ and 20 in a periodic substrate formed from a line of optical traps. We probed the metastable states available to this system by increasing and decreasing the substrate potential, measuring their structure, mobility and energy. Structurally, we observed

sharp changes in the average particle spacing as the potential was decreased and increased, always accompanied by a change in the number of kinks. In weak substrates, all studied chains had a single state which resembled the rigid chain limit, while in strong substrates a zero-kink state was seen in all chains, and an additional state with one or two kinks were observed in the two longer chains. The accessibility of each state was dependent on the position of the edge particles. Where two states were possible, the zero kink state was the highest in energy. The chains with $N = N_0$ and $N = 2N_0$ showed a sliding to pinned transition accompanied by a breaking of the reflective symmetry of the chain, which we interpret as the Aubry transition predicted by Braiman and Sharma *et al.* [179, 180]. To the best of our knowledge, this is the first time that both structural and dynamic features of this transition have been observed in undriven chains.

Acknowledgments

Berend van der Meer is thanked for providing simulation code. Joseph Hutchinson and Berend van der Meer are thanked for useful discussions.

Chapter 5

Friction of driven colloidal chains in a periodic potential

Abstract

In this chapter, we drive paramagnetic colloidal chains through a one-dimensional periodic optical potential at a constant velocity. By measuring the critical driving velocity needed to move the chains, we observe a transition from low to high friction as the optical potential increases and we analyse the dynamics before and after the transition. In the limit of weak potentials, we model the dynamics as small, uniform changes in the average spacing as the chain crosses the landscape, which have a minimal effect on the friction. In strong substrate potentials, we observe the nucleation of travelling kinks and measure their velocity, density, and profile. We develop a hard sphere model of the kinks, which we use to successfully predict the transition point from low to high friction.

5.1 Introduction

The behaviour of driven incommensurate systems is important in a wide array of problems, from the motion of certain proteins [29,193] to coupled superconducting Josephson junctions [194], the migration grain of boundaries under stress [40,177] and, of particular technological importance, atomic friction. Friction is responsible for reducing the efficiency and lifetime of machines, leading to large energy losses [195]. Reducing friction at the atomic scale could lead to both the development of micro- and nano-scale electromechanical devices and improved lubricants for macroscopic machines, with vast potential applications [196].

In 1983, Peyrard and Aubry's work on the Frenkel-Kontorova model [31] revealed the possibility of structural superlubricity – vanishingly low friction between atomically smooth, incommensurate surfaces. This model reduces the two atomic surfaces to a flexible chain of harmonically interacting particles sliding over a rigid sinusoidal substrate. When the chain and the substrate are incommensurate and the substrate depth is below a threshold value, the chain exists in a free sliding state. As the substrate depth increases, a "transition by breaking of analyticity", known as the Aubry transition, leads to the breakdown of structural superlubricity and the appearance of finite Peierls-Nabarro barriers to sliding [21].

Since Aubry's prediction, the development of atomic force microscopy has lead to experimental demonstrations of superlubric sliding in increasingly large scale systems, from nano- to micro-scale [35,36,197,198] graphite flakes, to macroscopic superlubricity in centimetre long carbon nanotubes [37] or via the formation of graphene nano-scrolls [38]. However, despite the seemingly general requirement for stiff, incommensurate surfaces [199,200], experimental observations of superlubricity have mostly been limited to graphene and carbon nanotubes, hexagonal boron nitride [39], and a few "MXenes" such as molybdenum disulphide [201]. Understanding why superlubricity so often breaks down requires knowledge of the dynamic processes occurring during sliding.

Probing the dynamics of atomic materials is extremely challenging [172], so this is typically only achieved through molecular dynamics simulations. These simulations have identified many mechanisms for the breakdown of superlubricity, including spontaneous re-orientation [202], out of plane buckling [203], elastic deformation [74,204], the presence of adsorbed contaminants, and edge effects [205–207]. Because edges have a lower coordination number than the bulk, they are

more prone to elastic deformation and can take on more of the normal load, leading to higher friction. As the bulk friction vanishes, edge friction dominates even in large systems [208, 209].

One approach to experimentally investigating the dynamics of friction involves using optical traps to create a tunable periodic substrate over which the motion of driven particles can be observed with single particle resolution. This approach has been used by Bylinskii *et al.* [34,210], who studied driven chains of up to six Yb^+ ions on a 1D optical substrate, and Brazda *et al.* [76, 211], using colloidal monolayers driven over a 2D optical lattice, to create experimental models of a one or two dimensional Frenkel-Kontorova model. Both observed a transition from low to high friction accompanied by structural changes characteristic of the Aubry transition, including the appearance of travelling defects called kinks. However, both experiments used charged, repulsive particles held together by an additional extended harmonic trap, which resulted in a gradual increase in the particle separation near the edge instead of a well defined edge that was able to freely expand and contract.

We use colloidal chains in optical traps to create an experimental system with which to observe the impact of free edges on friction. Paramagnetic colloids create flexible chains of up to 20 particles whose edges are able to freely expand and contract because the particles are only held together by their attractive interactions. The pair potential of our colloidal particles shares qualitative similarities with typical atomic interactions – namely, a hard core repulsion and convex attractive term. We drive the chains through an incommensurate 1D periodic substrate formed from a line optical traps and measure the friction force in terms of the critical driving velocity needed to de-pin the chain. We observe zero friction at well defined chain lengths in weak substrate potentials, and a transition from low to high friction as the substrate depth increases. We compare this driven friction to the mobility of undriven chains studied in chapter 4. We then analyse the dynamics of the chains in the limit of weak and strong substrates and use the results to develop expressions for the friction force in each regime. In the strong substrate regime, we develop a hard sphere kink model which we use to predict the substrate depth at which the transition from low to high friction occurs.

5.2 Theory

This section presents a theoretical description of flexible colloidal chains driven with a constant force through a sinusoidal substrate. The theory section of chapter 4.2, which covers the Frenkel-Kontorova model for flexible chains, its kinks, ground and metastable states, generalisations to finite chains, and the Langevin equation for a finite rigid chain, is used as a starting point. Beginning with the equation of motion of a rigid chain derived in the previous chapter, we derive expressions for the average velocity of a rigid chain driven over a sinusoidal substrate. We then discuss general features of the motion of flexible chains.

5.2.1 Langevin equation of a rigid chain driven through a sinusoidal potential

In section 4.2.5, we derived a Langevin equation for the centre of mass of an undriven rigid chain in a sinusoidal potential of depth V_s and wavelength λ. Adding a driving force, F_d, gives the equation of motion:

$$\frac{dx_{cm}}{dt} = \frac{1}{\zeta_N}\left[\mathcal{F}_{sub}(x_{cm}) + F_d + \xi_N(t)\right], \tag{5.1}$$

where $\xi_N(t)$ is a noise term with a correlation function of $\langle \xi_N(t)\xi_N(t')\rangle = 2k_BT\zeta_N\delta(t-t')$, and ζ_N is the drag constant of a chain of N particles. This is either equal to $N\zeta_1$ if we neglect hydrodynamics, as in the simulations, or $(N+1)/2\zeta_1$ in the experiments, as discussed in appendix A.

The force due to the substrate, shown in figure 5.1a for chains of $N = 1-9$ particles, is a

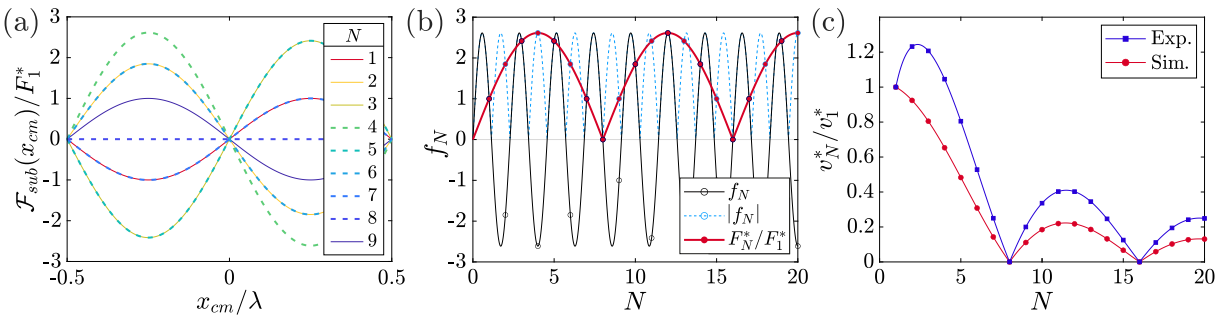


Figure 5.1: (a) Total force due to the substrate for chains of $N = 1-9$ particles (dark to light). (b) f_N (black), $|f_N|$ (blue dashed) and F_N^*/F_1^* (red). (c) Critical velocity versus N when $\zeta_N = \zeta_1 N$ (red), as in the simulations, and $\zeta_N = \zeta_1(N+1)/2$ (blue), as in experiments

sine wave given by

$$\mathcal{F}_{sub}(x_{cm}) = F_1^* f_N \sin\left(\frac{2\pi}{\lambda} x_{cm}\right), \qquad \text{with} \qquad f_N = \frac{\sin(\pi N\sigma/\lambda)}{\sin(\pi\sigma/\lambda)}. \tag{5.2}$$

Here, $F_1^* = V_s(2\pi/\lambda)$ is the maximum substrate force felt by a single particle and f_N is the ratio of the force felt by a rigid chain of N particles relative to that of a single particle, shown in black in figure 5.1b.

The sign of f_N determines the position of the minimum total substrate potential felt by the chain, $\mathcal{U}_{sub}(x_{cm}) = -\int \mathcal{F}_{sub}(x_{cm})dx$, which we will denote x_{min}. When f_N is positive, the potential acting on the chain ($\mathcal{U}_{sub}(x_{cm})$) has the same phase as the substrate potential acting on a single particle ($U_{sub}(x)$), so x_{min} is located at integer multiples of λ. When f_N is negative, so $\mathcal{U}_{sub}(x_{cm})$ has the opposite phase to $U_{sub}(x)$, x_{min} is instead at *half-integer* multiples of λ. This is important in section 5.4.2.

The magnitude of f_N determines the maximum force acting on the chain, $F_N^* = \max(\mathcal{F}_{sub})$, relative to F_1^*. This is more easily represented using the aliased form, f_N^a, which has the same magnitude as f_N when N is an integer and the same sign when N is odd:

$$\frac{F_N^*}{F_1^*} = |f_N^a| = \left|\frac{\sin(\pi NP)}{\sin(\pi P)}\right|, \tag{5.3}$$

where $P = \sigma/\lambda - \text{int}\{\sigma/\lambda\}$ is the misfit, approximately equal to $-1/8$ in our experiments. The maximum substrate force, F_N^*/F_1^*, is shown as a function of N in red in figure 5.1b. It has an oscillating shape which is equal to zero when N is an integer multiple of $|P^{-1}| \approx 8$. We denote this chain length as N_0. The total substrate force acting on chains with $N = N_0, 2N_0, ...$ is zero at any centre of mass position, so they can slide freely across the substrate.

5.2.2 Average velocity of a driven rigid chain

When the critical force, F_N^*, is large compared to the forces arising from thermal fluctuations, so that the Péclet number (defined in equation 2.10) is much larger than one, we can ignore thermal fluctuations and solve a deterministic version of the equation of motion (equation 5.1) [123]. In this case, driving forces less than the maximum substrate force, ($F_d < F_N^*$) are insufficient to move the chain, and a steady state where the velocity is zero is reached. When $F_d > F_N^*$, the

average velocity of the chain can be found by integrating the equation of motion as follows:

$$\langle v \rangle = \frac{\lambda}{\tau_\lambda} = \lambda \left[\int_0^\lambda \frac{\zeta_N}{F_d + \mathcal{F}(x_{cm})} dx_{cm} \right]^{-1}, \tag{5.4}$$

where τ_λ is the time taken for the chain to travel one wavelength. Equation 5.4 can be solved analytically to give the well known square-root law [123, 212]

$$\langle v \rangle = \zeta_N^{-1} \sqrt{F_d^2 - {F_N^*}^2}, \tag{5.5}$$

shown with a black dashed line in figure 5.2.

In our experiments we measure velocities, not forces, so it is more convenient to express equation 5.5 in terms of the driving velocity, $v_d = F_d/\zeta_N$, and critical velocity,

$$v_N^* = \frac{F_N^*}{\zeta_N} = v_1^* \frac{\zeta_1}{\zeta_N} \left| \frac{\sin(\pi N P)}{\sin(\pi P)} \right|. \tag{5.6}$$

Figure 5.1c shows v_N^* for the experiments ($\zeta_N = \zeta_1(N+1)/2$) and simulations ($\zeta_N = \zeta_1 N$). Converting equation 5.5 to velocities gives

$$\langle v \rangle = \begin{cases} 0 & v_d \leq v_N^* \\ \sqrt{v_d^2 - v_N^{*2}} & v_d > v_N^*. \end{cases} \tag{5.7}$$

When F_N^* is small enough that the Péclet number is less than one, thermal fluctuations become important. These allow the chain to jump over the substrate maxima at a rate given by Kramer's rate, $r \propto \exp(-\beta \Delta U)$, where ΔU is the barrier height of the tilted potential $U(x) = \mathcal{U}_{sub}(x) - F_d x$. When F_d is positive, ΔU is smaller in the forward direction than the backward direction, so forward motion is favoured. The chain can therefore move with a non-zero average velocity even though $F_d < F_N^*$. As $F_d \to F_N^*$, the forward barrier disappears altogether and the chains hops from one well to the next with an appreciable average velocity. When $F_d \gg F_N^*$, stochastic hopping becomes less important and the deterministic value of $\langle v \rangle$ in equation 5.7 is recovered. Overall, the average velocity is given by [213]

$$\langle v \rangle = \frac{2 k_B T}{\zeta_N \lambda} \frac{\sinh(\pi B_d)}{I_{iB_d}(B^*) I_{-iB_d}(B^*)}, \tag{5.8}$$

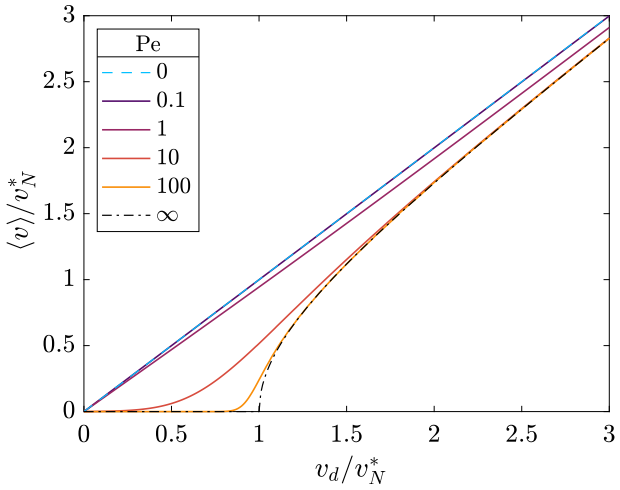


Figure 5.2: Average velocity, $\langle v\rangle$, versus driving velocity, v_d, scaled by the critical velocity of a rigid chain, v_N^*. The solid lines have different ratios between the critical velocity and the thermal noise term, quantified by the Péclet number $\mathrm{Pe} = \tau_B v^*/\sigma$, ranging from $\mathrm{Pe} = 100$ (yellow) to $\mathrm{Pe} = 0.1$ (purple). The black dashed line shows the deterministic limit where $\mathrm{Pe} \to \infty$ (equation 5.5) and the cyan dashed line shows the noisy limit where $\mathrm{Pe} \to 0$ ($\langle v\rangle = v_d$).

where $I_{i\nu}(x)$ is the modified Bessel function of the first kind with complex order and

$$B_d = \frac{v_d \lambda}{2\pi D}, \qquad B^* = \frac{v_N^* \lambda}{2\pi D}. \tag{5.9}$$

Equation 5.8 is the most well known form of the average velocity, but it is equivalent to the following continuous fraction [8]:

$$\langle v\rangle = v_d + v_N^* \mathrm{Im}\left(\frac{1}{i\alpha - \gamma + \frac{1}{i\alpha - 2\gamma + \frac{1}{i\alpha - 3\gamma + \cdots}}}\right), \text{ where } \alpha = \frac{2v_d}{v_N^*},\ \gamma = \frac{2}{v_N^*}\frac{k_B T}{\zeta_N}\frac{\lambda}{2\pi}, \tag{5.10}$$

which is computationally much easier to evaluate. The fraction generally converges after 20 to 100 terms.

Figure 5.2 shows the deterministic and noisy average velocity (equations 5.7 and 5.10) with several values of the Péclet number, which quantifies the magnitude of the critical velocity (not driving velocity) relative to thermal motion. When v_N^* is large, the noisy and deterministic equations are almost identical except in the region around the critical velocity ($v_d \approx v_N^*$). When v_N^* is small and thermal fluctuations become important, the noisy average velocity is always larger than the deterministic value. As the critical velocity approaches zero ($\mathrm{Pe} \to 0$), the average velocity approaches the driving velocity.

5.2.3 Driven flexible chains

So far, we have discussed the motion of rigid chains with and without thermal noise. The motion of flexible chains, which can expand and contract as they cross the substrate, is described by the Frenkel Kontorova (FK) model. The model and its phase behaviour were introduced in section 4.2. In summary, the ground state of a flexible chain in the limit of very strong substrates consists of one particle in each substrate minimum. In weak substrates, the ground state has a finite density of kinks, which are defined as regions where there is one extra particle in a potential well.

When finite, flexible chains are driven over a substrate, they have been shown to move via the creation of a kink at the left end of the chain (for motion to the right), followed by the displacement of any kinks in the chain, and finally the annihilation of a kink at the right end of the chain [188, 214]. An example of this process is illustrated in figure 5.3. Figure 5.3a shows snapshots of the particle positions at different stages of the kink translation, while 5.3b plots the displacement of each particle as a function of the kink position. Figure 5.3c shows the total energy of the chain as a function of the kink position. The energy barrier to the chain's motion contains both the kink creation energy, which appears in the first part of the graph, and the Peierls-Nabarro barrier to translating the kink along the chain [188], which is responsible for the oscillating energy in the middle of the graph. When the substrate is very strong, as in this example, the energy barrier to kink creation dominates, but both of these contributions decrease with decreasing substrate depth, V_s. When V_s is below a critical value, the energy barrier to kink creation vanishes and kink creation at the edges occurs spontaneously [21].

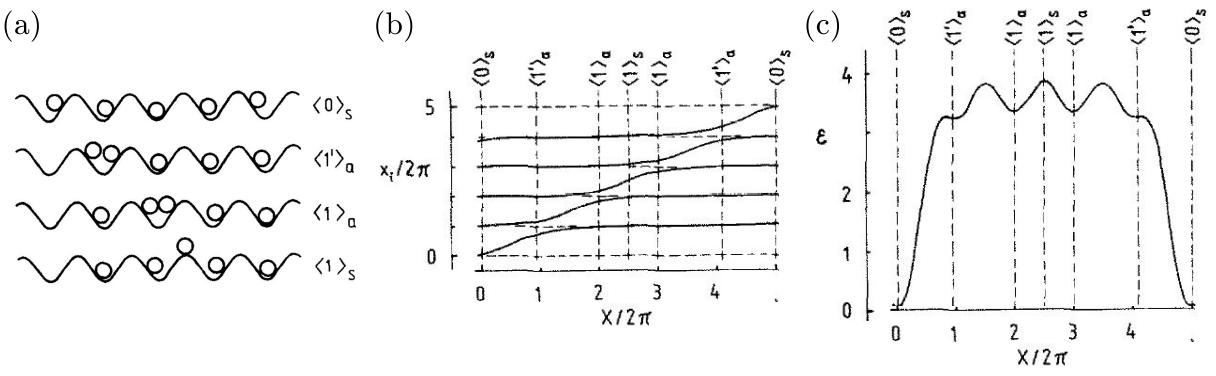


Figure 5.3: (a) Intermediate states, (b) trajectory and (c) energy of the lowest energy path for the translation of a flexible harmonic chain of five particles. Reproduced from [188].

5.3 Experimental methods

Our colloidal experiments consist of chains of $N = 1 - 20$ paramagnetic particles (equilibrium spacing $\sigma = (2.82 \pm 0.05)\,\mu\text{m}$) driven through a line of optical traps. We use the sample cells described in section 2.3.1. A magnetic field along the x direction is created using the permanent magnets described in section 2.3.2. This causes the particles to form chains along the field direction, so they can be treated as one-dimensional with an interaction strength of

$$U_{int}(x) = U_{HS}(x) - \Gamma \left(\frac{2a}{x}\right)^3. \tag{5.11}$$

The field strength is 0.55 mT, the same as in the previous chapter, so we assume the same interaction parameter of $\Gamma = 88 \pm 5$, measured in appendix B. This is large enough that thermal fluctuations in the x direction are very small.

The chains are driven at a constant velocity by a piezo stage as described in section 2.3.2. We create a sinusoidal substrate potential using a line of 30 optical traps with a wavelength of $\lambda = 3.21\,\mu\text{m}$, the same as the previous chapter. This wavelength was chosen to give a misfit of $P \approx -1/8$, so $N_0 \approx 8$, where N_0 is the chain length which experiences zero total substrate force in the rigid chain limit. We use laser powers of 100 mW to 450 mW, corresponding to substrate depths of $V_s = 4k_BT$ to $21k_BT$. The substrate depth was calculated from the critical velocity of a single particle [123], $v_1^* = (2\pi/\lambda)V_s/\zeta_1$, measured using the protocol described in the next section.

5.3.1 Critical velocity measurements

Throughout this chapter, we use iterative experiments to converge on the critical velocity of a chain or single particle as efficiently as possible, thereby reducing the total time of each experiment. We start each iterative experiment by choosing a minimum driving velocity of $v_- = 0$, a maximum driving velocity, v_+, at least two times larger than an initial guess of v^*, and an initial driving velocity of $v_d^1 = v_+$. At each iteration, we drive the stage 25λ in the forwards and backwards direction at a speed v_d^i. We measure the chain's position at the start and end of each drive by determining its centre of mass. The next driving speed, v_d^{i+1}, is then chosen based on the average velocity of the chain in the forward and backwards direction using

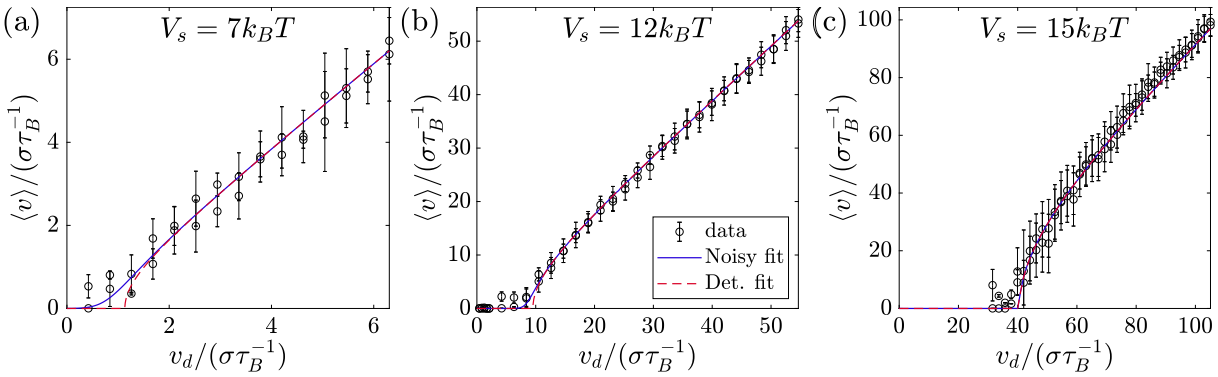


Figure 5.4: Average velocity vs. driving velocity (black circles) of a chain with $N = 16$ in a substrate with $V_s = 7k_BT$ (a), $12k_BT$ (b) and $15k_BT$ (c), with fits to the non-deterministic and deterministic average velocity (equations 5.10 and 5.5) shown with solid blue and dashed red lines respectively.

the following iterative scheme:

$$\begin{aligned} &\text{if } \langle v\rangle > 0.16v_d;\ v_d^{i+1} = (v_-^i + v_d^i)/2,\ v_+^{i+1} = v_d^i,\ v_-^{i+1} = v_-^i; \\ &\text{else; } v_d^{i+1} = (v_+^i + v_d^i)/2,\ v_+^{i+1} = v_+^i,\ v_-^{i+1} = v_d^i. \end{aligned} \tag{5.12}$$

In this way, we iteratively update v_- and v_+ so that they converge on the critical velocity. The experiment is terminated when a precision of $v_+ - v_- < 0.1\,\mu\text{ms}^{-1}$ is reached. We used a relatively high threshold of $\langle v\rangle > 0.16v_d$ when determining the critical velocity in the iterative scheme in order to account for the effect of noise. Thermal fluctuations can cause the chain to stochastically hop over a potential maximum even when the driving velocity is significantly smaller than the critical velocity. Because of this effect, using a lower threshold tended to lead to oversampling of the $v_d < v_N^*$ region, which made it difficult to accurately determine v_N^*. The chosen threshold gave a good spread of points just above v_N^*, which is necessary for accurately finding v_N^*.

Each experiment was repeated with two different initial driving velocities in order to sample a larger spread of driving velocities, which we then use to refine our estimate of v_N^* in post-processing by fitting $\langle v\rangle$ versus v_d to equation 5.10, the non-deterministic equation for the average velocity. We verify the validity of equation 5.10 by measuring the full average velocity versus driving velocity of a chain of $N = 16$ particles in three different substrate depths of $V_s = 7k_BT$, $12k_BT$ and $15k_BT$, shown in figure 5.4. All three curves resemble the characteristic "square-root law" and are well described by both the non-deterministic and deterministic expressions for $\langle v\rangle$ (equations 5.10 and 5.5). We use the non-deterministic version to determine v_N^* because it works better in the vicinity of the critical velocity, where the data points are

clustered in iterative experiments.

Chains occasionally broke apart while being driven. When this happened, the iterative experiment was repeated from the beginning and, if the chain broke again at the same driving velocity, a different starting velocity was chosen. The frames where the chain was broken were removed before further analysis. A plot of the breakage frequency is shown in appendix D.

5.3.2 Simulations

We use 1D Brownian Dynamics simulations to supplement our experiments. These are described in detail in section 2.4. We simulate chains of $N = 1 - 20$ particles using the following equation of motion:

$$x_i(t+\Delta t) = x_i(t) + \frac{\Delta t}{\zeta}\left[F^* \sin\left(\frac{2\pi x}{\lambda}\right) + F_d + \sum_{j\neq i} F_{int}(x_j(t) - x_i(t))\right] + \sqrt{\frac{2k_BT\Delta t}{\zeta}}\Xi. \quad (5.13)$$

The simulations are initialised at $\{x_n\} = n\sigma$ and run for $100\tau_B$ while saving positions at a rate of $1000\tau_B^{-1}$. We use a wavelength of $(8/7)\sigma$ to match the experiments, critical forces of $F_1^* = 5$ to $50k_BT/\sigma$, and driving forces between 0 and $2F_1^*$. The pairwise interactions consist of a repulsive screened coulomb term and an attractive magnetic term with a prefactor of $\Gamma = 88.3$ to match the experiments.

5.3.3 Kink tracking

In section 5.4.3, we analyse the experiments and simulations in terms of the kinks present in the chains. This was achieved by locating and tracking kinks from particle coordinates using a modified version of a kink tracking algorithm written by Amelia Jones [215] based on the work of Berend van der Meer *et al.* [175].

Firstly, kinks are located with a precision of one wavelength by finding the position of any wells, i.e. the region between two substrate maxima, containing more than one particle. This is shown for an example kink in figure 5.5a. Likewise, anti-kinks are located by finding any empty wells surrounded by full wells. Anti-kinks always appear adjacent to at least one kink. Kink/anti-kink/kink trios were treated as a single kink, while kink/anti-kink pairs were treated as to two ordinary wells each containing one particle.

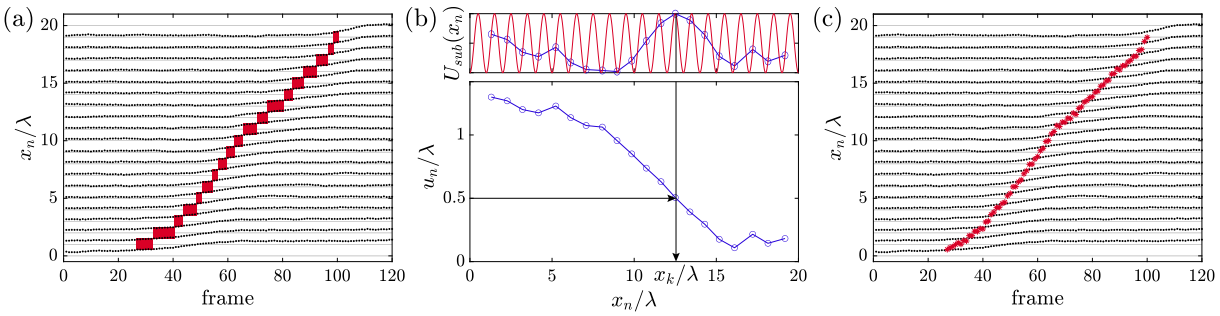


Figure 5.5: Kink location algorithm demonstrated with a typical trajectory. (a) Particle positions (black dots) and the wells containing more than on particle (red rectangles) in each frame. Horizontal grey lines show the substrate minima. (b) Energy (top) and u_n (bottom) of each particle in frame 75. The black vertical line shows the kink position. (c) Kink position (red star) and particle positions (black dots) in each frame. Horizontal grey lines show the substrate minima.

In order to refine the kink position to sub-wavelength accuracy, we use the kink profile described in section 4.2,

$$u_n = x_n - n\lambda, \tag{5.14}$$

where x_n is the position of the n^{th} particle and $n\lambda$ is the position of the n^{th} well. The well containing two particles was denoted $n = 0$, the two particles in the zeroth well were given an index of zero and one, and all other wells and particles were indexed with respect to these. Using these indexes, the kink profile is equal to $u_n \approx \lambda$ for particles far to the right of the kink, $u_n \approx 0$ far to the left of the kink, and $u_n = \lambda/2$ at the kink centre. We therefore calculate the kink centre, x_k, by interpolating between the values of u_n at each particle position, x_n, to find the value of x_n where $u_n = \lambda/2$. This process is illustrated in figure 5.5b, while the final kink positions are shown in 5.5c.

Once we have located each kink, we use the positions to calculate the average kink profile, kink velocity, and kink density. We calculate the average kink profile relative to the kink centre, x_k, by binning every individual u_n according to $n - x_k/\lambda$. In order to calculate the kink velocity, we track the kink positions using the algorithm of Crocker and Grier [149]. Because we find that the kinks move with a very high velocity of approximately $8v_d$, the displacement of a kink from one frame to the next was occasionally larger than the distance between kinks, causing the tracking algorithm to give incorrect results. We therefore shift each kink position down by $8v_dt$ in order to reduce the apparent frame to frame distance travelled by the kink. We track the shifted positions, and then remove the $8v_dt$ shift to recover the original kink position.

5.4 Results and discussion

This section begins by discussing the measured critical velocity of chains driven over substrates of varying depth. The dynamics of the chains in weak substrates are then analysed, followed by the dynamics in strong substrates.

5.4.1 Critical velocity

We perform iterative experiments to find the critical velocity, v_N^*, of chains of $N = 1 - 20$ particles in potentials with $V_s = 4k_BT$ to $21k_BT$. This is plotted in figure 5.6a relative to the critical velocity of a single particle, v_1^*, at several substrate depths, V_s. The measured v_N^*/v_1^* at $V_s = 9k_BT$ follows the distinctive oscillating shape predicted by equation 5.6, which describes the critical velocity of a rigid chain. A fit to this equation, shown with the dashed line in figure 5.6a, gives a misfit of $P = -0.122\,\mu\text{m}$, so that the critical velocity is zero at a chain length of $N_0 = 8.2$, very close to the expected value of $N_0 = |P^{-1}| = 8$. As expected for a rigid chain, the height of each peak decreases with increasing N proportional to $\zeta_1/\zeta_N = 2/(N+1)$, and we observe very low friction when $N = 8$ and 16. At a slightly higher V_s of $12k_BT$, the overall $2/(N+1)$ dependence of the critical velocity predicted by equation 5.6 is retained, but the critical velocity no longer goes to zero at any of the measured chain lengths. At a substrate depth of $16k_BT$, the oscillating shape predicted by the rigid chain equation is completely lost,

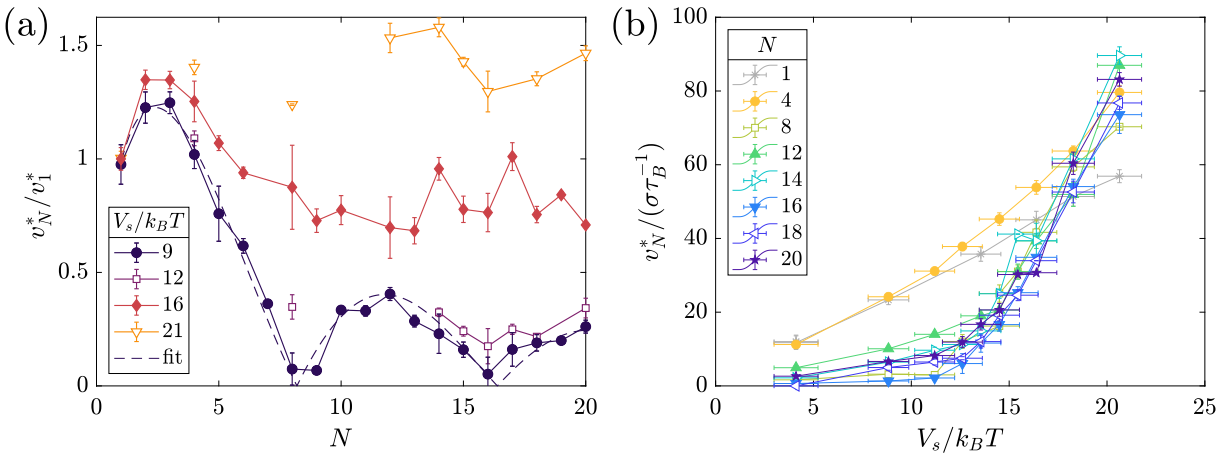


Figure 5.6: (a) Critical velocity of each chain, scaled by the critical velocity of one particle, versus N at substrates depths from $9k_BT$ (navy circles) to $21k_BT$ (yellow triangles). The navy dashed line shows a fit of the $V_s = 9k_BT$ points to equation 5.2. (b) Critical velocity versus substrate depth for 1 particle (grey) and chains of $N = 4$ (yellow circles) to 20 (dark blue star)

the magnitude of v_N^* is much larger than predicted by the rigid chain limit, and no longer decreases with increasing N. At the highest V_s of $21k_BT$, the critical velocity of chains with $N \geq 4$ exceeds the critical velocity of one particle.

Figure 5.6b shows v_N^* from the same experiments as in 5.6a, but now plotted against V_s at a selection of chain lengths. The critical velocity of the chains with $N > 4$ shows a sharp transition from low to high friction at $V_s = 13k_BT$. Above $V_s = 13k_BT$, all v_N^* fall onto the same line which increases rapidly with increasing V_s. This transition resembles the transitions from low to high friction observed in other experiments [181, 211] and simulations [191, 200].

In order to elucidate the origin of the onset of high friction, we now analyse the structure and dynamics of the chains as they are driven over the substrate. To this end, we analyse the chains in the limit of weak substrate potentials with $V_s < 13k_BT$ in the next section (5.4.2), followed by strong substrates ($V_s > 13k_BT$) in section 5.4.3.

5.4.2 Dynamics in the weak substrate limit

In this section, we analyse the dynamics of chains in weak substrates. We then develop a model to describe the key dynamic feature – namely, the change in the average spacing – then use this model to predict the critical driving velocity.

As illustrative examples of the typical dynamics of chains in weak substrates, figures 5.7a(i) and b(i) show the position of each particle in two chains of $N = 15$ and 17 driven over a landscape of depth $V_s = 9k_BT$. These chain lengths were chosen because they are either side of $2N_0 = 16$. The particles are coloured by their nearest neighbour spacing normalised by its average over time to account for polydispersity, $s_n = (x_{n+1} - x_{n-1})/\langle x_{n+1} - x_{n-1}\rangle_t$. Both chains undergo small expansions and contractions as they cross the substrate, indicated by changes from blue to yellow over time. By comparing the colours of particles in vertical sections, we can see that the changes in s_n are fairly uniform throughout the chain.

Because s_n changes uniformly, we can capture each chain's dynamics by looking at the average spacing of the whole chain, $s = (x_N - x_1)/(N - 1)$, as a function of time, shown in figures 5.7a(ii) and b(ii). Vertical lines indicate the positions where the total substrate potential acting on the chain is maximised, x_{max}. The average spacing of the $N = 15$ and 17 chains appears to show opposite modes of motion. The $N = 15$ chain (figure 5.7a(ii)) slowly contracts

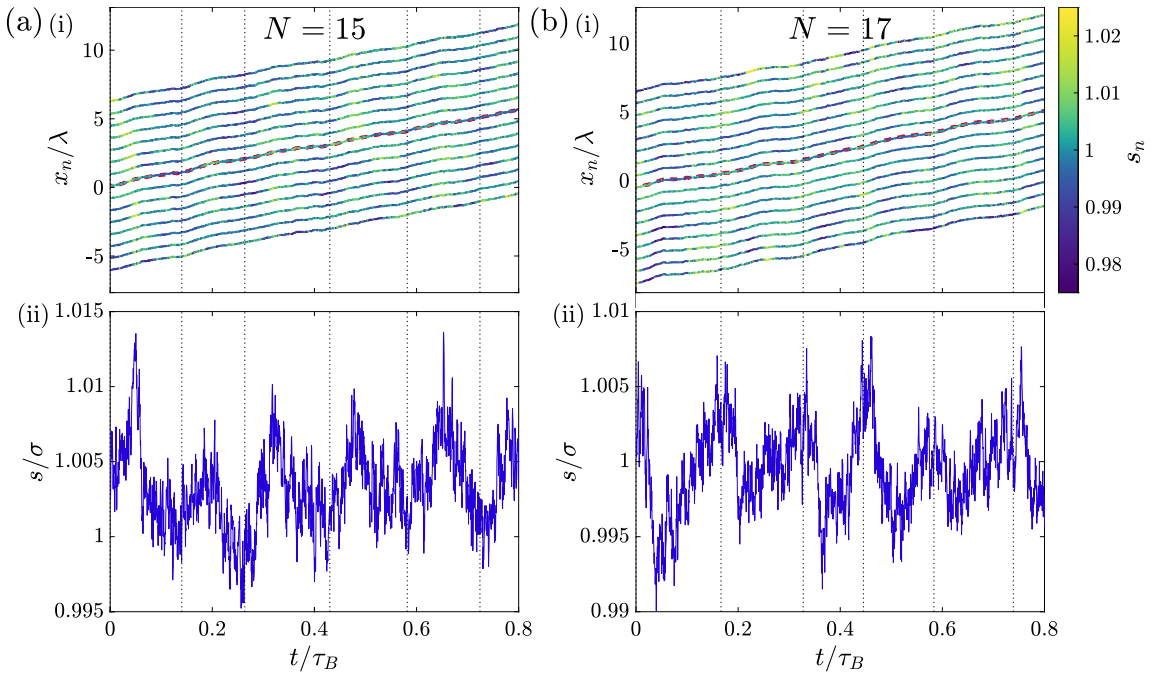


Figure 5.7: (i) Position of each particle, x_n, coloured by its normalised nearest neighbour distance, $s_n = (x_{n+1} - x_{n-1})/\langle x_{n+1} - x_{n-1} \rangle$, over time in a chain of (a) $N = 15$ and (b) $N = 17$. The red dashed line shows the centre of mass position. (ii) Average spacing, $s = (x_N - x_1)/(N - 1)$ of each chain over the same time period. Vertical lines show the times when the centre of mass crosses the position of the maximum total substrate potential.

as it moves towards the potential maximum, then quickly expands after crossing the barrier. The $N = 17$ chain (figure 5.7b(ii)) does the opposite; slow expansion followed by rapid compression.

The difference between the modes of motion of the two chains can be seen more clearly in figure 5.8, which shows the average spacing, s, as a function of the distance between the chain's centre of mass and the position of the nearest maximum in its total substrate potential, $x_{cm} - x_{max}$. When $N = 15$, s increases as the centre of mass goes from x_{max} to x_{min}, corresponding to the rapid "slip" motion down the total substrate potential. The chain's spacing then decreases again as it slowly moves from the minimum to the maximum. When $N = 17$, s decreases as the chain approaches the minimum, then increases as it moves towards the maximum. For both chain lengths, s is an approximately sinusoidal function of x_{cm}, but with opposite phases, and hence opposite modes of motion. Importantly, all driving velocities fall onto the same curve, suggesting that the chain always has time to relax into its optimal, lowest energy spacing as it crosses the landscape.

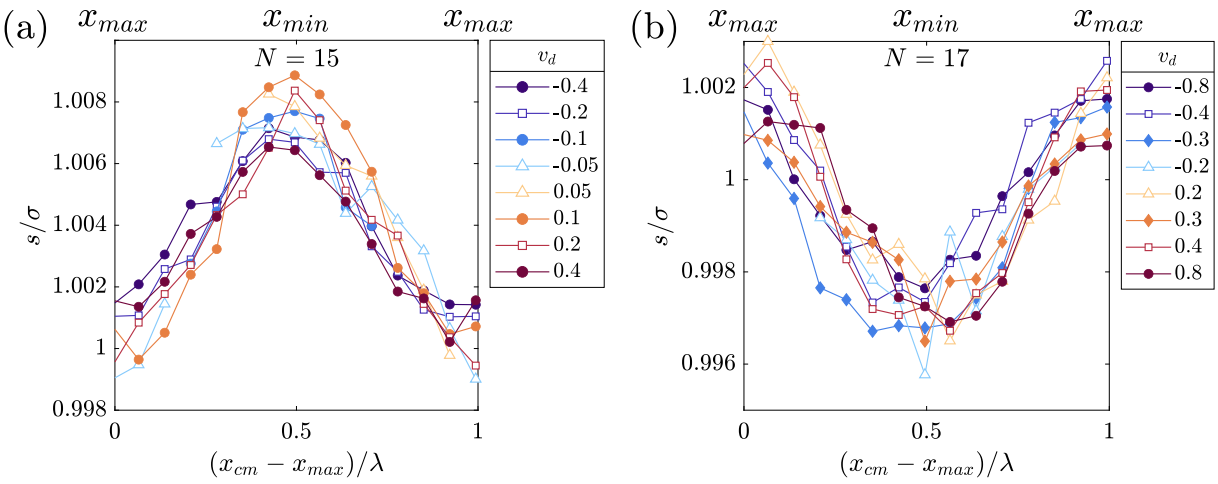


Figure 5.8: Average s against $x_{cm} - x_{max}$ for chains of 15 (a) and 17 (b) particles.

Calculation of the average spacing of the chain

We can explain different modes of motion undergone by the $N = 15$ and 17 chains by considering the total energy of each chain as it crosses the substrate, $\mathcal{U}_{tot}(x_{cm}, s) = \mathcal{U}_{int}(s) + \mathcal{U}_{sub}(x_{cm}, s)$, as a function of the average spacing, s. We include only nearest neighbour interactions in the inter-particle energy and assume that the chain undergoes uniform changes in s. As a result, the total substrate potential is the same as that of a rigid chain in equation 4.9, but with the mean inter-particle spacing, s, in place of the equilibrium spacing σ, in order to account for the expansions and contractions of the chain. The total energy of the chain is given by

$$\mathcal{U}_{tot}(x_{cm}, s) = (N-1)U_{int}(s) + V_s f_N(s) \cos\left(\frac{2\pi x_{cm}}{\lambda}\right), \tag{5.15}$$

where $f_N(s)$ is the ratio between the total substrate potential of the chain and that of a single particle as defined in equation 4.9, but with s in place of σ:

$$f_N(s) = \frac{\sin(\pi N s/\lambda)}{\sin(\pi s/\lambda)}. \tag{5.16}$$

Figure 5.9 shows the total energy of $N = 15$ and 17 chains as a function of their inter-particle spacing, s, when the centres of mass are located at $x_{cm} = x_{max}$ and x_{min}, the positions of the maximum and minimum total substrate potential. Starting from an average spacing of $s = \sigma$, the $N = 15$ chain can lower its energy by contracting when $x_{cm} = x_{max}$ and expanding when $x_{cm} = x_{min}$. In contrast, the $N = 17$ chain can lower its energy by expanding when $x_{cm} = x_{max}$ and contracting when $x_{cm} = x_{min}$. This matches the trend observed in figure 5.8.

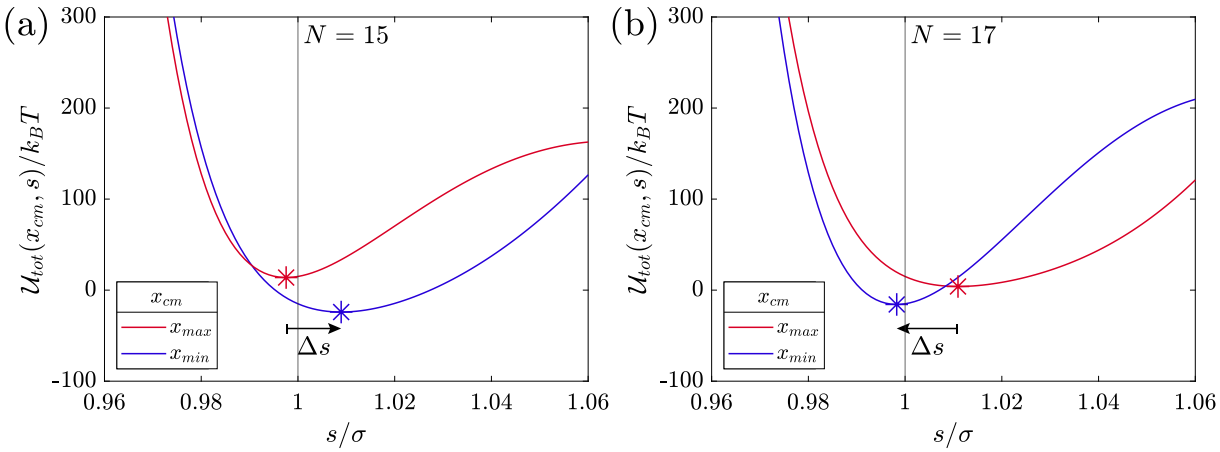


Figure 5.9: Total energy, $\mathcal{U}_{tot}(x_{cm}, s)$, versus average spacing, s, of chains with $N = 15$ (a) and $N = 17$ (b) particles in a substrate of depth $15k_BT$ and an arbitrary $U_{int}(s)$. Red and blue solid lines show $\mathcal{U}_{tot}$ at $x_{cm} = x_{max}$ and x_{min} respectively, with stars marking the energy minima.

We have now shown qualitatively that chains undergo uniform expansions and contractions as they cross the substrate which act to minimise their total energy. We will now develop a quantitative model to describe the amplitude of these changes in s and predict their impact on the critical velocity of the chain. We assume that the chain always expands or contracts to the value of s which minimises its total energy at any given centre of mass position. This assumption is valid as long as the driving velocity is slow enough for the chain to respond, as observed in figure 5.8. We then find the optimal spacing, s_{opt}, by writing the total energy in equation 5.15 as a Taylor expansion about the equilibrium spacing, σ, and minimising with respect to s. This yields the following expression for s_{opt} as a function of the centre of mass position:

$$s_{opt}(x_{cm}) = \sigma + \frac{V_s f'_N(\sigma)}{(N-1)U''_{int}(\sigma) - V_s f''_N(\sigma)\cos\left(2\pi x_{cm}/\lambda\right)}\cos\left(2\pi x_{cm}/\lambda\right), \tag{5.17}$$

where $U''_{int}(\sigma)$ is the stiffness of the internal potential at the equilibrium spacing, $U'_{int}(\sigma)$ is zero by definition, and the derivatives $f'_N(\sigma)$ and $f''_N(\sigma)$ are given by

$$\begin{aligned} f'_N(\sigma) &= \frac{\pi}{\lambda} s_1^{-2}\left(N s_1 c_N - c_1 s_N\right) \\ f''_N(\sigma) &= -\left(\frac{\pi}{\lambda}\right)^2 s_1^{-3}\left[s_N(N^2 s_1^2 - c_1^2 - 1) + N s_1 c_N\right], \end{aligned} \tag{5.18}$$

using the notation $s_1 = \sin(\pi\sigma/\lambda)$, $s_N = \sin(\pi N\sigma/\lambda)$, $c_1 = \cos(\pi\sigma/\lambda)$ and $c_N = \cos(\pi N\sigma/\lambda)$.

The Taylor expansion is valid as long as the change in s is small compared to the period of oscillation of $f_N(s) = \lambda/N$, which is true for the short, stiff chains in our experiments. In this

limit, the denominator of equation 5.17 is dominated by the inter-particle energy term, so that $s(x_{cm})$ approximately follows the cosine term in equation 5.17. The spacing therefore oscillated about an average value of approximately σ with an amplitude Δs given by

$$\Delta s = s_{opt}(x_{max}) - s_{opt}(x_{min}). \tag{5.19}$$

Combining equations 5.19, 5.17 and 5.18 gives an equation for the amplitude, Δs, of the small, uniform expansions and contractions undergone by a chain as it is driven across the substrate.

In order to compare this theoretical Δs to the experiments, we measure the average spacing versus $x_{cm} - x_{max}$, illustrated for $N = 15$ and $N = 17$ in figure 5.8, for all chain lengths and driving velocities at a substrate depth of $V_s = 9k_BT$. We then fit each measured $s(x_{cm})$ to a cosine curve to obtain the amplitude, Δs. The result of this measurement is shown in figure 5.10. The measured Δs has a distinctive sawtooth shape which abruptly changes sign at integer multiple of N_0, where the magnitude of Δs is also maximised, and continuously passes through zero at approximately half integer multiples of N_0. The red line shows a fit to the theoretical Δs where the effective stiffness of the inter-particle interactions, $U''_{int}(\sigma)$, has been used as the only fitting parameter. The fit gives a stiffness of $U''_{int}(\sigma) = (2.2 \pm 0.3) \times 10^4 k_BT\sigma^{-2}$ and perfectly captures the saw-tooth shape of Δs measured in the experiments. This validates our model of the dynamics in weak substrates, which based on the assumption that chains undergo small, uniform changes in s to minimise their energy.

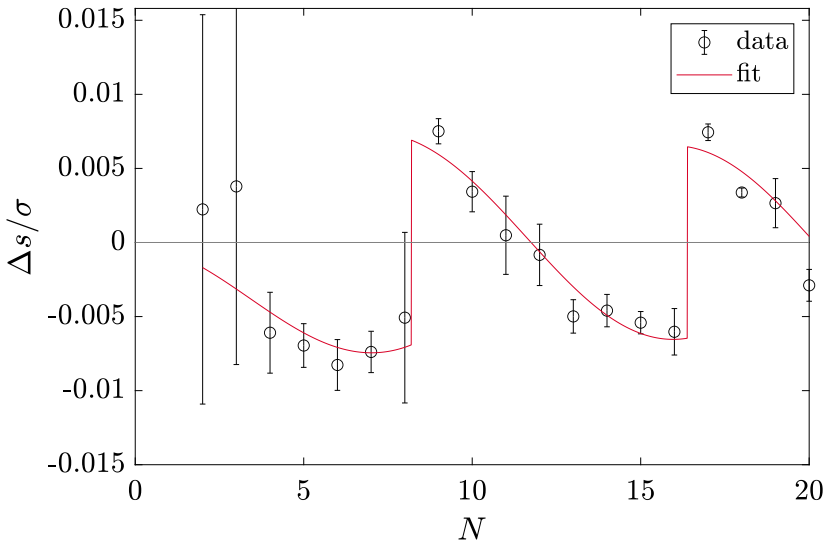


Figure 5.10: Experimental Δs (black circles), fitted to the theoretical Δs in equation 5.19 (red line).

Calculation of the critical driving velocity

We can now calculate the effect of the chains' expansions and contractions on the friction between the chain and the substrate. We do this by substituting equation 5.17 into the equation for the substrate force of a rigid chain (equation 5.2), but replacing σ with $s_{opt}(x_{cm})$, and so accounting for the variation in s as a function of the centre of mass:

$$\mathcal{F}_{sub}(x_{cm}) = V_s \frac{2\pi}{\lambda} \frac{\sin\left(\pi N s(x_{cm})/\lambda\right)}{\sin\left(\pi s(x_{cm})/\lambda\right)} \sin\left(\frac{2\pi x_{cm}}{\lambda}\right) \tag{5.20}$$

Figure 5.11a shows examples of the substrate force calculated from equation 5.17 and 5.20 at different chain lengths and substrate depths. As V_s increases, and therefore the magnitude of Δs increases, the maximum substrate force, F_N^*, also increases. The increase in F_N^* is very small at half integer multiples of N_0, where $\Delta s \approx 0$, and largest when N is close to an integer multiple of N_0, where the magnitude of Δs is maximised. The result is a loss of the characteristic oscillating shape of F_N^* versus N. This demonstrates why the ability of a flexible chain to expand and contract means that a truly free-sliding flexible finite chain cannot exist. Nevertheless, the N^{-1} dependence of the critical velocity is retained, so vanishingly low friction is still possible in long chains.

The critical velocity can be calculated from our flexible chain theory by numerically maximising the substrate force in equation 5.20. Figure 5.11 compares this theoretical v_N^* to the

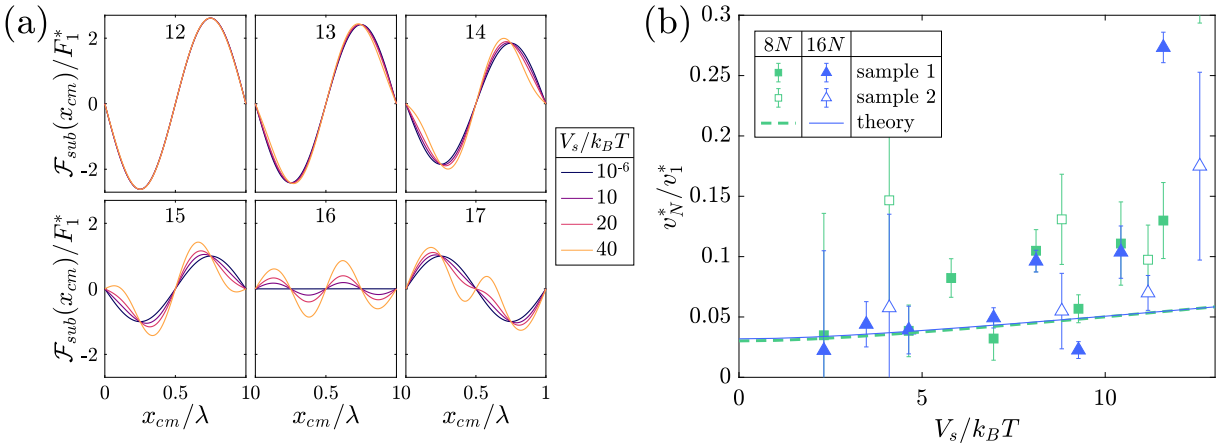


Figure 5.11: (a) Theoretical substrate force versus the centre of mass position calculated numerically from equations 5.20 and 5.17 using $U''_{int}(\sigma) = 2.2\times10^4\,\mathrm{k_B T}\sigma^{-2}$, $\sigma/\lambda = 7/8$, and $V_s = 0-40k_BT$ (black to yellow). (b) Theoretical (lines) and experimental (symbols) critical velocity of chains of 8 (green dashed line and squares) and 16 (blue solid line and triangles) particles at substrate depths $V_s = 2.5 - 14k_BT$. Note that the filled points are from a different sample to the main results, so may have a slightly different values of parameters such as σ and $U''_{int}(\sigma)$.

experimental v_N^* of chains with $N = 8$ and 16 in the weak substrate regime where $V_s < 13k_BT$. Note that we have used the experimentally measured N_0, which is slightly larger than 8. The theory correctly predicts an increase in the critical velocity of a chain relative to a single particle, v_N^*/v_1^*, with increasing V_s, although the magnitude of the increase is slightly underestimated.

Both the experimental and theoretical increases in v_N^*/v_1^* are very small compared to the large increase in friction observed in figure 5.6 when $V_s > 13k_BT$, suggesting that there is a fundamental change in the chain's dynamics at this point. In the next section, we approach the transition from low to high friction from the opposite direction, studying the dynamics of chains in the high V_s limit.

5.4.3 Dynamics in the strong substrate limit

In this section, we analyse the dynamics of chains in strong substrates. As in the previous section, we characterise the key features of the dynamics and use the results to develop a model, which we then use to predict the critical driving velocity in the strong substrate regime.

Figure 5.12 shows the position of particles in a chain with $N = 20$ driven over a substrate with the strongest substrate depth of $V_s = 21k_BT$. We compare two different driving velocities of $v_d = 84\sigma/\tau_B$, just above the critical velocity, and $v_d = 100\sigma/\tau_B$. Particles are coloured by their nearest neighbour spacing, s_n, from σ in blue to λ in yellow. At the lower v_d in 5.12a, the

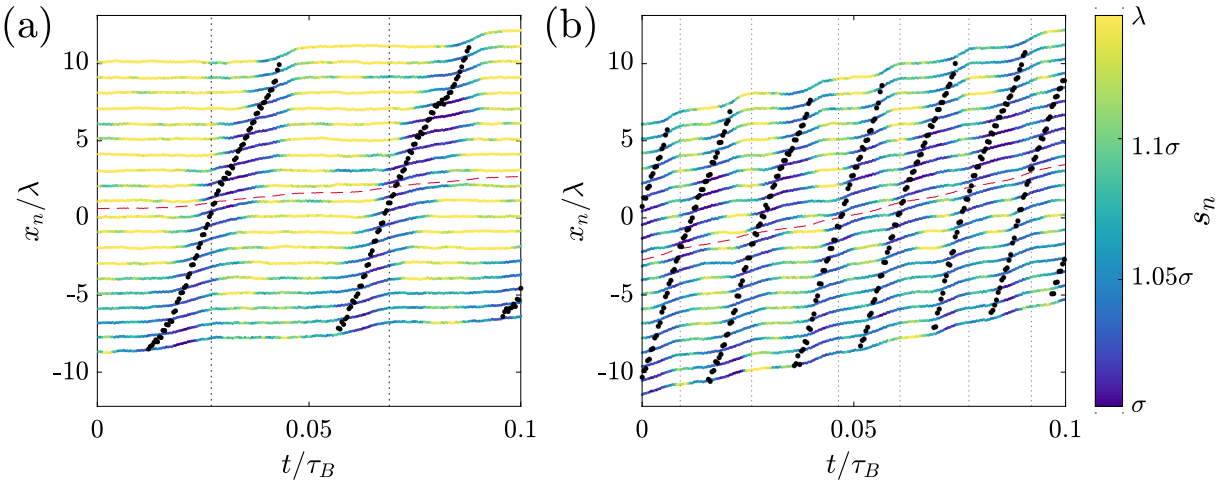


Figure 5.12: Position of each particle in a chain with $N = 20$ driven at (a) $v_d = 84\sigma/\tau_B$ and (b) $v_d = 100\sigma/\tau_B$ in a substrate depth of $V_s = 21k_BT$. The colour indicates the nearest neighbour distance, $s_n = (x_{n+1} - x_{n-1})/2$, from σ (blue) to λ (yellow). The red dashed line shows the centre of mass, vertical lines show the times when the centre of mass crosses a potential maximum, and black circles show kinks.

chain is initially stationary and all particles are yellow, indicating a separation of approximately one wavelength. Its centre of mass begins to move when a compressed region, visible as a blue diagonal stripe, moves from the back to the front of the chain. Once the compression has reached the front, the chain does not move any further until another compression appears at the back. At the fast driving velocity of $v_d = 100\sigma/\tau_B$, shown in figure 5.12b(i), we instead see very narrow stripes of yellow (indicating $s_n = \lambda$) between the blue regions (where $s_n \approx \sigma$).

These compressed regions are kinks. Their centres, located using the kink tracking algorithm described in section 5.3.3, are plotted with black circles over the particle positions in figure 5.12. In figure 5.12b, kinks are nucleated at the back of the chain before the previous kink has reached the front, so that there is a high kink density. This contrasts with figure 5.12a, where the rate of kink nucleation is much slower and the kink density is low.

The driving velocity dependence of the kink density and velocity is shown quantitatively in figure 5.13. The average kink velocity, v_k, in chains of 4 to 20 particles on a substrate with $V_s = 21k_BT$, is shown in 5.13a. The kink velocities, v_k, of all chains fall onto a straight line where v_k is approximately 10 times the driving velocity. Importantly, v_k is non-zero at the critical velocity, which is around $v_N^* = 78\sigma/\tau_B$ for all N. The kink density, in contrast, drops to zero as v_d decreases towards the critical velocity. This confirms the observation from figure 5.12 that chains only move when they nucleate a kink (note that this occasionally happens when $v_d < v_N^*$ due to thermal fluctuations). We can therefore infer that the critical force needed to nucleate a kink, not move it, is the limiting factor which determines the critical velocity of chains in the strong substrate limit. This is the crucial difference between the strong and weak

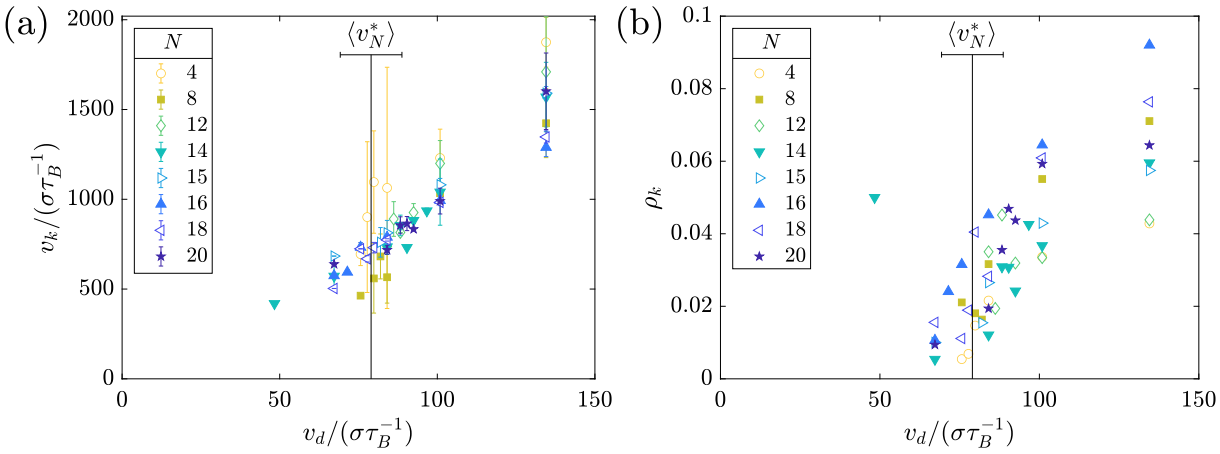


Figure 5.13: (a) Kink velocity and (b) kink density versus driving velocity for all experiments with $V_s = 21k_BT$ and $N = 4$ (yellow) to 20 (blue).

substrate limit; in weak substrates, the chain is always compressed to an average spacing of σ, so always has the maximum number of kinks, implying that kink nucleation has a negligible critical force in weak substrate potentials.

Kink profile

We have shown that the large increase in critical driving velocity with increasing substrate potential is related to the force required to nucleate a kink. In order to model the kink nucleation process, we need to understand the structure of a kink as it moves through the chain.

The structure of a kink is quantified by its profile, u_n, defined as the distance between the position of the n^{th} particle, x_n, to the n^{th} substrate minimum,

$$u_n = x_n - n\lambda. \tag{5.21}$$

Figure 5.14 shows the positions of the particles in an example kink and the resulting kink profile, u_n, in order to illustrate the key features of u_n. The particles far to the right of the kink centre, located at x_k, sit near the n^{th} substrate minimum, so $u_n \approx 0$ when $n \gg x_k/\lambda$. Far to the left of the kink, particles are shifted forward into the $(n+1)^{th}$ substrate minimum, so $u_n \approx \lambda$ when $n \ll x_k/\lambda$. Near the centre of the kink, particles sit between the n^{th} and $(n+1)^{th}$ substrate minimum, so u_n is between λ and 0. The number of particles in the region with $0 < u_n < \lambda$ is the kink width, while the gradient is related to the inter-particle spacing via $du_n/dn = s_n - \lambda$, so a steeper gradient indicates a more compressed kink.

We will now discuss the experimentally measured kink profiles, u_n, for different kink positions, chain lengths, substrate depths and driving velocities. We calculate the average u_n

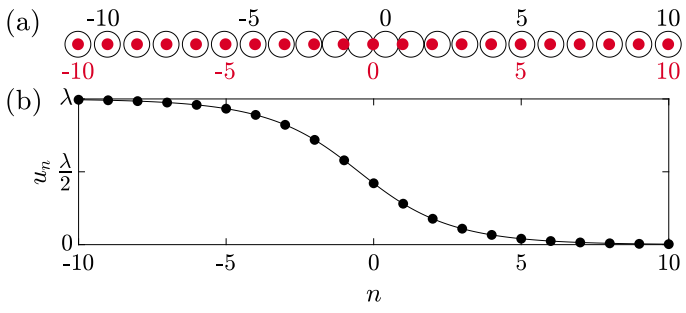


Figure 5.14: (a) Position and indices, n, of particles (black circles and numbers) relative to the substrate minima (red dots and numbers) in a model kink. (b) The kink profile, u_n.

relative to the kink centre, x_k. We first examine how the kink profile, u_n, changes as the kink moves through the chain, which is shown in figure 5.15a. The different lines show the average profile when the kink is located at different positions in the chain, from the left edge of the chain in blue to the right edge in red. In all cases, u_n has the expected stepped shape, with a plateau value of $u_n \approx 1.2\lambda$ when $n - x_k/\lambda < -6$, followed by a linear decrease in u_n, and finally a plateau at $u_n \approx 0.2\lambda$ when $n - x_k/\lambda > 3$. These limiting values of u_n are shifted up slightly compared to the theoretical equation of a kink in the FK model (equation 4.7), which has limits of λ and 0, as a result of the positive driving force pushing all particles slightly to the right of their potential minima. Importantly, all lines fall onto the same curve, indicating that the shape of the kink does not depend on its location in the chain.

Likewise, figure 5.15b shows the kink profile at different chain lengths from $N = 4-20$. All kink profiles are identical when $N \geq 8$, demonstrating that u_n has no chain length dependence.

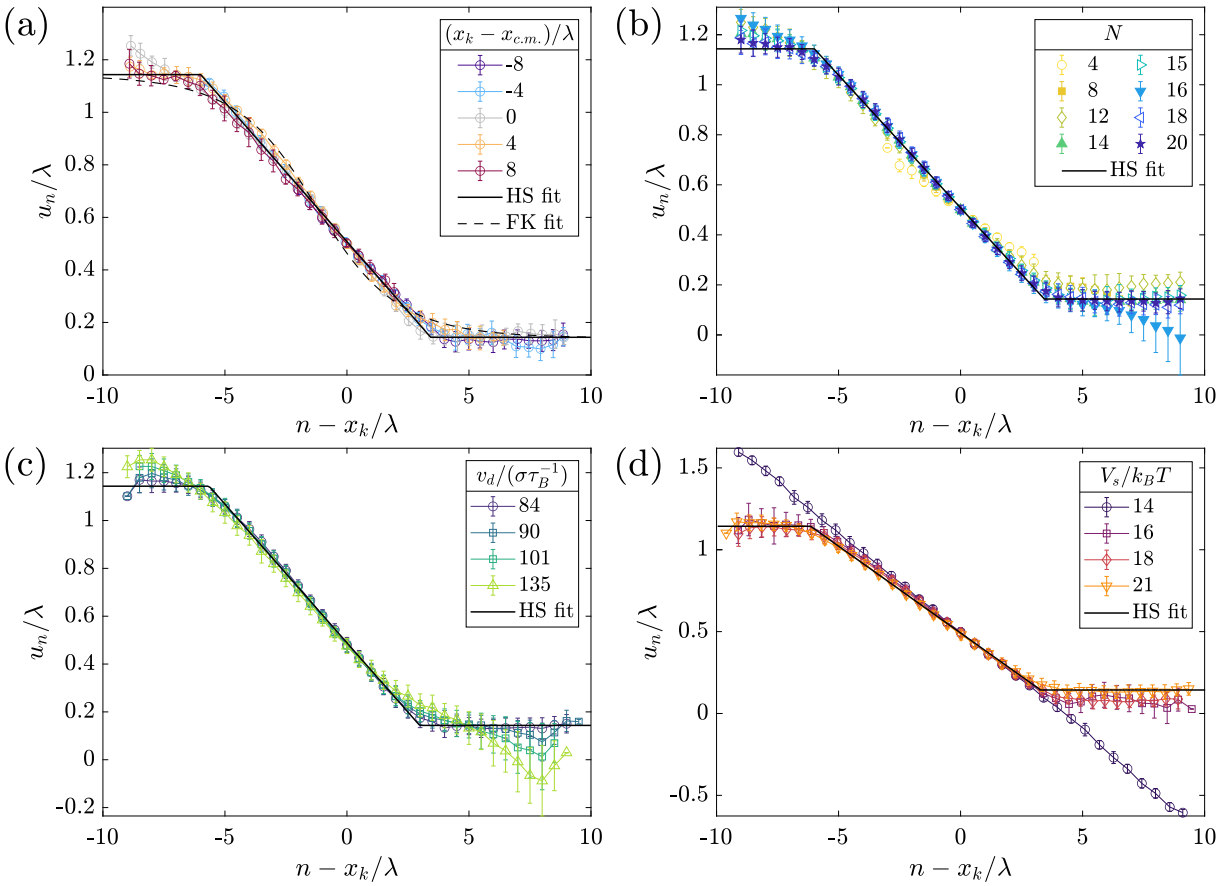


Figure 5.15: Average kink profile, u_n, verses $n - x_k/\lambda$, at different positions of the kink in the chain (a), chain lengths (b), driving velocities (c), and substrate depths (d). Unless otherwise stated in the key, $V_s = 21k_BT$, $N = 20$, and v_d is just above the critical velocity. The solid line in (a–d) is a fit of u_n from the experiment with $N = 20$, $V_s = 21k_BT$, $v_d = 84\sigma/\tau_B$ to the HSK profile (equation 5.22) and the dashed line in (a) is a fit to the FK kink profile (equation 4.7).

The $N = 4$ kink profile is different to the longer chains because the chain is shorter than the kink width.

The driving velocity dependence of the kink profile is shown in figure 5.15c. The highest driving velocity has a smoother, more S-shaped u_n than the lowest driving velocity, with a slightly lower gradient. This indicates that the kinks at higher v_d are less compressed and have longer tails, perhaps because the chain has less time to relax into its optimal shape as the kink rapidly moves through the chain.

Most strikingly, figure 5.15d shows that there is also almost no change in the kink profile as V_s decreases. When $V_s = 14$, u_n remains linear even at the at the edges, implying that the chain always contains the maximum number of kinks, but the centre of the kink profile is very similar at $V_s = 14k_BT$ and $V_s = 21k_BT$. In fact, there is a very slight increase in the kink width with increasing V_s, in contrast to the FK model, which predicts that the kink width should decrease with increasing V_s proportional to $(V_s/U''_{int})^{-1/2}$.

Furthermore, all kink profiles are quantitatively different to the kink profile predicted by the FK model (equation 4.7). The black dashed line in figure 5.15a shows a fit to the kink profile in equation 4.7, which has significantly higher curvature in the middle and longer tails than the measured u_n. Instead, the experimental kink profile is described by a piecewise linear function.

Hard sphere kink model

In order to explain this linear profile, we consider a chain of purely hard spheres with diameter σ in the absence of thermal fluctuations or an external driving force (see figure 5.16a). The substrate potential pushes the particles near the centre of the kink together until they are all in contact, with $s_n = \sigma$. The kink profile must therefore have a gradient of $du_n/dn = \sigma - \lambda = \lambda/N_0$, where N_0 is the chain length which feels zero total substrate force in the rigid chain limit. As a result, the kink must span N_0 particles. The profile of this hard sphere kink (HSK) is given by:

$$u_n = \begin{cases} \lambda & n \leq K - N_0 \\ -(n-K)\frac{\lambda}{N_0} & K - N_0 < n \leq K \\ 0 & n > K \end{cases}, \tag{5.22}$$

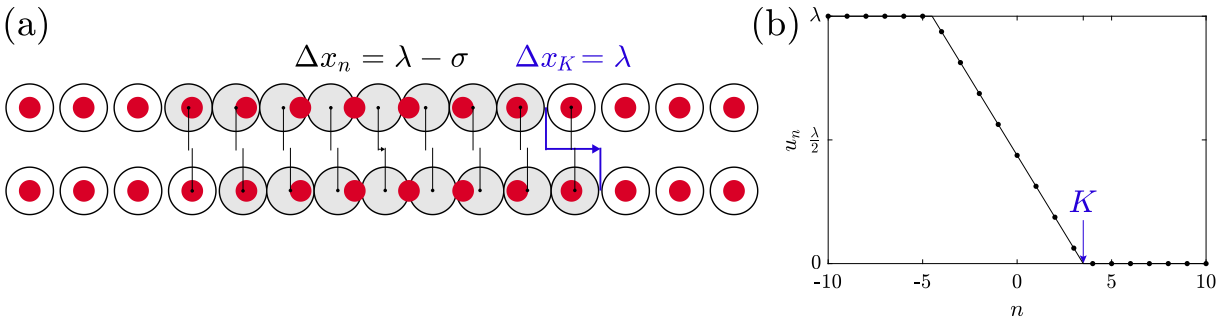


Figure 5.16: (a) Diagram of a kink in a chain of hard spheres. Red dots show the substrate minima, grey circles show the particles in the kink, and white circles show all other particles. The bottom row shows the particle positions when the kink has moved one wavelength to the right. Vertical lines show the movement of the kink, Δx_K, and each particle, Δx_n, in blue and black respectively. (b) Hard sphere kink profile.

where $K = x_k/\lambda + (N_0 - 1)/2$ is the index of the right hand end of the kink where u_n first reaches 0, as shown in figure 5.16b. We use K rather than x_k to denote the kink position in order to simplify the equations in the next section.

Figure 5.15 shows a fit of this HSK u_n to the experimentally measured u_n. The fit gives $N_0 = 9.4 \pm 0.2$, similar to the value of $N_0 = 8.2$ measured in weak substrates. The agreement between the experiment and HSK theory is far better than for the FK kink profile, suggesting that the kink profile at high V_s cannot be described by the effective stiffness of the pair potential, $U''_{int}(\sigma)$, but is instead determined solely by the hard sphere diameter. This explains why the kink width is not proportional to $(V_s/U''_{int}(\sigma))^{-1/2}$, as in the harmonic FK model.

The HSK model also explains the kink velocity measured in figure 5.13a. When the kink moves forward by one wavelength ($\Delta x_k = \lambda$), each particle in the kink moves a distance of $\Delta x_n = \lambda - \sigma = \lambda/N_0$, as illustrated in figure 5.16a. The velocity of the HSK is therefore N_0 times the particle velocity. Because the HSK always contains N_0 particles with an inter-particle separation of σ, the total substrate force acting on the kink sums to zero if N_0 is an integer, just as the substrate force felt by a chain of N_0 particles sums to zero. All particles in the kink therefore move with a velocity v_d, so the kink velocity is equal to $v_k = N_0 v_d$. This is close to the experimentally measured kink velocity of $v_k \approx 10 v_d$.

Critical force of kink creation

We have shown that the average velocity of a chain in the strong substrate limit depends on the rate of kink nucleation, and developed a new hard sphere kink (HSK) model which describes the

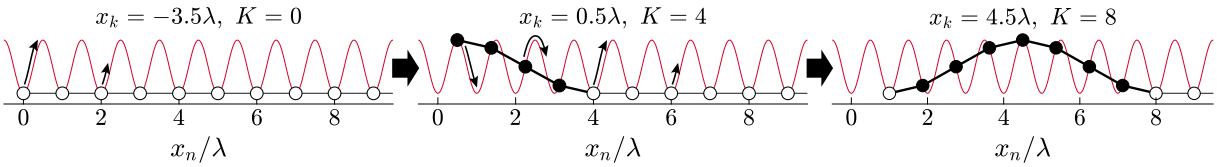


Figure 5.17: Position of each particle as a kink is nucleated. The particles in the kink are shown in black and arrows show the motion of every other particle.

experimental kink profile in all chain lengths, substrate depths and locations of the kink within the chain, and at driving velocities just above the critical velocity. We will now use this HSK profile to derive the total energy of a chain during the process of nucleating a HSK, and hence calculate the critical driving velocity in the strong substrate limit.

Figure 5.17 shows the process of nucleating a kink. The force needed to overcome the energy barrier associated with this process can be calculated from the kink profile using

$$\mathcal{F}(x_{cm}) = -\frac{\partial \mathcal{U}_{tot}}{\partial x_k}\frac{dx_k}{dx_{cm}}, \tag{5.23}$$

where the total energy of the chain, $\mathcal{U}_{tot}$, is found by substituting $x_n = u_n + n\lambda$ into the equation for the total energy of a chain (equation 4.8):

$$\mathcal{U}_{tot} = \sum_{n=0}^{N-1}\left[U_{sub}(n\lambda + u_n) + \sum_{m=n+1}^{N-1} U_{int}\left(u_m - u_n + (m-n)\lambda\right)\right]. \tag{5.24}$$

Similarly, the centre of mass in terms of the kink profile is given by

$$x_{cm} = \frac{1}{N}\sum_{n=0}^{N-1} n\lambda + u_n. \tag{5.25}$$

We assume that the kink has the HSK profile described by equation 5.22, ignoring the effect of driving velocity on u_n. We substitute the HSK u_n into equations 5.24 and 5.25 to find the energy and centre of mass of a chain as a function of the kink index, K. There are two contributions to the energy; the energy of kink creation and the Peierls-Nabarro (PN) potential, which describes the energy needed to move the kink over one wavelength. The latter contribution has a negligible amplitude, so we ignore it by only calculating $\mathcal{U}_{tot}$ and x_{cm} when K is an integer. We calculate the kink creation energy when the kink is in the process of entering the chain, so $K < N_0$, as shown in figure 5.17. During the kink nucleation process, it is clear from figure 5.17 that the chain has K particles which are not sitting in a potential minimum. The total substrate

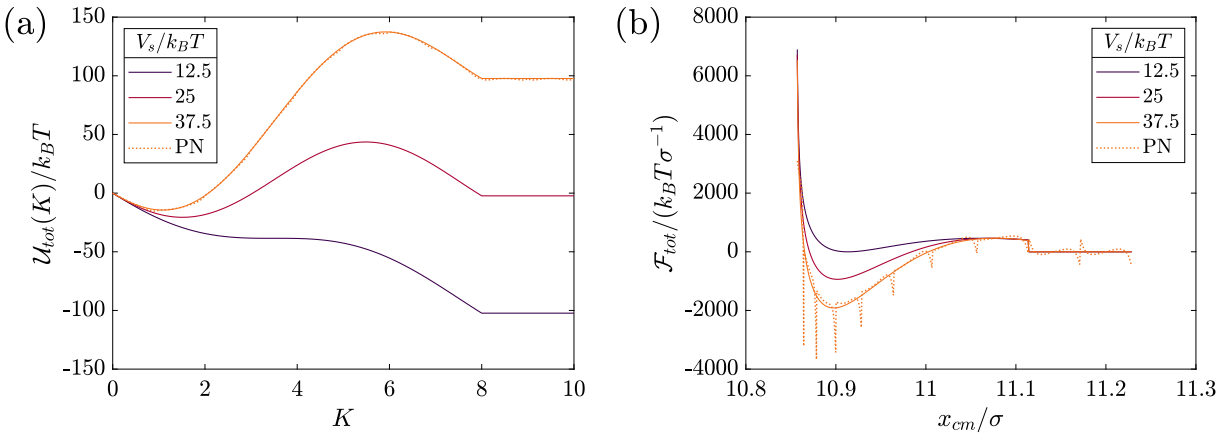


Figure 5.18: (a) Total energy, $\mathcal{U}_{tot}$, versus K during kink nucleation when $V_s = 12.5k_BT$ to $37.5k_BT$ (purple to yellow). The yellow dotted line is the numeric calculation of the total energy, which includes the PN potential, whereas all other lines analytical expressions from equation 5.28 which are only true at integer K. (b) Total force versus centre of mass. Lines are the same as in (a).

potential is therefore

$$\mathcal{U}_{sub} = -V_s \left[(N-K) + \sum_{n=1}^{K} \cos\left(\frac{2\pi n}{N_0}\right) \right]. \tag{5.26}$$

There is no inter-particle energy term for truly hard spheres, but our particles have an additional attractive term to their pair potential. We assume that the nearest-neighbour attractions contribute to the total energy without perturbing the kink profile. The K particles in the kink contribute K inter-particle interactions with an energy of $U_{int}(\sigma)$, while the other $N-1-K$ inter-particle interactions each contribute an energy of $U_{int}(\lambda)$. The inter-particle contribution to $\mathcal{U}_{tot}$ is therefore

$$\mathcal{U}_{int} = KU_{int}(\sigma) - (N-1-K)U_{int}(\lambda). \tag{5.27}$$

The total energy as a function of the kink position, K, is therefore given by

$$\mathcal{U}_{tot}(K) - \mathcal{U}_{tot}(0) = K\left[U_{int}(\sigma) - U_{int}(\lambda)\right] + V_s\left[K + \frac{1}{2} - \frac{\sin\left(\pi(2K+1)/N_0\right)}{2\sin\left(\pi/N_0\right)}\right], \tag{5.28}$$

where the sum in equation 5.26 has been simplified in the same way as the total energy of a rigid chain in equation 4.9, and we have calculated the energy relative to a chain with no kinks ($K = 0$).

Figure 5.18a shows the total energy as a function of the kink index, K, at several different

substrate depths. When V_s is large compared to ΔU_{int}, there is a large energy barrier to kink nucleation and the final state is higher in energy than the state with no kinks. When V_s is slightly smaller, the two states are similar in energy but there is still a significant energy barrier between them. When V_s is sufficiently small, however, the barrier disappears and the chain will spontaneously nucleate the maximum number of kinks. This change in behaviour defines the point at which we see a transition from high to low friction. We find this transition point, where the energy barrier disappears, by differentiating equation 5.28 to obtain

$$V_s^{\dagger} = \frac{U_{int}(\lambda) - U_{int}(\sigma)}{1 + (\pi/N_0)\csc(\pi/N_0)} \approx \frac{U_{int}(\lambda) - U_{int}(\sigma)}{2}. \tag{5.29}$$

The approximate expression, obtained by applying the small angle approximation to the denominator of the exact expression, is valid when N_0 is large (so σ/λ is close to an integer).

We have now calculated the energy barrier required to nucleate a kink, but in order to convert this into the critical force required to overcome this barrier, we also need the centre of mass of the chain as a function of K, found by substituting equation 5.22 into equation 5.25 to obtain

$$x_{cm} = \lambda\left(\frac{N-1}{2} + \frac{K(K+1)}{2NN_0}\right). \tag{5.30}$$

Substituting equations 5.28 and 5.30 into 5.23 gives a force of

$$F(K) = -\frac{2NN_0}{\lambda(2K+1)}\left[U_{int}(\sigma) - U_{int}(\lambda) + V_s\left(1 - \frac{\pi}{N_0}\frac{\cos\left(\pi(2K+1)/N_0\right)}{\sin\left(\pi/N_0\right)}\right)\right], \tag{5.31}$$

which plotted against the centre of mass in figure 5.18b. The critical driving velocity needed to overcome this force is equal to

$$v_N^* = -\zeta_N^{-1}\min(F(K)). \tag{5.32}$$

Equation 5.31 is impossible to minimise analytically, but a second order Taylor expansion of $F(K)$ about $K = (N_0 - 1)/2$ gives the following approximate value of v_N^*:

$$v_N^* \approx \frac{N}{\zeta_N}\frac{2}{\lambda}\left(U_{int}(\sigma) - U_{int}(\lambda) + 2V_s\right), \tag{5.33}$$

where we have once again assumed $(N_0/\pi)\sin(\pi/N_0) \approx 2$. Note that v_N^* is proportional to

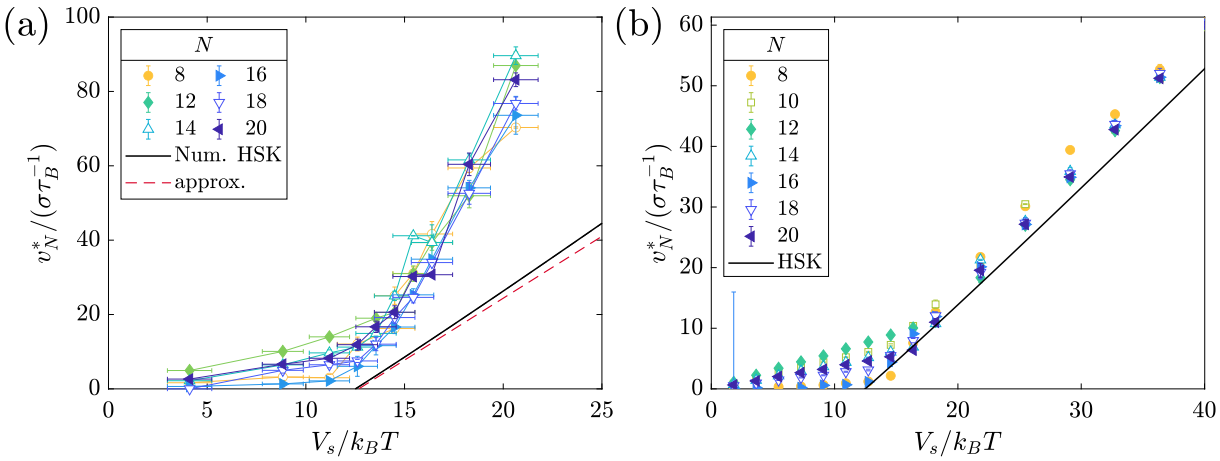


Figure 5.19: (a) Experimental critical velocity verses substrate depth, with the numeric solution to equation 5.32 (black line) and the approximate solution in equation 5.33 (red dashed line). (b) Simulated critical velocity with the numeric solution to equation 5.32 (black line).

N/ζ_N. When we use the non-hydrodynamic drag constant of $\zeta_N = N\zeta_1$, equation 5.33 does not depend on N, but using the experimentally measured $\zeta_N = (N+1)\zeta_1/2$ means that v_N^* is proportional to $2N/(N+1)$, which is approximately constant at high N.

Figure 5.19a compares the HSK theory (with $\zeta_N = \zeta_1(N+1)/2$ and $N = 20$) to the experiments. Both the numerical and approximate expressions for v_N^* correctly predict the transition point from high to low friction within experimental error. However, the theory underestimates the rate of increase of v_N^* at high V_s by a factor of two.

In order to establish the reason for the deviation between the experiments and theory at high V_s, we also compare the theory to Brownian dynamics simulations in figure 5.19b. The theory shows remarkable agreement with the simulations, correctly predicting the transition from low to high friction and only slightly underestimating the critical velocity at high V_s. This deviation is not surprising given that we have ignored the Peierls-Nabarro barriers and the effect of the driving velocity on the kink profile.

Because the simulations and the theory show excellent agreement, as well as the fact that the simulations display the same dynamics as the experiments and that the theory correctly predicts the experimental transition from low to high friction, we assume that the difference between the experiments and theory at high V_s occurs because one of the constants in equation 5.33 in fact changes as a function of the substrate depth, V_s. The possible candidates are the inter-particle interactions, $U_{int}(\sigma) - U_{int}(\lambda)$, the drag constant of each particle, ζ_1, and the function relating the drag constant of a chain of N particles to the drag constant of each

particle, assumed to be $\zeta_N = \zeta_1(N+1)/2$. Only the latter, ζ_N, can be expected to decrease by the factor of two required to match the theory and simulations to the experiments. In fact, the drag constant of $\zeta_N/\zeta_1 = {}^2\!/_3 N/\ln(N)$ measured by Yang *et al.* [190] is a factor of two smaller than our assumed drag constant of $\zeta_N/\zeta_1 = (N+1)/2$; approximately the ratio between the experimental and theoretical v_N^* at high V_s. While it is not clear why the hydrodynamic drag constant might decrease as the laser power increases and the dynamics of the chain change, it nonetheless remains a plausible explanation for the difference between the experiments, simulations and HSK theory.

5.5 Conclusions

We have measured the friction between colloidal chains driven over a sinusoidal optical substrate of varying depth. In weak substrates, we observed ultra-low friction at well defined chain lengths. As the substrate potential increased, a transition from low to high friction was observed, which we attribute to the appearance of an energy barrier to kink nucleation.

In the weak substrate regime, we developed a modified version of the rigid chain model in which chains underwent small, uniform expansions and contractions as they crossed the substrate. This small uniform expansion model correctly predicted the observed dynamics and showed qualitative agreement with the experimental critical driving velocity. Furthermore, it was shown that when the potential is highly anisotropic with a very strong effective stiffness ($U''_{int}(\sigma)$), the magnitude of the change in the chain's spacing, and hence the resulting increase in friction, is insignificant.

In the strong substrate limit, we showed that the transition to high friction is accompanied by a change in the kink density as a function of driving velocity, and that the friction is determined by the rate of kink nucleation. We measured the kink profile, finding that it was best described by a new hard sphere model. This model was then used to derive a simple expression for the critical velocity of a chain. The theory closely matched our simulations and correctly predicted the substrate depth at which the transition from high to low friction occurred.

We hypothesise that the deviation between the hard sphere kink theory and the experiments is due to a decrease in the hydrodynamic drag constant as the structure of the chain changes with increasing substrate potential. Further experiments and modelling are required to determine how

the drag constant of a chain depends on its structure, and hence quantify any changes in the drag constant as a function of the substrate depth which may be used to modify the hard sphere kink theory.

Acknowledgments

This work was done in collaboration with Josh Abbot-Scott. Amelia Jones is thanked for the kink tracking code and Berend van der Meer is thanked for providing simulation code. Berend van der Meer and Joseph Hutchinson are thanked for their useful discussions.

Chapter 6

Synchronisation of driven colloidal chains in an oscillating periodic potential

Abstract

In this chapter, we analyse the average velocity and dynamics of chains of paramagnetic colloids driven through a periodic optical potential whose depth oscillates with time. We observe unusually large steps where the average velocity is synchronised to the oscillations of the optical potential. Steps with an order of up to three are visible. The step width does not depend on the chain length, and increases with increasing oscillation amplitude and frequency. We then analyse the dynamics of the chains, observing two distinct modes of motion. At the beginning of each synchronised step, a single kink travels from the back to the front of the chain each time its centre of mass moves forward by one wavelength. At the end of each synchronised step, the chains travel by a novel mode of motion in which multiple kinks and anti-kink are simultaneously nucleated in the middle of the chain. We suggest that the ability of the chain to switch between these two modes is responsible for the anomalously large steps.

6.1 Introduction

It is well established that vibrations can be used to reduce friction and wear at specific frequencies. This phenomenon has been observed experimentally from the nano-scale to the micro- [216], macro- [217–219] and even geological scale [220]. Atomic force experiments have been used to study the effect of normal [42, 221–224], lateral [225] and transverse [226] vibrations, as well as combinations of all directions [227]. These experiments demonstrate that vibrations of all types can decrease friction by stabilising the system against stick-slip motion. However, there is little consistency in the range of frequencies required, with some experiments reporting friction reduction over several narrow resonances [222–224], and others over orders of magnitude [42, 221]. Vibrations can also increase friction in some circumstances. Molecular dynamics simulations and numerical models point to a wide range of factors influencing the effect of vibrations, including the nature of the atomic interactions [228] and the stiffness and response times of different parts of the experimental setup [229,230]. A fundamental understanding of the underlying mechanism, however, is still lacking.

Theoretically, Prantl-Tomlinson type models, consisting of a single particle pulled over a sinusoidal substrate by a spring moving at a constant velocity, have been used to provide a qualitative explanation for the observed reduction in friction [216, 231–235]. They attribute the phenomenon to either enhanced diffusion at low vibration frequencies and driving velocities, or, at high vibration frequencies, the appearance of "parametric resonances" between the vibrations and the washboard frequency associated with stick-slip motion in the absence of oscillations. Jeon *et al.* [42] extended these models by treating the tip of the cantilever of the atomic force apparatus as a Frenkel-Kontorova style 1D chain of particles. They suggested that the vibrations significantly change the frictional dynamics of the chain, but did not discuss the nature of these changes. Further analysis of the dynamics of Frenkel-Kontorova style models in the presence of vibrations is therefore warranted.

Most studies of Frenkel-Kontorova models with a vibrating component [236–243] use a constant driving force, rather than being driven by a spring-like cantilever moving at a constant velocity. While this does not describe atomic force experiments, it is a relevant model for other applications where the frictional surfaces are driven by a constant force. By focusing on the interplay between the frequency and the driving force, these studies are able to observe mode-

locked steps, where the frequency at which the particles move over the substrate is synchronised to the vibration frequency [8]. At well defined frequencies and driving velocities, synchronisation leads to a large reduction in friction. Large high order and even sub-harmonic steps have been predicted for lateral vibrations, equivalent to an oscillating driving force, under many different conditions [236–242].

Less attention has been paid to the case of normal vibrations, which can be modelled by oscillating the depth of the substrate. Ticco *et al.* [243] simulated a colloidal monolayer of charged particles, which behaves as a two-dimensional overdamped Frenkel-Kontorova system, driven over an oscillating substrate at zero temperature. They observed wide high order mode locked steps and even sub-harmonic steps when the substrate and monolayer were incommensurate. This is very different to the synchronisation of single particles driven over a periodic substrate with an oscillating driving force [72, 244] or substrate depth [100], which do not exhibit sub-harmonic steps. They showed that these sub-harmonic steps were mediated by the movement of anti-kinks in an under-dense system, where the wavelength of the substrate is smaller than the particle spacing. However, they did not study the over-dense scenario. Related colloidal experiments, which used a commensurate monolayer of charged particles at room temperature and with weaker interactions, observed a single mode-locked step [211]. They attributed the lack of higher order steps to the formation of kinks, but did not consider the effects of temperature [240] and only studied one frequency. Moreover, both the simulations [243], which use periodic boundary conditions, and the experiment [211], which uses an extended attractive optical trap to hold the monolayer together, do not exhibit edge effects. Edge effects begin to dominate as the bulk friction decreases [40] even in large systems, particularly under high normal loads [205], and have received increasing attention in the last five years [39, 196, 201, 206, 208, 209, 245–247].

Previous studies of friction reduction via synchronisation in the Frenkel-Kontorova model with an oscillating substrate leave several gaps – namely, a systematic experimental study of the dynamics of over-dense chains with free edges – which we address by studying one-dimensional colloidal chains in an optical potential oscillated at different amplitudes and frequencies. The interactions between our particles, which consist of a hard core repulsion and a long-ranged, convex attraction, mimic atomic interactions more closely than previous colloidal experiments. The wavelength of the substrate is slightly larger than the diameter of the particles so that the system is over-dense. We study the effect of chain length, oscillation amplitude and frequency

on the friction felt by the chains compared to theoretical predictions for a rigid chain. By using small chains of 10 to 20 particles, we observe kink production and annihilation at the edges of the chain, and analyse the kink dynamics across each mode-locked step.

6.2 Theory

This section contains a theoretical description of the synchronisation of a rigid chain driven over an oscillating substrate potential. While our experiments are certainly not in the rigid chain limit, this theory provides a useful reference point.

Synchronisation may be described as the "adjustment of rhythms due to an interaction" [8]. Synchronisation occurs when two self-sustaining oscillators with inherent frequencies f_1 and f_2 are coupled by a weak interaction, causing them to adjust their rhythms to a new set of frequencies f_1' and f_2'. When the mismatch between the frequencies, $\Delta f = f_1 - f_2$, is small enough, the oscillators will synchronise to the same frequency such that $\Delta f' = f_1' - f_2' = 0$. If one of the oscillators is perturbed, the two oscillators will eventually re-synchronise. As well as first order synchronisation where $f_1' = f_2'$, synchronisation can occur with any rational order n such that $f_1' = nf_2'$, although integer values of n are more common and typically occur over a wider frequency range.

A chain moving over a periodic substrate with wavelength λ at an average velocity of $\langle v \rangle$ behaves as an oscillator with a frequency of $f_p = \langle v \rangle / \lambda$ [8]. When the depth of the substrate is also oscillated at a frequency f_s, the frequency of the particle's motion may lock to the substrate frequency such that its average velocity becomes $\langle v \rangle = nf_s\lambda$, where $n = 0, 1, 2, ...$ is the order of the synchronisation.

The oscillations of the depth of the substrate potential are described by the time-dependent function $1 + A\cos(2\pi ft)$, where f is the frequency and A, the amplitude of the oscillations, must be between 0 and 1. The substrate potential is therefore a equal to

$$U_{sub}(x,t) = V_s\left(1 + A\cos(2\pi ft)\right)\cos\left(\frac{2\pi x}{\lambda}\right). \tag{6.1}$$

The instantaneous substrate depth, equal to $U_{sub}(0,t)$, oscillates between $1 - A$ and $1 + A$ such that the average substrate depth is equal to V_s.

The equation of motion of a rigid chain driven through the oscillating substrate is given by the following Langevin equation:

$$\frac{dx}{dt} = v^* \left(1 + A\cos(2\pi f t)\right) \sin\left(\frac{2\pi x}{\lambda}\right) + v_d + \xi(t), \tag{6.2}$$

where $v^* = (2\pi/\lambda)V_s/\zeta$ is the critical velocity of the chain in a non-oscillating substrate of the same average depth, ζ is the drag constant of the chain, and $\xi(t)$ is a noise term whose magnitude is given by $\langle \xi(t)\xi(t')\rangle = 2(k_B T/\zeta)\delta(t-t')$. Note that these terms are the same as v_N^*, ζ_N, and $\xi_N(t)$ in chapters 4 and 5, but we have dropped the subscript for simplicity.

6.2.1 Deterministic average velocity

When the critical velocity is high enough to give a Péclet number much larger than one, as is usually the case in this chapter, we can ignore the effect of noise and solve the following deterministic version of equation 6.2 to find the average velocity:

$$\frac{dx}{dt} = v^* \left(1 + A\cos(2\pi f t)\right) \sin\left(\frac{2\pi x}{\lambda}\right) + v_d. \tag{6.3}$$

Approximate solutions to this equation exist in the high and low frequency limits, which we will now discuss.

High frequency limit

In the high frequency limit where $f \gg v^*/\lambda$, an approximate solution to equation 6.3 can be found in the vicinity of each mode-locked step at $v_d \approx nf\lambda$, where $n = 0, 1, 2...$ is the order of the step. Near the zeroth step, the average velocity is given by [100]

$$\langle v\rangle = \begin{cases} 0 & |v_d| \le v^* \\ \sqrt{v_d^2 - v^{*2}} & |v_d| > v^* \end{cases}, \tag{6.4}$$

while the first order step gives an average velocity of

$$\langle v\rangle = f\lambda + \begin{cases} 0 & |v_d - f\lambda| \le Av^*/2 \\ \sqrt{v_d^2 - A^2 v^{*2}/4} & |v_d - f\lambda| > Av^*/2 \end{cases}, \tag{6.5}$$

and for all subsequent steps,

$$\langle v \rangle = v_d. \tag{6.6}$$

Figure 6.1a shows the average velocity predicted by equations 6.4, 6.5 and 6.6 with $A = 1$ and $f \gg v^*$. The width of the zeroth step is equal to v^*, the same as the non-oscillating case. The first step has a width of Av^*, and there are no higher order steps.

Low frequency limit

In the low frequency limit, when $f \to 0$, we can treat the oscillations of the substrate potential depth as a reversible change where the particle has time to relax into the steady state trajectory of a particle in a static substrate of the same depth. The average velocity is therefore the average over time of the average velocity in a static landscape of depth $v^*(1 + A\cos(2\pi ft))/2$,

$$\langle v \rangle = f \int_0^{f^{-1}} \sqrt{v_d^2 - v^{*2}\left(1 + A\cos(2\pi ft)\right)^2}\, dt, \tag{6.7}$$

which we solve numerically. Figure 6.1b shows the average velocity predicted by this equation with $A = 1$ and $f \ll v^*$. Note that this does not predict the step widths, only their position, because the distance between the steps vanishes as $f \to 0$. At low driving velocities in the low frequency limit, and when $A = 1$, the integral in equation 6.7 reduces to the following power

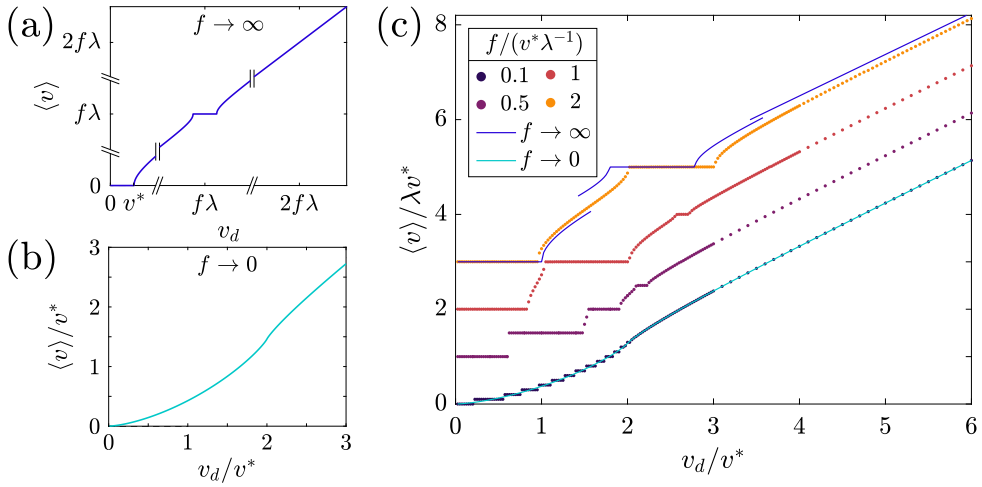


Figure 6.1: Average velocity versus driving velocity of a deterministic particle in an oscillating potential with $A = 1$ in (a) the high frequency regime, (b) the low frequency regime, and (c) intermediate frequencies of $f = 0.1v^*/\lambda$ (navy) to $2v^*/\lambda$ (yellow), shifted upwards for clarity. Cyan and blue lines show the low and high frequency regimes respectively.

law:

$$\langle v \rangle \approx v_d \left[-\frac{\Gamma(-3/4)}{4\sqrt{2\pi}\Gamma(3/4)} \left(\frac{v_d}{v^*}\right)^{1/2} + \mathcal{O}\left(\left(\frac{v_d}{v^*}\right)^{1/2}\right)\right] \tag{6.8}$$

where $\Gamma(n) = (n-1)!$.

Numerical solutions

The frequencies used in this chapter are on the order of v^*/λ, between the high and low frequency regimes. We therefore solve equation 6.3 numerically. Figure 6.1c shows the average velocity at a range of frequencies, compared to the high and low frequency theory. The high frequency regime, which predicts step widths of $w_0 = v^*,\ w_1 = Av^*,\ w_{n\geq 2} = 0$, is valid when $f > v^*/\lambda$. Below this point, many high order steps are visible. The low frequency regime correctly predicts the position of these steps when $f \lesssim 0.5v^*/\lambda$.

6.2.2 Noise

So far, we have only considered a deterministic version of the Langevin equation, in which the trajectory of a particle is either synchronised to the oscillating substrate or deviates from synchronisation in a consistent way. When a particle is subject to thermal noise, however, there is always a finite probability of the particle slipping out of sync with the oscillations and later returning to the mode locked trajectory with a higher or lower phase. Examples of these "phase slips" are shown in figure 6.2a. A trajectory can only be truly synchronised if the probabilities of the forward and backwards phase slips are equal, which only occurs in the middle of the step. Otherwise, there is a bias in the forward or backwards direction, so the average velocity deviates from the mode-locked value, thus reducing the step width.

The effect of noise can be calculated analytically in the high frequency regime. In the region of the n^{th} step, the average velocity is given by the following continuous fraction [8]:

$$\langle v \rangle = nf\lambda + v_d + 2w\mathrm{Im}\left(\frac{1}{i\alpha - \gamma + \frac{1}{i\alpha - 2\gamma + \frac{1}{i\alpha - 3\gamma + \cdots}}}\right),\ \text{where } \alpha = \frac{v_d}{w},\ \gamma = \frac{D}{w}\frac{\lambda}{2\pi}, \tag{6.9}$$

where w is the step width and $D = k_B T/\zeta$ is the diffusion coefficient of the chain. Figure 6.2

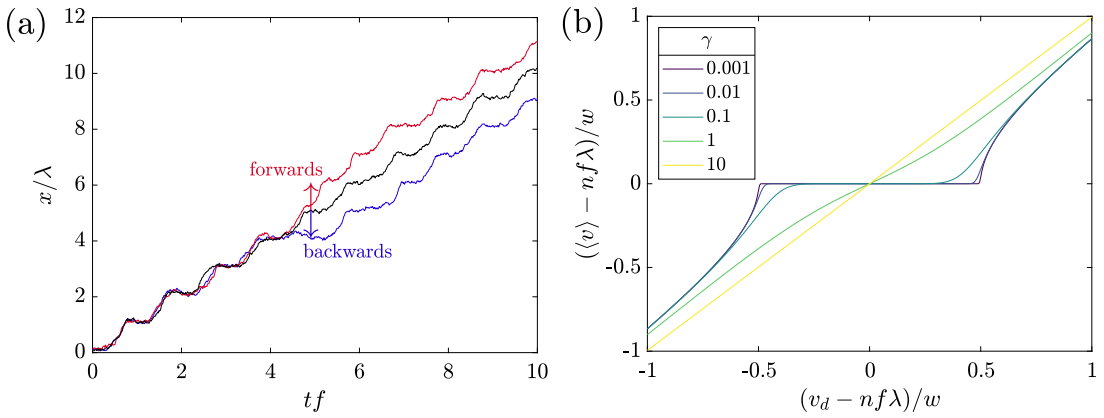


Figure 6.2: (a) Forward (red) and backwards (blue) phase slips of a mode-locked trajectory (black) with $n = 1$. (b) Noisy average velocity vs. driving velocity from equation 6.9 near a step of width w and order n, at different values of γ from 0.001 (purple) to 10 (yellow).

shows the average velocity at different values of the noise parameter, γ. As the magnitude of the noise increases relative to the step width, the steps are increasingly smoothed out until there is no longer a plateau, reducing the step width to zero.

6.3 Experimental methods

The experiments performed in this chapter use the same particles and experimental setup as the previous two chapters, and are described in detail in chapter 2. In short, the particles are paramagnetic hard spheres with a radius of $a = 1.4\,\mu\text{m}$ and a Brownian time of $\tau_B = 59\,\text{s}$. A horizontal magnetic field in the x direction causes the particles to form chains parallel to the field. The pairwise interaction along this axis is

$$U(x_{ij}) = U_{HS} - \Gamma \left(\frac{\sigma}{x_{ij}} \right)^3 . \tag{6.10}$$

We use a field strength of $B = 0.32\,\text{mT}$, giving an interaction parameter of $\Gamma = 30 \pm 2$ using the same magnetic susceptibility as in chapters 4 and 5, measured in appendix B. Note that we choose a lower interaction strength than in chapters 4 and 5 to ensure that the chain is always in the high friction regime described in chapter 5.4.3. We confirm this assumption by measuring the critical velocity of a chain of 16 particles using the method described in chapter 5.3, shown in figure 6.3. We do indeed see a transition from low to high friction at $V_s \approx 5k_BT$, much earlier than in chapter 5, and agreeing well with the hard sphere kink theory developed in section 5.4.3. We can therefore expect our chains to have similar dynamics to those described in section 5.4.3

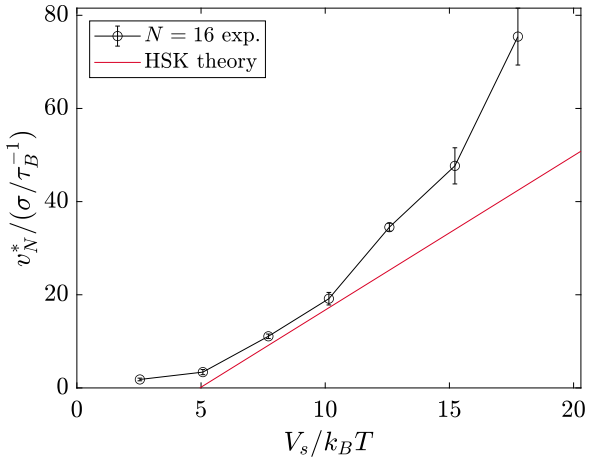


Figure 6.3: Measured critical velocity of a chain with $N = 16$ in a static landscape of depth $2.5k_BT$ to $17.5k_BT$. The red line shows the theoretical critical velocity of a chain from equation 5.33 (the hard sphere kink theory).

when the amplitude of oscillation is low.

Lines of optical traps are used to create a sinusoidal substrate potential with a wavelength of $\lambda = 3.2\,\mu\text{m}$, the same as in previous chapters. The depth of the substrate is oscillated at frequencies ranging from 0.1 Hz to 0.4 Hz, equivalent to $6 - 24\,\tau_B^{-1}$, by using the AOD to modulate the laser power with an update rate of 20 Hz. The laser power was oscillated around a mean value of 300 mW, giving an average substrate depth of $V_s = 10k_BT$. The laser power was monitored in real time by placing a second camera, controlled by a different computer, above mirror 2 in figure 2.7. The total brightness of the image was used to verify when the AOD was performing as expected. Any sections of the experiment in which the AOD had not updated for over a second were removed.

The particles were driven through the optical traps at velocities of 0 to 4 µm/s, equivalent to $84\,\sigma\tau_B^{-1}$. During most of the experiments, the stage travelled a distance of 80 µm $\equiv 25\lambda$ and each driving velocity was repeated twice in the forwards and backwards direction. Due to the increased computational demand from the oscillating landscape, the piezo stage froze more often than in previous chapters, so we removed any frames where the stage had not updated for more than one second. We also removed any frames where the chain had broken, which we defined as containing an inter-particle distance larger than two wavelengths. A plot of the breakage frequency is shown in appendix D.

6.4 Results and discussion

In this section, we first analyse how the average velocity of chains in an oscillating landscape depends on the chain length, amplitude and frequency. We then discuss the dynamics of the chains in terms of the nucleation and translation of kinks and anti-kinks across each mode locked step.

6.4.1 Average velocity measurements

First we investigate the effect of chain length on the average velocity in an oscillating landscape. Figure 6.4a shows the average velocity of a single particle in a substrate of depth $V_s = 10k_BT$ which is oscillated at a frequency of $f = 12\,\tau_B^{-1}$ with an amplitude of $A = 1$. There is a clear first order mode-locked step at $\langle v \rangle = f\lambda$; the characteristic feature of synchronisation. We compare the experiment to the theoretical average velocity of a deterministic particle outlined in section 6.2.1, found by numerically solving the equation of motion of a rigid chain (which behaves as a single particle) in equation 6.3. The theory agrees well with the experiment, correctly predicting the position of the mode-locked steps. This confirms the accuracy of the rigid chain theory. The experimental average velocity has narrower steps due to the effect of thermal noise described in section 6.2.2.

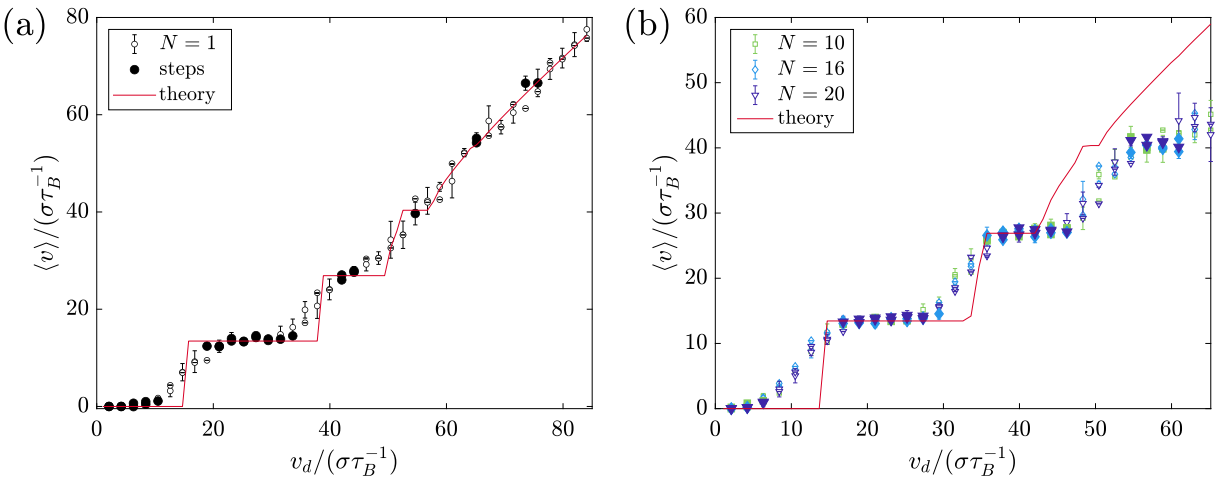


Figure 6.4: Average velocity of (a) one particle and (b) chains of 10 (green squares), 16 (blue diamonds) and 20 (purple triangles) particles in an oscillating substrate with $V_s = 10k_BT$, $A = 1$ and $f = 12\,\tau_B^{-1}$. Large filled points show the location of the mode locked steps. The red lines show the theoretical $\langle v \rangle$ of a deterministic rigid chain.

Figure 6.4b shows the average velocity of chains with $N = 10$, 16 and 20 particles in the same oscillating substrate potential. Importantly, the three chains have identical average velocities, indicating that chain length is not an important parameter in these experiments. This is to be expected given that the chains are in the high friction regime at the average substrate depth of $V_s = 10k_BT$ (see figure 6.3). In the high friction regime, which is described in section 5.4.3, we showed that all chain lengths have the same critical velocity and dynamics. Unlike the single particle, the average velocity of the chains has a wide first, second and even third mode locked step, showing that the chains synchronise strongly to the substrate oscillations. Comparing the experimental average velocity to that of a theoretical deterministic rigid chain, found by numerically solving the equation of motion as described in section 6.2.1, shows that the experiments have much wider high order steps than predicted, as well as a smaller zeroth order step and very different step positions. We discuss this difference further in the rest of this section, where we measure the average velocity, $\langle v \rangle$, at several different amplitudes and frequencies.

Figures 6.5a and b show $\langle v \rangle$ for a chain of 16 particles in an oscillating substrate with $V_s = 10k_BT$, $f = 12\,\tau_B^{-1}$, and amplitudes varying from 0 to 1. Note that at the largest amplitude, chains frequently broke apart at high driving velocities of $v_d > 60\,\sigma/\tau_B$, so we have excluded

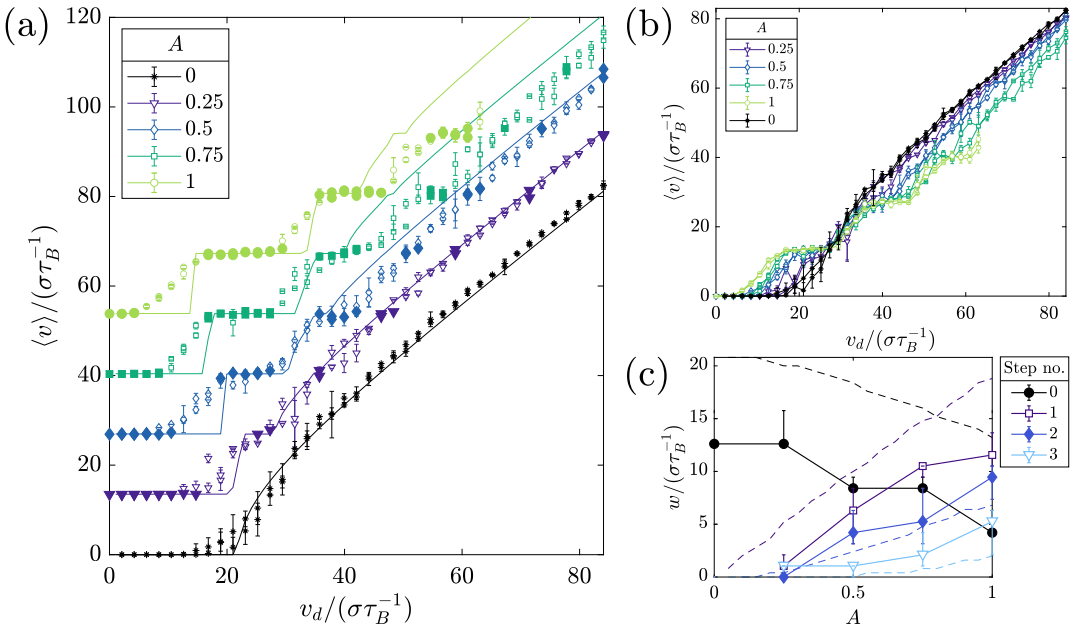


Figure 6.5: (a) Average velocity, $\langle v \rangle$, of a chain of 16 particles in an oscillating landscape with $f = 12\,\tau_B^{-1}$, and $A = 0$ (black stars) to 1 (light green circles), shifted upwards for clarity. Large filled points highlight the steps. Lines show $\langle v \rangle$ for a theoretical deterministic rigid chain with the same v^*, f and A. (b) $\langle v \rangle$ from the same experiments as in (a), but plotted on top of each other. (c) Width of the 0th (black circles) to 3rd (light blue triangles) step versus A. Dashed lines show the rigid chain theory.

these measurements.

In the absence of oscillations, i.e. $A = 0$, the average velocity follows the expected square-root law, but as A increases, $\langle v \rangle$ begins to deviate from the square-root law due to the appearance of increasingly wide, high order mode-locked steps. When $A = 0.25$, only a small first step is visible, but when A reaches 0.75, there is a large first, second and third step. The width of the steps with order $n \geq 1$, shown in figure 6.5c, decrease with increasing n and increase with increasing A, while the zeroth step width decreases. These trends in the step width are predicted by the rigid chain theory, plotted as dashed lines in figure 6.5c, but the relative magnitudes of the step widths are very different. The experiments have a narrower first and second step than predicted by the theory, which can partially be attributed to the effect of thermal noise, but the second and third steps are wider.

As a result, increasing the oscillation amplitude increases $\langle v \rangle$ at low v_d relative to both the $A = 0$ experiment and the rigid chain theory. This is shown more clearly in figure 6.5b. This corresponds to a large reduction in the friction force between the chain and the substrate at small driving velocities. At high v_d, after the beginning of the second step, $\langle v \rangle$ decreases with increasing A, corresponding to an increase in friction.

We now examine the effect of the frequency, f, on the average velocity of a chain of 16 particles in an oscillating substrate, shown in figure 6.6. The experimental $\langle v \rangle$ and step widths are compared to the rigid chain theory in figures 6.6a and c respectively. Figure 6.5a shows that the step positions differ from the rigid chain theory; at low driving velocities and frequencies, the experiments have a larger average velocity than the theory, but at high driving velocities and frequencies, the opposite is true. Plotting all experiments on top of each other in figure 6.6b shows that step centres of all the $f > 0$ experiments fall onto the same curve, resembling a power law with an exponent of 1.4 ± 0.4. This power law behaviour is reminiscent of the low frequency regime described in section 6.2.1, in which $\langle v \rangle \propto v_d^{1.5}$ at low driving velocities (equation 6.8). This suggests that the step positions may be described by a modification of the low frequency theory, which we will discuss in section 6.4.2.

All step widths, shown in 6.6c, increase with increasing frequency faster than predicted by the theory. When $f = 6\,\tau_B^{-1}$, the step widths are smaller than the theory due to thermal fluctuations, but when $f = 24\,\tau_B^{-1}$, the steps are significantly wider. The width of the second order step reaches a peak when $f = 18\,\tau_B^{-1}$, much later than predicted by the rigid chain theory.

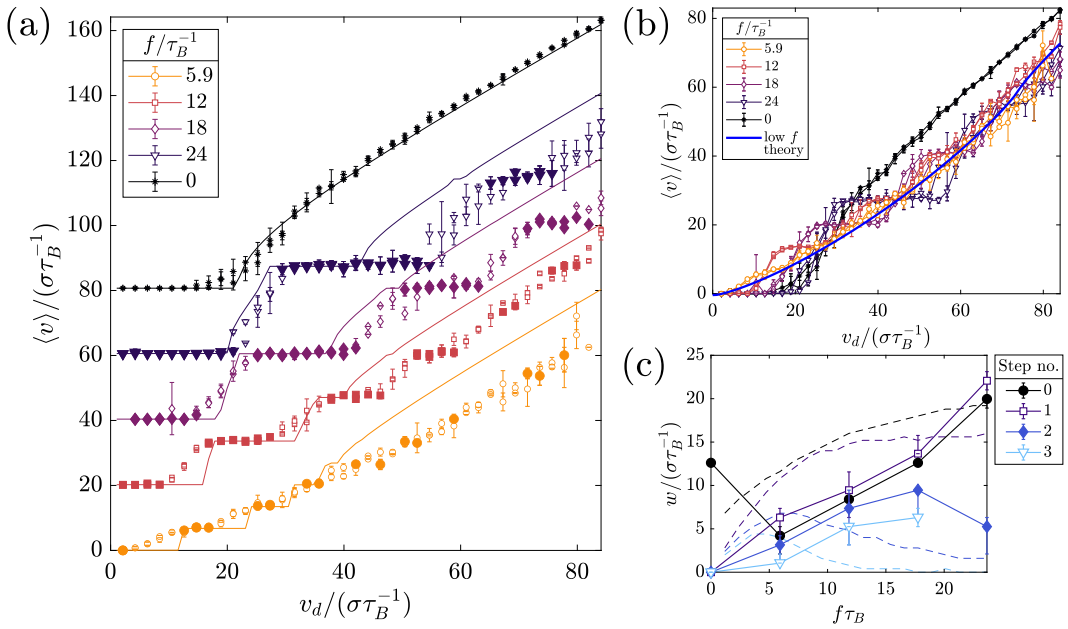


Figure 6.6: (a) $\langle v\rangle$ of a chain of 16 particles in an oscillating landscape with $A = 0$ (black stars) and $A = 0.75$, $f = 6\,\tau_B^{-1}$ (yellow circles) to $24\,\tau_B^{-1}$ (navy triangles), shifted upwards for clarity. Large filled points highlight the steps. Lines show $\langle v\rangle$ for a theoretical deterministic rigid chain with the same v^*, f and A. (b) $\langle v\rangle$ from the same experiments as in (a), but plotted on top of each other. The blue line shows the numerical integration of equation 6.12. (c) Width of the 0th (black circles) to 3rd (light blue triangles) step versus frequency. Dashed lines show the rigid chain theory.

6.4.2 Modified low frequency theory

In this section, we explain the deviation between the step positions in the experiments and the rigid chain theory using the low frequency framework introduced in section 6.2.1. Strictly speaking, the low frequency regime applies when $f \ll v^*/\lambda$, which is only true of the experiments with $f = 6\tau_B^{-1}$ and $f = 12\tau_B^{-1}$. Nevertheless, we use the low frequency regime because it allows to account for the non-linear dependence of the critical velocity of our chains with increasing substrate depth, shown in figure 6.3.

To this end, we assume that the average velocity of the chain at a substrate depth of u follows the square-root law

$$\langle v\rangle = \sqrt{v_d^2 - v^*(u)^2}, \tag{6.11}$$

where $v^*(u)$ is the non-linear function relating the critical velocity to the instantaneous substrate depth $u(t) = V_s(1 + A\sin 2\pi ft)$. We estimate $v^*(u)$ by fitting the measured critical velocity at

different substrate potentials, shown in figure 6.3, with the power law $v^* \approx 1.92u^{2.39}$. While the power law has no theoretical basis, it describes the critical velocity at high V_s better than the hard sphere kink theory or a linear fit. In the low frequency limit, the average velocity of the chain is given by equation 6.7, which averages equation 6.11 over time as follows:

$$\langle v \rangle = f \int_0^{f^{-1}} \sqrt{v_d^2 - v^* \left(u(t)\right)^2} dt. \tag{6.12}$$

We calculate this integral numerically. The blue line in figure 6.6b shows the result. The modified low frequency theory accurately describes the average velocity at the lowest frequency of $f = 6\,\tau_B^{-1}$, and predicts the step centres of the higher frequencies. From this agreement, we can conclude that the non-linearity of the critical velocity is responsible for the deviation of the step positions from the rigid chain theory.

However, the modified low frequency theory does not explain the existence of large high order steps at high frequencies of $f = 18$ and $24\,\tau_B^{-1}$, which we expect to be in the high frequency limit defined by $f > v^*/\lambda = 18\,\tau_B^{-1}$. In order to rationalise these wide steps, we now examine the dynamics of the chains in each experiment.

6.4.3 Kink dynamics

We showed in chapters 4 and 5 that the friction (and hence average velocity) of a chain is governed by its kink density. In this section, we therefore analyse the dynamics of chains in oscillating substrates in terms of their kinks and anti-kinks. Kinks are tracked using the algorithm described in section 5.3.3, with the modification that anti-kinks are not filtered out.

Figure 6.7 shows typical trajectories from the experiment with $N = 16, A = 0.75, f = 18\,\tau_B^{-1}$ and driving velocities corresponding to the beginning, middle and end of the first mode-locked step. At the beginning of the step (figure 6.7a), a single kink is nucleated at the start of each period and then travels through the chain, reaching the other end more than one period later such that there is always at least one kink in the chain. This mode of motion resembles the dynamics of flexible chains in a strong static substrate described in chapter 5. The kink dynamics are markedly different at the end of the step (figure 6.7c). Here, the chain's movement from one minimum to the next is accompanied by the nucleation of several alternating kinks and anti-kinks. The difference between these two modes of motion, which we refer to as the pure

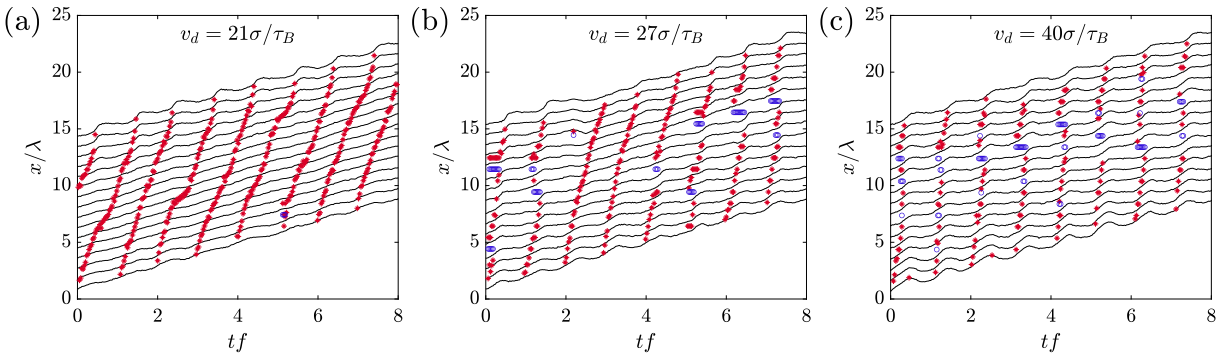


Figure 6.7: Trajectories from the experiment with $N = 16, A = 0.75, f = 18\,\tau_B^{-1}$ and (a) $v_d = 21\,\sigma/\tau_B$, (b) $v_d = 27\,\sigma/\tau_B$, (c) $v_d = 40\,\sigma/\tau_B$, corresponding to the beginning, middle and end of the first step. The time is scaled by the frequency so that the maximum trap strength occurs every integer. Black lines show the particle positions, red stars show kinks and blue circles show anti-kinks.

kink or mixed kink modes, is highlighted in figures 6.8a and b. In the mixed kink mode, the number of kink–anti-kink pairs varies, but there is always one more kink than anti-kink, such that the overall effect is to compress the chain slightly. In the middle of the first step (figure 6.7b), the chain randomly switches between the two modes.

A similar transition between the pure and mixed kink modes of motion occurs across the second step. Figure 6.9 shows trajectories from a driving velocity between the first and second steps, at the beginning of the second step, and at end of the second step. Between the steps (figure 6.9a), the chain either moves one wavelength per period via the mixed kink mode, or it nucleates two pure kinks per period and so moves two wavelengths. At the beginning of the second step (figure 6.9b), the chain mostly alternates between the two modes, nucleating one mixed kink followed by one pure kink each period. By the end of the second step (figure 6.9c), the chain almost exclusively nucleates two mixed kinks per period.

In order to quantify the proportion of pure kink versus mixed modes, we classify each defect

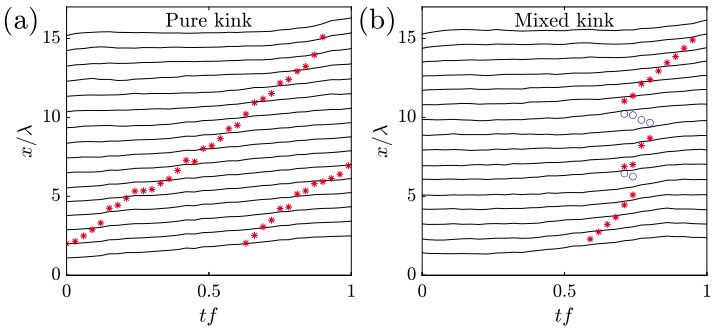


Figure 6.8: Example of a pure kink (a) and mixed kink (b). Blue circles show anti-kink positions and red stars show kinks.

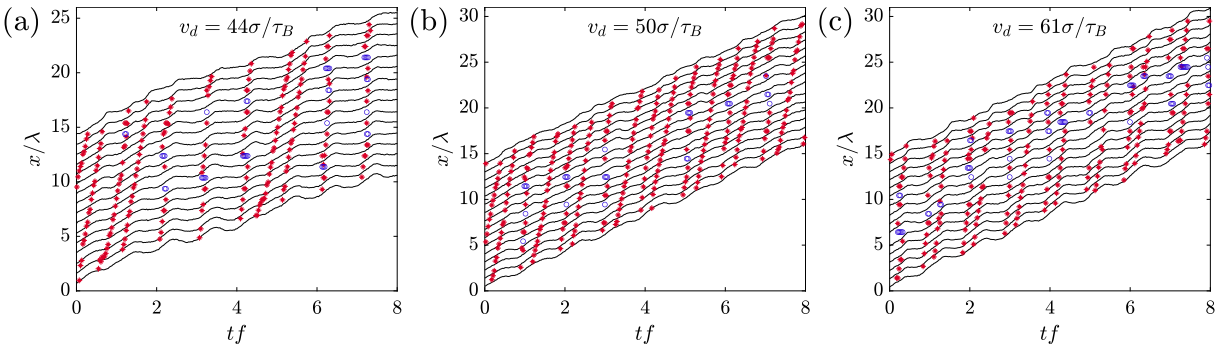


Figure 6.9: Trajectories from the experiment with $N = 16, A = 0.75, f = 18\,\tau_B^{-1}$ and (a) $v_d = 44\,\sigma/\tau_B$, in between the first and second step, (b) $v_d = 50\,\sigma/\tau_B$, at the start of the second step, and (c) $v_d = 61\,\sigma/\tau_B$, at the end of the second step. The time is scaled by the frequency so that the maximum trap strength occurs every integer. Black lines show the particle positions, red stars show kinks and blue circles show anti-kinks.

nucleated in the chain as either mixed or pure depending on whether the percentage of anti-kink positions in the defect is more or less than 10% of the total number of kink and anti-kink positions in the defect. Figure 6.10a and b show the proportion of defects which are pure kinks as a function of driving velocity at different frequencies and amplitudes. The experiments with $A = 0$ and 0.25 both have a high proportion of pure kinks at all driving velocities, confirming that these experiments have similar kink dynamics to the experiments described in chapter 5.4.3. In the experiments with $A \geq 0.5$, the proportion of pure kinks is close to one at low driving velocities, before the beginning of the first step, but then drops to zero across the first step. The proportion of pure kinks then peaks at the beginning of all subsequent steps, while the mixed kink mode dominates at the end of each step. The same behaviour is seen in the experiments with different frequencies, shown in figure 6.10b, confirming that the example dynamics shown

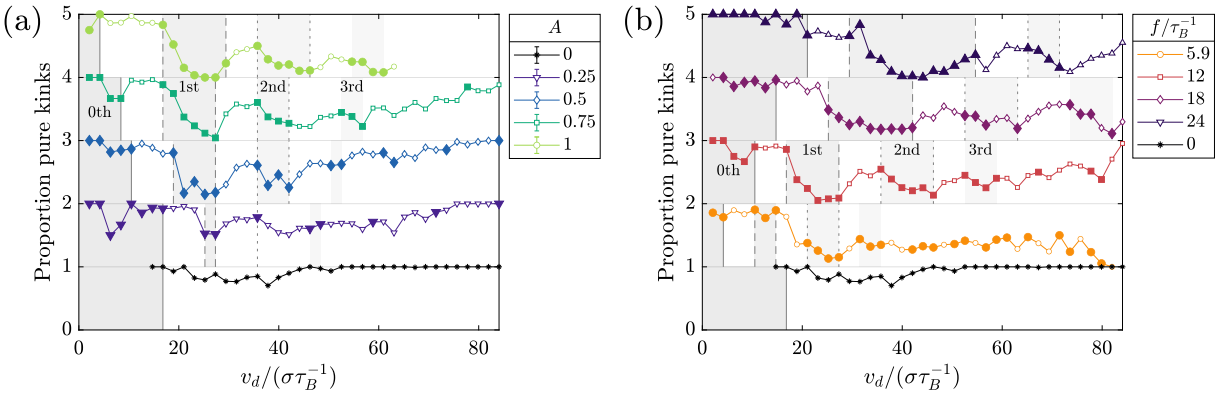


Figure 6.10: Proportion of defects made of more than 90% kinks at different amplitudes (a) and frequencies (b). Different experiment are shifted upwards by 1 for clarity. Colours and symbols are the same as in figures 6.5 and 6.6. The steps are marked with large filled points and grey rectangles bordered with a solid line (0th step), dashed line (1st), dotted (2nd) and no line (3rd).

in figures 6.7 and 6.9 are representative of the other high amplitude experiments.

As well as being more likely at different driving velocities, pure and mixed kinks move at different speeds. Figure 6.11a shows the average velocity of pure and mixed kinks with different anti-kink concentrations as a function of the driving velocity. The average velocity increases with increasing anti-kink concentration and there is no discernable relationship between the velocity and the position of the mode-locked steps. The velocity of the pure kinks (defined as containing $< 10\%$ anti-kinks) increases linearly with increasing driving velocity with a gradient of 12, similar to the kink velocity measured in chapter 5.4.3, where we showed that the kink velocity was equal to the driving velocity times the kink width. The mixed kinks containing 30% anti-kinks move twice as quickly as the pure kinks, suggesting that the presence of anti-kinks effectively doubles the kink width. Figure 6.8b shows how this is possible; each kink in the anti-kink pair moves forward at the same speed as an ordinary kink, while its corresponding anti-kink moves backwards, but because there are multiple kinks moving at once, the overall defect moves faster.

We now investigate whether pure and mixed kinks tend to be nucleated at different phases, ϕ, of the substrate oscillation cycle – that is, whether the kinks are most likely to be nucleated when the substrate depth is at its maximum value ($\phi = 0$ and 2π), in the process of decreasing ($\phi = \pi/2$), near its minimum value ($\phi = \pi$), or in the process of increasing ($\phi = (3/2)\pi$). Figure 6.11b shows the average nucleation phase, $\phi = 2\pi(tf - \lfloor tf \rfloor)$, where t is the time at which a kink first appears at the beginning of the chain, as a function of driving velocity. Vertical

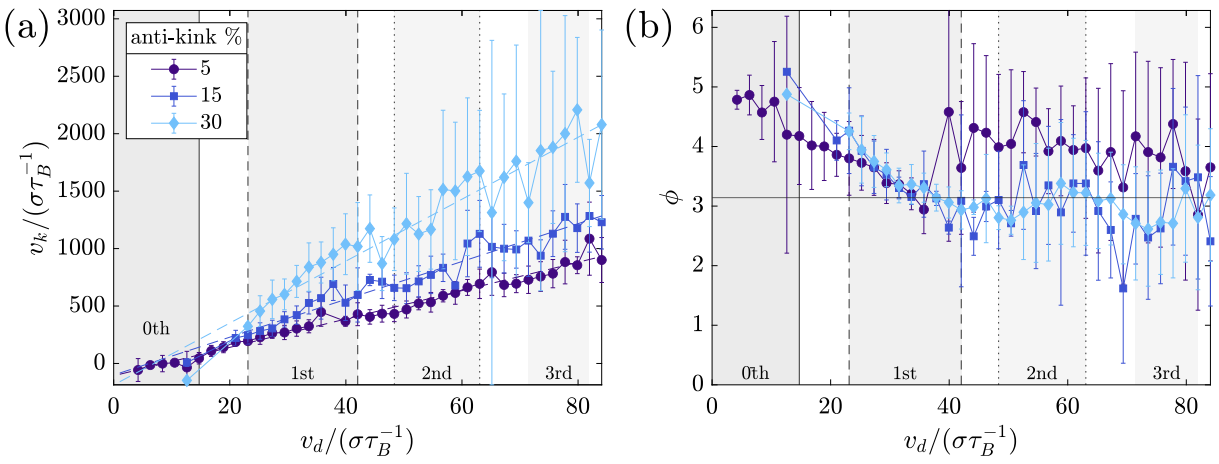


Figure 6.11: (a) Average velocity and (b) nucleation phase of pure kinks with an anti-kink percentage of 0-10% (dark blue circles) and mixed kinks with an anti-kink percentage of 10-20% (blue squares) and 20-40% (light blue diamonds). Dashed lines in (a) are linear fits. The 0th, 1st, 2nd and 3rd steps are marked with grey rectangles bordered by a solid, dashed, dotted and no line respectively.

lines mark the location of each step. As the driving velocity increases, the phase at which both the pure and mixed kinks are nucleated initially decreases, reaching π near the end of the first step. There is initially very little difference between the nucleation phase of the pure and mixed kinks. After the end of the first step, however, the nucleation phase of the mixed kinks reaches a plateau close to π, the phase where the substrate depth is minimised, while the pure kinks are nucleated later. This shows that after the end of the first step, when more than one kink must be nucleated per period, the chain tends to nucleate mixed kinks first, when the substrate depth is small, followed by pure kinks when the substrate depth increases again. This difference shows that there is a fundamental difference between the pure and mixed kink modes.

We have shown that the chain has two distinct modes of motion defined by the nucleation of either a pure kink or a mixed kink. The pure kink mode is slower, more favourable at the beginning of each step, and tends to be nucleated later than the mixed kinks when multiple kinks are nucleated per period. All of these factors suggest that the pure and mixed kink modes represent two different energy pathways. The relative probabilities of the two modes suggest that the pure kink mode has a smaller activation barrier at low driving velocities and when the substrate depth is increasing. The mixed kink mode is otherwise more favourable. The ability of the chain to adopt either of these two very different pathways may explain the unusually large step widths observed in all of our experiments.

6.5 Conclusions

We have shown that the friction between a flexible chain and a sinusoidal substrate may be reduced by oscillating the substrate depth as a result of synchronisation between the chain's average velocity and the oscillations of the substrate. The largest friction reduction occurs at low driving velocities and at the beginning of a first order mode-locked step, whereas increases in friction were observed at high driving velocities. The position and width of the mode locked steps were measured as a function of the oscillation frequency and amplitude. At all frequencies measured, wide steps with an order of up to three were observed, in contrast to the rigid chain theory. The step positions were well described by a numerical modification of the low-frequency limit which accounted for the non-linear dependence of the critical velocity on the substrate depth. We analysed the kink dynamics of the chains at different frequencies and

driving velocities, observing a novel mode of motion in which the kink nucleated a mixture of kinks and anti-kinks. This type of defect moved twice as fast as a pure kink. We observed a transition from the pure kink mode of motion to the anti-kink mode across the each mode-locked step. We hypothesise that the chains' ability to switch between these two modes enables them to support such wide mode-locked steps.

Acknowledgments

This work was done in collaboration with Josh Abbot-Scott. Joseph Hutchinson and Arran Curran are thanked for useful discussions.

Chapter 7

Time-delayed feedback of a colloidal particle in an optical trap

Abstract

In this chapter, we analyse experiments and simulations in which a colloidal dumbbell particle, acting as a particle on a ring, is followed by a repulsive optical trap controlled by a time-delayed feedback protocol. The dynamics are described by a persistent random walk, with a transition from predominantly diffusive to driven behaviour at a critical delay time. We model the dynamics in the short and long delay regimes using stochastic delay-differential equations and derive a condition for stable driven motion. We study the stochastic thermodynamic properties of the system, finding that the maximum work done by the trap coincides with a local minimum in the mutual information between the trap and the particle position at the onset of stable driven dynamics.

7.1 Introduction

Maxwell's demon uses information to create a temperature gradient in a heat bath without performing any work, seemingly violating the second law of thermodynamics [248]. The demon observes the velocity of molecules in two chambers and, by opening and closing a hole between the chambers, allows only hot molecules to pass from left to right, and only cold molecules from right to left, thus increasing the temperature difference between the chambers without performing any work. This paradox was resolved by the realisation that there is an entropy change associated with the processes of acquiring information [249], leading to the birth of information thermodynamics [114].

In any experimental realisation of Maxwell's demon, there is always a time delay between taking a measurement, performing information processing, and then implementing the feedback, often to the detriment of the feedback engine's efficiency [109]. However, time delays can also be beneficial, for example in the use of delayed feedback to stabilise chaotic motion in engineering applications [250]. When delayed feedback is applied continuously, the system is described by a stochastic delay differential equation (SDDE); a general class of equations which describe any system whose evolution depends on its state some delay time in the past. There are many examples of time-delayed systems across the scientific disciplines [251], including biological motors [9, 252, 253], communication and neurological networks [254, 255], and even financial markets [256]. Depending on the method by which the delayed feedback is implemented, time delays can either stabilise [257, 258] or amplify chaotic motion [259], produce stochastic resonances [260], or display other types of complex dynamics [261, 262].

Colloidal particles are often seen as the paradigmatic feedback engine due to the ease of obtaining single particle information and applying feedback via optical traps after a short time delay relative to the particle's motion. Colloidal feedback experiments have successfully demonstrated the possibility of information to work conversion with very high efficiency [108, 263, 264] or power [110, 265, 266], investigated the effect of delay time [109] and measurement error [267], and provided experimental confirmation of several important theoretical findings in information thermodynamics [111, 268]. These experiments all apply feedback in discrete steps. Continuous time delayed feedback experiments are less common [110], despite simulations predicting many interesting uses. These include enhancing or reversing transport in washboard

potentials [269, 270], suppressing diffusion using attractive harmonic traps [271], and forming travelling bands of driven colloids using repulsive Gaussian traps [272]. Kopp *et al.* [273] recently showed that a single particle interacting with a repulsive Gaussian trap controlled via the same feedback protocol as [272] also displays driven motion.

An experimental one-dimensional equivalent of Kopp *et al.*'s simulation [273], consisting of a single particle interacting with a repulsive optical trap, was performed by Liu *et al.* [274], a former PhD student in our group. Here, we analyse this data, observing a transition from diffusive to driven dynamics with increasing time delay similar to the results of [272, 273]. We characterise the dynamics across this transition and describe the diffusive and driven regimes using the framework of stochastic delay differential equations. We then analyse the mutual information and work done on the system.

7.2 Theory

7.2.1 Particle on a ring

In this chapter, we create a feedback experiment where a particle on a ring interacts with a repulsive optical trap, as illustrated in figure 7.1. The dynamics of the particle are governed by a 1D Langevin equation in *polar* coordinates. In order to convert the position of the particle from Cartesian to polar coordinates, we use

$$dx_P + dy_P = dr_P + r_P d\theta_P \tag{7.1}$$

The radius of the ring, r_P, is fixed, while the angle, θ_P evolves according to the Langevin equation

$$r_P \frac{d\theta_P}{dt} = \frac{1}{\zeta} F_T + \xi(t), \tag{7.2}$$

where ζ is the drag constant of the particle, $\xi(t)$ is Gaussian white noise with $\langle \xi(t) \rangle = 0$, $\langle \xi(t)\xi(t') \rangle = 2(k_B T/\zeta)\delta(t - t')$, and F_T is the force from the trap. Each term in this expression has units of $\mathrm{m\,s^{-1}}$; in order to convert to $\mathrm{rad\,s^{-1}}$, we define an angular drag constant, $\zeta_{\mathrm{rad}} = \zeta r_P^2$ and an angular noise term, ξ_{rad}, with $\langle \xi_{\mathrm{rad}}(t)\xi_{\mathrm{rad}}(t') \rangle = (2k_B T/\zeta_{\mathrm{rad}})\delta(t - t')$. This gives the following

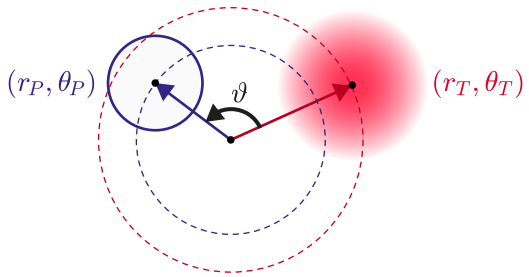


Figure 7.1: Coordinates of the particle, (r_P, θ_P), feedback-controlled optical trap, (r_T, θ_T), and the angle between them, ϑ.

equation of motion:

$$\frac{d\theta_P}{dt} = \frac{1}{\zeta_{\text{rad}}}(r_P F_T) + \xi_{\text{rad}}(t), \tag{7.3}$$

where $F_{\text{rad}} = (r_P F_T)$ is the force of the particle in units of $\text{kg}\,\text{rad}\,\text{s}^{-2}$. From now on, we will only use terms in units of radians unless stated otherwise, and drop the rad subscript on F_{rad} and ζ_{rad}.

The optical trap moves on a ring of fixed radius r_T which is slightly larger than r_P, and is at an angular distance $\vartheta = \theta_P - \theta_T$ from the particle. It has the repulsive Gaussian potential described by equation 2.21. Converting this to polar coordinates gives a trap force of

$$F(\vartheta) = k r_P r_T \sin(\vartheta) \exp\left[-\frac{k}{2V_0}(r_P^2 + r_T^2)\right] \exp\left[\frac{k}{V_0} r_P r_T \cos(\vartheta)\right], \tag{7.4}$$

where k is the trap stiffness, V_0 is the trap depth, and F has units of $\text{kg}\,\text{rad}\,\text{s}^{-2}$. It is convenient to define the following constants:

$$K = \frac{k}{\zeta} r_P r_T \exp\left[-\frac{k}{2V_0}(r_P - r_T)^2\right] \qquad \text{and} \qquad \phi = \sqrt{\frac{V_0}{k r_P r_T}}. \tag{7.5}$$

Here, ϕ can be interpreted as the trap width in radians, while K is a frequency proportional to the trap stiffness. K is an angular equivalent of the corner frequency of a trap, $f_c = k/(2\pi\zeta)$, which defines the frequency at which the particle explores the trap [82]. These constants simplify the trap force in equation 7.4 to

$$F(\vartheta) = \zeta K \sin\vartheta \exp\left(\frac{1 - \cos\vartheta}{\phi^2}\right). \tag{7.6}$$

When the trap width is small compared to the particle radius ($\phi \ll r_P$), we can apply the small

angle approximation to reduce equation 7.6 to the following Gaussian function:

$$F \approx \zeta K \vartheta \exp\left(-\frac{\vartheta^2}{2\phi^2}\right). \tag{7.7}$$

Note that ϑ must always be within $[-\pi, \pi]$ as this expression is not periodic. The maximum trap force occurs when $\vartheta = \phi$ and has a value of $e^{-1/2}\zeta K\phi$, giving a maximum velocity of $v_m = e^{-1/2}K\phi$.

7.2.2 Time-delayed feedback

We use a feedback protocol to control the position of the repulsive optical trap. We measure the position of the particle at time t, then wait a certain delay time τ before moving the trap to the particle's position, such that

$$\theta_T(t) = \theta_P(t - \tau). \tag{7.8}$$

The feedback is applied in discrete steps, but if we assume that it is continuous on the timescale of the particle, we can write the Langevin equation in equation 7.3 as the following so-called stochastic delay-differential equation (SDDE):

$$\frac{d\theta_P}{dt} = \zeta^{-1}F(\theta_P(t) - \theta_P(t - \tau)) + \xi(t). \tag{7.9}$$

The delay term, $\theta_P(t-\tau)$, introduces an extra level of complexity into the dynamics which rules out the standard techniques for predicting the behaviour of Langevin systems. Instead, we use two different approaches to analysing delay differential equations, both of which are valid in the limit of small delay times.

In the first approach, Guillouzic *et al.* [275] showed that any delay-differential equation can be approximated by a delay-free Langevin equation in the limit of small delay times ($\tau \to 0$). Using their method, we obtain the following approximate equation of motion:

$$\frac{d\theta_P}{dt} \approx \zeta^{-1}F_a(\theta_P) + G_a\xi(t), \tag{7.10}$$

where the noise amplitude multiplier, G_a, and approximate force, $F_a(x)$, are given by

$$G_a = 1 - \frac{\tau}{\zeta}\left(\frac{\partial}{\partial\theta_T}F(\theta_P,\theta_T)\right)_{\theta_P=\theta_T} \qquad \text{and} \qquad F_a(\theta_P) = G_a F(\theta_P = \theta_T). \tag{7.11}$$

Substituting in the approximate Gaussian trap force (equation 7.7) gives $G_a = (1 + K\tau)$ and $F_a = 0$. The equation of motion is therefore purely diffusive in the limit of small delay times, with an enhanced long-time diffusion coefficient of

$$D_L = D\left(1 + K\tau\right)^2, \tag{7.12}$$

where $D = k_B T/\zeta$ is the short-time diffusion coefficient. Increasing the corner frequency, K, or the delay time, τ, therefore increases the long-time diffusion coefficient of the particle.

The second approach improves upon this approximation using the work of Ando *et al.* [271]. They simulated a Brownian particle in an attractive harmonic trap controlled by the same feedback protocol as us ($\theta_T(t) = \theta_P(t-\tau)$). Our experiment is equivalent to theirs, but with a repulsive rather than attractive trap, in the the limit of small ϑ where our trap is approximately harmonic. Ando *et al.* [271] showed that the long-time diffusion coefficient of a particle in a harmonic trap is given by

$$D_L = \lim_{t\to\infty}\frac{D}{t}\int_0^t y(s)^2 ds, \tag{7.13}$$

where $y(s)$ is the stationary solution to the deterministic version of their SDDE from Kuchler and Mensch [276],

$$y(t) = \sum_{n=0}^{\lfloor t/\tau\rfloor}\frac{(-K)^n}{n!}\left(t - n\tau\right)^n \exp\left(K(t-n\tau)\right). \tag{7.14}$$

When the trap is attractive, as in Ando *et al.*'s simulations, so K is negative, equation 7.14 converges to a constant at all τ [271] and the system is always diffusive. When K is positive – the case in our experiments – equation 7.14 converges to a constant of $(1 - K\tau)^{-1}$ only at short delay times of $\tau < K^{-1}$. In this short delay regime, the system is purely diffusive with a long-time diffusion coefficient of

$$D_L = \frac{D}{(1-K\tau)^2}. \tag{7.15}$$

D_L increases with increasing τ until $\tau \to K^{-1}$, at which point equation 7.15 diverges. When the delay time is larger than K^{-1}, equation 7.14 diverges exponentially, with the implication that a diffusive state is not stable. Note that equation 7.15 is related to equation 7.12 via a Taylor expansion.

7.2.3 Stochastic thermodynamics

Stochastic thermodynamics is the study of the thermodynamic properties of stochastic, mesoscopic systems. Just as statistical mechanics links the macroscopic thermodynamic properties of a system to the ensemble average of its microstates via the partition function, so too can we measure thermodynamic quantities in a mesoscopic system from the average of its stochastic trajectories [114].

Heat and work

An archetypal mesoscopic system consists of a particle in a solvent which obeys the general Langevin equation

$$\zeta \frac{dx}{dt} = F(x,t) + \xi(t), \tag{7.16}$$

where the total force, $F(x,t)$, arises from a combination of non-conservative driving forces, $f(x,t)$, and conservative forces arising from a potential, $-\left(\frac{\partial U}{\partial x}\right)_t$ [277]. The energy change of the particle is

$$dU = \left(\frac{\partial U}{\partial x}\right)_t dx + \left(\frac{\partial U}{\partial t}\right)_x dt. \tag{7.17}$$

The rate of work done on the particle is a combination of the work done by applying a force to the particle, $f(x,t)dx$, and the work done by changing the potential, $\left(\frac{\partial U}{\partial t}\right)_x dt$ [277]:

$$dw = \left(\frac{\partial U}{\partial t}\right)_x dt + f(x,t)dx = dU + F(x,t)dx. \tag{7.18}$$

The second expression arises from substituting equation 7.17 into equation 7.18.

The particle is in contact with a solvent, which acts as a heat reservoir. Heat transfer

occurs through a combination of thermal fluctuations, $\xi(t)$, and drag, $\zeta dx/dt$. The rate of heat transfer from the particle to the solvent is therefore defined as [278]

$$dq = \left(-\zeta\frac{dx}{dt} + \xi(t)\right)dx = F(x,t)dx. \tag{7.19}$$

The second expression can be found by substituting in equation 7.16.

Combining equations 7.18 and 7.19 gives a stochastic thermodynamics equivalent of the first law of thermodynamics [278]:

$$dU = dw - dq. \tag{7.20}$$

Note that stochastic thermodynamics uses the opposite sign convention for dq to standard thermodynamics because it usually deals with systems which dissipate work into heat, rather than engines which convert heat into work.

In order to find the average work done or heat transferred over a given protocol, we must find the average integration of dq and dw over all possible trajectories of the system during that protocol. The integral over each trajectory is performed as follows [14]:

$$q(\mathbf{x}) = \int_{t_i}^{t_f} F(x(t),t)\dot{x}(t)dt = \sum_{n=1}^{N} F(x_n,t_n)\frac{x_{n+1}-x_{n-1}}{t_{n+1}-t_{n-1}}, \tag{7.21}$$

$$w(\mathbf{x}) = q(\mathbf{x}) + \Delta U = \sum_{n=1}^{N} F(x_n,t_n)\frac{x_{n+1}-x_{n-1}}{t_{n+1}-t_{n-1}} + U\left(\frac{x_{N+1}+x_N}{2}\right) - U\left(\frac{x_1+x_0}{2}\right). \tag{7.22}$$

When a particle is driven with a constant force, f, which causes it to move at a constant average velocity, $\langle v\rangle = f/\zeta$, the average rate of work done on the particle is given by [279]

$$\langle \dot{w}\rangle = \zeta\langle v\rangle^2. \tag{7.23}$$

Driving a particle with a constant force is the most efficient way of moving it at a constant average velocity [279]. All of the work done on the particle is converted into motion and then dissipated as heat into the solvent.

Information

During a feedback process, a measurement device gathers information about the state of the system and uses that information to apply feedback. As the device performs a measurement, its state may change, leading to a change in its entropy. The thermodynamics of the feedback process therefore depends not just on the system and surrounding solvent, but also the measurement device. By accounting for the entropy change associated with a measurement, it can be shown that the average work done by a feedback process is bounded by [280]

$$W \geq \Delta F - k_B T I, \tag{7.24}$$

where ΔF is the change in the free energy of the system and I is the mutual information between the states of the system at time t_0, x, and the states of the device, y, at the end of the measurement process at time t_m. The mutual information is defined as [114]

$$I = \sum_{x,y} p(x,y) \ln \left(\frac{p(x,y)}{p(x)p(y)} \right), \tag{7.25}$$

where $p(z)$ is the probability of state z. If x and y are continuous, as in our experiments, the sum is replaced by the integral

$$I = \iint dxdy \; p(x,y) \ln \left(\frac{p(x,y)}{p(x)p(y)} \right), \tag{7.26}$$

where $p(z)$ now represents a probability density function. I is a measure of how narrowly $p(x,y)$ is distributed; it is largest when $p(x,y)$ has a single sharp peak, and smaller when $p(x,y)$ has several broad peaks.

In our feedback experiment, there is a delay time τ between the start and end of the measurement. The state of the system is therefore the particle position at time t, while the state of the measurement device is the particle position at time $t - \tau$, which we set as the trap position at time t. The mutual information is given by

$$I = \int_{-\pi}^{\pi} \int_{-\pi}^{\pi} d\theta_P d\theta_T p(\theta_P|\theta_T) p(\theta_T) \ln \left(\frac{p(\theta_P|\theta_T)}{p(\theta_P)} \right), \tag{7.27}$$

where we have replaced the joint probability of θ_P and θ_T with the conditional probability of

θ_P at a given θ_T using $p(\theta_P, \theta_T) = p(\theta_p|\theta_T)p(\theta_T)$. If we assume that all positions around the ring have the same energy, so are equally probable, then $p(\theta_P) = p(\theta_T) = (2\pi)^{-1}$ for all $\theta_{P/T}$. Furthermore, $p(\theta_P|\theta_T)$ only depends on the angle between the particle and the trap, $\vartheta = \theta_P - \theta_T$, so we can replace $p(\theta_P|\theta_T)$ in equation 7.27 with $p(\vartheta)$ by integrating over $d\theta_T$. This reduces equation 7.27 to

$$I = \int_{-\pi}^{\pi} d\vartheta p(\vartheta) \ln p(\vartheta) + \ln(2\pi). \tag{7.28}$$

In order to illustrate how I depends on the delay time, τ, it is useful to consider the case of free diffusion. In the small τ limit when $4D\tau/\pi^2 \ll 1$, so that particle has not had time to diffuse around the ring, ϑ has the following Gaussian probability distribution:

$$p(\vartheta) = \frac{1}{\sqrt{4\pi D\tau}} \exp\left(\frac{-\vartheta^2}{4D\tau}\right), \tag{7.29}$$

which leads to a mutual information of

$$I \approx \frac{1}{2}\left[\ln\left(\frac{\pi}{D}\right) - 1 - \ln(\tau)\right]. \tag{7.30}$$

Conversely, in the long τ limit, all positions on the ring become equally likely, so $p(\vartheta) \to (2\pi)^{-1}$ and $I \to 0$ when $\tau \to \infty$. The mutual information therefore decreases linearly with $\ln \tau$ until it reaches a plateau at $I = 0$, as shown in figure 7.2.

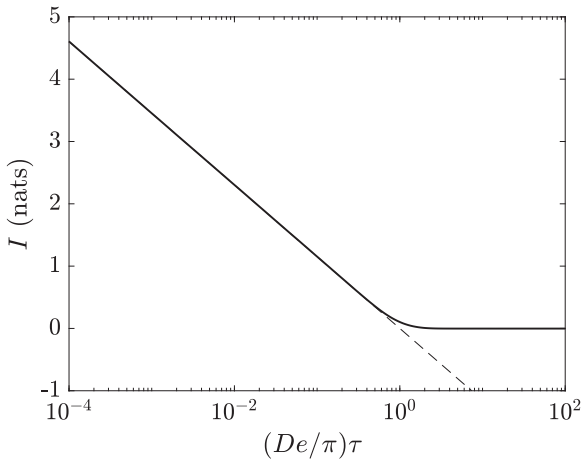


Figure 7.2: Mutual information between $\theta_P(t)$ and $\theta_P(t-\tau)$ for a freely diffusing particle on a ring. The solid line is the exact value and the dashed line is equation 7.30

7.3 Experimental methods

In this chapter we use experimental data from the PhD thesis of Liu *et al.* [274]. In this section we first describe the particles and experimental setup used in these experiments, then we show the results of several calibration experiments used to calculate the drag constant, ζ, corner frequency, K, and trap width, ϕ, defined in section 7.2.1. Finally, we describe the Brownian dynamics simulations used to supplement the experimental results.

7.3.1 Colloidal dumbbell particles and experimental setup

Figure 7.3 shows a diagram of the microscope and optical tweezing setup used for these experiments [274]. The sample is illuminated from above and a bright-field image is formed using the remote refocusing system and the CMOS camera [281]. The IR laser is controlled using an SLM (spatial light modulator), which we use to create two optical traps which trap the particle from below.

Figure 7.4a shows an SEM image of the dumbbell particles used here to act as a particle on a ring. The smaller lobe is made of made of melamine formaldehyde (MF), while the larger lobe is 3-trimethoxysilyl-propylmethacrylate (TPM). They have refractive indices of 1.68 and 1.52 respectively. When placed in tetralin, which has a refractive index of 1.54, the MF lobe has a positive refractive index mismatch so experiences an attractive Gaussian potential from

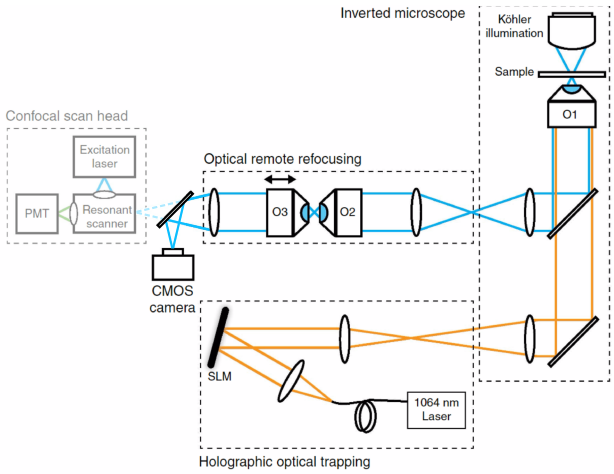


Figure 7.3: Optical tweezing and microscopy setup reproduced from [274]. Blue lines show the imaging pathway and orange shows the laser.

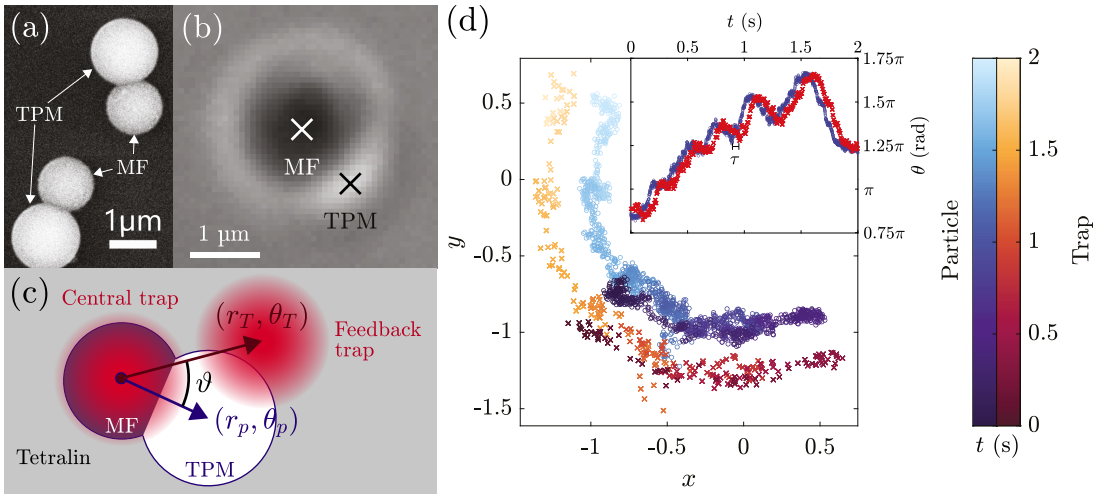


Figure 7.4: (a) SEM image of a dumbbell. (b) Example image from the experiments. (c) Diagram of the experimental setup, showing the MF lobe (dark grey) and TPM lobe (white) of the dumbbell, the tetralin solvent (light grey), the two optical traps (red). Blue arrows show the coordinates of the central trap, (r_T, θ_T), and the TPM lobe, (r_p, θ_p), relative to the central trap. (d) Example trajectory of the TPM lobe (blue) and feedback trap (red). In the main plot, positions are in Cartesian coordinates from $t = 0\,\mathrm{s}$ (light) to $t = 2\,\mathrm{s}$ (dark), and in the inset the angle $\theta_{p,T}$ is plotted over the same time period.

optical traps, while the TPM lobe has a negative refractive index mismatch so feels a repulsive potential.

Figure 7.4c shows a diagram of the experimental setup and the coordinate system. The central trap is stationary throughout the experiment. The MF lobe sits in a centre of this trap while the TPM lobe rotates around it, acting as a particle on a ring of radius $r_P = 1.23\,\mu\mathrm{m}$. We track the TPM lobe at 1000 fps and, after a delay time τ, place the feedback trap on top of the TPM lobe at

$$r_T(t = 0) = 1.3 r_P(t = -\tau) \qquad \text{and} \qquad \theta_T(t = 0) = \theta_P(t = -\tau). \tag{7.31}$$

The MF lobe is far away enough that it does not interact with the feedback trap, but the TPM lobe is repelled and attempts to move around the ring away from the trap. We continue to update the position of the feedback trap every 6.4 ms according to the feedback protocol in equation 7.31. Figure 7.4d illustrates the feedback protocol with an example trajectory. The positions of the trap in (x, y) are shown in the main plot and the positions in θ are shown in the inset. The trap moves around a larger radius than the particle and follows its position in θ after a delay time τ.

Figure 7.4b shows an example image from one of the experiments. The dark spot sur-

rounded by a light ring is the MF lobe and the light spot with a dark ring is the TPM lobe. The TPM lobe was tracked in real time by thresholding the image and calculating its centre of mass. The brightness of the TPM lobe occasionally falls below the threshold when it moves out of the imaging plane, in which case the algorithm returns the centre of the image. As a result, the feedback trap is temporarily placed in the centre of the image, on the MF lobe. This occurs most often in the short delay time experiments.

7.3.2 Measurement of the background potential and drag constant

From this point onwards we ignore the MF lobe and treat the TPM lobe as a particle confined to a ring. We measure the potential around the ring and the particle's drag constant using a free diffusion experiment with no feedback trap. Figure 7.5a shows the particle's probability distribution in xy, showing that the particle diffuses around the whole circumference of the ring, albeit with a slight bias to the bottom left. In figure 7.5b, we calculate the potential around the ring using $\beta U(\theta) = -\ln p(\theta)$, finding a potential difference around the ring of $\Delta U(\theta) \approx 3.5 k_B T$. This background potential is an order of magnitude weaker than the potential of the feedback trap, so should have a small effect on the experiments.

To obtain the friction coefficient, we measure the mean squared displacement in r, θ and xy, shown in figure 7.5c. The MSD in θ is linear up to 10 s and has a drag constant of $\zeta = 6.64 \times 10^{-8}\,\mathrm{kg\,\mu m^2\,s^{-1}}$. When multiplied by r_P^2, it falls on top of the MSD in xy, confirming our use of $\zeta_{\mathrm{rad}} = r_P^2 \zeta_{\mathrm{cart.}}$ in equation 7.3. The MSD in r reaches a plateau at $0.04\,\mu\mathrm{m}^2$, confirming that the particle is strongly confined to the ring so we can assume that the system is one-dimensional.

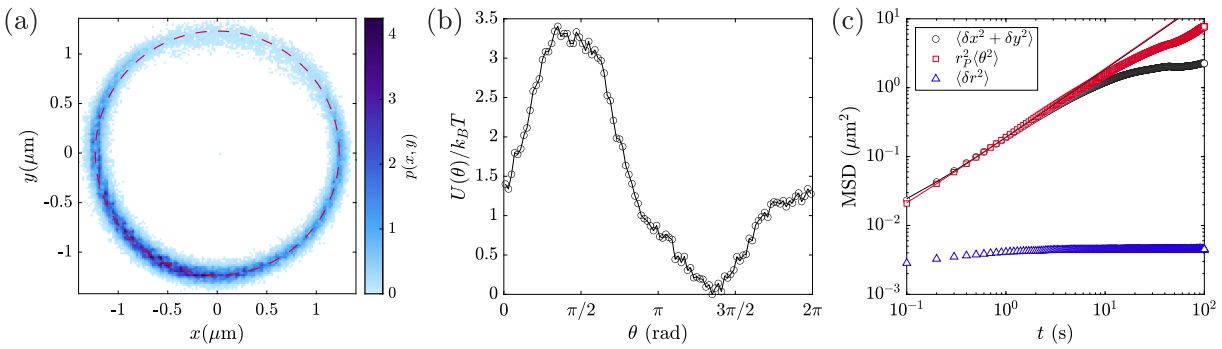


Figure 7.5: (a) 2D histogram of the particle positions during the free diffusion experiment (b) Background potential around the ring in θ. (c) Mean squared displacements in xy (black circles), r (blue triangles) and θ (red squares), with a linear fit (red line).

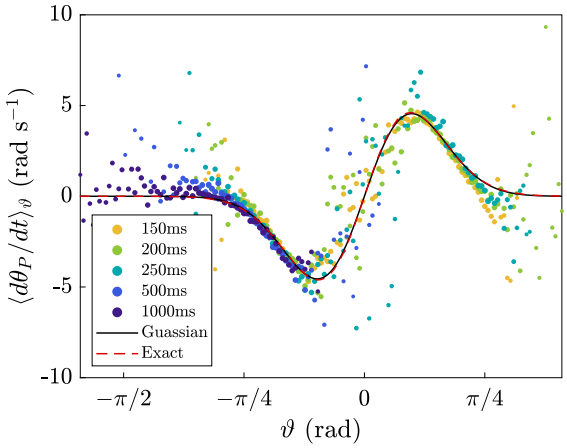


Figure 7.6: Trap force measured from experiments with $\tau = 0.15\,\mathrm{s}$ (yellow) to 1 s (purple), fit with a the approximate Gaussian force (equation 7.7, black $-$) and the exact force (equation 7.6, red $--$).

7.3.3 Trap force measurement

We measure the force exerted by the feedback trap on the particle *in situ* during each feedback experiment using the method of Juniper *et al.* [72] described in section 2.3.2. The force is the same in all experiments. Juniper's method works best for experiments where a particle is driven over a potential at a high velocity, so we only use the experiments with $\tau > 0.15\,\mathrm{s}$, which, as will be seen in the results section, behave as driven systems. We calculate the trap force from the average instantaneous velocity of the particle as a function of the angle between the particle and trap, ϑ:

$$\left\langle \frac{d\theta_P}{dt} \right\rangle_\vartheta = \frac{1}{\zeta} \langle F(\vartheta) \rangle_\vartheta \,. \tag{7.32}$$

Figure 7.6 shows the result of this measurement from each experiment with delay times from $\tau = 0.15\,\mathrm{s}$ to 5 s. We fit both the exact and the Gaussian trap force given by equations 7.6 and 7.7, which are shown in figure 7.6 with dashed red and solid black lines respectively. Both are almost identical, so we can use the Gaussian equation in our analysis. Table 7.1 lists the fitted constants and other characteristic values which will be important in later sections.

Quantity	symbol	equation	Value
Trap width	ϕ	eqn. 7.5	$0.313\,\mathrm{rad}$
Angular corner frequency	K	eqn. 7.5	$23\,\mathrm{s}^{-1}$
Trap depth	V_0	$\phi^2 K \zeta$	$1.50 \times 10^{-7}\,\mathrm{kg\,rad^2\,s^{-2}}$
Maximum velocity	v_m	$e^{-1/2}\phi K$	$4.37\,\mathrm{rad\,s^{-1}}$
Time to travel ϕ at v_m	τ_m	$e^{1/2}/K$	$0.0717\,\mathrm{s}$

Table 7.1: Important quantities relating to the trap force.

7.3.4 Simulations

To complement the experiments and further explore the parameter space, we also carry out one-dimensional Brownian Dynamics simulations based on the angular Langevin equation (equation 7.3). For each iteration, the position of the particle (θ_P) is calculated according to

$$\theta_P(t+\Delta t) = \theta_P(t) + \frac{\Delta t}{\zeta} F(\theta_P(t), \theta_T(t)) + \sqrt{2D\Delta t}\Xi, \tag{7.33}$$

where $D = k_B T/\zeta$ is the diffusion coefficient, Ξ is a normally distributed random number with mean 0 and standard deviation 1, and the simulation time is $\Delta t = 10^{-5}\,\mathrm{s}$. The drag force is the experimentally determined value of ζ calculated in section 7.3.2 and defined in equation 7.3. The trap force is the exact expression defined in equation 7.6. One set of simulations used the values of the trap parameters (K, ϕ) measured from the experiments in section 7.3.3. These simulations ran for $10^3\,\mathrm{s}$, slightly longer than the experiments. In the second set, K was varied by a factor of 2, $1/2$, $1/4$ and $1/8$, while keeping the trap depth, V_0, fixed. These were run for 300 s. Figure 7.7 shows the force and corresponding potential used in each simulation.

As in the experiments, the trap position was set by the feedback protocol $\theta_T(t) = \theta_P(t-\tau)$, with lag times ranging from $10^{-3}\,\mathrm{s}$ to 5 s. In order to keep the simulations as close as possible to the experiment, the trap position, θ_T, was updated every 600 iterations $\equiv 6\,\mathrm{ms}$, and the particle position, θ_P, was saved every 100 iterations $\equiv 1\,\mathrm{ms}$.

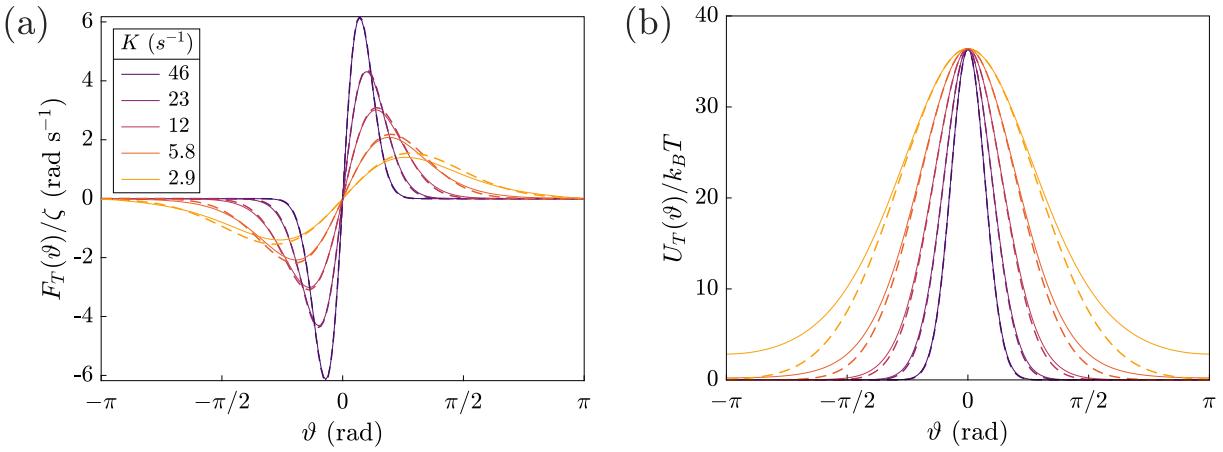


Figure 7.7: (a) Exact (−) and approximate (−−) trap force, $F(\vartheta)/\zeta$, and (b) trap energy, $U_T(\vartheta)/k_BT$, used in the five sets of simulations with stiffnesses of $K = 46\,\mathrm{s}^{-1}$ (blue) to $K = 2.9\,\mathrm{s}^{-1}$ (yellow). The purple line with $K = 23\,\mathrm{s}^{-1}$ is the same as the measured experimental trap force

7.4 Results and discussion

In this section, we analyse the particle trajectories of the feedback experiments and simulations described in sections 7.3.1 and 7.3.4. We begin by characterising the dynamics at different delay times, focussing on the experiments and those simulations which have the same trap force. We then use the theory of stochastic delay differential equation (SDDEs) to describe the system's behaviour in the short and long delay time regimes. Finally, we describe the stochastic thermodynamic properties of the system.

7.4.1 Dynamics

First, we characterise the dynamics of the particle at different delay times. Figure 7.8a shows typical trajectories from four representative experiments with delay times of τ =0.01, 0.05, 0.1, and 0.5 s. Note that the effect of the periodic boundary conditions has been removed by constraining the change in angle from one frame to the next to $|\Delta\theta| < \pi$, and therefore allowing θ to have any value. The corresponding MSDs are shown in figure 7.8b, while figure 7.8c shows histograms of the angle between the particle and the trap, $\vartheta = \theta_P(t) - \theta_T(t) = \theta_P(t) - \theta_P(t-\tau)$ (equivalent to the angle between the particle at time t and time $t-\tau$). As we increase the lag time, the trajectories, MSDs and ϑ distributions all show a dramatic change in behaviour. We will now describe each lag time separately.

When $\tau = 0.01$ s, the trajectory appears to be trapped at around 1.5π, where the background potential measured in section 7.3.2 is minimised. The MSD is diffusive ($\propto t^1$) at short times but sub-diffusive at long times as a result of the background potential. The short-time diffusion coefficient is slightly larger than the free-diffusion measurement, possibly because the trap pushes the particle upwards away from the bottom of the sample cell, decreasing its drag constant. The histogram of the angle between the particle and the trap, $P(\vartheta)$, shown in figure 7.8c, is a narrow Gaussian centred around 0, consistent with diffusive short time behaviour. The dotted line at the top of figure 7.8c shows the trap force profile, showing that the particle spends most of the time near the trap centre, where the force is small. This explains why the trajectory is diffusive – the feedback trap always applies a small force to the particle, so has a minimal effect on its diffusive trajectory.

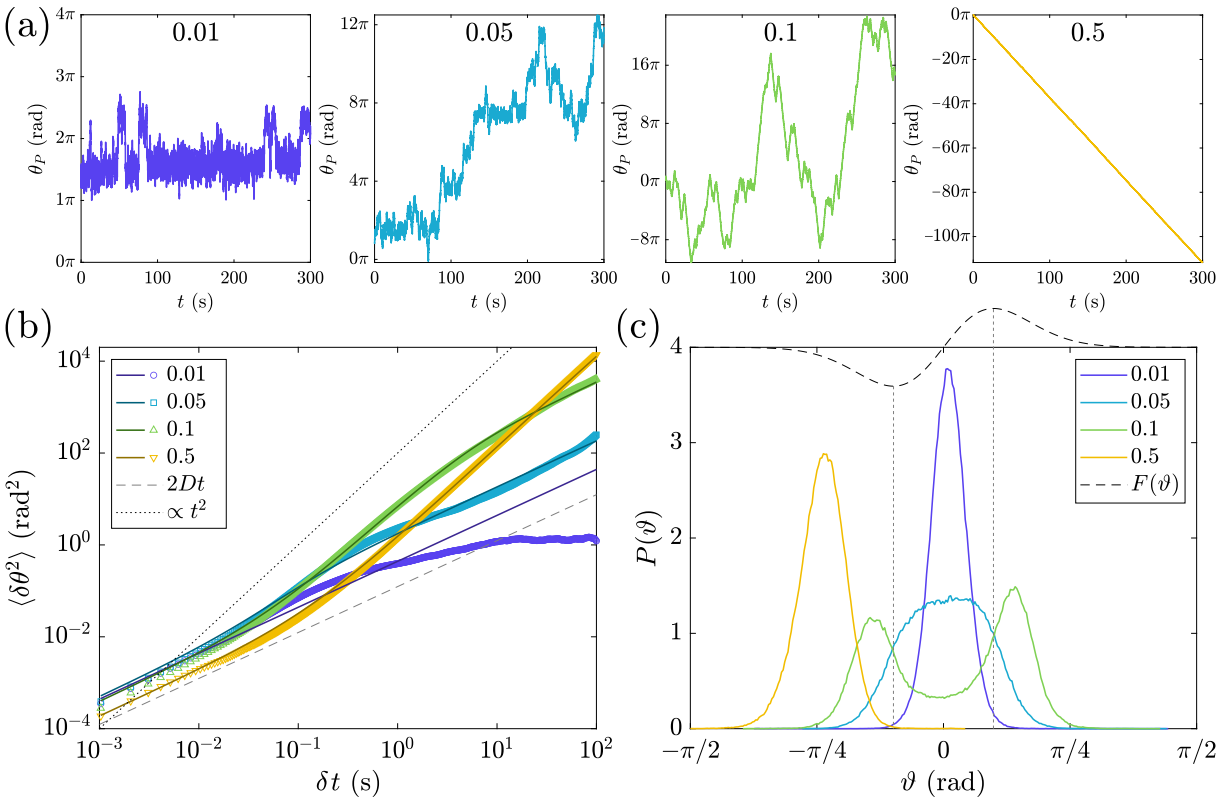


Figure 7.8: (a) Particle positions, θ_P, from the 1st 200s of experiments with τ =0.01 s (blue), 0.05 s (turquoise), 0.1 s (green), and 0.5 s (yellow). (b) MSDs (symbols) with fits to equation 7.34 (lines). The dashed line shows $\langle \delta\theta^2 \rangle = 2Dt$ and the dotted line shows $\langle \delta\theta^2 \rangle \propto t^2$. (c) Histogram of the angle between the particle and the trap, $\vartheta = \theta_P - \theta_T$. The dashed line shows $F(\vartheta)$ on an arbitrary vertical axis.

When $\tau = 0.05$ s, the particle's trajectory appears more diffusive, albeit with a slight preference for values of $(1.5 + 2n)\pi$ as a result of the background potential. The mean squared displacement is diffusive at short and long times with a transient super-diffusive ($\propto t^2$) section in between. This t^2 scaling implies driven motion. The histogram of the angle between the particle and the trap, $P(\vartheta)$, is broader and has less Gaussian character. As the particle diffuses further from the trap centre, it is then pushed even further by the repulsive trap force, which causes both the non-Gaussian $P(\vartheta)$ and the transient driven behaviour in the MSD. This force is sufficient to overcome the background potential, resulting in long-time diffusive motion.

When $\tau = 0.1$ s, the particle moves at a constant velocity over a sustained period before randomly switching direction, resulting in a persistent random walk. This manifests as an MSD which is diffusive at short times, super-diffusive over a large intermediate time range, and diffusive at long times. The long time diffusive section is a result of the random direction changes and has a significantly larger diffusion coefficient than at short times. $P(\vartheta)$ has two sharp peaks near the position of maximum force. The sharpness of the peaks is consistent with

the uniformity of the velocity in the driven segments of the trajectory. The large angle between the particle and the trap centre, and hence large energy barrier to moving to the other side of the trap, explains the low frequency at which the trajectory switches direction.

At the largest delay time of 0.5 s, the particle moves at a constant velocity without switching direction over the course of the whole experiment. The MSD switches from diffusive at short times to driven at long times. The $P(\vartheta)$ distribution shows that this is because the particle is always far from the trap centre, so there is a large energy barrier to switching direction. The driven section has a lower velocity than at $\tau = 0.1$ s, reflecting the large average $|\vartheta|$.

The same trends can be seen more clearly in the simulations, where there are no effects from the background potential, out of plane motion or tracking errors, which confirms our interpretation of the experimental results in figure 7.8. Figure 7.9 shows the trajectories, MSDs, and $P(\vartheta)$ from simulations with the same delay times as the experiments in figure 7.8. The simulations all have the same diffusion coefficient at short times. At intermediate times, the

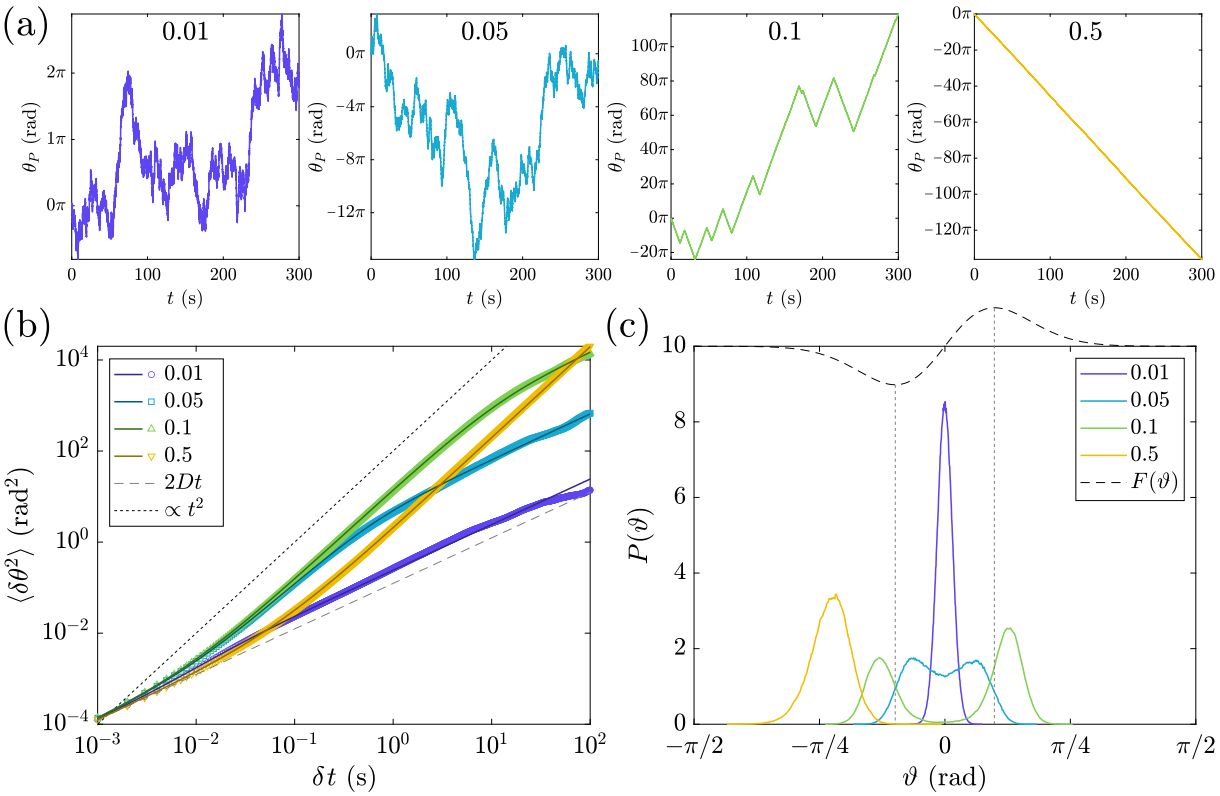


Figure 7.9: (a) Particle positions, θ_P, from the 1st 200s of simulations with τ =0.01 s (blue), 0.05 s (cyan), 0.1 s (green), and 0.5 s (yellow). (b) MSDs (symbols) with fits to equation 7.34 (lines). The dashed line shows $\langle \delta\theta^2 \rangle = 2Dt$ and the dotted line shows $\langle \delta\theta^2 \rangle \propto t^2$. (c) Histogram of the angle between the particle and the trap, $\vartheta = \theta_P - \theta_T$, for the same simulations. The dashed line shows $F(\vartheta)$ on an arbitrary vertical axis.

trajectories all have a transient driven, super-diffusive section. For long delay times, this corresponds to motion at a constant speed, as shown in figure 7.9a. As the delay time increases, the driven section last for longer as the particle hops from one side of the trap to the other less frequently. This is a result of its larger distance from the trap centre, as shown in figure 7.9c. Diffusive motion is recovered at long times for all but the largest delay time.

Overall, except for the sub-diffusive long-time behaviour of the experiment with $\tau = 0.01\,\mathrm{s}$ due to the background potential, the experiments and simulations can all be described by short-time diffusive motion characterised by the free diffusion coefficient, D, combined with driven movement at a constant speed, v, and random changes of direction at an average rate of λ. This is exactly the type of motion displayed by a model 1D active Brownian particle, which has an MSD of [282, 283]

$$\langle \delta\theta^2 \rangle = \left(2D + \frac{v^2}{\lambda}\right) t + \frac{v^2}{2\lambda^2}\left(e^{-2\lambda t} - 1\right). \tag{7.34}$$

The limiting values at short and long times are

$$\langle \delta\theta^2 \rangle (t \ll \lambda^{-1}) = 2Dt + v^2 t^2, \tag{7.35}$$

$$\langle \delta\theta^2 \rangle (t \gg \lambda^{-1}) = \left(2D + \frac{v^2}{\lambda}\right) t = 2D_L t. \tag{7.36}$$

We fit each MSD with equation 7.34 to obtain the driving velocity, v, and re-orientation rate, λ. The fits are shown as dark lines in figures 7.8b and 7.9b. The experiments and simulations show good agreement with the fits, confirming our use of this model.

The values of v, λ and $D_L = D + v^2/2\lambda$ from each fit are shown in figure 7.10. There is

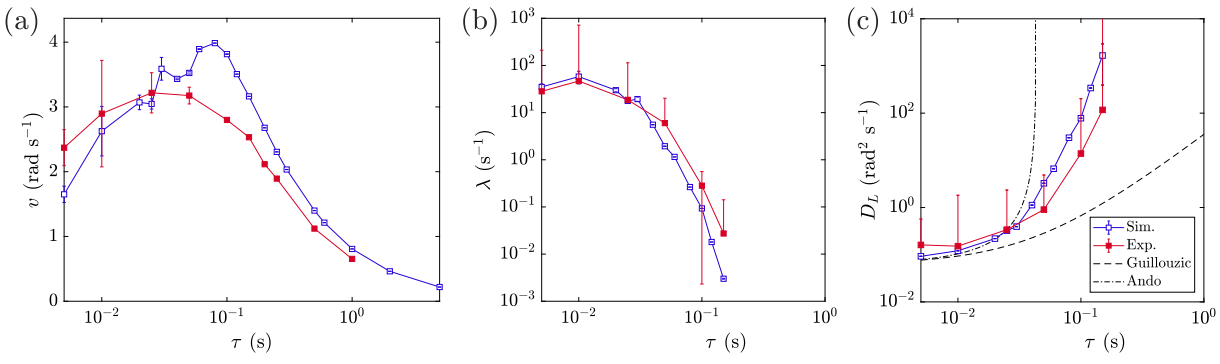


Figure 7.10: v (a), λ (b), and D_L (c) from experiments (red) and simulations (blue). In (c), the dashed and dash-dotted lines show equations 7.37 and 7.38 respectively.

good agreement between the experiments and simulations. The speed, v, initially increases with increasing τ, then peaks between $\tau = 0.05 - 0.1\,\mathrm{s}$, where it is close to the maximum velocity of $v_m = 4.2\,\mathrm{rads}^{-1}$, then decreases as τ increases beyond 0.1 s. The re-orientation rate, λ, can only be measured when λ^{-1} is less than the duration of the experiment (600 s) or simulations (1000 s). Except for the first point, λ decreases rapidly with increasing τ until it becomes too small to measure at $\tau = 0.2\,\mathrm{s}$. Likewise, D_L increases rapidly from around the free diffusion value of $0.62\,\mathrm{rad}^2\,\mathrm{s}^{-1}$ at low τ to $300\,\mathrm{rad}^2\,\mathrm{s}^{-1}$ at $\tau = 0.2\,\mathrm{s}$, above which the long-time diffusive regime is no longer accessible.

7.4.2 Stochastic delay differential equations

Next, we will explain the measured trends in v, λ and D_L using the framework of stochastic delay differential equations. At short delay times, we use the results of Guillouzic *et al.* [275] and Ando *et al.* [271] to find the diffusion coefficient in the limit of either short delay times ($\tau \to 0$) or an approximately harmonic trap (valid at short delay times of $\tau < K^{-1}$) respectively. Both theories, discussed in section 7.2.2, predict purely diffusive motion with an enhanced long-time diffusion coefficient of

$$D_L = D\,(1 + K\tau)^2 \tag{7.37}$$

and

$$D_L = \frac{D}{(1 - K\tau)^2} \tag{7.38}$$

respectively, where K is the angular equivalent of the corner frequency and D is the free diffusion coefficient, which is the same as the short-time diffusion coefficient in the MSDs. Both expressions for D_L, shown in figure 7.10c, accurately describe the long-time diffusion coefficient of the experiments and simulations when the delay time is less than $K^{-1} \approx 0.05\,\mathrm{s}$. Therefore, the short delay time regime with $\tau < K^{-1}$ is accurately described by purely diffusive motion with an enhanced long-time diffusion coefficient.

At long delay times of $\tau \geq K^{-1}$, both expressions fail to predict the measured D_L. Equation 7.37 significantly underestimates D_L because the theory does not predict a driven component to the motion, while equation 7.38 diverges at $\tau = K^{-1}$ because it does not account for the

random reorientations in the driving direction, without which $D_L \to \infty$. In order to describe the diffusion coefficient in the large τ regime, we start by finding an expression for the driving speed, v, which we then use to derive an expression for the re-orientation rate, λ, and finally we combine these two quantities to obtain D_L. We assume that the system settles into a driven non-equilibrium steady state, and consider a deterministic version of the Langevin equation of motion (equation 7.9). If the particle moves at a constant velocity of $dx/dt = v_{ss}$, the angle between the particle and the trap is fixed at $\vartheta = v_{ss}\tau$. Substituting these into equation 7.9 gives

$$v_{ss} = K v_{ss} \tau \exp\left(-\frac{v_{ss}^2 \tau^2}{2\phi^2}\right), \tag{7.39}$$

and solving for v_{ss} yields the steady state velocity,

$$v_{ss} = \begin{cases} \pm\frac{\phi}{\tau}\sqrt{2\ln(K\tau)} & \tau \geq K^{-1} \\ 0 & \forall\tau \end{cases}. \tag{7.40}$$

The diffusive state with $v_{ss} = 0$ exists at all delay times, but a driven steady state is only possible at long delay times of $\tau > K^{-1}$. This agrees with the short time theory of Ando *et al.* in equation 7.38, which also predicted a transition from diffusive to driven motion at $\tau = K^{-1}$.

Figure 7.11a compares the steady state velocity, v_{ss}, from equation 7.40 to the measured speed, v, from fitting the MSDs of all experiments and simulations, including those with different values of K to the experiment. Scaling the delay time by K^{-1} and the velocities by v_m collapses all experiments and simulations onto the same curve, which reaches the maximum possible value

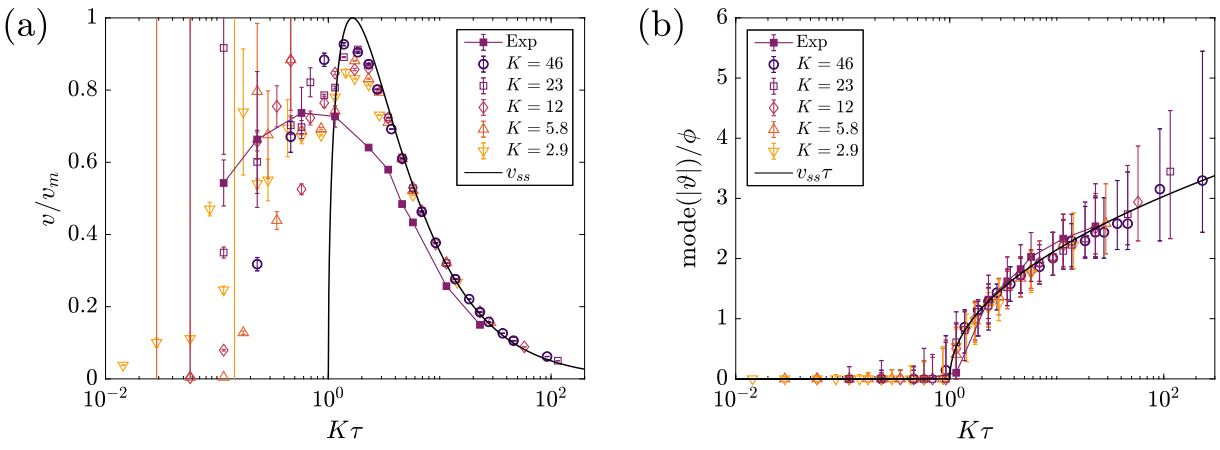


Figure 7.11: (a) Speed, v, scaled by v_m, against $K\tau$ for all simulations and experiments. (b) Most probable $|\vartheta|$, scaled by ϕ, against $K\tau$, for the same experiments and simulations.

of v_m when $\tau = \tau_m = e^{1/2}K^{-1}$ and then decreases with increasing τ. The measured velocities show good agreement with v_{ss} at long delay times of $K\tau > 1$, confirming that these experiments and simulations exist in the driven steady state. Additionally, equation 7.40 predicts a steady state angle between the particle and the trap of $\vartheta_{ss} = v_{ss}\tau$. Figure 7.11b shows that this steady state angle agrees very well with the most probable $|\vartheta|$ taken from the maximum point of a histogram of $|\vartheta|$, once again confirming the validity of the steady state approach.

We will now use the steady state velocity in equation 7.40 to find an expression for the switching rate, λ. While the trap moves at a constant velocity v_{ss}, the particle experiences a tilted potential $U(\vartheta) = U_T(\vartheta) - \zeta v_{ss}\vartheta$ due to a combination of the Gaussian trap potential and a linear potential arising from motion at a constant velocity. This potential has a potential minimum and maximum at

$$\vartheta_{min} = \pm\phi\sqrt{2\ln(K\tau)}, \qquad \vartheta_{max} = \pm\phi\sqrt{-W_0\left(\frac{-2\ln(K\tau)}{(K\tau)^2}\right)}, \tag{7.41}$$

where $W_0(x)$ is the 0^{th} branch of the Lambert function. Example effective potentials at three different delay times are shown in figure 7.12.

Figure 7.12a shows the effective potentials, $U(\vartheta)$, for positive and negative v_{ss} when the delay time is between K^{-1} and $\tau_m = e^{1/2}K^{-1}$, the delay times at which a non-zero steady state velocity first appears and the delay time with the maximum steady state velocity. In this case, the steady state angle between the particle and the trap, $\theta_{ss} = v_{ss}\tau$, corresponds to the local maximum in the tilted potential, shown with crosses in figure 7.12a. Consequently, there is no energy barrier to the particle moving to the other side of the trap, making the driven state as unstable as the diffusive state with $v_{ss} = 0$. When the delay time is larger than τ_m, as shown in figure 7.12c, the steady state position, θ_{ss}, instead corresponds to a local minimum in the tilted

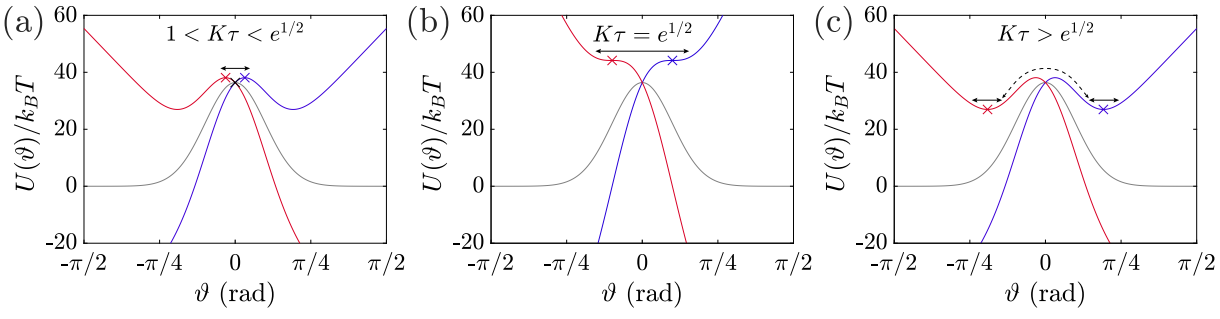


Figure 7.12: Effective potential, $U(\vartheta) = U_T(\vartheta) - \zeta v_{ss}\vartheta$, for positive (red) and negative (blue) v_{ss}, when (a) $1 < K\tau < e^{1/2}$, (b) $K\tau = e^{1/2}$, and (c) $K\tau > e^{1/2}$. Crosses mark the steady state position, ϑ_{ss}.

potential, shown with crosses in figure 7.12a. In this case, the trajectory switches direction when the particle hops from one potential minimum to the other over the potential barrier, which happens at a rate λ given by Kramer's escape problem:

$$\lambda_{\mathrm{Kr}}^{-1} = \frac{2\pi\zeta}{\sqrt{|U''_{max}U''_{min}|}} \exp\left(\frac{U_{max} - U_{min}}{k_B T}\right). \tag{7.42}$$

This expression assumes that escape is a Poisson process, which is valid in the limit of $\tau \gg \tau_m$, when the energy barrier is large and the local maximum and minimum are far apart.

Figure 7.13a shows the measured switching rate, λ, from the MSDs of the experiments and simulations. At short τ, the uncertainty in λ is too large to determine the trend because the driven part of the MSD is too small for accurate fitting. After $K\tau \gtrsim 0.5$, λ rapidly decreases. We only have a few measurements of λ in the region in which we can calculate λ_{Kr}, but these points agree well with λ_{Kr}.

We can now combine the steady state velocity, v_{ss} (equation 7.40), and the escape rate, λ_{Kr} (equation 7.42), to calculate an expression for the long time diffusion coefficient of the system, $D_L = D + v_{ss}^2/2\lambda_{\mathrm{Kr}}$, in the driven regime where $\tau \gg \tau_m$. Figure 7.13b compares this theory to the measured D_L from all experiments and simulations. There is reasonably good agreement, although we can only measure D_L for a few data points where the Kramer's escape equation is valid. This confirms that the dynamics in the long delay time regime are well described by a driven steady state with a tilted effective potential.

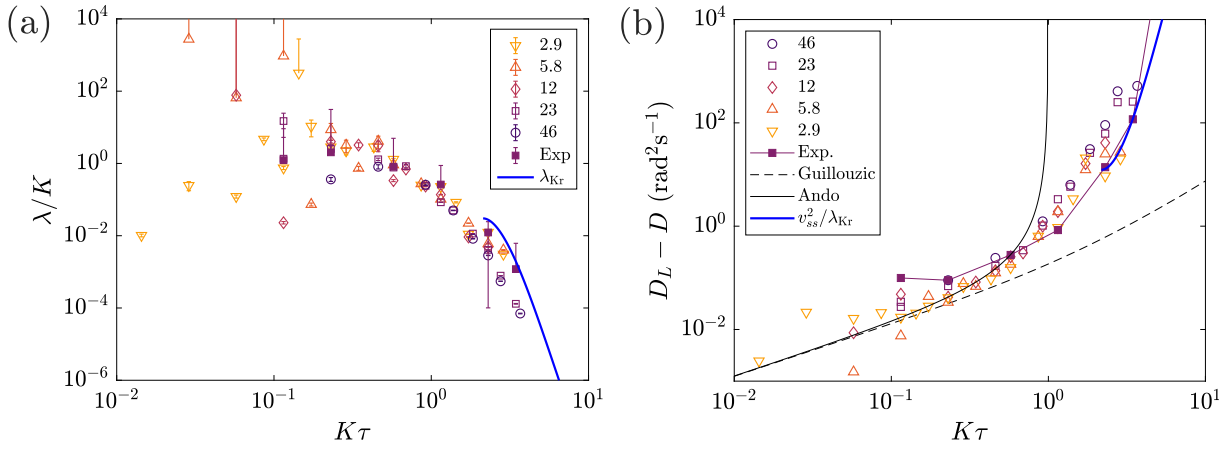


Figure 7.13: (a) Switching rate, λ, from the experiments and simulations. The blue line shows equation 7.42. (b) Long time diffusion coefficient, $D_L - D$, from all experiments and simulations. The black dashed and solid lines show equations 7.12 and 7.15 respectively, while the blue line shows $D_L = D + v_{ss}^2/2\lambda_{Kr}$ from equations 7.40 and 7.42. Colours and symbols are the same as in figure 7.11.

7.4.3 Stochastic thermodynamics

We have shown that our feedback experiment has two regimes; at short delay times of $\tau < \tau_m$, the feedback trap increases the diffusion coefficient of the particle, while at long delay times the trap drives the particle at a constant speed but in a random direction. In this section we discuss the stochastic thermodynamics of this process.

We use equation 7.22 to measure the average rate of work done by the feedback trap on the particle, $\langle \dot{w}(\mathbf{x}) \rangle$, which is shown in figure 7.14a. The rate of work done, or power input, follows the same shape as the speed, v, shown in figure 7.11a; the power input peaks at $\tau = \tau_m = e^{1/2} K^{-1}$, where the steady state velocity is maximised. The inset shows $\langle \dot{w} \rangle$ for the simulations and experiments with $\tau > \tau_m$ as a function of the speed, v, measured from the MSDs. The points all sit very close to the $\langle \dot{w} \rangle = \zeta v^2$ line, which is the minimum power required to drive a particle at a constant speed from equation 7.23. This implies that almost all of the work done on the particle is used to drive it at the average speed, making the feedback driving almost as efficient as driving the particle with a constant force.

Another important thermodynamic quantity in a feedback experiment is the mutual information, I, between the particle position (the system) and the trap position (the measurement), in equation 7.28. We use a mirrored probability distribution, $p_m(\vartheta) = (p(\vartheta) + p(-\vartheta))/2$, to

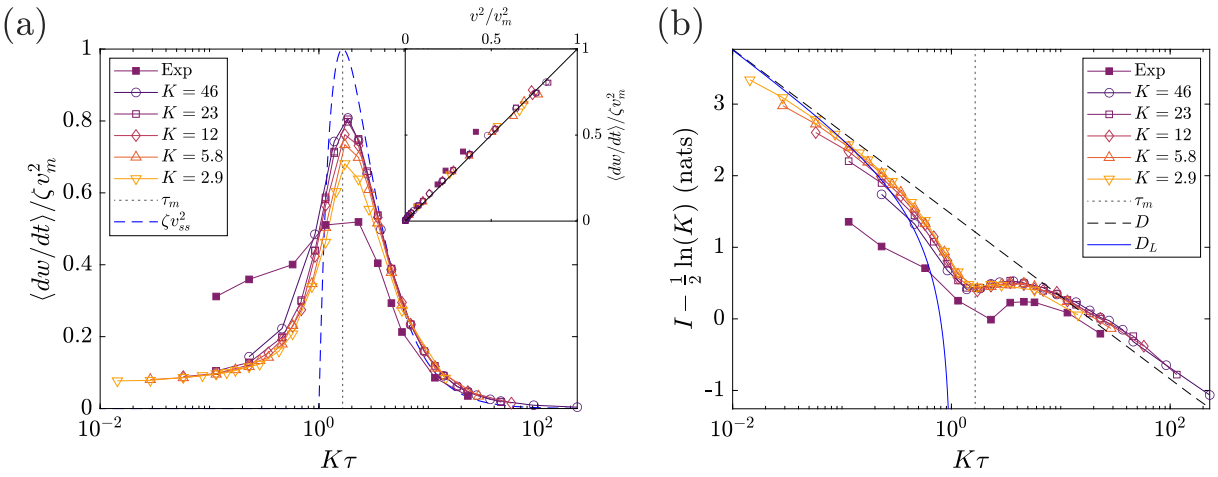


Figure 7.14: (a) Rate of work done relative to the maximum value, $\dot{w}/(\zeta v_m^2)$, against rescaled delay time, $K\tau$, for all experiments and simulations. Inset: Rate of work done, $\dot{w}/\zeta v_m^2$, against measured steady state velocity, v^2/v_m^2. (b) Mutual information between the particle and trap position, I, shifted by $\frac{1}{2}\ln(K)$, against $K\tau$, for all experiments and simulations. The black dashed and solid blue line shows the theoretical value for a freely diffusing particle (equation 7.30) with diffusion coefficients of D and $D_L = D(1 - K\tau)^{-2}$ respectively.

account for the fact that the measured $p(\vartheta)$ from a single finite experiment is not always symmetric, despite the equal probability of the particle being driven to the left or the right. The result is shown in figure 7.14b for all experiments and simulations. The mutual information shows interesting non-monotonic behaviour with a local minimum at τ_m, the delay time where the power was maximised. Intuitively, this inverse relationship makes sense; when a process does not change the free energy of the system, the work done is bounded by $W \geq -k_B T I$ [108], so a process requires more work when we have less information about the system, and vice versa. It is interesting that this relationship holds even though the work done is always much larger than the $-k_B T I$ limit.

The inverse relationship between the work and the mutual information can be rationalised by considering the effective potential experienced by the particle, which combines the repulsive trap potential with the tilted effective potential from the steady state driving velocity. At short delay times of $\tau < \tau_m$, the particle sits on a local maximum of this effective potential, as shown in figure 7.12a, so the particle diffuses freely. The angle distribution, $p(\vartheta)$, therefore becomes broader with increasing τ, causing the work done on the particle to increases and the mutual information to decrease in line with the theoretical value for free diffusion in equation 7.30. When $\tau > \tau_m$, the particle instead sits in a local minimum in the effective potential, as illustrated in figure 7.12c. The particle is confined by this effective potential, causing the $p(\vartheta)$ distribution to become more sharply peaked, and so increasing the mutual information. At $\tau = \tau_m$, shown in figure 7.12b, the particle is driven at the maximum velocity while existing in an unstable state, resulting in a broad $p(\vartheta)$ and hence the local minimum in I. The local minimum in the mutual information between the particle and the trap and the local maximum in the work done on the particle therefore both occur as a result of the system switching from a diffusive steady state to a stable driven steady state.

7.5 Conclusions

In this chapter we characterised the dynamics of a particle on a ring interacting with a feedback controlled repulsive optical trap over several orders of magnitude of the delay time, τ. We have shown that at short delay times, the system exists in a diffusive state which is well described by the theory of stochastic delay differential equations. At long delay times, there is a transition

to a driven steady state in which the particle and trap move at a constant speed, but randomly switch direction. We showed that the driven state exists when there a non-zero solution to $v_{ss} = F(v_{ss}\tau)$, and that it is stable when $v_{ss}\tau$ is at a local minimum of the tilted effective potential $U_T(\vartheta) - v_{ss}\vartheta$. These results can be applied more generally to determined whether any system described by a stochastic delay differential equation has a stable driven state. We also analysed the stochastic thermodynamics of the feedback driven system and found that almost all of the work done on the particle is converted into driving it at a constant speed. The maximum work coincided with the minimum mutual information. We rationalise this relationship by considering the particle's diffusion in the tilted effective potential $U_T(\vartheta) - v_{ss}\vartheta$, showing that the minimum mutual information occurs when the system switches from an unstable to a stable driven steady state.

Acknowledgments

Yanyan Liu and Arran Curran are thanked for the original experimental data. Arthur Straube, Arran Curran and Joseph Hutchinson are thanked for useful discussions.

Appendix

A Drag constant of chains of N particles

Yang *et. al.* [190] measured the drag constant of a chain of N particles using Invitrogen Dynabeads M280 in a strong magnetic field gradient. They found good agreement with theoretical expressions modelling the chain as rigid, rod-like objects including ellipses, cylinders and strings of spheres. These expressions all have the form

$$\zeta^{||} = \frac{2}{3}\zeta_1 \frac{N}{\ln N + \gamma_{||}} \qquad \zeta^{\perp} = \frac{4}{3}\zeta_1 \frac{N}{\ln N + \gamma_{\perp}}, \tag{A.1}$$

with several different values for the correction factors, all around $\gamma_{||} \approx 0$ and $\gamma_{\perp} \approx 1$.

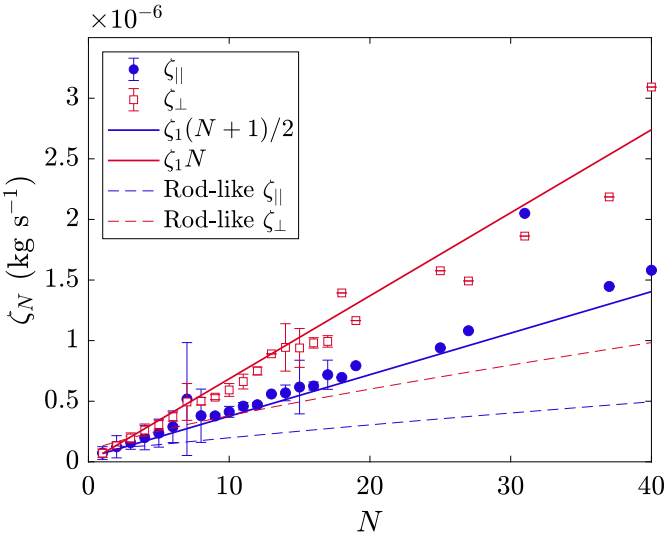


Figure A.1: Drag constant of chains of $N = 1 - 40$ parallel (filled blue circles) and perpendicular (empty red squares) to the magnetic field. Red and blue solid lines are $\zeta_{\perp} = \zeta_1 N$ and $\zeta_{||} = \zeta_1(N+1)/2$ respectively. Red and blue dashed lines are the perpendicular and parallel drag constants in equation A.1 with $\gamma_{\perp} = \gamma_{||} = 0$

We test these expressions in our system by measuring the mean squared displacement of chains as they assemble in a dilute sample of paramagnetic particles in a magnetic field of strength $B = 0.55\,\mathrm{mT}$ oriented along the x direction. The result is shown in figure A.1.

The drag constants both parallel and perpendicular to the field are significantly larger than those in [190] and have a linear dependence on N. The perpendicular drag constant, $\zeta_\perp$, agrees well with $\zeta_\perp = \zeta_1 N$, the expected value of the drag constant of particles which do not interact hydrodynamically. The parallel drag constant, $\zeta_\parallel$, obeys the empirical expression $\zeta_\parallel = \zeta_1(N+1)/2$. It is possible that the difference between our measurement and [190] is that we use a much weaker magnetic field, so our chains are more flexible.

B Matching the experimental interaction parameter to simulations

We use Brownian dynamics simulations to imitate the experiments in chapter 4. This allows us to estimate the effective interaction parameter, Γ, by comparing the experiments to the simulations. We use this value of Γ to estimate the energy of each state adopted by the chains in section 4.4.4.

The simulations are described in detail in section 2.4. In short, we simulate a chain of of $N = 16$ particles in a substrate with a wavelength of $\lambda = (8/7)\sigma$ and substrate depths up to $V_s = 36 k_B T$. The pairwise interactions consist of a repulsive screened coulomb term and an attractive magnetic term. Magnetic interaction parameters of $\Gamma = 47$ to 107 were tested in order to find the best match with the experiments. We also compared the 1D simulation with $\Gamma = 60$ to an equivalent 2D simulation, confirming that one dimension is sufficient to capture the phase behaviour of the chain. The experiments in chapter 4 were mimicked by initialising the chain with every particle at the bottom of a potential minimum so that that $s = \lambda$. We then ran successive simulations where the substrate depth was decreased and then increased in steps, and each simulation was initialised with the final coordinates from the previous simulation. 600 frames were taken for each simulation at a rate of $200\tau_B^{-1}$.

Figure A.2 shows the average spacing between particles in simulations of a chain of 16 particles with interaction parameters between $47 k_B T$ and $107 k_B T$. When scaled by the substrate

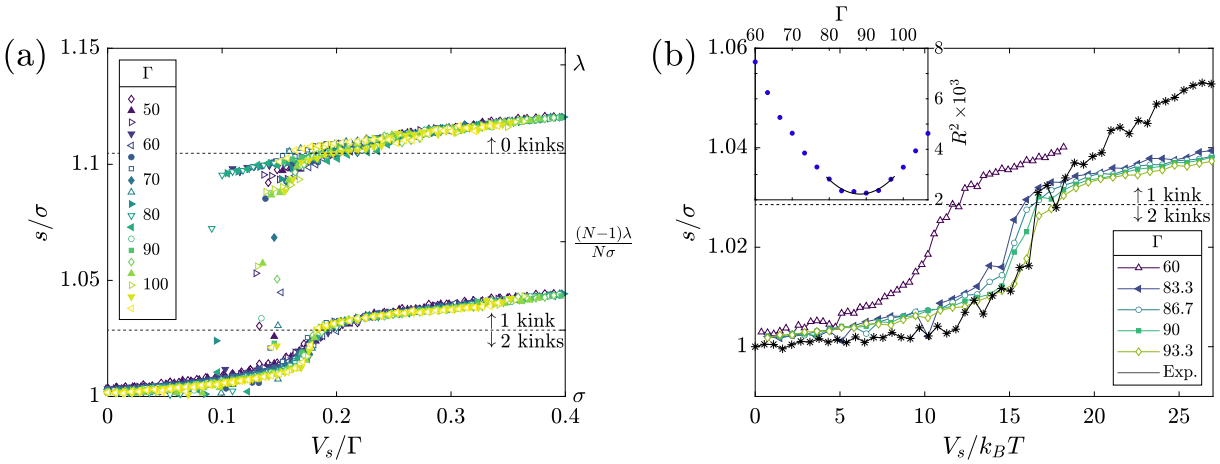


Figure A.2: (a) Simulated s/σ with against V_s/Γ for an $N = 16$ chain with $\Gamma = 47k_BT$ (purple) to $107k_BT$ (yellow). (b) Experimental (black stars) and simulated s/σ against V_s/k_BT for an $N = 16$ chain with $\Gamma = 60k_BT$ (purple triangles) and $83.3k_BT$ to $107k_BT$ (blue to yellow). Inset: Mean squared difference between the experimental and simulated s/σ versus Γ (blue circles). The black line shows a parabolic fit to the lowest 6 points.

depth, all simulations collapse onto one curve. As in the experiments, we see a transition from $N_k = 0 \to 2 \to 1$. The $N_k = 0 \to 2$ transition in the decreasing V_s half of the experiment occurs randomly over a range of $V_s = 0.1 - 0.15\Gamma$, but the $N_k = 2 \to 1$ transition in the second half consistently occurs at $V_s = 0.35\Gamma$. We therefore use the increasing V_s half to match the simulations to the experiment, and thus find the effective value of Γ.

We fit the experiment to the simulations by calculating the mean squared distance, R^2 between each point in the experiments to the simulations. The R^2 values, shown in the inset of figure A.2b, plateaued between $\Gamma = 83.3$ and 93.3, significantly higher than the value of $\Gamma = 60$ measured in chapter 3. The optimal Γ was then estimated with greater precision by fit a parabola to the lowest six points, giving $\Gamma = 88.4 \pm 1$.

The four closest fitting simulations are compared to the experiment in figure A.2b, along with the simulation with $\Gamma = 60$. No simulations perfectly match the experiment, perhaps implying that the experimental inter-particle energy deviates slightly from the magnetic $-x^{-3}$ form. This may be a result of only probing the potential very close to contact, where the dipole approximation is predicted to break down [161], but it could also be caused by other short ranged attractive contributions to the potential. Nevertheless, the agreement is good enough to justify using an inter-particle energy of $U_{int}(x) = -88.4(\sigma/x)^3$ when estimating the relative energies of each state section 4.4.4.

C Average distance between particles in a flat landscape

The pair potential of the Dynabeads is influenced by the laser power. The laser heats the particles, leading to a long ranged thermo-phoretic attraction. We also see a short-ranged repulsion which is assumed to be caused by the light scattered off the particle. These two competing interactions have a visible effect only when the laser power is very strong. This is illustrated in figure A.3, in which a Dynabead in a single 400mW trap attracts particles from across the field of view, which surround the trapped particle at a radius of 4 µm, significantly larger than the diameter.

In order to determine the impact of both of these interactions on our experiments, we place a chain in a landscape with a wavelength of 0.4 µm, so that the potential is flat, and measure the average spacing between particles as a function of the laser intensity, which is proportional to Laser Power/($N_{traps}\lambda$). Figure A.3b shows the average spacing of chains in magnetic fields of 0.32 mT, the field used in chapter 6, and 0.55 mT, used in chapters 4 and 5. The laser intensities used in the experiments in chapters 4 and 5 do not cause a significant change in the particle spacing. The maximum intensity used in chapter 6, however, is enough to increase the spacing to more than one wavelength. This region can be avoided by using a substrate oscillation amplitude of 0.75 rather than 1, giving a maximum spacing of 3 µm, halfway between the diameter and the wavelength.

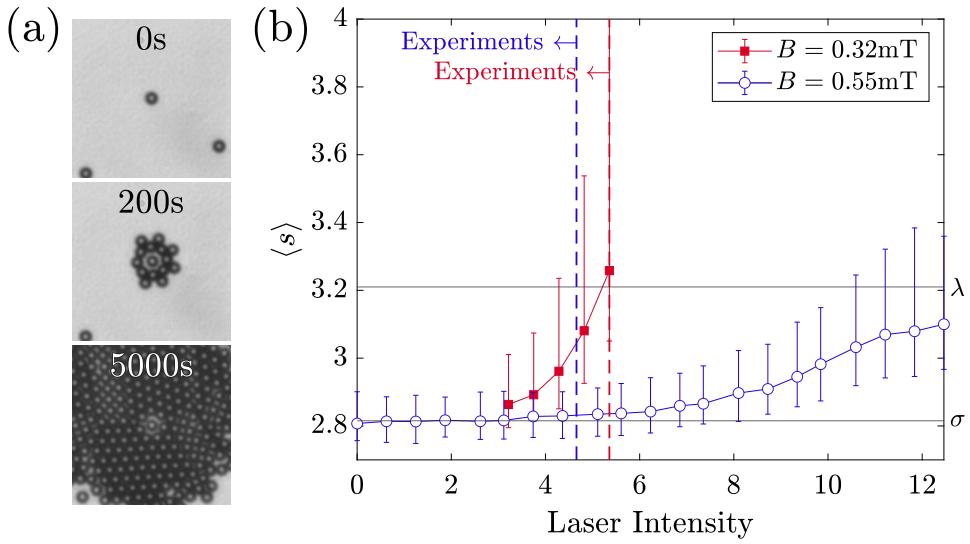


Figure A.3: (a) Time series of a particle in a 400mW trap. (b) Average spacing, $\langle s \rangle$, verses the laser intensity when $B = 0.32\,\mathrm{mT}$ (used in chapter 6) and $B = 0.55\,\mathrm{mT}$ (used in chapters 4 and 5). Vertical red and blue lines show the maximum laser intensity of the experiments in chapters 6 and 4 respectively.

D Chain breakage

Figure A.4 shows the incidence of chain breakage as a function of substrate depth and driving velocity in the experiments in chapter 5. Chain breakage was rare, and mostly happened to long chains in the high friction regime at driving velocities just above their critical velocity.

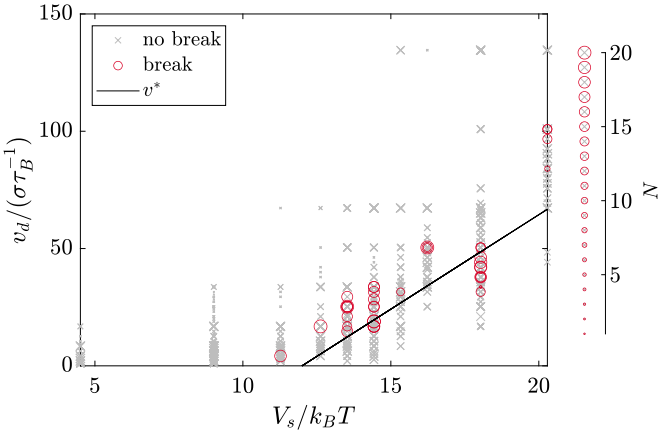


Figure A.4: Measurements at a given substrate depth and driving velocity in which the chain broke (red circles) and didn't break (grey crosses). The size of each point indicates the chain length. The black line is a fit to the critical velocity in strong substrates.

Figure A.5 shows the incidence of chain breakage as a function of driving velocity, oscillation frequency and amplitude in the experiments in chapter 6. The colour indicates the fraction of repeats of a given driving velocity, amplitude and frequency in which the chain broke. The probability of breaking increased with increasing amplitude and decreasing frequency. There was no clear relationship between the breakage probability and the driving velocity.

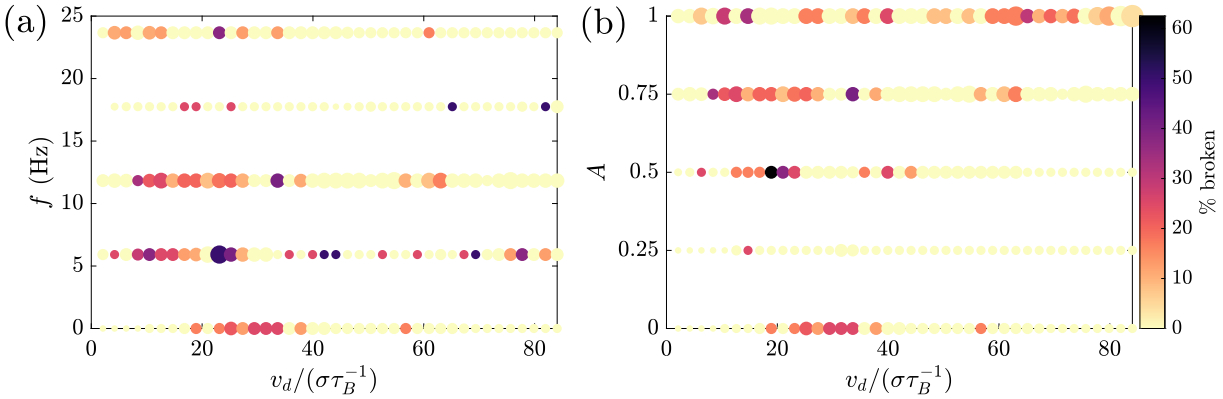


Figure A.5: Percentage of the measurements in which a chain broke at a given driving velocity, v_d and (a) amplitude, A, (when $f = 12\tau_B^{-1}$) and (b) frequency, f, (when $A = 0.75$). The size of the point is proportional to the number of measurements, and the colour indicates the percentage which broke.

Bibliography

[1] X. Zhou, J. Shi, Y. Qi, M. Liu, D. Ma, Y. Zhang, Q. Ji, Z. Zhang, C. Li, Z. Liu, and Y. Zhang. Periodic modulation of the doping level in striped MoS_2 superstructures. *ACS Nano*, 10(3):3461–3468, 2016.

[2] G. Li, L. Huang, W. Xu, Y. Que, Y. Zhang, J. Lu, S. Du, Y. Liu, and H.-J. Gao. Constructing molecular structures on periodic superstructure of graphene/Ru(0001). *Phil. Trans. R. Soc. A.*, 372(2013):20130015, 2014.

[3] S. Tang, Z. Wang, J. Wang, K. Jiang, C. Liang, Y. Ma, W. Liu, and Y. Du. An atomic scale study of two-dimensional quasicrystal nucleation controlled by multiple length scale interactions. *Soft Matter*, 16(24):5718–5726, 2020.

[4] A. V. Kyrylyuk, A. Wouterse, and A. P. Philipse. Percolation and jamming in random heterogeneous materials with competing length scales. In *Trends in Colloid and Interface Science XXIII*, Berlin, Heidelberg, 2010. Springer.

[5] P. S. Salmon and A. Zeidler. Identifying and characterising the different structural length scales in liquids and glasses: an experimental approach. *Phys. Chem. Chem. Phys.*, 15(37):15286–15308, 2013.

[6] M. S. Dresselhaus and G. Dresselhaus. Intercalation compounds of graphite. *Adv. Phys.*, 51(1):1–186, 2002.

[7] Z. M. Stadnik. *Physical properties of quasicrystals*, volume 126. Springer-Verlag, Berlin; Heidelberg, 1998.

[8] A. Pikovsky, M. Rosenblum, and J. Kurths. *Synchronization: A Universal Concept in Nonlinear Sciences*. Cambridge University Press, Cambridge, 2001.

[9] B. Novák and J. J. Tyson. Design principles of biochemical oscillators. *Nat. Rev. Mol.*, 9(12):981–991, 2008.

[10] N. Macdonald. Time delay in prey-predator models. *Math. Biosci.*, 28(3):321–330, 1976.

[11] G. Orosz, R. E. Wilson, and G. Stépán. Traffic jams: dynamics and control. *Philos. Trans. Royal Soc. A*, 368(1928):4455–4479, 2010.

[12] C. Blomberg. *Physics of life: the physicist's road to biology.* Elsevier, Amsterdam, 2007.

[13] D. S. Wilks and R. L. Wilby. The weather generation game: a review of stochastic weather models. *Prog. Phys. Geogr.*, 23(3):329–357, 1999.

[14] U. Seifert. Stochastic thermodynamics, fluctuation theorems and molecular machines. *Rep. Prog. Phys.*, 75(12):126001, 2012.

[15] A. E. Roy. *Orbital motion.* Institute of Physics Publishing, Bristol, 4th ed. edition, 2020.

[16] D. L. Nelson, M. M. Cox, and A. L. Lehninger. *Lehninger principles of biochemistry.* Macmillan, New York; Basingstoke, 5th ed. edition, 2008.

[17] P. Coullet, J. M. Gilli, M. Monticelli, and N. Vandenberghe. A damped pendulum forced with a constant torque. *Am. J. Phys.*, 73(12):1122–1128, 2005.

[18] P. Fulde, L. Pietronero, W. R. Schneider, and S. Strässler. Problem of Brownian motion in a periodic potential. *Phys. Rev. Lett.*, 35(26):1776–1779, 1975.

[19] Y. Dong, A. Vadakkepatt, and A. Martini. Analytical models for atomic friction. *Tribol. Lett.*, 44(3):367, 2011.

[20] C. H. Scholz. *The Mechanics of Earthquakes and Faulting.* Cambridge University Press, Cambridge, 2 edition, 2002.

[21] O. M. Braun and Y. S. Kivshar. *The Frenkel-Kontorova model: concepts, methods, and applications.* Springer, Berlin, 2004.

[22] J. Frenkel and T. Kontorova. On the theory of plastic deformation and twinning. *Izv. Akad. Nauk, Ser. Fiz.*, 1:137–149, 1939.

[23] F. Lançon. Aubry transition in a real material: Prediction for its existence in an incommensurate gold/gold interface. *EPL*, 57(1):74, 2002.

[24] J. B. Sokoloff. Sliding charge-density waves in periodic and disordered lattices. *Phys. Rev. B*, 16(8):3367–3372, 1977.

[25] L. M. Floría and J. J. Mazo. Dissipative dynamics of the Frenkel-Kontorova model. *Adv. Phys.*, 45(6):505–598, 1996.

[26] S. V. Belim and I. V. Tikhomirov. Composition of the Frenkel–Kontorova and Ising models for investigation the magnetic properties of a ferromagnetic monolayer on a stretching substrate. *Sci. Reps.*, 11(1):1–8, 2021.

[27] S. E. Burkov. Magnetization curves for thin films of layered type-II superconductors, Kolmogorov-Arnold-Moser theory, and the devil's staircase. *Phys. Rev. B*, 44:2850–2852, 1991.

[28] S. Homma and S. Takeno. A coupled base-rotator model for structure and dynamics of DNA: Local fluctuations in helical twist angles and topological solitons. *Prog. Theor. Phys.*, 72(4):679–693, 1984.

[29] J. Clopés, J. Shin, M. Jahnel, S. W. Grill, and V. Zaburdaev. Thermal fluctuations assist mechanical signal propagation in coiled-coil proteins. *Phys. Rev. E*, 104(5):054403, 2021.

[30] P Bak. Commensurate phases, incommensurate phases and the devil's staircase. *Rep. Prog. Phys.*, 45(6):587–629, 1982.

[31] M. Peyrard and S. Aubry. Critical behaviour at the transition by breaking of analyticity in the discrete Frenkel-Kontorova model. *J. Phys. C: Solid State Phys.*, 16(9):1593–1608, 1983.

[32] O. M. Braun and Y. S. Kivshar. Nonlinear dynamics of the Frenkel-Kontorova model. *Phys. Rep.*, 306(1):1–108, 1998.

[33] O. M. Braun, Y. S. Kivshar, and I. I. Zelenskaya. Kinks in the Frenkel-Kontorova model with long-range interparticle interactions. *Phys. Rev. B*, 41(10):7118–7138, 1990.

[34] D. A. Gangloff, A. Bylinskii, and V. Vuletić. Kinks and nanofriction: Structural phases in few-atom chains. *Phys. Rev. Research*, 2(1):013380, 2020.

[35] M. Dienwiebel, G. S. Verhoeven, N. Pradeep, J. W. M. Frenken, J. A. Heimberg, and H. W. Zandbergen. Superlubricity of graphite. *Phys. Rev. Lett.*, 92(12):1–4, 2004.

[36] Z. Liu, J. Yang, F. Grey, J. Z. Liu, Y. Liu, Y. Wang, Y. Yang, Y. Cheng, and Q. Zheng. Observation of microscale superlubricity in graphite. *Phys. Rev. Lett.*, 108(20):205503, 2012.

[37] R. Zhang, Z. Ning, Y. Zhang, Q. Zheng, Q. Chen, H. Xie, Q. Zhang, W. Qian, and F. Wei. Superlubricity in centimetres-long double-walled carbon nanotubes under ambient conditions. *Nat. Nanotechnol.*, 8(12):912–916, 2013.

[38] D. Berman, S. A. Deshmukh, S. K. R. S. Sankaranarayanan, A. Erdemir, and A. V. Sumant. Macroscale superlubricity enabled by graphene nanoscroll formation. *Science*, 348(6239):1118–1122, 2015.

[39] D. Mandelli, I. Leven, O. Hod, and M. Urbakh. Sliding friction of graphene/hexagonal –boron nitride heterojunctions: a route to robust superlubricity. *Sci. Rep.*, 7(1):10851, 2017.

[40] F. Lançon, J. Ye, D. Caliste, T. Radetic, A. M. Minor, and U. Dahmen. Superglide at an internal incommensurate boundary. *Nano Lett.*, 10(2):695–700, 2010.

[41] C. C. Grimes and S. Shapiro. Millimeter-Wave Mixing with Josephson Junctions. *Phys. Rev.*, 169:397–406, 1968.

[42] S. Jeon, T. Thundat, and Y. Braiman. Effect of normal vibration on friction in the atomic force microscopy experiment. *Appl. Phys. Lett.*, 88(21):214102, 2006.

[43] W. Poon. Colloids as big atoms. *Science*, 304(5672):830–831, 2004.

[44] D. F. Evans and H. Wennerström. *The Colloidal Domain: Where Physics, Chemistry, Biology, and Technology Meet.* Wiley, New York, 1999.

[45] W. Norde. *Colloids and interfaces in life sciences and bionanotechnology.* CRC Press, Boca Raton; London; New York, 2nd ed. edition, 2011.

[46] T. F. Tadros. *Handbook of colloid and interface science: Volume 3, Industrial applications : Pharmaceuticals, cosmetics and personal care.* De Gruyter Reference, Berlin; Boston, 2018.

[47] T. F. Tadros. *Handbook of colloid and interface science: Volume 4, Industrial applications II : agrochemicals, paints, coatings and food systems.* De Gruyter Reference, Berlin; Boston, 2018.

[48] J. P. Hansen, D. Levesque, and J. Zinn-Justin. *Liquids, freezing and glass transition, Pt. 2.* Elsevier, Amsterdam, 1991.

[49] A. Einstein. Über die von der molekularkinetischen theorie der wärme geforderte bewegung von in ruhenden flüssigkeiten suspendierten teilchen. *Annalen der Physik*, 322(8):549–560, 1905.

[50] J. K. G. Dhont. *An introduction to dynamics of colloids.* Elsevier, Amsterdam, 1996.

[51] J. C. Crocker and D. G. Grier. Microscopic measurement of the pair interaction potential of charge-stabilized colloid. *Phys. Rev. Lett.*, 73(2):352–355, 1994.

[52] A. Vrij. Polymers at interfaces and the interactions in colloidal dispersions. *Colloids Surf.*, 48(4):471–483, 1976.

[53] W. C. K. Poon. The physics of a model colloid–polymer mixture. *J. Condens. Matter Phys.*, 14(33):R859, 2002.

[54] A. Kuijk, T. Troppenz, L. Filion, A. Imhof, R. van Roij, M. Dijkstra, and A. van Blaaderen. Effect of external electric fields on the phase behavior of colloidal silica rods. *Soft Matter*, 10(33):6249–6255, 2014.

[55] A. Spatafora-Salazar, D. M. Lobmeyer, L. H. P. Cunha, K. Joshi, and S. L. Biswal. Hierarchical assemblies of superparamagnetic colloids in time-varying magnetic fields. *Soft Matter*, 17(5):1120–1155, 2021.

[56] Y. Lan, A. Caciagli, G. Guidetti, Z. Yu, J. Liu, V. E. Johansen, M. Kamp, C. Abell, S. Vignolini, O. A. Scherman, and E. Eiser. Unexpected stability of aqueous dispersions of raspberry-like colloids. *Nat. Commun.*, 9(1):3614, 2018.

[57] Y. Liu, K. V. Edmond, A. Curran, C. Bryant, B. Peng, D. G. A. L. Aarts, S. Sacanna, and R. P. A. Dullens. Core–shell particles for simultaneous 3d imaging and optical tweezing in dense colloidal materials. *Adv. Mater.*, 28(36):8001–8006, 2016.

[58] S. Sacanna and D. J. Pine. Shape-anisotropic colloids: Building blocks for complex assemblies. *Curr. Opin. Colloid Interface Sci.*, 16(2):96–105, 2011.

[59] C Fernández-Rico, M. Chiappini, T. Yanagishima, H. de Sousa, D. G. A. L. Aarts, M. Dijkstra, and R. P. A. Dullens. Shaping colloidal bananas to reveal biaxial, splay-bend nematic, and smectic phases. *Science*, 369(6506):950–955, 2020.

[60] A. Kuijk, A. van Blaaderen, and A. Imhof. Synthesis of monodisperse, rodlike silica colloids with tunable aspect ratio. *J. Am. Chem. Soc.*, 133(8):2346–2349, 2011.

[61] Z. Gong, T. Hueckel, G.-R. Yi, and S. Sacanna. Patchy particles made by colloidal fusion. *Nature*, 550(7675):234–238, 2017.

[62] J.-M. Meijer, V. Meester, F. Hagemans, H. N. W. Lekkerkerker, A. P. Philipse, and A. V. Petukhov. Convectively assembled monolayers of colloidal cubes: Evidence of optimal packings. *Langmuir*, 35(14):4946–4955, 2019.

[63] P. N. Pusey and W. van Megen. Phase behaviour of concentrated suspensions of nearly hard colloidal spheres. *Nature*, 320(6060):340–342, 1986.

[64] A. L. Thorneywork, D. G. A. L. Aarts, J. Horbach, and R. P. A. Dullens. Self-diffusion in two-dimensional binary colloidal hard-sphere fluids. *Phys. Rev. E*, 95(1):012614, 2017.

[65] A. L. Thorneywork, J. L. Abbott, D. G. A. L. Aarts, and R. P. A. Dullens. Two-dimensional melting of colloidal hard spheres. *Phys. Rev. Lett.*, 118(15):158001, 2017.

[66] F. A. Lavergne, D. G. A. L. Aarts, and R. P. A. Dullens. Anomalous grain growth in a polycrystalline monolayer of colloidal hard spheres. *Phys. Rev. X*, 7:041064, 2017.

[67] N. H. P. Orr, T. Yanagishima, I. P. Dolbnya, A. V. Petukhov, and R. P. A. Dullens. Single-orientation colloidal crystals from capillary-action-induced shear. *J. Chem. Phys.*, 157(22):224903, 2022.

[68] R. Wittmann, L. B. G. Cortes, H. Löwen, and D. G. A. L. Aarts. Particle-resolved topological defects of smectic colloidal liquid crystals in extreme confinement. *Nat. Commun.*, 12(1):623, 2021.

[69] A. Kuijk, D. V. Byelov, A. V. Petukhov, A. van Blaaderen, and A. Imhof. Phase behavior of colloidal silica rods. *Faraday Discuss.*, 159(0):181–199, 2012.

[70] S. Vivek, C. P. Kelleher, P. M. Chaikin, and E. R. Weeks. Long-wavelength fluctuations and the glass transition in two dimensions and three dimensions. *Proc. Natl. Acad. Sci. U.S.A*, 114(8):1850–1855, 2017.

[71] E. Zaccarelli. Colloidal gels: equilibrium and non-equilibrium routes. *J. Condens. Matter Phys.*, 19(32):323101, 2007.

[72] M. P. N. Juniper, A. V. Straube, R. Besseling, D. G. A. L. Aarts, and R. P. A. Dullens. Microscopic dynamics of synchronization in driven colloids. *Nat. Commun.*, 6(1):7187, 2015.

[73] T. O. E. Skinner, D. G. A. L. Aarts, and R. P. A. Dullens. Grain-Boundary Fluctuations in Two-Dimensional Colloidal Crystals. *Phys. Rev. Lett.*, 105(16):168301, 2010.

[74] A. Vanossi, C. Bechinger, and M. Urbakh. Structural lubricity in soft and hard matter systems. *Nat. Commun.*, 11(1):4657, 2020.

[75] J. D. Hutchinson, F. A. Lavergne, and R. P. A. Dullens. Crystallization and grain growth in impurity-doped colloidal polycrystals. *Phys. Rev. Mater.*, 6(7):075604, 2022.

[76] T. Bohlein, J. Mikhael, and C. Bechinger. Observation of kinks and antikinks in colloidal monolayers driven across ordered surfaces. *Nat. Mater.*, 11(2):126–130, 2012.

[77] P. Tierno. Geometric frustration of colloidal dimers on a honeycomb magnetic lattice. *Phys. Rev. Lett.*, 116(3):038303, 2016.

[78] P. Tierno, S. V. Reddy, M. G. Roper, T. H. Johansen, and T. M. Fischer. Transport and separation of biomolecular cargo on paramagnetic colloidal particles in a magnetic ratchet. *J. Phys. Chem. B*, 112(12):3833–3837, 2008.

[79] F. Martinez-Pedrero and P. Tierno. Magnetic Propulsion of Self-Assembled Colloidal Carpets: Efficient Cargo Transport via a Conveyor-Belt Effect. *Phys. Rev. Applied*, 3(5):051003, 2015.

[80] A. van Blaaderen, M. Dijkstra, R. van Roij, A. Imhof, M. Kamp, B. W. Kwaadgras, T. Vissers, and B. Liu. Manipulating the self assembly of colloids in electric fields. *Eur. Phys. J. Spec. Top.*, 222(11):2895–2909, 2013.

[81] A. Ashkin. Acceleration and trapping of particles by radiation pressure. *Phys. Rev. Lett.*, 24(4):156–159, 1970.

[82] P. H. Jones, O. M. Maragó, and G. Volpe. *Optical Tweezers: Principles and Applications.* Cambridge University Press, Cambridge, 2015.

[83] R. R. Brau, J. M. Ferrer, H. Lee, C. E. Castro, B. K. Tam, P. B. Tarsa, P. Matsudaira, M. C. Boyce, R. D. Kamm, and M. J. Lang. Passive and active microrheology with optical tweezers. *J. Opt. A: Pure Appl. Opt.*, 9(8):S103, 2007.

[84] I. Buttinoni and R. P. A. Dullens. Mechanical properties of colloidal crystals at fluid interfaces. *J. Phys. Chem. Mater.*, 4(2):025001, 2021.

[85] L. G. Wilson, A. W. Harrison, A. B. Schofield, J. Arlt, and W. C. K. Poon. Passive and active microrheology of hard-sphere colloids. *J. Phys. Chem. B*, 113(12):3806–3812, 2009.

[86] A. Mossa, M. Manosas, N. Forns, J. M. Huguet, and F. Ritort. Dynamic force spectroscopy of dna hairpins: I. force kinetics and free energy landscapes. *J. Stat. Mech. Theory Exp.*, 2009(02):P02060, 2009.

[87] J.-P. Collet, H. Shuman, R. E. Ledger, S. Lee, and J. W. Weisel. The elasticity of an individual fibrin fiber in a clot. *Proc. Natl. Acad. Sci. U.S.A*, 102(26):9133–9137, 2005.

[88] J. C. Crocker, J. A. Matteo, A. D. Dinsmore, and A. G. Yodh. Entropic attraction and repulsion in binary colloids probed with a line optical tweezer. *Phys. Rev. Lett.*, 82(21):4352–4355, 1999.

[89] M. Polin, Y. Roichman, and D. G. Grier. Autocalibrated colloidal interaction measurements with extended optical traps. *Phys. Rev. E*, 77(5):051401, 2008.

[90] R. D. L. Hanes, C. Dalle-Ferrier, M. Schmiedeberg, M. C. Jenkins, and S. U. Egelhaaf. Colloids in one dimensional random energy landscapes. *Soft Matter*, 8(9):2714–2723, 2012.

[91] F. Evers, R. D. L. Hanes, C. Zunke, R. F. Capellmann, J. Bewerunge, C. Dalle-Ferrier, M. C. Jenkins, I. Ladadwa, A. Heuer, R. Castañeda-Priego, and S. U. Egelhaaf. Colloids in light fields: Particle dynamics in random and periodic energy landscapes. *Eur. Phys. J. Spec. Top.*, 222(11):2995, 2013.

[92] F. Evers, C. Zunke, R. D. L. Hanes, J. Bewerunge, I. Ladadwa, A. Heuer, and S. U. Egelhaaf. Particle dynamics in two-dimensional random-energy landscapes: Experiments and simulations. *Phys. Rev. E*, 88(2):022125, 2013.

[93] A. Chowdhury, B. J. Ackerson, and N. A. Clark. Laser-induced freezing. *Phys. Rev. Lett.*, 55(8):833–836, 1985.

[94] K. Mangold, P. Leiderer, and C. Bechinger. Phase transitions of colloidal monolayers in periodic pinning arrays. *Phys. Rev. Lett.*, 90:158302, 2003.

[95] R. F. Capellmann, A. Khisameeva, F. Platten, and S. U. Egelhaaf. Dense colloidal mixtures in an external sinusoidal potential. *J. Chem. Phys.*, 148(11):114903, 2018.

[96] A. S. Nunes, S. K. P. Velu, I. Kasianiuk, D. Kasyanyuk, A. Callegari, G. Volpe, M. M. Telo da Gama, G. Volpe, and N. A. M. Araújo. Ordering of binary colloidal crystals by random potentials. *Soft Matter*, 16(17):4267–4273, 2020.

[97] M. P. MacDonald, G. C. Spalding, and K. Dholakia. Microfluidic sorting in an optical lattice. *Nature*, 426(6965):421–424, 2003.

[98] K. Ladavac, K. Kasza, and D. G. Grier. Sorting mesoscopic objects with periodic potential landscapes: Optical fractionation. *Phys. Rev. E*, 70(1):010901, 2004.

[99] S.-H. Lee, K. Ladavac, M. Polin, and D. G. Grier. Observation of flux reversal in a symmetric optical thermal ratchet. *Phys. Rev. Lett.*, 94:110601, 2005.

[100] J. L. Abbott, A. V. Straube, Aarts D. G. A. L., and Dullens R. P. A. Transport of a colloidal particle driven across a temporally oscillating optical potential energy landscape. *New J. Phys.*, 21(8):083027, 2019.

[101] I. Williams, E. C. Oğuz, T. Speck, P. Bartlett, H. Löwen, and C. P. Royall. Transmission of torque at the nanoscale. *Nat. Phys.*, 12(1):98–103, 2015.

[102] Y. Sokolov, D. Frydel, D. G. Grier, H. Diamant, and Y. Roichman. Hydrodynamic pair attractions between driven colloidal particles. *Phys. Rev. Lett.*, 107(15):158302, 2011.

[103] T. Bohlein and C. Bechinger. Experimental observation of directional locking and dynamical ordering of colloidal monolayers driven across quasiperiodic substrates. *Phys. Rev. Lett.*, 109(5):058301, 2012.

[104] G. M. Wang, E. M. Sevick, E. Mittag, D. J. Searles, and D. J. Evans. Experimental demonstration of violations of the second law of thermodynamics for small systems and short time scales. *Phys. Rev. Lett.*, 89(5):050601, 2002.

[105] V. Blickle, T. Speck, L. Helden, U. Seifert, and C. Bechinger. Thermodynamics of a colloidal particle in a time-dependent nonharmonic potential. *Phys. Rev. Lett.*, 96(7):70603, 2006.

[106] T. M. Hoang, R. Pan, J. Ahn, J. Bang, H. T. Quan, and T. Li. Experimental test of the differential fluctuation theorem and a generalized Jarzynski equality for arbitrary initial states. *Phys. Rev. Lett.*, 120(8):80602, 2018.

[107] I. A. Martínez, É. Roldán, L. Dinis, D. Petrov, J. M. R. Parrondo, and R. A. Rica. Brownian carnot engine. *Nat. Phys.*, 12(1):67–70, 2016.

[108] T. Admon, S. Rahav, and Y. Roichman. Experimental realization of an information machine with tunable temporal correlations. *Phys. Rev. Lett.*, 121(18):180601, 2018.

[109] S. Toyabe, T. Sagawa, M. Ueda, E. Muneyuki, and M. Sano. Experimental demonstration of information-to-energy conversion and validation of the generalized Jarzynski equality. *Nat. Phys.*, 6(12):988–992, 2010.

[110] B. J. Lopez, N. J. Kuwada, E. M. Craig, B. R. Long, and H. Linke. Realization of a feedback controlled flashing ratchet. *Phys. Rev. Lett.*, 101(22):220601, 2008.

[111] G. Paneru and H. K. Pak. Colloidal engines for innovative tests of information thermodynamics. *Adv. Phys-X*, 5(1):1823880, 2020.

[112] J. Happel and H. Brenner. *Low Reynolds number hydrodynamics: with special applications to particulate media.* Martinus Nijhoff Publishers, The Hague, 1st edition, 1983.

[113] D. S. Lemons and A. Gythiel. Paul Langevin's 1908 paper "On the Theory of Brownian Motion" ["Sur la théorie du mouvement brownien," C. R. Acad. Sci. (Paris) 146, 530–533 (1908)]. *Am. J. Phys.*, 65(11):1079–1081, 1997.

[114] L. Peliti and S. Pigolotti. *Stochastic Thermodynamics: An Introduction*. Princeton University Press, Princeton, 2021.

[115] R. J. Hunter. *Foundations of colloid science*. Oxford University Press, Oxford, 2nd edition, 2001.

[116] J. Leach, H. Mushfique, S. Keen, R. Di Leonardo, G. Ruocco, J. M. Cooper, and M. J. Padgett. Comparison of Faxén's correction for a microsphere translating or rotating near a surface. *Phys. Rev. E*, 79(2):026301, 2009.

[117] H. C. Hamaker. The London-van der Waals attraction between spherical particles. *Physica*, 4(10):1058–1072, 1937.

[118] A. L. Thorneywork, R. Roth, D. G. A. L. Aarts, and R. P. A. Dullens. Communication: Radial distribution functions in a two-dimensional binary colloidal hard sphere system. *J. Chem. Phys.*, 140(16):161106, 2014.

[119] M. J. Santander-Ortega, A. B. Jódar-Reyes, N. Csaba, D. Bastos-González, and J. L. Ortega-Vinuesa. Colloidal stability of Pluronic F68-coated PLGA nanoparticles: A variety of stabilisation mechanisms. *J. Colloid Interface Sci.*, 302(2):522–529, 2006.

[120] G. Fonnum, C. Johansson, A. Molteberg, S. Mørup, and E. Aksnes. Characterisation of Dynabeads® by magnetization measurements and Mössbauer spectroscopy. *J. Magn. Magn. Mater.*, 293(1):41–47, 2005.

[121] D. J. Griffiths. *Introduction to Electrodynamics*. Cambridge University Press, Cambridge, 4th edition, 2017.

[122] A. P. Goutzoulis, D. R. Pape, and S. V. Kulakov. *Design and fabrication of acousto-optic devices*. Dekker, New York, 1994.

[123] M. P. N. Juniper, A. V. Straube, D. G. A. L. Aarts, and R. P. A. Dullens. Colloidal particles driven across periodic optical-potential-energy landscapes. *Phys. Rev. E*, 93(1):012608, 2016.

[124] Thermo Fisher Scientific. Dynabeads™ M-270 carboxylic acid: Catalog number: 14305D. https://www.thermofisher.com/order/catalog/product/14305D?SID=srch-srp-14305D.

[125] M. P. N. Juniper, R. Besseling, D. G. A. L. Aarts, and R. P. A. Dullens. Acousto-optically generated potential energy landscapes: potential mapping using colloids under flow. *Opt. Express*, 20(27):28707, 2012.

[126] M. P. Allen and D. J. Tildesley. *Computer simulation of Liquids*. Oxford University Press, Oxford, 2017.

[127] L. Belloni. Colloidal interactions. *J. Phys.: Condens. Matter*, 12(46):R549, 2000.

[128] W. B. Russel, D. A. Saville, and W. R. Schowalter. *Colloidal dispersions*. Cambridge university press, Cambridge, 1991.

[129] D. T. Grob, N. Wise, O. Oduwole, and S. Sheard. Magnetic susceptibility characterisation of superparamagnetic microspheres. *J. Magn. Magn. Mater.*, 452:134–140, 2018.

[130] W. Schommers. A pair potential for liquid rubidium from the pair correlation function. *Phys. Lett. A*, 43(2):157–158, 1973.

[131] D. Levesque, J. J. Weis, and L. Reatto. Pair interaction from structural data for dense classical liquids. *Phys. Rev. Lett.*, 54(5):451–454, 1985.

[132] A. K. Soper. Empirical potential Monte Carlo simulation of fluid structure. *Chem. Phys.*, 202(2):295–306, 1996.

[133] M. D. Carbajal-Tinoco, F. Castro-Román, and J. L. Arauz-Lara. Static properties of confined colloidal suspensions. *Phys. Rev. E*, 53(4):3745–3749, 1996.

[134] R. Rajagopalan and K. S. Rao. Interaction forces in charged colloids: Inversion of static structure factors. *Phys. Rev. E*, 55(4):4423–4432, 1997.

[135] M. Quesada-Pérez, A. Moncho-Jordá, F. Martínez-López, and R. Hidalgo-Álvarez. Probing interaction forces in colloidal monolayers: Inversion of structural data. *J. Chem. Phys.*, 115(23):10897–10902, 2001.

[136] M. Brunner, C. Bechinger, W. Strepp, V. Lobaskin, and H. H. von Grünberg. Density-dependent pair interactions in 2D. *EPL*, 58(6):926, 2002.

[137] C. P. Royall, M. E. Leunissen, and A. van Blaaderen. A new colloidal model system to study long-range interactions quantitatively in real space. *J. Phys.: Condens. Matter*, 15(48):S3581, 2003.

[138] C. R. Iacovella, R. E. Rogers, S. C. Glotzer, and M. J. Solomon. Pair interaction potentials of colloids by extrapolation of confocal microscopy measurements of collective suspension structure. *J. Chem. Phys.*, 133(16):164903, 2010.

[139] S.-Y. Huang and X. Zou. Statistical mechanics-based method to extract atomic distance-dependent potentials from protein structures. *Proteins*, 79(9):2648–2661, 2011.

[140] A. E. Stones, R. P. A. Dullens, and D. G. A. L. Aarts. Model-free measurement of the pair potential in colloidal fluids using optical microscopy. *Phys. Rev. Lett.*, 123(9):098002, 2019.

[141] J. Kotar, M. Vilfan, N. Osterman, D. Babič, M. Čopič, and I. Poberaj. Interparticle potential and drag coefficient in nematic colloids. *Phys. Rev. Lett.*, 96(20):207801, 2006.

[142] S. K. Sainis, V. Germain, and E. R. Dufresne. Statistics of particle trajectories at short time intervals reveal fn-scale colloidal forces. *Phys. Rev. Lett.*, 99(1):018303, 2007.

[143] K. Kegler, M. Salomo, and F. Kremer. Forces of interaction between DNA-grafted colloids: An optical tweezer measurement. *Phys. Rev. Lett.*, 98(5):058304, 2007.

[144] D. L. El Masri, P. van Oostrum, F. Smallenburg, T. Vissers, A. Imhof, M. Dijkstra, and A. van Blaaderen. Measuring colloidal forces from particle position deviations inside an optical trap. *Soft Matter*, 7(7):3462–3466, 2011.

[145] B. J. Park and E. M. Furst. Attractive interactions between colloids at the oil–water interface. *Soft Matter*, 7(17):7676–7682, 2011.

[146] K. Takahashi, M. Ichikawa, and Y. Kimura. Direct measurement of force between colloidal particles in a nematic liquid crystal. *J. Phys. Condens. Matter*, 20(7):075106, 2008.

[147] J. Baumgartl, J. L. Arauz-Lara, and C. Bechinger. Like-charge attraction in confinement: myth or truth? *Soft Matter*, 2(8):631–635, 2006.

[148] P. L. Biancaniello and J. C. Crocker. Line optical tweezers instrument for measuring nanoscale interactions and kinetics. *Rev. Sci. Instrum.*, 77(11):113702, 2006.

[149] J. Crocker and D. Grier. Methods of digital video microscopy for colloidal studies. *J. Colloid Interface Sci.*, 179(1):298–310, 1996.

[150] R. Verma, J. C. Crocker, T. C. Lubensky, and A. G. Yodh. Entropic colloidal interactions in concentrated DNA solutions. *Phys. Rev. Lett.*, 81(18):4004–4007, 1998.

[151] J. Dobnikar, M. Brunner, H.-H. von Grünberg, and C. Bechinger. Three-body interactions in colloidal systems. *Phys. Rev. E*, 69(3):031402, 2004.

[152] D. W. Kang, K. H. Choi, S. J. Lee, and B. J. Park. Mapping anisotropic and heterogeneous colloidal interactions via optical laser tweezers. *J. Phys. Chem. Lett.*, 10(8):1691–1697, 2019.

[153] C. P. Reynolds, K. E. Klop, F. A. Lavergne, S. M. Morrow, D. G. A. L. Aarts, and R. P. A. Dullens. Deterministic aggregation kinetics of superparamagnetic colloidal particles. *J. Chem. Phys.*, 143(21):214903, 2015.

[154] T. Palberg. Crystallization kinetics of colloidal model suspensions: recent achievements and new perspectives. *J. Phys.: Condens. Matter*, 26(33):333101, 2014.

[155] T. M. Squires and M. P. Brenner. Like-charge attraction and hydrodynamic interaction. *Phys. Rev. Lett.*, 85(23):4976–4979, 2000.

[156] T. P. Koehler, C. M. Brotherton, and A. M. Grillet. Comparison of interparticle force measurement techniques using optical trapping. *Colloids Surf. A: Physicochem. Eng. Asp.*, 384(1-3):282–288, 2011.

[157] A. van Reenen, Y. Gao, A. H. Bos, A. M. de Jong, M. A. Hulsen, J. M. J. den Toonder, and M. W. J. Prins. Accurate quantification of magnetic particle properties by intra-pair magnetophoresis for nanobiotechnology. *Appl. Phys. Lett.*, 103(4):043704, 2013.

[158] V. Blickle, D. Babič, and C. Bechinger. Evanescent light scattering with magnetic colloids. *Appl. Phys. Lett.*, 87(10):101102, 2005.

[159] P. Li, D. Kilinc, Y.-F. Ran, and G. U. Lee. Flow enhanced non-linear magnetophoretic separation of beads based on magnetic susceptibility. *Lab Chip*, 13(22):4400–4408, 2013.

[160] L. E. Helseth. Paramagnetic particles as sensitive force detectors in liquids. *J. Phys. D.*, 40(10):3030–3037, 2007.

[161] D. Du, F. Toffoletto, and S. L. Biswal. Numerical calculation of interaction forces between paramagnetic colloids in two-dimensional systems. *Phys. Rev. E*, 89(4):043306, 2014.

[162] N. Osterman, I. Poberaj, J. Dobnikar, D. Frenkel, P. Ziherl, and D. Babć. Field-induced self-assembly of suspended colloidal membranes. *Phys. Rev. Lett.*, 103(22):228301, 2009.

[163] Tom Skinner. *Two-dimensional colloidal systems: grain boundaries and confinement.* PhD thesis, University of Oxford, 2012.

[164] A. T. Pham, R. Seto, J. Schönke, D. Y. Joh, A. Chilkoti, E. Fried, and B. B. Yellen. Crystallization kinetics of binary colloidal monolayers. *Soft Matter*, 12(37):7735–7746, 2016.

[165] D. Du, D. Li, M. Thakur, and S. L. Biswal. Generating an in situ tunable interaction potential for probing 2-D colloidal phase behavior. *Soft Matter*, 9(29):6867–6875, 2013.

[166] S. C. Erwin, A. A. Baski, L. J. Whitman, and R. E. Rudd. Frenkel-Kontorova model of vacancy-line interactions on Ga/Si(112). *Phys. Rev. Lett.*, 83(9):1818–1821, 1999.

[167] J. C. Hamilton, R. Stumpf, K. Bromann, M. Giovannini, K. Kern, and H. Brune. Dislocation structures of submonolayer films near the commensurate-incommensurate phase transition: Ag on Pt(111). *Phys. Rev. Lett.*, 82(22):4488–4491, 1999.

[168] L. Trallori. Magnetic superlattices, classical spin chains, and the Frenkel-Kontorova model. *Phys. Rev. B*, 57(10):5923–5932, 1998.

[169] T. M. Paronyan, A. K. Thapa, A. Sherehiy, J. B. Jasinski, and J. S. D. Jangam. Exceptional lithium intercalation capacity of incommensurate graphene foam in rechargeable batteries. *ECS Trans.*, 77(11):311, 2017.

[170] J. Cumings and A. Zettl. Low-friction nanoscale linear bearing realized from multiwall carbon nanotubes. *Science*, 289(5479):602–604, 2000.

[171] S. Kawai, A. Benassi, E. Gnecco, H. Söde, R. Pawlak, X. Feng, K. Müllen, D. Passerone, C. A. Pignedoli, P. Ruffieux, R. Fasel, and E. Meyer. Superlubricity of graphene nanoribbons on gold surfaces. *Science*, 351(6276):957–961, 2016.

[172] Y. He, D. She, Z. Liu, X. Wang, L. Zhong, C. Wang, G. Wang, and S. X. Mao. Atomistic observation on diffusion-mediated friction between single-asperity contacts. *Nat. Mater.*, 21(2):173–180, 2022.

[173] P. M. Derlet, D. Nguyen-Manh, and S. L. Dudarev. Multiscale modeling of crowdion and vacancy defects in body-centered-cubic transition metals. *Phys. Rev. B*, 76(5):054107, 2007.

[174] S. P. Fitzgerald. Kink pair production and dislocation motion. *Sci. Rep.*, 6(1):39708, 2016.

[175] B. van der Meer, R. van Damme, M. Dijkstra, F. Smallenburg, and L. Filion. Revealing a vacancy analog of the crowdion interstitial in simple cubic crystals. *Phys. Rev. Lett.*, 121(25):258001, 2018.

[176] R. Ji, T. Phan, H. Chen, and L. Xiong. Quantifying the dynamics of dislocation kinks in iron and tungsten through atomistic simulations. *Int. J. Plast.*, 128:102675, 2020.

[177] V. A. Ivanov and Y. Mishin. Dynamics of grain boundary motion coupled to shear deformation: An analytical model and its verification by molecular dynamics. *Phys. Rev. B*, 78(6):064106, 2008.

[178] D. Ricinschi, Y. Ishibashi, and M. Okuyama. Theoretical study of atomic relaxation in 90° domain walls of ferroelectric perovskite films. *Jpn. J. Appl. Phys.*, 43(9S):6803, 2004.

[179] Y. Braiman, J. Baumgarten, J. Jortner, and J. Klafter. Symmetry-breaking transition in finite Frenkel-Kontorova chains. *Phys. Rev. Lett.*, 65(19):2398–2401, 1990.

[180] S. R. Sharma, B. Bergersen, and B. Joos. Aubry transition in a finite modulated chain. *Phys. Rev. B*, 29(11):6335–6340, 1984.

[181] A. Bylinskii, D. Gangloff, I. Counts, and V. Vuletić. Observation of Aubry-type transition in finite atom chains via friction. *Nat. Mater.*, 15(7):717–721, 2016.

[182] J. Kiethe, R. Nigmatullin, D. Kalincev, T. Schmirander, and T. E. Mehlstäubler. Probing nanofriction and Aubry-type signatures in a finite self-organized system. *Nat. Commun.*, 8(1):15364, 2017.

[183] J. Kiethe, R. Nigmatullin, T. Schmirander, D. Kalincev, and T. E. Mehlstäubler. Nanofriction and motion of topological defects in self-organized ion coulomb crystals. *New J. Phys.*, 20(12):123017, 2018.

[184] T. Brazda, A. Silva, N. Manini, A. Vanossi, R. Guerra, E. Tosatti, and C. Bechinger. Experimental observation of the Aubry transition in two-dimensional colloidal monolayers. *Phys. Rev. X*, 8(1):011050, 2018.

[185] I. Markov and A. Trayanov. Epitaxial interfaces with realistic inter-atomic forces. *J. Phys. C: Solid State Phys.*, 21(13):2475, 1988.

[186] O. Biham and D. Mukamel. Global universality in the Frenkel-Kontorova model. *Phys. Rev. A*, 39(10):5326–5335, 1989.

[187] Y. Braiman, J. Baumgarten, and J. Klafter. Symmetry properties of finite Frenkel-Kontorova chains. *Phys. Rev. B*, 47(17):11159–11166, 1993.

[188] O.M. Braun. Adiabatic motion of an atomic chain in periodic potential. *Surf. Sci.*, 230(1-3):262–276, 1990.

[189] Joshua L Abbott. *Driven colloidal particles in optical potential energy landscapes*. Thesis, University of Oxford, 2018.

[190] K. Yang, C. Lu, X. Zhao, and R. Kawamura. From bead to rod: Comparison of theories by measuring translational drag coefficients of micron-sized magnetic bead-chains in Stokes flow. *PLoS One*, 12(11):e0188015, 2017.

[191] D. Mandelli, A. Vanossi, M. Invernizzi, S. Paronuzzi, N. Manini, and E. Tosatti. Superlubric-pinned transition in sliding incommensurate colloidal monolayers. *Phys. Rev. B*, 92(13):134306, 2015.

[192] G. Pesce, G. Volpe, O. M. Maragó, P. H. Jones, S. Gigan, A. Sasso, and G. Volpe. Step-by-step guide to the realization of advanced optical tweezers. *J. Opt. Soc. Am. B*, 32(5):B84–B98, 2015.

[193] I. M. Kulić and H. Schiessel. Chromatin dynamics: Nucleosomes go mobile through twist defects. *Phys. Rev. Lett.*, 91(14):148103, 2003.

[194] W. Quapp and J. M. Bofill. Description of zero field steps on the potential energy surface of a Frenkel-Kontorova model for annular Josephson junction arrays. *EPJ B*, 94(5):105, 2021.

[195] K. Holmberg and A. Erdemir. Global impact of friction on energy consumption, economy and environment. *Fme Trans*, 43(3):181–185, 2015.

[196] O. Hod, E. Meyer, Q. Zheng, and M. Urbakh. Structural superlubricity and ultralow friction across the length scales. *Nature*, 563(7732):485–492, 2018.

[197] W. Wang, J. Shen, and Q.-C. He. Microscale superlubricity of graphite under various twist angles. *Phys. Rev. B*, 99(5):054103, 2019.

[198] C. C. Vu, S. Zhang, M. Urbakh, Q. Li, Q.-C. He, and Q. Zheng. Observation of normal-force-independent superlubricity in mesoscopic graphite contacts. *Phys. Rev. B*, 94(8):081405, 2016.

[199] K. Shinjo and M. Hirano. Dynamics of friction: superlubric state. *Surf. Sci.*, 283(1-3):473–478, 1993.

[200] E. Gao, B. Wu, Y. Wang, X. Jia, W. Ouyang, and Z. Liu. Computational prediction of superlubric layered heterojunctions. *ACS Appl. Mater. Interfaces*, 13(28):33600–33608, 2021.

[201] J. Yuan, R. Yang, and G. Zhang. Structural superlubricity in 2D van der Waals heterojunctions. *Nanotechnology*, 33(10):102002, 2022.

[202] A. E. Filippov, M. Dienwiebel, J. W. M. Frenken, J. Klafter, and M. Urbakh. Torque and twist against superlubricity. *Phys. Rev. Lett.*, 100(4):046102, 2008.

[203] D. Zhang, Z. Li, L. H. Klausen, Q. Li, and M. Dong. Friction behaviors of two-dimensional materials at the nanoscale. *Mater. Today Phys.*, 27:100771, 2022.

[204] D. Dietzel, J. Brndiar, I. Štich, and A. Schirmeisen. Limitations of structural superlubricity: Chemical bonds versus contact size. *ACS Nano*, 11(8):7642–7647, 2017.

[205] M. M. van Wijk, M. Dienwiebel, J. W. M. Frenken, and A. Fasolino. Superlubric to stick-slip sliding of incommensurate graphene flakes on graphite. *Phys. Rev. B*, 88(23):235423, 2013.

[206] L. Gigli, N. Manini, A. Benassi, E. Tosatti, A. Vanossi, and R. Guerra. Graphene nanoribbons on gold: understanding superlubricity and edge effects. *2D Mater.*, 4(4):045003, 2017.

[207] H. Zhang and T. Chang. Edge orientation dependent nanoscale friction. *Nanoscale*, 10(5):2447–2453, 2018.

[208] N. Varini, A. Vanossi, R. Guerra, D. Mandelli, R. Capozza, and E. Tosatti. Static friction scaling of physisorbed islands: the key is in the edge. *Nanoscale*, 7(5):2093–2101, 2015.

[209] C. Qu, K. Wang, J. Wang, Y. Gongyang, R. W. Carpick, M. Urbakh, and Q. Zheng. Origin of friction in superlubric graphite contacts. *Phys. Rev. Lett.*, 125(12):126102, 2020.

[210] A. Bylinskii, D. Gangloff, and V. Vuleti. Tuning friction atom-by-atom in an ion-crystal simulator. *Science*, 348(6239):1115–1118, 2015.

[211] T. Brazda, C. July, and C. Bechinger. Experimental observation of Shapiro-steps in colloidal monolayers driven across time-dependent substrate potentials. *Soft Matter*, 13(22):4024–4028, 2017.

[212] M. Gitterman. *The Noisy Pendulum.* World Scientific, Singapore, 2008.

[213] R. L. Stratonovich and R. A. Silverman. *Topics in the theory of random noise.* Mathematics and its applications; vol.3. Gordon and Breach, New York, revised english edition, 1963.

[214] I. Markov and V.D. Karaivanov. A one-dimensional model for the mobility of small epitaxial islands II: Sinusoidal potential. *Thin Solid Films*, 65(3):361–372, 1980.

[215] A. Jones. Dynamics of colloidal particles in a circular potential energy landscape. Master's thesis, University of Oxford, 2021.

[216] W. M. van Spengen, G. H. C. J. Wijts, V. Turq, and J. W. M. Frenken. Microscale friction reduction by normal force modulation in MEMS. *J. Adhes. Sci. Technol.*, 24(15-16):2669–2680, 2010.

[217] A. Cochard, L. Bureau, and T. Baumberger. Stabilization of frictional sliding by normal load modulation. *J. Appl. Mech.*, 70(2):220–226, 2003.

[218] L. Yan, Q. Zhang, J. Wang, and J. Yu. Effect of ultrasonic vibration on tribological behavior of carbon-carbon composite. *Tribol. Int.*, 136:469–474, 2019.

[219] S.-S. Yoo and D.-E. Kim. Effects of vibration frequency and amplitude on friction reduction and wear characteristics of silicon. *Tribol. Int.*, 94:198–206, 2016.

[220] P. A. Johnson, H. Savage, M. Knuth, J. Gomberg, and C. Marone. Effects of acoustic waves on stick–slip in granular media and implications for earthquakes. *Nature*, 451(7174):57–60, 2008.

[221] M. Heuberger, C. Drummond, and J. Israelachvili. Coupling of normal and transverse motions during frictional sliding. *J. Phys. Chem. B*, 102(26):5038–5041, 1998.

[222] M. A. Lantz, D. Wiesmann, and B. Gotsmann. Dynamic superlubricity and the elimination of wear on the nanoscale. *Nat. Nanotechnol.*, 4(9):586–591, 2009.

[223] A. Socoliuc, E. Gnecco, S. Maier, O. Pfeiffer, A. Baratoff, R. Bennewitz, and E. Meyer. Atomic-scale control of friction by actuation of nanometer-sized contacts. *Science*, 313(5784):207–210, 2006.

[224] J. Cao and Q. Li. Vibration-induced nanoscale friction modulation on piezoelectric materials. *Friction*, 10(10):1650–1659, 2022.

[225] R. Roth, O. Y. Fajardo, J. J. Mazo, E. Meyer, and E. Gnecco. Lateral vibration effects in atomic-scale friction. *Appl. Phys. Lett.*, 104(8):083103, 2014.

[226] V. C. Kumar and I. M. Hutchings. Reduction of the sliding friction of metals by the application of longitudinal or transverse ultrasonic vibration. *Tribol. Int.*, 37(10):833–840, 2004.

[227] S. Shi, D. Guo, and J. Luo. Micro/atomic-scale vibration induced superlubricity. *Friction*, 9(5):1163–1174, 2021.

[228] R. Capozza, A. Vanossi, A. Vezzani, and S. Zapperi. Triggering frictional slip by mechanical vibrations. *Tribol. Lett.*, 48(1):95–102, 2012.

[229] J. Gao, W. D. Luedtke, and U. Landman. Friction control in thin-film lubrication. *J. Phys. Chem. B*, 102(26):5033–5037, 1998.

[230] X. Mao, V. L. Popov, J. Starcevic, and M. Popov. Reduction of friction by normal oscillations. II. In-plane system dynamics. *Friction*, 5(2):194–206, 2017.

[231] O. Y. Fajardo, E. Gnecco, and J. J. Mazo. Out-of-plane and in-plane actuation effects on atomic-scale friction. *Phys. Rev. B*, 89(7):075423, 2014.

[232] R. Guerra, A. Vanossi, and M. Urbakh. Controlling microscopic friction through mechanical oscillations. *Phys. Rev. E*, 78(3):036110, 2008.

[233] Y. Guo, Z. Wang, Z. Qu, and Y. Braiman. Atomic-scale friction control by vibration using friction force microscope. *Control Eng. Pract.*, 19(11):1387–1397, 2011.

[234] Z. Tshiprut, A. E. Filippov, and M. Urbakh. Tuning diffusion and friction in microscopic contacts by mechanical excitations. *Phys. Rev. Lett.*, 95(1):016101, 2005.

[235] V. Zaloj, M. Urbakh, and J. Klafter. Modifying friction by manipulating normal response to lateral motion. *Phys. Rev. Lett.*, 82(24):4823–4826, 1999.

[236] S N Coppersmith. Overdamped Frenkel-Kontorova model with randomness as a dynamical system: Mode locking and derivation of discrete maps. *Phys. Rev. A*, 36(7):3375–3382, 1987.

[237] F. Falo, L. M. Floría, P. J. Martínez, and J. J. Mazo. Unlocking mechanism in the ac dynamics of the Frenkel-Kontorova model. *Phys. Rev. B*, 48(10):7434–7437, 1993.

[238] L. M. Floría and F. Falo. Shapiro steps in the steady-state dynamics of incommensurate structures. *Phys. Rev. Lett.*, 68(18):2713–2717, 1992.

[239] I. Sokolović, P. Mali, J. Odavić, S. Radošević, S. Y. Medvedeva, A. E. Botha, Y. M. Shukrinov, and J. Tekić. Devil's staircase and the absence of chaos in the dc- and ac-driven overdamped Frenkel-Kontorova model. *Phys. Rev. E*, 96(2):022210, 2017.

[240] J. Tekić, D. He, and B. Hu. Noise effects in the ac-driven Frenkel-Kontorova model. *Phys. Rev. E*, 79(3):036604, 2009.

[241] J. Tekić and B. Hu. Properties of the Shapiro steps in the ac driven Frenkel-Kontorova model with deformable substrate potential. *Phys. Rev. E*, 81(3):036604, 2010.

[242] Y. Wei and Y. Lei. Shapiro steps and chaos in the Frenkel-Kontorova model with substrate lateral vibration. *Phys. Rev. E*, 106(4):044204, 2022.

[243] S. V. P. Ticco, G. Fornasier, N. Manini, G. E. Santoro, E. Tosatti, and A. Vanossi. Subharmonic Shapiro steps of sliding colloidal monolayers in optical lattices. *J. Phys.: Condens. Matter*, 28(13):134006, 2016.

[244] M. P. N. Juniper, U. Zimmermann, A. V. Straube, R. Besseling, D. G. A. L. Aarts, H. Löwen, and R. P. A. Dullens. Dynamic mode locking in a driven colloidal system: experiments and theory. *New J. Phys.*, 19(1):013010, 2017.

[245] L. Gigli, N. Manini, E. Tosatti, R. Guerra, and A. Vanossi. Lifted graphene nanoribbons on gold: from smooth sliding to multiple stick-slip regimes. *Nanoscale*, 10(4):2073–2080, 2018.

[246] M. Z. Baykara, M. R. Vazirisereshk, and A. Martini. Emerging superlubricity: A review of the state of the art and perspectives on future research. *Appl. Phys. Rev.*, 5(4):041102, 2018.

[247] H. Shekhar and R. Dumpala. Overcoming friction and steps towards superlubricity: A review of underlying mechanisms. *Appl. Surf. Sci. Advances*, 6:100175, 2021.

[248] H. S. Leff and A. F. Rex. *Maxwell's demon 2 : entropy, classical and quantum information, computing*. Institute of Physics Pub., Bristol, 2003.

[249] L. Szilard. über die Entropieverminderung in einem thermodynamischen System bei Eingriffen intelligenter Wesen. *Zeitschrift für Physik*, 53(11):840–856, 1929.

[250] Y. N. Kyrychko and S. J. Hogan. On the use of delay equations in engineering applications. *J. Vib. Control*, 16(7-8):943–960, 2010.

[251] J.-P. Richard. Time-delay systems: an overview of some recent advances and open problems. *Automatica*, 39(10):1667–1694, 2003.

[252] Y. Tu. The nonequilibrium mechanism for ultrasensitivity in a biological switch: Sensing by maxwell's demons. *Proc. Natl. Acad. Sci. U.S.A*, 105(33):11737–11741, 2008.

[253] R. K. Schmitt, J. M. R. Parrondo, H. Linke, and J. Johansson. Molecular motor efficiency is maximized in the presence of both power-stroke and rectification through feedback. *New J. Phys.*, 17(6):065011, 2015.

[254] A. Longtin, J. G. Milton, J. E. Bos, and M. C. Mackey. Noise and critical behavior of the pupil light reflex at oscillation onset. *Phys. Rev. A*, 41(12):6992–7005, 1990.

[255] K. Mergenthaler and R. Engbert. Modeling the control of fixational eye movements with neurophysiological delays. *Phys. Rev. Lett.*, 98(13):138104, 2007.

[256] P. S. Grassia. Delay, feedback and quenching in financial markets. *EPJ B*, 17(2):347–362, 2000.

[257] K. Pyragas. Continuous control of chaos by self-controlling feedback. *Phys. Lett. A*, 170(6):421–428, 1992.

[258] P. Hövel and E. Schöll. Control of unstable steady states by time-delayed feedback methods. *Phys. Rev. E*, 72(4):046203, 2005.

[259] T. Albers, D. Müller-Bender, L. Hille, and G. Radons. Chaotic diffusion in delay systems: Giant enhancement by time lag modulation. *Phys. Rev. Lett.*, 128(7):074101, 2022.

[260] S. Kim, S. H. Park, and H.-B. Pyo. Stochastic resonance in coupled oscillator systems with time delay. *Phys. Rev. Lett.*, 82(8):1620–1623, 1999.

[261] L. S. Tsimring and A. Pikovsky. Noise-induced dynamics in bistable systems with delay. *Phys. Rev. Lett.*, 87(25):250602, 2001.

[262] T. Albers, D. Müller-Bender, and G. Radons. Antipersistent random walks in time-delayed systems. *Phys. Rev. E*, 105(6):064212, 2022.

[263] G. Paneru, D. Y. Lee, T. Tlusty, and H. K. Pak. Lossless brownian information engine. *Phys. Rev. Lett.*, 120(2):020601, 2018.

[264] M. Ribezzi-Crivellari and F. Ritort. Large work extraction and the landauer limit in a continuous maxwell demon. *Nat. Phys.*, 15(7):660–664, 2019.

[265] D. Y. Lee, J. Um, G. Paneru, and H. K. Pak. An experimentally-achieved information-driven brownian motor shows maximum power at the relaxation time. *Sci. Rep.*, 8(1):12121, 2018.

[266] G. Paneru, D. Y. Lee, J.-M. Park, J. T. Park, J. D. Noh, and H. K. Pak. Optimal tuning of a brownian information engine operating in a nonequilibrium steady state. *Phys. Rev. E*, 98(5):052119, 2018.

[267] T. K. Saha, J. N. E. Lucero, J. Ehrich, D. A. Sivak, and J. Bechhoefer. Bayesian information engine that optimally exploits noisy measurements. *Phys. Rev. Lett.*, 129(13):130601, 2022.

[268] A. Bérut, A. Arakelyan, A. Petrosyan, S. Ciliberto, R. Dillenschneider, and E. Lutz. Experimental verification of landauer's principle linking information and thermodynamics. *Nature*, 483:187–189, 2012.

[269] D. Hennig. Current control in a tilted washboard potential via time-delayed feedback. *Phys. Rev. E*, 79(4):041114, 2009.

[270] K. Lichtner and S. H. L. Klapp. Feedback-controlled transport in an interacting colloidal system. *EPL*, 92(4):40007, 2010.

[271] H. Ando, K. Takehara, and M. U. Kobayashi. Time-delayed feedback control of diffusion in random walkers. *Phys. Rev. E*, 96(1):012148, 2017.

[272] S. Tarama, S. U. Egelhaaf, and H. Löwen. Traveling band formation in feedback-driven colloids. *Phys. Rev. E*, 100(2):022609, 2019.

[273] R. A. Kopp and S. H. L. Klapp. Persistent motion of a brownian particle subject to repulsive feedback with time delay, 2022.

[274] Y. Liu. *Colloidal particles for confocal microscopy and optical tweezing.* Thesis, University of Oxford, 2017.

[275] S. Guillouzic, I. L'Heureux, and A. Longtin. Small delay approximation of stochastic delay differential equations. *Phys. Rev. E*, 59(4):3970, 1999.

[276] U. Küchler and B. Mensch. Langevins stochastic differential equation extended by a time-delayed term. *Stoch. and Stoch. Rep.*, 40(1-2):23–42, 1992.

[277] U. Seifert. Stochastic thermodynamics: principles and perspectives. *EPJ B*, 64(3):423–431, 2008.

[278] K. Sekimoto. Langevin equation and thermodynamics. *Prog. Theor. Phys*, 130:17–27, 1998.

[279] H. Wang and G. Oster. The stokes efficiency for molecular motors and its applications. *EPL*, 57(1):134, 2002.

[280] T. Sagawa and M. Ueda. Generalized Jarzynski equality under nonequilibrium feedback control. *Phys. Rev. Lett.*, 104(9):90602, 2010.

[281] A. Curran, S. Tuohy, D. G. A. L. Aarts, M. J. Booth, T. Wilson, and R. P. A. Dullens. Decoupled and simultaneous three-dimensional imaging and optical manipulation through a single objective. *Optica*, 1(4):223–226, 2014.

[282] J. R. Howse, R. A. L. Jones, A. J. Ryan, T. Gough, R. Vafabakhsh, and R. Golestanian. Self-motile colloidal particles: From directed propulsion to random walk. *Phys. Rev. Lett.*, 99(4):048102, 2007.

[283] E. A. Codling, M. J. Plank, and S. Benhamou. Random walk models in biology. *J. R. Soc. Interface*, 5(25):813–834, 2008.

Acknowledgements

First and foremost, thank you Roel for being such an amazing tutor, supervisor, table football rival, and provider of (mostly drinkable) tea. Thank you for making Physical Chemistry so enjoyable, making sure I stayed for a PhD, and all the Chemistry dinners, Christmas parties, cups of (mostly drinkable) tea, and spontaneous whiteboard sessions without which this PhD would be a lot less interesting.

I could not name everyone in the group who has contributed scientifically to this thesis, but I am especially grateful to Mike for reigning in the chaos of my Part II, Arran for endless optics help and particularly for my lovely new setup, Berend for simulation code and sharing some of your vast knowledge of the FK model, and Amelia for changing the way I thought about kinks.

Most importantly, a massive thank you to everyone who has made this research group such a supportive, positive, fun environment. Harriet for endless tea breaks, Ruth and Caitlin for general life advice, Balkis for brightening up (and warming up) the big office with your wonderful drawings, Josh, Mike, Louis, Siyu, Ivo, Marianna and Jack for so many memorable Pub Fridays, Arran for an education in everything from minecraft to fly-fishing (but not for the cycling chat) and Ruth for putting up with my endless complaints about Dutch beer.

Joe, thank you for keeping me going throughout this mad adventure with your constant reassurance, support, and great company. I couldn't have done this without the tea breaks, crosswords, pub trips, escapes to Dresden... you know the rest. Also thank you for your very generous proofreading.

Finally, thank you to my amazing family for all of your support and suggestions. I'm sorry I never got the colloids to do the eightsome!